CRICKET INSPIRED FLOW-SENSOR ARRAYS

Ramasubramanian Kottumakulal Jaganatharaja

Graduation committee:
Chairman and secretary:

Prof. dr. ir. A. J. Mouthaan	University of Twente

Promotor:

Prof. dr. ir. G. J. M. Krijnen	University of Twente

Members:

Prof. dr. ir. J.C.T. Eijkel	University of Twente
Prof. J. Casas	University de Tours
Prof. G. Jeronimidis	University of Reading
Prof. K. Grosh	University of Michigan
Dr. ir. R.J. Wiegerink	University of Twente

The research described in this thesis was carried out at the Transducers Science and Technology Group of the MESA$^+$ research institute, University of Twente, The Netherlands. It has been financially supported by the Future and Emergent Technologies arm of the IST Programme under the Customized Intelligent Life-Inspired Arrays (CILIA) project and by the BioEARS Vici grant of the Dutch Technology Foundation (STW/NWO).

Cover design and wood carving by R. Kottumakulal Jaganatharaja.

Printed by Wöhrmann Print Service, Zutphen, The Netherlands.

© R. Kottumakulal Jaganatharaja, Eindhoven, The Netherlands, 2011.
All rights reserved.

ISBN: 978-90-365-3215-0
DOI: 10.3990./1.9789036532150

CRICKET INSPIRED FLOW-SENSOR ARRAYS

DISSERTATION

to obtain
the degree of doctor at the University of Twente,
on the authority of the rector magnificus,
Prof. dr. H. Brinksma,
on account of the decision of the graduation committee,
to be publicly defended
on Wednesday, 29 June 2011 at 16:45 hrs.

by

Ramasubramanian Kottumakulal Jaganatharaja
born on 24 Decemeber 1980
in Rajapalayam, India

This dissertation has been approved by:

The promoter: Prof. dr. ir. G. J. M. Krijnen

Dedication

To my parents

இன்னொரு பிறவி...
இன்னொரு உலகம்...
இன்னொரு தடவை...

என்னைப்
பொறுத்துக் கொள்வீர்களெனில்...

இன்னொரு பிறவி...
இன்னொரு உலகம்...
இன்னுமொரு தடவை...

உங்களுக்கே
பிறந்து கொள்ளட்டுமா?

Table of contents

1

Artificial hair sensor arrays: An introduction

In a nutshell...

Crickets are evolved with a pair of sensory appendages on their abdomen called cerci. Each cercus contains numerous mechano-sensory filiform hairs, which are capable of sensing small air flows, even at the thermal noise thresholds. These filiform hairs of the crickets are one of the nature's best sensors with remarkable sensory attributes that keep inspiring scientists. Inspired by the filiform hairs, the development of artificial hair sensor arrays using advanced MEMS technologies is presented in this thesis. This chapter briefly introduces the motivation behind the presented work.

1.1. Medium flow sensing in nature

Survival of an organism depends on constant monitoring of its environment and reacting appropriately to the essential stimuli (e.g. from a prey, mate or a predator). Fluid is present everywhere and any movement by a body (immersed in the fluid) is immediately transferred into the surrounding fluid as a local disturbance. This disturbance in the fluid medium holds in it the information about the stimulus source and propagates in the medium. Every organism has evolved with special sensory systems to perceive and process the available stimulus energy in the fluid. Sensory organs like eyes, ears or nose, sense the stimuli

and initiate neural responses which are locally processed or in higher parts of the neural hierarchy, e.g. the brains. Depending on the stimulus information an appropriate biological reaction is then activated. In this coordinated process, the effective transfer of available stimulus energy from the medium to the sensory cells in the periphery plays an important role. One effective way of medium flow sensing is achieved by mechano-sensation [1]. Mechano-sensation is a special mechanism in which the fluid flow initiates a mechanical movement of the sensory structure, which is internally coupled with a dedicated neuron that fires an appropriate signal depending on the mechanical action [1]. Before we look into such fascinating mechanisms, we need to understand the nature of the stimulus.

1.1.1 Propagation of stimulus energy in the medium

A moving organism in a fluid medium immediately becomes a source of combined pressure-flow waves. Any movement causes the fluid particles to move along, which results in local increase in the pressure. And vice verse: local pressure gradients in the medium initiate fluid movement. Depending on compressibility of the medium and distance to the moving source, the pressure-flow disturbances may manifest themselves as acoustic waves [2]. Propagating acoustic waves (longitudinal movement of the fluid particles) travel with the speed of sound, which is dependent on the medium. However, except very near to the source, the particle velocity is much smaller than the speed of the source itself [2].

A stimulus for the medium flow can be represented by a series of multi-pole sources, given that its dimensions are smaller than the wavelength of the waves it generates. While higher-order poles loose their significance with increasing distance from the source, medium flow fields are often approximated by monopole (pulsating sphere) and dipole (vibrating sphere) moments. A monopole moment results from volume changes while a dipole moment results from mass displacement. Since most biological stimuli in the fluid generate flow by their movement, dipole moments are considered more relevant for field representation [3].

The medium flow characteristics can be distinguished based on the distinct flow field regimes determined by the radial distance from the source, r and frequency ω. The characteristics of the pressure (p) and particle-velocity (radial component v_r and tangential component v_θ) of the propagating flow generated by a dipole are given by [4,5]:

$$p = -\rho \cdot \frac{\partial \Phi}{\partial t} = \frac{\rho \cdot c \cdot (k \cdot a)^3}{2} \cdot \left[\frac{1}{(k \cdot r)} - \frac{j}{(k \cdot r)^2} \right] \cdot V_0 \cos\theta \cdot e^{j \cdot (\omega \cdot t - k \cdot r)} \qquad (1.1)$$

$$v_r = \frac{\partial \Phi}{\partial r} = \frac{(k \cdot a)^3}{2} \cdot \left[\frac{1}{(k \cdot r)} - \frac{2j}{(k \cdot r)^2} - \frac{2}{(k \cdot r)^3} \right] \cdot V_0 \cos\theta \cdot e^{j \cdot (\omega \cdot t - k \cdot r)} \qquad (1.2)$$

$$v_\theta = \frac{1}{r} \cdot \frac{\partial \Phi}{\partial \theta} = -\frac{(k \cdot a)^3}{2} \cdot \left[\frac{j}{(k \cdot r)^2} + \frac{1}{(k \cdot r)^3} \right] \cdot V_0 \sin\theta \cdot e^{j \cdot (\omega \cdot t - k \cdot r)} \qquad (1.3)$$

where ρ is the medium density, $k=2\pi/\lambda$ is the wave number and Φ is the vector potential of a vibrating sphere (dipole) of radius a in a compressible, inviscid and irrotational field given as [6]:

$$\Phi = \frac{a^3}{2\cdot r^2}\left(1 + j\cdot k\cdot r\right)\cdot V_0 \cos\theta \cdot e^{j\cdot(\omega\cdot t - k\cdot r)} \qquad (1.4)$$

where $V=V_0e^{j\omega t}$ is the vibrational velocity of the sphere in the medium. At small distances from the source such that $k\cdot r$ <<1, the flow exhibits incompressible nature and this regime is called near-field.

Equation (1.1) shows that at smaller distances ($k\cdot r$ <<1) the pressure is proportional to k and r^{-2}. At larger distances such that $k\cdot r$ >>1, the pressure is proportional to k^2 (hence, square of frequency) and r^{-1}. This dominates the pressure of the propagating wave at larger distances from the source. At larger distances ($k\cdot r$ >>1) the radial particle velocity (equation (1.2)) is proportional to k^2 and r^{-1}. Only at very small distances ($k\cdot r$ <<1) the velocity is proportional to r^{-3} and is in phase with the velocity of the source itself (as only at such small distances, the flow near the dipole source exhibits the incompressible nature) [5]. It has to be noted that this term becomes independent of k (hence, frequency). At other intermediate distances, there is a term of particle velocity which becomes significant and is proportional to k and r^{-2}. With respect to the tangential particle velocity, equation (1.3) shows that it is significant only in the near-field ($k\cdot r$ <<1). Summing up, source size a, distance from the source ($k\cdot r$) and frequency of the flow determine the characteristics of the propagating wave (stimulus energy) in the medium.

1.1.2 Mechano-sensory hairs

As discussed above, depending on the size of the source, distance from the moving source and its frequency, either the pressure component or the particle-velocity component of the flow may becomes biologically relevant source of stimulus energy [2]. Based on their intended mode of operation to sense pressure-variations or particle velocity of the flow, mechano-sensory structures found in organisms differ largely. Pressure-sensitive mechano-sensors are usually in the shape of a drum, with stretched-out membranes. Flow-sensitive mechano-sensors are usually slender, thin and mostly hair-shaped with compliances small enough to easily move with the flow [2].

The choice of effective sensing mechanism at the sensory receptor, or evolutionary development thereof in nature, depends chiefly on the nature of the stimulus, fluid medium and the distance of the sensory structure from the source. Of these, the stimulus-sensor interaction distance is a key factor. If the interaction distance is large, then the sensing mechanism could rely on sensing the pressure variations in the fluid flow. On the other hand, if the interaction distance is small and the frequencies are low, the particle velocity component has a comparatively strong presence, and is preferred, especially when flow-direction information is vital.

Mechano-sensory hairs are common among arthropods and crustaceans [1]. In most fish, special flow sensory structures are present along the lateral line [7]. Among arthropods, most spiders [8] and crickets [1,9,10] have hairy appendages specialized for sensing flows. Sensory hairs are not exclusive to invertebrates; tiny hair-like structures are e.g. also found in the mammalian cochlea [11]. The sensory hairs of crickets are among the most sensitive mechano-sensory structures found in nature as far as energy-requirements in order to excite an action potential are concerned, being on the order of kT [10].

1.2. Crickets' cerci and filiform hairs

Crickets are insects often found in human habitats, either as pests or pets [12]. Some cultures have seen them as singers in the royal palaces [12] and in religious temples [13] and some as fierce fighters for entertainment [14]. Due to this special closeness, crickets have garnered enough scientific attention to study their anatomy, physiology, behavior, etc. [12]. Thanks to this their mechano-receptive sensory system, used as a part of their escape mechanism, was extensively studied and the presented work is inspired from this special sensory system.

Crickets form important parts of the diet of several invertebrates and smaller animals [12]. Due to this, evolutionary pressure has equipped them with several escape mechanisms to thrive in their habitat. Common escape strategies are hiding, freezing or fleeing [12]. But to enable one of these behaviors, it is important for the cricket to sense the approaching predators. Most predators signal their presence by means of low-frequency disturbances of the fluid medium. Crickets are evolved with a pair of special sensory appendages called cerci to sense these minute fluctuations [15-25].

1.2.1 Filiform hairs of cercus

The cerci of the crickets are found at the lower abdomen of their body (see figure 1.1) and comprise of several sensory structures for sensing a range of attributes – orientation, touch, vibration, acceleration and particle-velocity – all in one [2,11]. Each cercus is supplied with a rich neural network connected mostly, but not exclusively, with the terminal abdominal ganglion for processing of the neural signals. Of these sensory structures, the filiform hairs found on the cercus are capable of sensing minute air flows. These hairs are slender and placed in an elastic socket, facilitating sensing of flows. Depending on species filiform hairs range in length, e.g. for wood cricket (Nemobius sylvestris) about 0.1 to 1.5 mm in average and a diameter ranging from 1 to 9 μm respectively [15-21]. The cercal hair lengths are observed to have a bimodal distribution (figure 1.1), with large number of hairs having their lengths around ~200 μm and around ~750 μm. On both cerci, roughly several hundreds of filiform hairs can be found packed as radially arranged arrays [20,21,25]. Each cercus is about several mm long, depending on the species and its age [20,21].

The filiform hairs are sensitive to minute flows: when there is air flow, the slender hairs are subject to the drag-forces exerted by the flow and they move along with it. Under the hair socket, the moving hair shaft strains a sensory neuron that fires appropriate neural signals down the neural pathway. The interesting aspect of the filiform hairs is that each hair has its own responsive behavior to the flows. A hair can be modeled as a second-order mechanical system and each hair has a specific moment of inertia, torsional stiffness and torsional resistance (i.e. damping). Smaller hairs are more sensitive to high frequencies (>250 Hz) while longer hairs are more sensitive at low frequencies (<150 Hz) [15,16]. As an entire array, the sensory system (hairs and neural system) is transducing a wide range of flow characteristics like amplitude, frequency, acceleration and direction [19].

The flow sensitivity of a filiform hair is remarkably high with thresholds as low as 30 μm/s. Not only that, this exceptional sensing requires only little energy to be delivered by the flow: comparable to the thermal noise levels [10]. Studies have shown that, at the lowest flow values, hair-sensors even benefit from noise, reducing the flow-sensing threshold by a principle called stochastic resonance [10]. Such facts have induced interest from engineers and fueled some bio-inspired work.

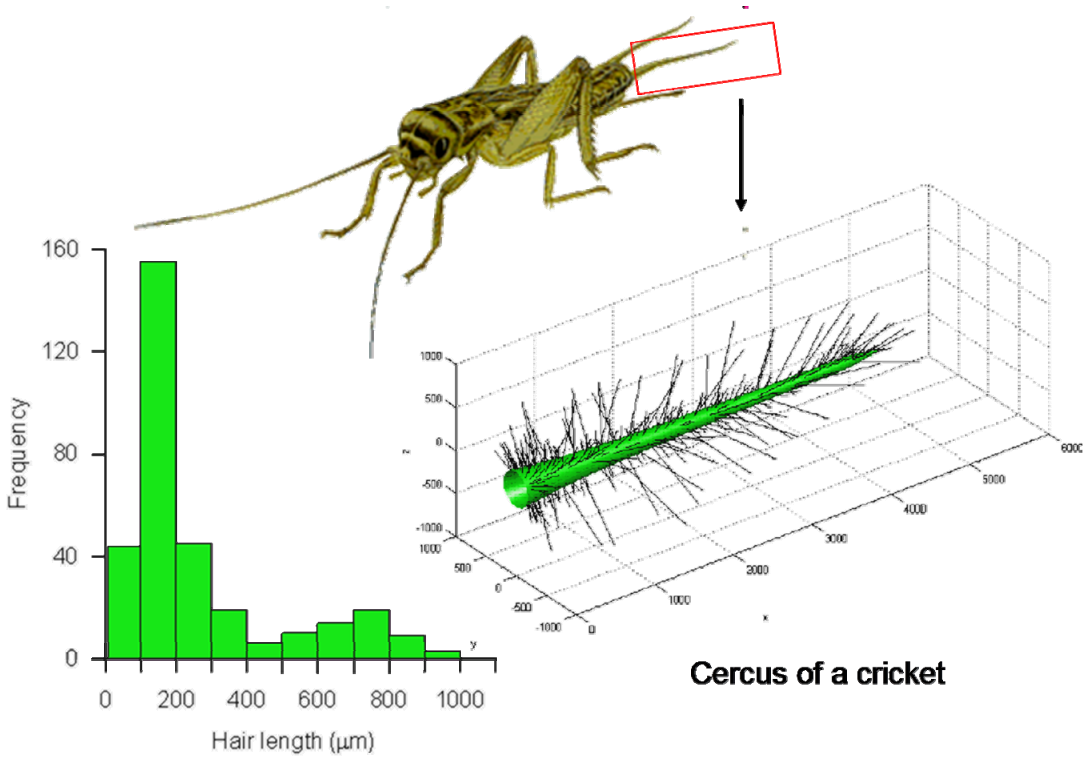

Figure 1.1 *3D map of the cercus of a cricket, featuring numerous filiform hairs. The hairs are individually measured for their length and occurrences (composed from [20]).*

1.3. Artificial flow-sensitive hair sensors

1.3.1 Biomimetics: biology meets MEMS

Biomimetics is an upcoming field in science where scientists and engineers take inspiration from an existing biological process, structure, function or entire bio-system [26,27]. If we take a certain organism, during evolution it will have adapted to survive, maybe even flourish, as species, in a specific eco-system. Relevant structures, processes and systems have evolved through repeated mutations, selectively promoting the successful combinations of properties of which the information is passed on to newer generations. This highlights the fact that biological organisms and systems are continuously evolving towards optimal execution of function at minimal energy and material costs [28].

It is important to emphasize that it is not in the motivation of biomimicking, to exactly replicate a biological function by means of man-made materials and technologies. What matters more is the know-how of the underlying principles that govern the basis of the biological function (which is achieved usually by means of detailed experimental studies and extensive modeling) and applying that knowledge in the development of useful applications. Understanding relevant biological principles may provide an extended design space and lead to non-trivial optimal designs, potentially out performing well-known engineering solutions [29]. Common and popular examples of bio-inspired functions, or even applications are presented in [28,30,31]. With increasing popularity over recent years, biomimetics is spreading in many fields of science.

Equally successful and popular is the field of micro-system technology (MST) or micro-electro-mechanical system (MEMS) [32]. The field of MEMS deals with the realization of miniature systems capable of performing specific functionalities- chiefly, transduction. It is aided by state-of-the-art fabrication technologies innovated for the demanding and fast-growing semiconductor industry. MEMS makes use of fabrication technologies like photolithography, thin film deposition and reactive etching for realizing a variety of micro devices. Several of these are already established as commercially available products and their numbers keep growing, enabling applications in a wide range from consumer to industrial sectors (from medicine to military) [32].

The meeting point of these two fields (biomimetics and MEMS) is special as it brings in diverse scientific expertise to work on a scale (sub-micron to millimeter) that it is especially meaningful to both biological and technical transducers, especially (mechanical) sensing. While there exists a large variety of sensory systems in biology, fluid flow sensing arrays in biomimetic MEMS could be helpful in developing real-time flow observation applications. One could think of the analogy with how a single photo-diode compares in functionality to an entire CCD-sensor: having arrays of independently operating flow-sensors allows for the observation and detection of spatio-temporal flow patterns. When combined with appropriate signature detection such 'flow-cameras' could be powerful aids in bio-robotic, micro-fluidic and aerodynamic systems.

1.3.2 Mechano-sensory hairs for bio-inspiration

The sensory filiform hairs undoubtedly are a source of inspiration for developing artificial flow pattern sensing system. While there are numerous systems for flow sensing at a single volume, flow field sensing is more challenging and hardly implemented in the form of sensor arrays[1]. The striking aspects of the cricket's hair-based mechano-sensory system that attract our attention can be summarized as follows:

1. flow sensitivity
2. minimal energy consumption
3. directivity
4. variability of sensing characteristics
5. miniature size
6. complex sensory signal processing
7. spatial density and resulting spatio-temporal flow resolution
8. robustness
9. large population (to ensure uninterrupted sensing)

Developing inexpensive, artificial flow sensing arrays is useful for flow visualization and flow feature extraction applications. For instance, such arrays could be used to visualize local (micro-) turbulence over specific surfaces or could be used in maritime applications for object detection (e.g. in robotic applications) [5]. The first step is to realize an array that responds to flows with high sensitivity and sufficiently low threshold flows. Numerous challenges are found in choosing an appropriate sensing mechanism and in subsequently finding appropriate materials and associated fabrication technologies.

[1] Flow-field sensing by methods like Particle Image Velocimetry, particle seeding and camera observations, etc. are of course well-known but are generally limited to scientific or engineering purposes and not applied in operational schemes.

1.4. MEMS-based flow-sensory hairs

With micro sensors that sense acoustic pressure variations prevailing, sensors capable of sensing particle velocity are rare [33, 34]. On the other hand, particle velocity sensing in an array facilitates the possibility of sensing complex flow patterns, instead of the conventional flow measurement at the point-of-interest only. Such flow pattern sensing could be attractive to certain fields of medicine, aerospace, industrial and military applications.

For sensing flows, there exist several proven sensing schemes, for instance: (i) thermal anemometry [35], (ii) particle image velocimetry [36], (iii) Doppler frequency shift [37] and (iv) pressure difference sensing [38]. Seminal research has been done in realizing micromachined array sensors inspired by the mammalian cochlea [39] and in understanding the complex signal processing of it [40]. Several works, which were inspired by flow sensitive cilia, have been realized [41]. These works could be classified based on the underlying flow sensing scheme and on the materials used for fabricating such sensors. For bio-inspired work based on lateral-line of fish, piezo-resistive sensing has been used frequently [41-46]. All the works have in common that they employ elongated structures for drag-force reception. Most of the works are developed to be used in water as surrounding medium and only few are meant for operation in air. Some are designed to sense dc flows. Apart form the sensor principles used, differences among these works lie in the variation of materials used to fabricate the sensors. Some of the above said seminal works are discussed briefly here.

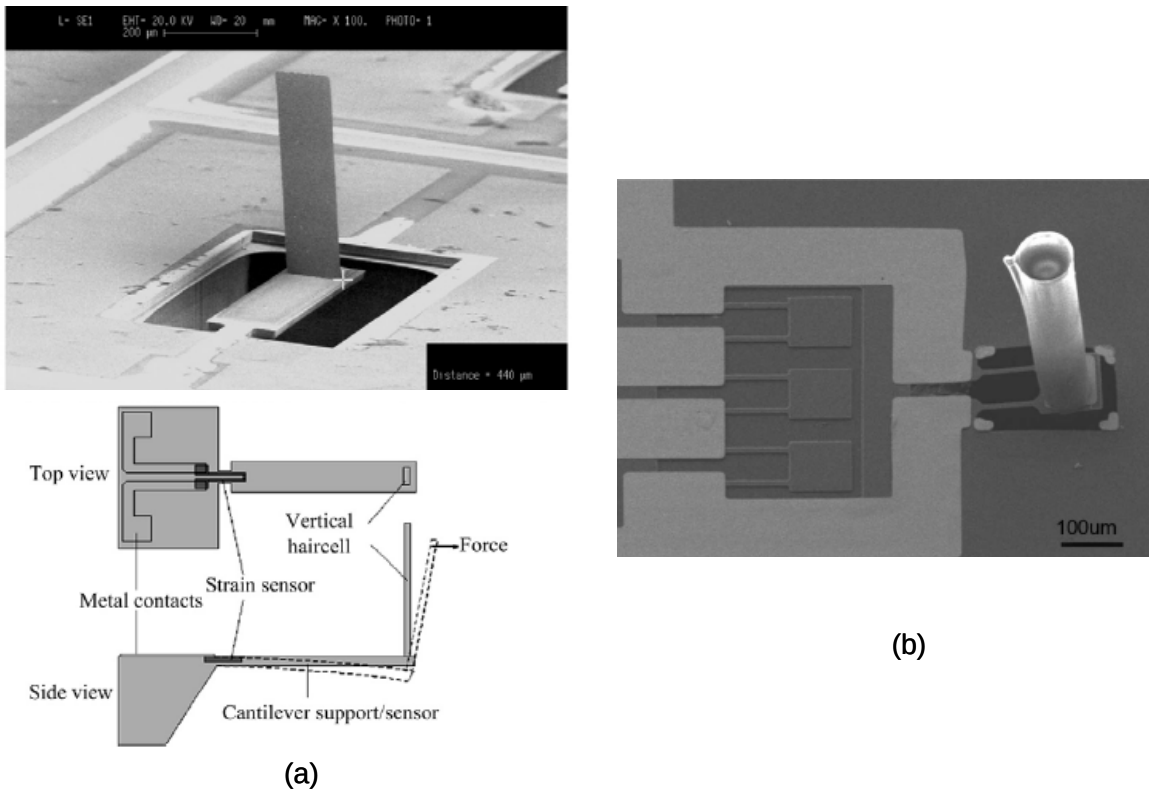

Figure 1.2 *Piezoresistive flow sensors, inspired from lateral-line of fish: (a) flow sensors made by plastic deformation of magnetic assembly (PDMA)[43], (b) Similar sensors except a polymer cylinder of ~500 μm length is used [44].*

Z. Fan *et.al*. [43] used plastic deformation magnetic assembly to fabricate plate-like flow receptive structures on cantilevers (see figure 1.2(a)). A magnetic field is used to

plastically deform the plate-like structures (made with gold and Permalloy) to stand out-of-plane. When there is flow, the plate deflects causing the cantilever to strain, which is sensed by piezo-resistors. Parylene is used as a protective insulation sheath, as the application of this work was in liquid medium. Such a sensor showed flow sensitivity for laminar water flows (dc) of 0.2 to 1 m/s.

N. Chen *et. al*. [44], varied the sensor by using an SU-8 hair of ~500 μm length and a diameter of 80 μm (see figure 1.2(b)), instead of the gold-permalloy magnetic assembly (see figure). The sensor was similar to the work of Z. Fan et. al. [43]. Such a sensor was used both in air and water medium and tested with both dc and oscillating flows. For oscillating flows of 40 Hz in water, the sensor detection limit was 0.7 mm/s at 50 Hz measured at an FFT bandwidth of 2 Hz. Modified, all-polymer versions of such sensors were also reported from the same research group [45]. In this, polyurethane hairs were fabricated on polyurethane force sensitive resistors. They reported a detection limit of 0.1 degrees for the hair rotation (3 μm at tip deflection) at a tip load of 25 μN.

Y. Ozaki et. al. [46], fabricated two types of flow sensitive structures based on strain sensing (see figure 1.3). One type was sensitive in one direction and consisted of cantilevers with integrated strain gauges. The other type consisted of cross-shaped beams integrated with strain gauges and a thin and long (~5 mm) long hair manually placed at the center. This type was capable of flow-sensing in two directions. Both types were shown to be sensitive to dc-flows ranging from several 10s of cm/s.

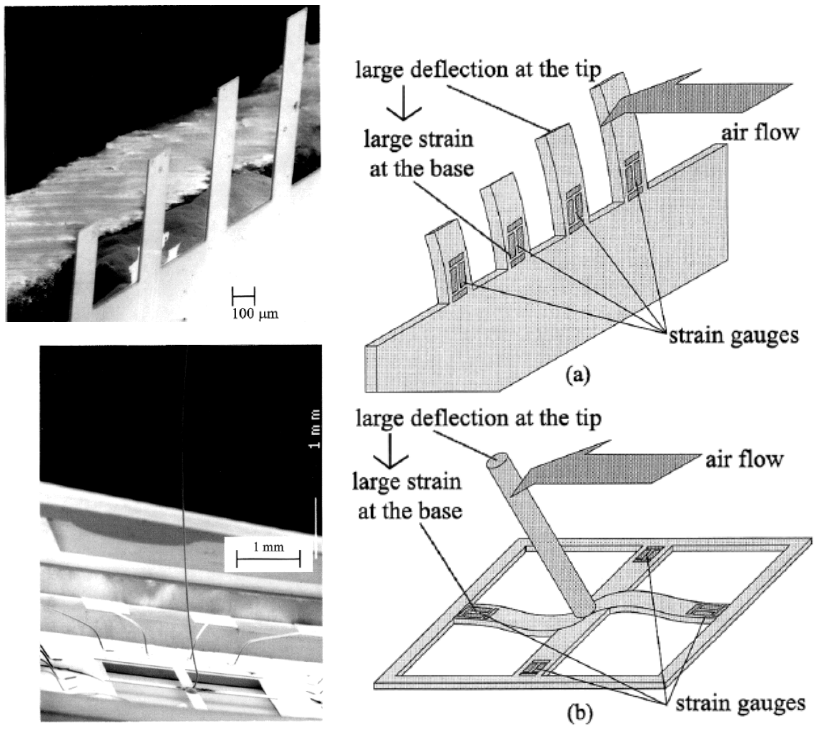

Figure 1.3 *MEMS flow sensitive arrays with 1-DOF and 2-DOF realized by integrating strain sensors. The hair-like metal structure is manually placed at the center of the cross-beam [46].*

1.5. Our artificial hair sensor arrays

Taking a different path, the novelty in our approach lies in the sensing mechanism and density of sensor-arrays. Our sensors use differential capacitive sensing to measure the deflection of a membrane. Capacitive sensing can yield high sensitivities. However, it is also more complex with regard to fabrication and read-out electronics.

The principle of operation of our approach comprises of an artificial hair centrally mounted on a suspended membrane. A pair of electrodes is present on top of the suspended membrane, which forms a pair of sensor capacitances with the conductive substrate that acts as a common bottom electrode. Whenever there is airflow, it exerts drag-torque on the hair, causing membrane rotation. This rotation alters both capacitances but in opposite ways. If the top electrodes are supplied with a high frequency electrical signal, these capacitance changes result in amplitude modulation of the output signal on the common substrate electrode, proportional to the flow.

The journey of our research began in 2001 and was funded by means of three projects, namely CICADA (2001-2005), Cilia (2005-2010) and BioEARS (2006-2013). Early generations of our sensors, were focused on the fabrication of the artificial hair and on the sensing scheme. Silicon nitride was the first candidate as a material for hairs. Different shapes and lengths of silicon nitride hairs were realized as a first step. [47,48].

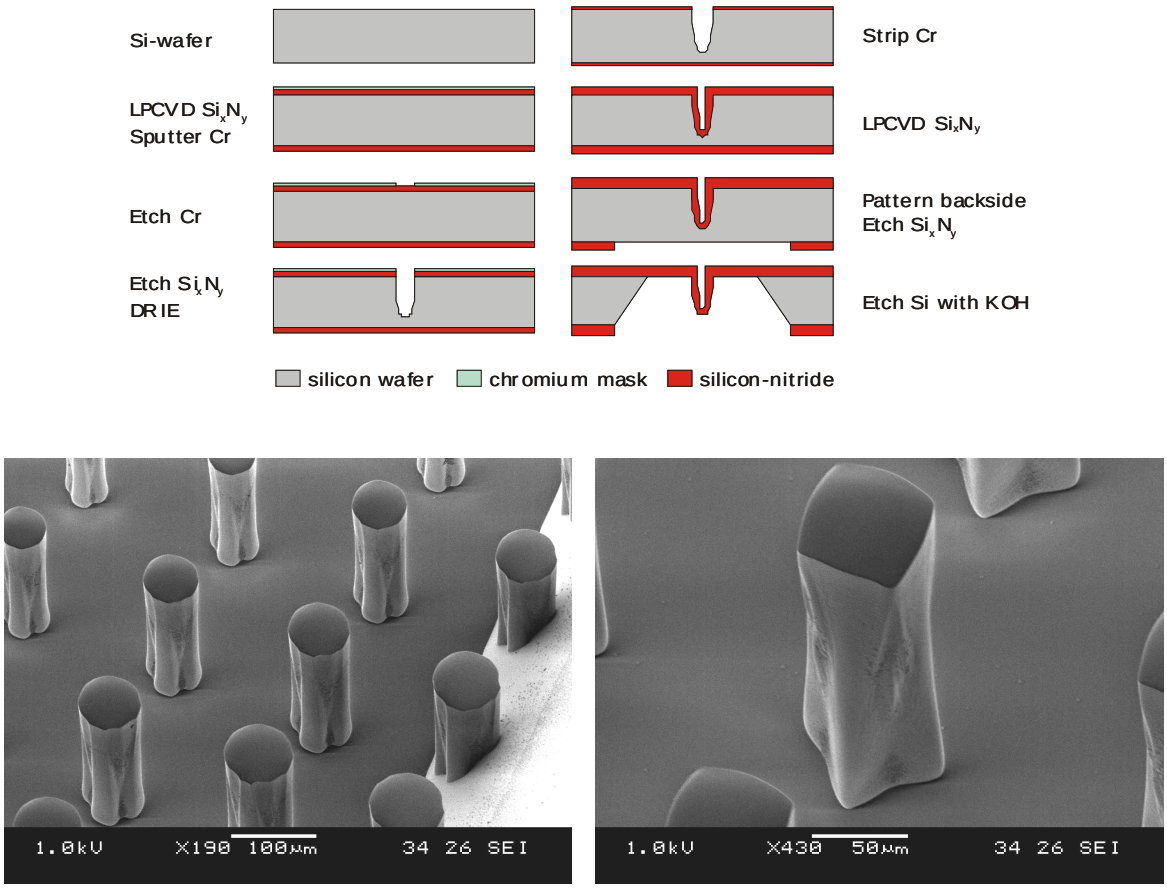

Figure 1.4 *Silicon rich nitride hairs fabricated using narrow trenches on silicon substrate as a mold [47,48].*

Silicon nitride hairs were fabricated by first etching holes in the silicon substrate (used as molds) and then depositing and filling up the trenches, to form the hairs. Figure 1.4 shows the conceptual fabrication scheme and SEM images of the realized silicon nitride hairs. Such a hair was later integrated to form a complete capacitive sensor by means of a complex fabrication scheme [48].

Following this, hairs of SU-8 [49] were considered and fabricated [50]. More detailed introduction to SU-8 hairs will be presented in forth-coming chapters of this thesis. A second generation of sensors was designed to feature SU-8 hairs of ~450 μm long as shown in figure 1.5 [50]. Chromium metal, on top of silicon rich nitride membranes, was used as top electrodes and a conductive silicon substrate as the common bottom electrode of the capacitive sensors. Arrays of hair sensors were successfully fabricated and the first-ever functional performance was shown (see figure 1.5). [Note: The detailed description of the process flow and the measurements will be dealt elaborately in the later chapters].

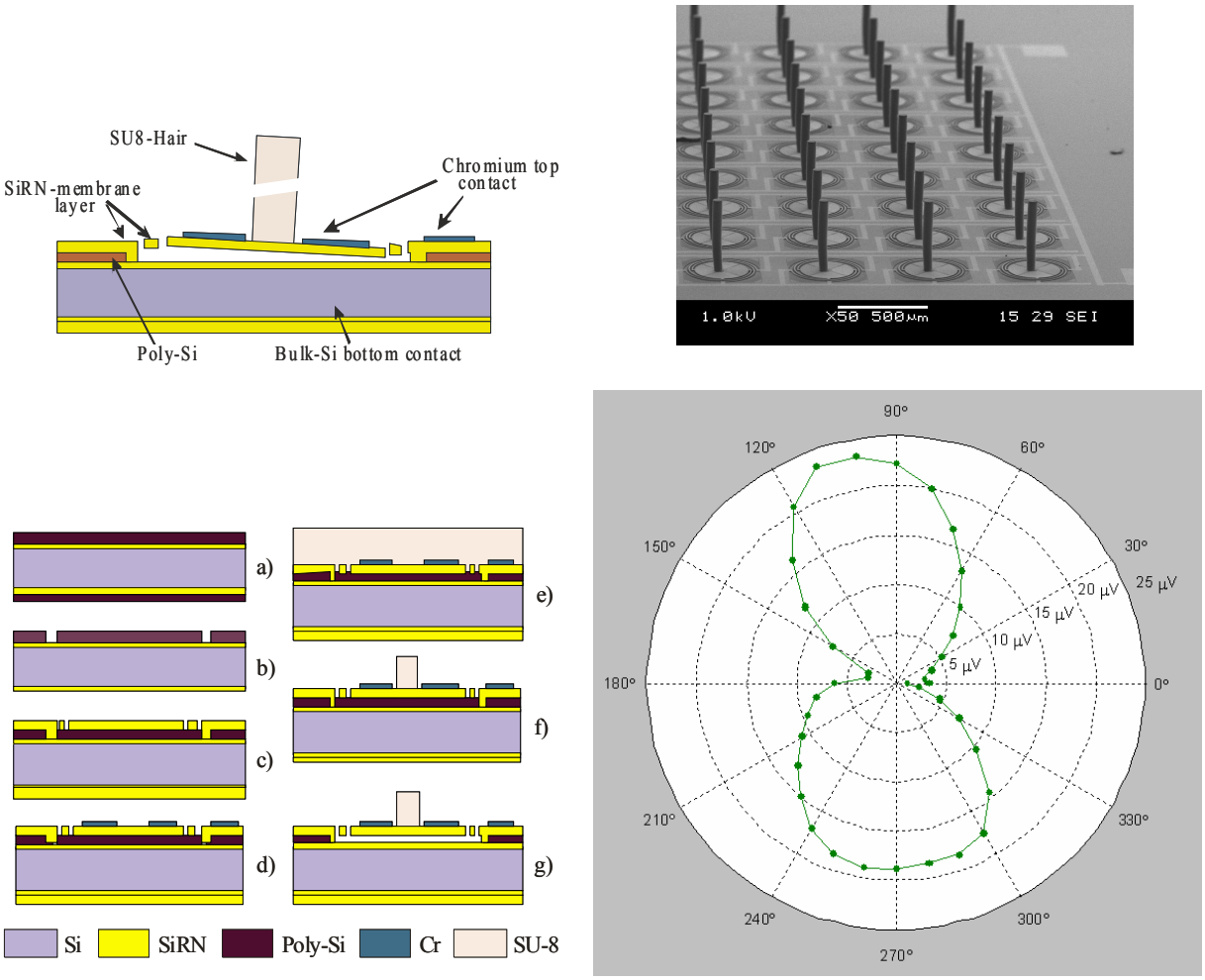

Figure 1.5 *Capacitive sensing MEMS flow sensor arrays using SU-8 hairs, instead of silicon nitride hairs [50]. The sensor arrays were functionally characterized and showed a reasonable directional response.*

The sensor array showed a good directional response, however it required large driving flows (~1 m/s) for measurable, minute capacitance changes. The sensitivity limit of the sensor array was roughly about ~5 cm/s. The membranes with top electrodes suffered from internal stress-induced curvature, which affected the sensitivity. In later chapters of this thesis, this problem will be addressed and the improved effects will be discussed. Additionally, the use of bulk silicon will pose issues with parasitic capacitances, hindering the intended addressing of individual hair sensors.

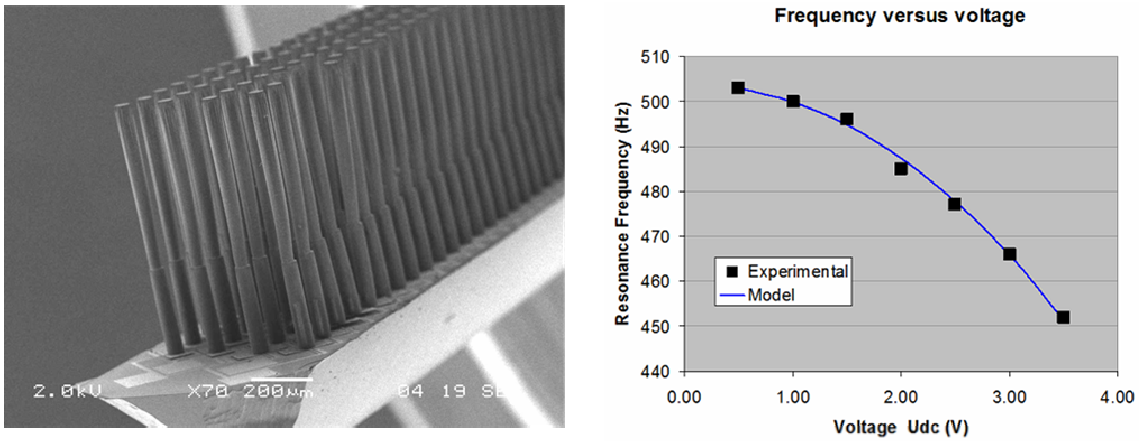

Figure 1.6 *Hair sensor arrays featuring long SU-8 hairs of constant diameter. Such arrays were characterized optically and their frequency-tuning capability (by applying DC-bias and electrostatic spring softening effect) was confirmed [51,53].*

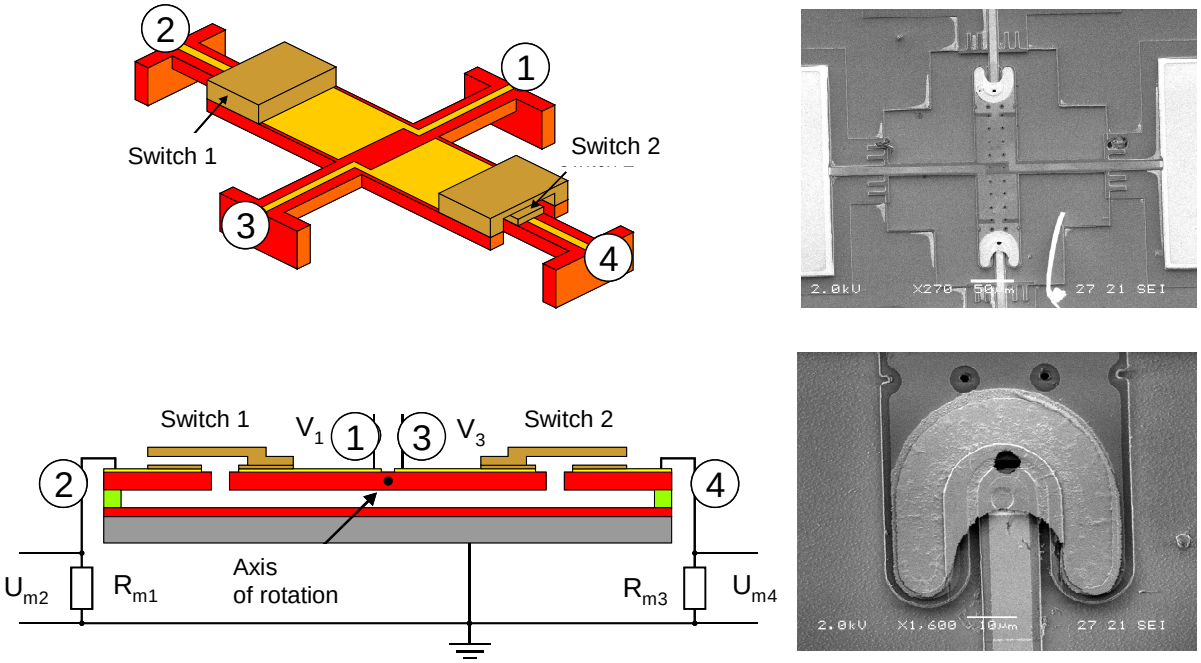

Figure 1.7 *An alternative sensing scheme of using bistable microswitches for digital output of the hair sensors. SEM images of the successfully fabricated test structures [54].*

More investigations on the fabrication of SU-8 hairs was done (see figure), resulting in two-staged hairs and longer than the previous generation of sensors [51]. As a first step, in the process scheme shown in the figure, long hairs were incorporated. Figure 1.6 shows a fabricated device and optical characterization of the sensors is presented in [52,53]. In this work, the adaptivity of the sensors, by means of applying DC-bias and exploring the so-called electrostatic spring softening (ESS) effect, is presented. The adaptive feature of the sensors is an added advantage of using capacitive sensing, i.e. generator type transduction.

Further investigations were focused on addressing the serious issues of parasitic capacitance and membrane curvature [51]. In this work, a buried layer of highly-doped poly-silicon was tested as the bottom electrode, to counteract the parasitic capacitance. Importantly, a thin layer of Aluminum layer (~20 nm), replacing the Chromium metal as top electrodes to counteract the membrane curvature, was tested. Test structures (not functional) comprising only the suspended sensor membranes showed reduced curvature. This desired technological aspect is incorporated in our present sensor arrays and explored more in detail in the later chapters.

As an alternative approach to the analog capacitive sensing mechanism, early investigations were performed to incorporate digital sensing by means of bistable microswitches [46]. Microswitches were designed to be of conductive switching type, where the output current is measured when the switches are in contact (see figure 1.7). An artificial hair, placed centrally on the suspended membrane consisting of a pair of switches, acts to drive the mechanism. Whenever there is sufficient flow, the hair rotation causes one of the switches to close. The sensor current flows only during the contact and hence, it is advantageous with respect to power consumption. The fact that measuring minute currents is less complex compared to capacitive sensing was seen as a positive aspect of this approach. However, only the devices without the hair were completed and characterized [54] and stiction issues prevented full operation and further development.

1.6. In this thesis

The aim of this research is to realize an optimal design for the hair sensor, compatible with operation in (large) arrays, while combining the experience and lessons learnt from our previous works. A thorough understanding of the sensor performance is developed by means of a sensor model, derived from the biophysical models, as developed by biophysicists for studying the actual insect filiform hairs, and complemented by the specifics of the geometry and transduction principle of our artificial hair-sensors. This work is guided by the following important questions:

What means optimal performance?

Model-based optimization is set as a goal by defining a figure of merit concerning the overall sensor performance. This figure of merit (*FoM*) provides the guidelines for setting the design targets for the sensors [55]. Having the figure of merit as a starting point, every aspect of the sensors is revisited for optimization. For the design of a new generation of hair sensors, the quality of the sensor membranes, i.e. to achieve membranes free from any stress-induced curvature, is emphasized and new ways to reduce the membrane curvature are analyzed [56]. One approach used in this work is a change of material for the electrodes (i.e. aluminum replacing chromium) and the other approach is to optimally reduce the electrode area, present near the torsional axis of the sensor.

How good are our new sensor arrays?

A new generation of hair sensor arrays is developed and the results from extensive characterization measurements are presented [57,58]. The quality of the membranes is analyzed by measuring their height profile using white light interference micros-copy [59]. To appreciate the sensor performance, the sensors are subjected to a wide-range of characterization measurements. The measured capacitive sensor performances for low-frequency airflows reveal their flow sensitivity, threshold and directionality. Optical characterization of the sensors using laser vibrometry [60] is done to analyze the actual dynamics of the sensor membrane.

What is the best shape for the hair?

Hairs play a central role in the sensing mechanism. Their shape determines the reception of flow-induced drag force. But their geometry also determines the mechanical characteristics of the sensor itself. At present, the artificial hair sensors have approximately a cylindrical shape. The filiform hairs are of elongated-conical shape, which motivates to analyze the best shape for the mechanical transduction. New fabrication techniques are investigated with the aim to realize nature-like artificial hairs that resemble the shape of filiform hairs themselves. The feasibility to integrate such hairs in the actual fabrication process of the artificial hair sensors is discussed.

How to realize the optimal sensor springs?

For better mechanical sensitivity the torsional stiffness should be small. But springs of small torsional stiffness are likely to be compliant for vertical motion as well, impeding the robustness of the sensors, possibly resulting in failure (due to stiction). Optimal springs are those having a small torsional stiffness (for better membrane rotation) and stiffer in all other modes (for example to reduce vertical displacements). New ideas and process schemes aimed at realizing optimal sensor springs are proposed and tested. Optimal springs can be achieved by either using a soft material (for example, SU-8 polymers) or a modified cross-section of the springs (using T-shaped cross-section, instead of rectangular sections). The challenges for such process changes are discussed in detail.

How to optimally arrange hair sensors in an array?

Good spatial resolution for flow pattern sensing requires hairs to be arranged in dense arrays. Placing hairs too close to each other might affect their individual performance depending on the spacing, hair geometry and stimulus properties. To answer the questions for optimality, investigations are made on the presence of viscosity-mediated coupling effects between artificial hair sensors [61-63]. Such effects have been reported previously for natural trichobothria hairs of spiders [64]. The impact of coupling effects on the placement of sensors in an array is discussed.

1.6.1 Organization of chapters

Assuming the previous discussion as a foundation, this thesis is constructed as follows:

Chapter 2 introduces the necessary theoretical background of the physical interaction of the hair-sensor with airflows. Basic concepts necessary for the design optimization of the sensors are discussed. A brief overview of the upcoming chapters in the context of design improvements is presented.

Chapter 3 is dedicated to the basic design of sensor arrays featuring long and two-staged hairs. Focus is laid on the quality of the sensor membranes and to eliminate membrane curvature. The performance of the sensor arrays is discussed by means of extensive characterization results.

Chapter 4 explores the possibility of an alternate method of making SU-8 hairs by means of bottom-side exposure. The results from the fabrication and characterization of nature-like and novel hollow hairs are presented. The feasibility study and fabrication results involved in making hollow hairs are also presented.

Chapter 5 deals with elaborate investigations on alternative methods for realizing optimal sensor springs. The usability of SU-8 as a sensor material is explored. Fabrication of test structures and results are discussed. The second part is dedicated to the design of a novel fabrication scheme for sensors with T-section springs. The fabrication involves an edge-lithography based process, developed exclusively for realization of uniform, sub-μm wide trenches needed to make springs with T-shaped cross-sections.

Chapter 6 deals with investigations on viscous coupling effects between artificial hairs. It presents the design and characterization of specially designed devices, aimed to explore the effects of viscous coupling on the arrangement of hair sensors in an array. Moreover it presents important viscous coupling results for a variety of hair-sensor arrangements.

Chapter 7 summarizes the thesis and takes a detailed look at different aspects of the sensor arrays that still need to be addressed. It also reflects briefly on the next steps of this work.

1.7. References

[1] J.A.C. Humphrey and F.G. Barth, *"Medium flow-sensing hairs:Biomechanics and models"*, Chapter 1, Advances in Insect Physiology, ed: Vol. 34, (2007) pp. 1-80

[2] L.C. Osborne, *"Signal processing in a mechanosensory array: Dynamics of cricket cercal hairs"*, PhD thesis, University of California, Berkeley (1996)

[3] A. J. Kalmijn, *"Hydrodynamic and acoustic field detection"*, in *Sensory biology of aquatic animals*, ed. J. Atema et. al, Springer-Verlag (1988), pp. 83-130.

[4] D. T. Blackstock, *"Fundamentals of physical acoustics"*, John Wiley & Sons (2000).

[5] N. Izadi, *"Bio-inspired MEMS aquatic flow sensor arrays"*, PhD thesis, University of Twente, Enschede, the Netherlands (2011).

[6] H. Lamb, *"The dynamical theory of sound"*, E. Arnold, London (1910).

[7] S. Coombs, *"Smart skins: Information processing by lateral line flow sensors"*, Autonomous Robots, (2001), Vol. 11, pp. 255-261.

[8] F.G. Barth, U. Wastl, J.A.C. Humphrey, R. Devarakonda, *"Dynamics of arthropod filiform hairs. II. Mechanical properties of spider trichobothria"*, Phil. Trans. R. Soc, (1993), B, pp. 445-461.

[9] (Edited by) F. Huber, T.E. Moore and W. Loher, *"Cricket behavior and neurobiology"*, Cornell University Press, 1989

[10] T. Shimozawa, J. Murakami, T. Kumagai, *"Cricket wind receptors: thermal noise for the highest sensitivity known"*, Chapter 10, Sensors and Sensing in Biology and Engineering, ed. F.G. Barth, J.A.C. Humphrey and T.W. Secomb, Springer, Vienna, 2003.

[11] A.J. Hudspeth, *"How the ear's works work: mechanoelectrical transduction and amplification by hair cells"*, C. R. Biologies (2005), Vol. 328, pp. 155-162

[12] T.J. Walker and S. Masaki, *"Natural History"*, Chapter 1, Cricket behavior and neurobiology, (Ed:) F. Huber, T.E. Moore and W. Loher, Cornell University Press, 1989

[13] http://www.travel-around-japan.com/k62-74-suzumushidera.html

[14] http://en.wikipedia.org/wiki/Cricket_fighting

[15] T. Shimozawa, T. Kumagai, Y. Baba, *"Structural and functional scaling of the cercal wind-receptor hairs in cricket"*, J. Comp. Physiol. A (1998) 183, pp. 171-186

[16] T. Shimozawa, M. Kanou, *"The aerodynamics and sensory physiology of range fractionation in the cercal filiform sensilla of the cricket Gryllus bimaculatus"*, J. Comp. Physiol. A (1984) 155, pp. 495-505

[17] J.A.C. Humphrey, R. Devarakonda, I. Iglesias, F.G. Barth, *"Dynamics of arthropod filiform hairs. I. Mathematical modeling of the hair and air motions"*, Philosophical Transactions: Biological Science (1993) 340, pp. 423-444

[18] R. Kant and J.A.C. Humphrey, *"Response of cricket and spider motion-sensing hairs to airflow pulsations"*, J. R. Soc. Interface (2009) Vol. 6, pp. 1047

[19] T. Steinmann, J. Casas, G. Krijnen and O. Dangles, "*Air-flow sensitive hairs: boundary layers in oscillatory flows around arthropod appendages*", J. of Exp. Biol. (2006) 209, pp. 4398-4408

[20] O. Dangles, T. Steinmann, D. Pierre, F. Vannier and J. Casas, "Relative contributions of organ shape and receptor arrangement to the design of cricket's cercal system", J Comp Physiol A (2008) 194 (7), pp. 653–663

[21] O. Dangles, D. Pierre, C. Magal, F. Vannier and J. Casas, *"Ontogeny of air-motion sensing in cricket"*, J. Exp. Biol. (2006) Vol. 209, pp. 4363-4370.

[22] J. Palka, R.B. Levine, M. Schubiger, *"The circus-to-giant inter-neuron system of crickets. I. Some attributes of the sensory cells"*, J. Comp. Physiol. (1977), Vol. 119, pp. 267-283.

[23] M.A. Landolfa and J.P. Miller, *"Stimulus-response properties of cricket cercal filiform receptors"*, J. Comp. Physiol. A (1995), Vol. 177, pp. 749-757.

[24] F.E. Theunissen and J.P. Miller, *"Representation of sensory information in the cricket cercal sensory system. II. Information theoretic calculation of system accuracy and optimal tuning curve widths of four primary interneurons"*, J. Neurophysiol. (1991), Vol. 66, pp. 1690-1703.

[25] M.A. Landolfa and G.A. Jacobs, *"Direction sensitivity of the filiform hair population of the cricket cercal system"*, J. Comp. Physiol. A (1995), Vol. 177, pp. 759-766.

[26] http://en.wikipedia.org/wiki/Bionics

[27] J.V.C. Vincent, *"Stealing ideas from nature"*, Deployable structures, ed: S. Pellegrino, Springer, Vienna, pp. 51-58

[28] Y. Bar-Cohen, *"Biomimetics-using nature to inspire human innovation"*, Bioinsp. Biomim. (2006), Vol. 1, pp. 1-12.

[29] P. Ball, *"Life's lessons in design"*, Nature (2001), Vol. 409, pp. 413-416.

[30] http://ngm.nationalgeographic.com/2008/04/biomimetics/tom-mueller-text

[31] P.Gruber, *"The signs of life in architecture"*, Bioinsp. Biomim. (2008), Vol. 3, pp. 1-9.

[32] M.J. Madou, *"Fundamentals of microfabrication: The science of miniaturization"*, CRC Press (2002).

[33] R. Raangs, *"Exploring the use of the microflown"*, Chapter 5, PhD thesis, University of Twente, Enschede, the Netherlands (2005)

[34] H-E. de Bree, *"The microflown"*, PhD thesis, University of Twente, Enschede, the Netherlands (1997)

[35] J. Chen and C. Liu, *"Development and characterization of surface micromachined, out-of-plane hot-wire anemometer"*, J. Microelectromech. Syst. (2003) Vol. 12(6), pp. 979-988.

[36] J. Casas, T. Steinmann and O. Dangles, *"The aerodynamic signature of running spiders"*, PLoS ONE (2008) 3(5): e2116.

[37] H.W. Jentink, J.A.J. van Beurden, M.A. Helsdingen, F.F.M. de Mul, J.G. Aarnoudse and J. Greve, *"A compact differential laser Doppler velocimeter using a semiconductor laser"*, J. Phys. E.: Sci. Instrum. (1987) Vol. 20, pp.1281-1283

[38] V.I. Fernandez, S.M. Hou, F.S. Hover, J.H. Lang and M.S. Triantafyllou, *"Lateral-line-inspired MEMS-array pressure sensing for passive underwater navigation"*, Proc. of Int. Symp. on Unmanned Untethered Submercible Technology, 2007, pp.

[39] R.D. White and K. Grosh, *"Design and characterization of a MEMS piezoresistive cochlear-like acoustic sensor"*, Proc. of ASME Int. Mech. Engg. Cong. and Expo. (IMECE '02), New Orleans, USA, 17-22 Nov, 2002, pp.1-10.

[40] R. Sarpeshkar, R.F. Lyon and C. Mead, *"A low-power wide-dynamic analog VLSI cochlea"*, Analog Integrated Circuits and Signal Processing, (1998), Vol. 16, pp.245-274.

[41] Z. Zhou and Z. Liu, *"Biomimetic cilia based on MEMS technology"*, J. Bionic Engineering (2008) Vol. 5, pp. 358-365.

[42] C. Liu, *"Micromachined biomimetic artificial haircell sensors"*, Bioinspiration & Biomimetics (2007) Vol. 2, S162.

[43] Z. Fan, J. Chen, J. Zou, D. Bullen, C. Liu and F. Delcomyn, *"Design and fabrication of artificial lateral line flow sensors"*, J. Micromech. Microeng. (2002) Vol. 12, pp. 655-661.

[44] N. Chen, J.M. Engel, Y. Yang, S. Pandya and C. Liu, *"Design and characterization of artificial hair cell sensor for flow sensing with ultrahigh velocity and angular sensitivity"*, J. Microelectromech. Syst. (2007) Vol. 16(5), pp. 999-1013.

[45] J.M. Engel, J. Chen and C. Liu, *"Polyurethane rubber all-polymer artificial hair cell sensor"*, J. Microelectromech. Syst. (2006) Vol. 15(4), pp. 729-736.

[46] Y. Ozaki, T. Ohyama, T. Yasuda and I. Shimoyama, *"An air flow sensor modeled on wind receptor hairs of insects"*, Proc. of 13th IEEE Int. Conf. MEMS (2000), pp. 531-536.

[47] J.J. van Baar, M. Dijkstra, R.J. Wiegerink, T.S.J. Lammerink and G.J.M. Krijnen, "*Fabrication of arrays of artificial hairs for complex flow pattern recognition*", Proceedings of IEEE Sensors conference, Toronto, Canada, October 22-24, 2003.

[48] M. Dijkstra, "*Capacitive flow sensors based on wind-receptors of crickets*", Master thesis, University of Twente (2003).

[49] SU-8 product sheet, http://www.microchem.com/products/su_eight.htm

[50] M. Dijkstra, J.J. van Baar, R J Wiegerink, T S J Lammerink, J H de Boer and G J M Krijnen, "*Artificial sensory hairs based on the flow sensitive receptor hairs of crickets*", J. Micromech. and Microeng. (2005) 15, pp. 132-138.

[51] S.S. Siripurapu, "*Cricket-inspired sensory hairs with capacitive motion detection*", Master thesis, University of Twente (2005).

[52] J. Floris, N. Izadi, R.K. Jaganatharaja, R.J. Wiegerink, T.S.J. Lammerink, and G.J.M. Krijnen, "*Adaptation for frequency focusing and increased sensitivity in biomimetic flow sensors using electrostatic spring softening*", Proc. of 14th Int. conf. on solid-state sensors, actuators and microsystems (Transducers & Eurosensors '07), Lyon, France, 10-14 June 2007.

[53] G. J. M. Krijnen, J. Floris, M.A. Dijkstra, T.S.J. Lammerink, and R.J. Wiegerink, "*Biomimetic micromechanical adaptive flow-sensor arrays*", Proc. of SPIE Europe Microtechnologies for the New Millennium, Gran Canaria, Spain, 2-4 May 2007.

[54] W.J. Kuipers, "*Drag-force actuated microswitch*", Master thesis, University of Twente (2005).

[55] R.K. Jaganatharaja, N. Izadi, J. Floris, T.S.J. Lammerink, R.J. Wiegerink and G.J.M. Krijnen, "*Model-based optimization and adaptivity of cricket-inspired biomimetic artificial hair sensor arrays*", MicroMechanics Europe Workshop, Guimaraes, Portugal, 16-18 Sep 2007.

[56] N. Izadi, R.K. Jaganatharaja, J. Floris and G.J.M. Krijnen, "*Optimization of cricket-inspired, biomimetic, artificial hair sensors for flow sensing*", Proc. of 9th Int. symp. on Design, Test, Integration and Packaging of MEMS/MOEMS (DTIP) (2007), Stresa, Italy, pp. 112-115.

[57] C.M. Bruinink, R.K. Jaganatharaja, M.J. de Boer, E. Berenschot, M.L. Kolster, T.S.J. Lam-merink, R.J. Wiegerink and G.J.M. Krijnen, *"Advancements in technology and design of biomimetic flow-sensor arrays"*, Proc. IEEE Int. Conf. MEMS, Sorrento, Italy, 25-29 Jan, 2008, pp. 152-155

[58] R.K. Jaganatharaja, C.M. Bruinink, B.M. Hagedoorn, M.L. Kolster, T.S.J. Lammerink, R.J. Wiegerink and G.J.M. Krijnen, *"Highly-sensitive, biomimetic hair sensor arrays for sensing low-frequency air flows"*, Proc. of 15th Int. conf. on solid-state sensors, actuators and microsystems, Denver, USA, 21-25 June, 2009, pp. 1541-1545

[59] http://www.polytec.com/int/solutions/3-d-surface-profiling/basics-of-white-light-interferometry/

[60] http://www.polytec.com/eu/products/vibration-sensors/scanning-vibrometers/

[61] J. Casas, T. Steinmann and G. Krijnen, *"Why do insects have such a high density of flowsensing hairs*? *Insights from the hydromechanics of biomimetic MEMS sensors"*, J. R. Soc. Interface (2010) Vol. 7 (51), pp. 1487-1495.

[62] R.K. Jaganatharaja, H. Droogendijk, S. Vats, B. Hagedoorn, C.M. Bruinink and G.J.M. Krijnen, "*Unraveling the viscosity-mediated coupling effect in biomimetic hair sensor arrays*", Proc. of 24th IEEE Int. conf. on MEMS, Cancun, Mexico, 23-27 Jan, 2011.

[63] B. Hagedoorn, "*Viscous coupling between bio-inspired hair-sensors*", Master thesis, University of Twente (2009).

[64] B. Bathellier, F.G. Barth, J.T. Albert and J.A.C. Humphrey, *"Viscosity-mediated motion coupling between pairs of trichobothria on the leg of the spider Cupiennius salei"*, J. Comp. Physiol. A (2005) Vol. 191, pp. 733-746. Erratum: J. Comp. Physiol. A (2010) Vol. 196, p. 89.

2

Sensor model and design optimization

In a nutshell...

This chapter deals with the analytical modeling of the artificial hair sensors. The core models are chiefly based on the biomechanical models developed by the bio-physicists in order to understand the mechanical performance of the actual mechano-receptive filiform hairs of crickets' cerci. These models are extended to inspire and provide insights for optimizing the existing sensor design. A figure of merit is defined for optimal sensor performance and the key design factors are identified and analyzed. The finalized design modifications and their resulting inspiration and links to the forth-coming chapters of this thesis are discussed as closing remarks. In doing so, this chapter, thus becomes the blueprint for the work of the whole thesis.

2.1. Introduction

The structural functionality of crickets' filiform hair has been extensively analyzed in terms of mechanical and aerodynamical models in literature [1-4]. A filiform hair is described as an inverted pendulum, a second-order mechanical system, which is characterized by the torsional spring constant S, the hair moment of inertia J and the torsional resistance R. Whereas biologists have used the models to arrive at estimates of the above said mechanical

parameters, we have implemented the models to optimize the existing sensor design with respect to the actual sensor properties. This model approach and the extensively discussed results of it are found in [4]. The motive is to identify the key design parameters that influence the performance of the sensors under the given flow conditions. It is to be mentioned that sensor system scaling and the mechanical system behavior are much similar to those of the cercal filiform hairs. This fact makes it easy for biomimetic sensors to be inspired by the actual design evolved in nature and to optimize their designs to perform on a par to their natural counterparts. Possible design optimizations, concerning different aspects of our hair sensors, are discussed and their connections to the forth coming chapters in this book are presented. Additionally, the effect of viscous coupling between the hairs is introduced and how artificial hair sensors could be helpful in analyzing such an effect is discussed.

2.2. Hair sensor model

The basic schematic representation of our hair sensor is shown in figure 2.1. Each artificial hair sensor comprises of a hair that acts as a feature on which the surrounding air flows act by viscous drag forces. The hair is centrally mounted on top of a thin membrane, which is suspended via a pair of suspensions. The membrane is left suspended above a highly conductive substrate by selective removal of a sacrificial layer and is free to rotate about the axis of the suspensions. The suspended membrane has a pair of isolated electrode layers, which together with the highly conductive substrate form two individual sensor capacitances (in the figure, C1 and C2).

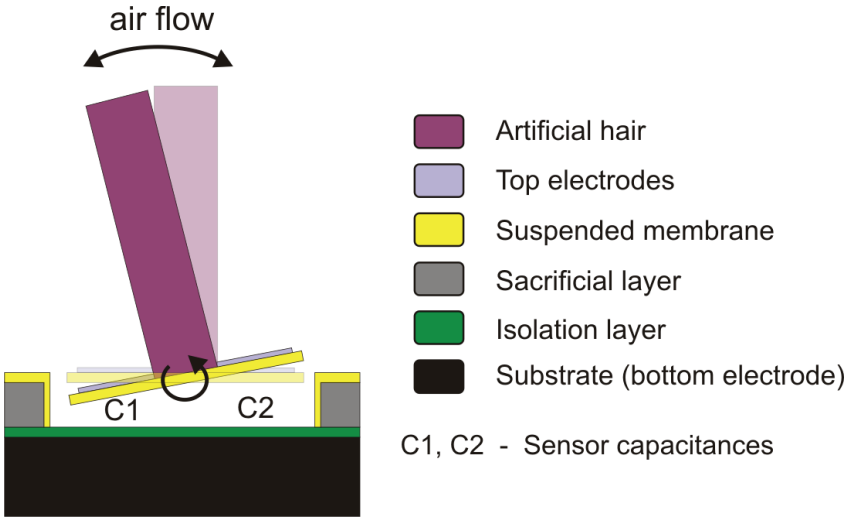

Figure 2.1 *Schematic representation of the hair sensor*

Whenever the air flow interacts with the hair, it induces certain drag-force along the length of the hair. Depending on the direction of the flow, it can result in a torsional deflection of the hair which simultaneously tilts the suspended membrane. Such drag-torque induced membrane tilt causes significant and countering changes in distances separating the top and bottom electrodes of sensor capacitances i.e. the inter-electrode distance of one decreases due to the tilt while that of the other increases. By appropriately sensing the difference between these two capacitances, the flow information can be obtained.

The performance of the hair sensors directly depends on the mechanics of the system and the effective transduction of the mechanical work into changes in electrostatic energy. Careful choice of design parameters becomes the central goal of this work and hence, developing an analytical model to predict the sensor performance will aid to identify the key design parameters and assigning the right values to them. Since the actual cercal filiform hairs of the crickets are exposed to the relevant flow environments, the models developed by the bio-physicists to study the filiform hairs themselves apply equally well to our artificial hair sensors. Figure 2.2 provides a quick overview of the physical concepts involved in the following modeling of the sensors.

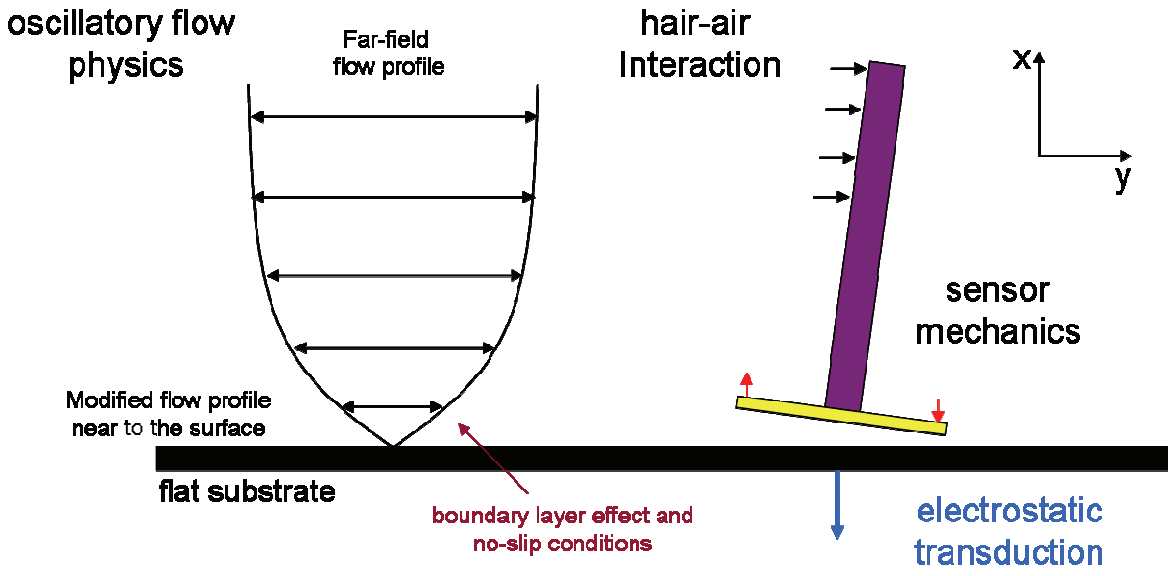

Figure 2.2 *Conceptual schematic introducing the key physical interactions related to the model of sensor performance*

The first part of the model is about the physics of the oscillatory air flows and we will discuss about the characteristics of the flow over a flat substrate. By modeling the interaction between the hair and air flow, the drag force acting on the hair can be calculated. It is then followed by modeling the mechanical system of the hair sensor and the chief parameters governing the hair deflection. With the model governing the sensor mechanics, the deflection of the sensor membrane in response to the drag-torque can be theoretically predicted. The predicted mechanical deflection of the sensor membrane is used to analyze the electrostatic transduction which is used to predict the final electromechanical sensor response.

2.2.1 Harmonic flows

In the model the hair sensors are subjected to harmonic air flows which exert drag on the hairs. The model of the oscillatory flows is extensively borrowed from [1-3]. Harmonic flows are biologically relevant since most predators of crickets are inevitably generating low-frequency harmonic flows (e.g.: wing-beatings of wasps, crawling legs of spiders, etc.) [Refer Chapter 1]. The hair sensor is modeled as a long circular cylinder on a flat substrate, surrounded by a fluid medium which is subjected to the driving harmonic flows. A reciprocal problem, the effects of an oscillatory fluid on an infinitely long pendulum, was studied in

detail by Stokes in 1851 and his model was later used by almost all studies related to cricket hairs [5]. The drag force exerted on the cylinder depends upon the properties of the fluid medium surrounding the cylinder (in our case, air) driven by the harmonic flows, which has long-been studied under the fundamentals of fluid dynamics.

Air, which surrounds the hair sensors (both natural and artificial), is a viscous medium in nature and the flow velocities studied here falls in the low-Reynolds' number regime. Reynolds number is a dimensionless number that relates the inertial forces to the viscous forces in the fluid. The typical air flow velocities that drive the hair sensors (and also the actual filiform hairs of the cricket) and the tiny size of the hairs itself puts them in a low Reynolds number regime (Re = 0.001 – 0.02 [1, 2]), which means the viscous forces are predominant over the inertial forces.

Viscosity is the physical characteristic that distinguishes fluids and solids, in terms of their response to the shearing forces acting on them. For fluids, unlike solids, due to their lack of structural rigidity, an applied shear force on their surface induces a fluid motion which subsequently develops a velocity gradient in the fluid medium. The rate of the shearing strain is then equal to the velocity gradient. Hence, for fluids, the shear stress is proportional to the rate of the shearing strain. The proportionality constant is defined as the dynamic viscosity (μ). The value of dynamic viscosity of air is $1.82 \cdot 10^{-5}$ N.s/m^2 (at 20° C and standard atmospheric pressure).

The interaction of fluids with solids is an interesting field of research. Under the so-called 'no-slip condition', the situation in which the fluid at a solid-fluid interface is assumed to have the same velocity as the solid, there exists a boundary layer in which the fluid-flow transitions from equal to the solid's velocity to a far-field velocity at some distance from the interface. As the fluid flows past a solid surface, it experiences a shearing action at the vicinity of the solid surface

To put it in relevant terms, let us first consider a harmonic air flow velocity parallel to a flat substrate (Figure 2.2) and is defined by a far-field velocity given by:

$$V_{\mathrm{f},\infty}(t) = V_0 \cdot \sin(\omega \cdot t) \tag{2.1}$$

where ω is the angular frequency of the harmonic flow and V_0 the amplitude of the oscillatory flow. Such air flows, irrespective of their far-field velocities, reduce down to zero velocity at the interface with the flat substrate (which for simplicity is assumed not to move in this example). Thus there exists a velocity gradient in the harmonic flow between the far-field and the substrate. The resulting boundary layer is defined as the layer (increasing along the x-direction from the substrate) in which the fluid velocity changes from zero velocity to 99% of the far-field velocity [2,6]. And for such a boundary layer, its depth or thickness (δ_b) is dependent on the frequency of the fluid motion and is given as:

$$\delta_\mathrm{b} \propto \frac{1}{\beta}$$
$$\beta = \sqrt{\frac{\omega}{2 \cdot \nu}} \tag{2.2}$$

where υ is the kinematic viscosity (defined as $\nu = (\mu/\rho)$ with ρ being the mass density of the air medium). The kinematic viscosity of air is $15.1 \cdot 10^{-6}$ m^2/s (at 20° C and standard

atmospheric pressure). Figure 2.3 shows the boundary layer thickness plotted over a wide frequency range from 10 to 10 kHz and it is found that the thickness is large at low frequencies. The frequency-dependent flow velocity profile near a flat substrate, when the flow is parallel to the substrate, is given by [1,2]:

$$V_{\mathrm{f}}(x,t) = V_0 \cdot \sin(\omega t) - V_0 \cdot e^{-\beta x} \cdot \sin(\omega t - \beta x) \qquad (2.3)$$

where x is the perpendicular distance from the substrate.

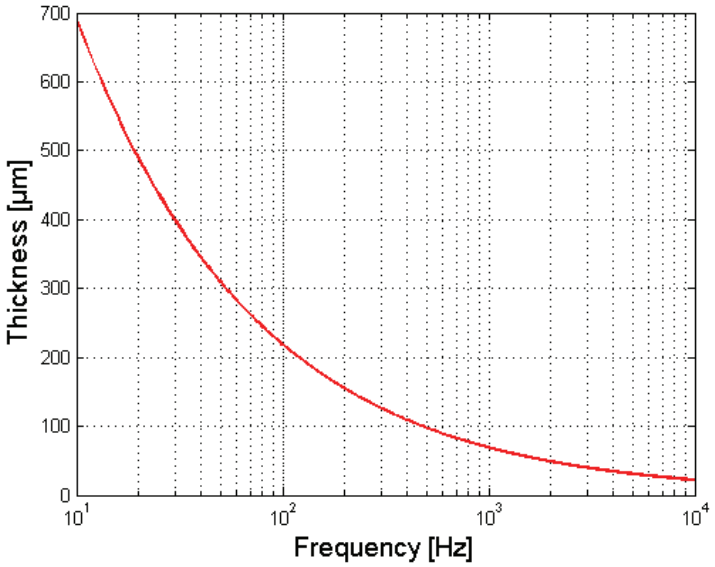

Figure 2.3 *Boundary layer thickness plotted against frequency for an harmonic air flow above a flat substrate.*

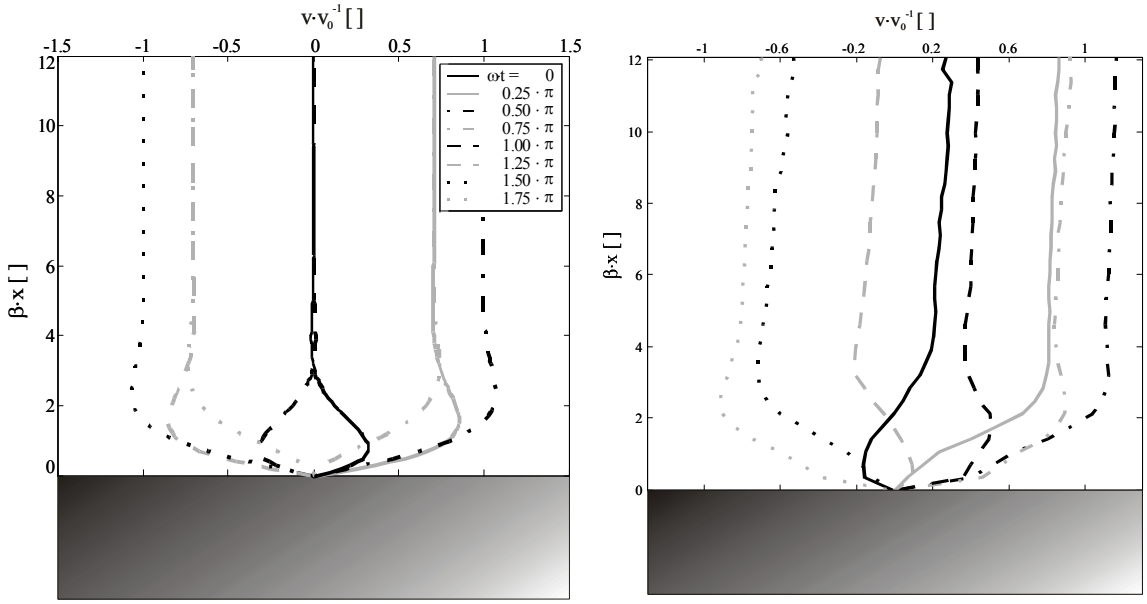

Figure 2.4 *Oscillating boundary layer on a flat surface: (left) model and (right) measured using a Particle Image Velocimetry setup [7], normalized with V_o=3 cm/s and f=60 Hz. (Courtesy: T. Steinmann et. al., University of Tours, France [7]).*

Figure 2.4 shows a comparison of model and measured values of normalized flow velocity profiles, parallel to and above a flat substrate, plotted against the normalized distance from the substrate for different instances of time for one period of oscillation. The measurements were performed (by T. Steinmann *et. al*., University of Tours, France) using Particle Image Velocimetry setup [7]. There is satisfying agreement between the model and the measurements, assuring the validity of equation (2.3) and justifying using the model in the forth-coming analysis.

2.2.2 Air-hair interaction

The hair sensors are subjected to the velocity profile given by equation (2.3). At the interface of the hair surface and the air flow, there exists another boundary layer due to the velocity difference between the moving hair and the flow velocity. This velocity gradient between the flow and the hair gives rise to frictional forces acting over the surface of the hair for its entire length called 'viscous drag forces'. Bio-physicists used Stokes' equations to calculate the drag forces acting on the filiform hairs of the cricket [1,2]. For the sake of simplicity and applicability of Stokes' equations, they considered the hair as a cylinder harmonically rotating on a pivot point by the periodic air flow. Stokes' equations give a direct relation between the relative velocity and the generated drag torque on the moving cylinder. The flow velocity of the oscillating air is given by eq. (2.3) previously. The velocity of the moving cylinder at a specific height, x, depends on the vertical distance from the substrate and the angular velocity of the cylinder about its base and is given as [8]:

$$V_{\mathrm{h}}(x) = x\dot{\alpha} \tag{2.4}$$

where α is the angular displacement. The relative velocity between the air flow and the cylinder is then given as:

$$V_{\mathrm{r}} = V_{\mathrm{f}} - V_{\mathrm{h}} \tag{2.5}$$

In order to apply Stokes' equations, it is important to note the three approximations for which the analysis is valid. They are: (i) for a cylinder of length L and diameter, d_{h}, the ratio of $L/d_{\mathrm{h}} >> 1$ (ii) the angular displacement amplitude of the cylinder (or hair) is small and (iii) the parameter $s << 1$ where s is given as [8]:

$$s = \left(\frac{d_{\mathrm{h}}}{4}\right)\left(\frac{2\pi f}{\upsilon}\right)^{0.5} \tag{2.6}$$

where f is the oscillation frequency of the air and υ is kinematic viscosity of air. It has to be noted that satisfying the condition of $s << 1$ also implies that the Reynold's number, (Re) $<<1$. The drag force generated per unit length of the cylinder by a harmonic flow velocity consists of three components as described by the below equation [8]:

$$F_{\mathrm{d}} = F\left(\mu, V_{\mathrm{r}}\right) + F\left(\mu, \dot{V}_{\mathrm{r}}\right) + F\left(\rho, \dot{V}_{\mathrm{r}}\right) \tag{2.7}$$

where each of the force components are defined as:

$$F\left(\mu, V_{\mathrm{r}}\right) = 4\pi\mu G V_{\mathrm{r}} \tag{2.8}$$

$$F\left(\mu, \dot{V}_{\mathrm{r}}\right) = -\frac{\pi\mu G \dot{V}_{\mathrm{r}}}{2gf} \tag{2.9}$$

$$F\left(\rho, \dot{V}_{\mathrm{r}}\right) = \pi\rho\left(d_{\mathrm{h}} / 2\right)^2 \dot{V}_{\mathrm{r}} \tag{2.10}$$

As seen above, two of these components (eq. (2.8) and (2.9)) are proportional to the dynamic viscosity (μ) of the fluid and the other one (eq. (2.10)) is proportional to the density of the fluid (ρ). The parameter G in the above equations is defined as [8]:

$$G = -\frac{g}{\left(g^2 + \pi^2 / 16\right)} \tag{2.11}$$

where g is given by:

$$g = \ln\left(s\right) + \gamma \tag{2.12}$$

where s is defined previously by eq. (2.6) and γ is Euler's constant (of which the value is 0.577).

Drag forces acting on the cylinder impart a certain drag-torque on it and inducing an angular deflection with respect to the base. Using the expressions for the drag force per unit length, the drag-torque acting on the entire length can be calculated as:

$$T = \int_0^L F_{\mathrm{d}}\left(x\right) \cdot x dx \tag{2.13}$$

where L is the length of the cylinder from the flat substrate.

Figure 2.5 shows the generated drag-torque on an immobilized cylinder obtained using the above models for different lengths and diameters of the hair for harmonic air flows of a wide range of frequencies. From figure 2.5(a), it is evident that the drag-torque increases proportional to the cube of the hair length (L^3) for $L < \delta_{\mathrm{b}}$ and it increases proportional to the square of the hair length (L^2) for $L > \delta_{\mathrm{b}}$. Such behavior clearly shows the prominence of the hair length in determining the drag-torque. At any instance, for a hair to effectively pick-up drag-torque, its length has to scale with the boundary layer thickness (δ_{b}). From figure 2.5(b), as expressed in the equation (2.4), the diameter of the hair has far little impact on the drag-torque.

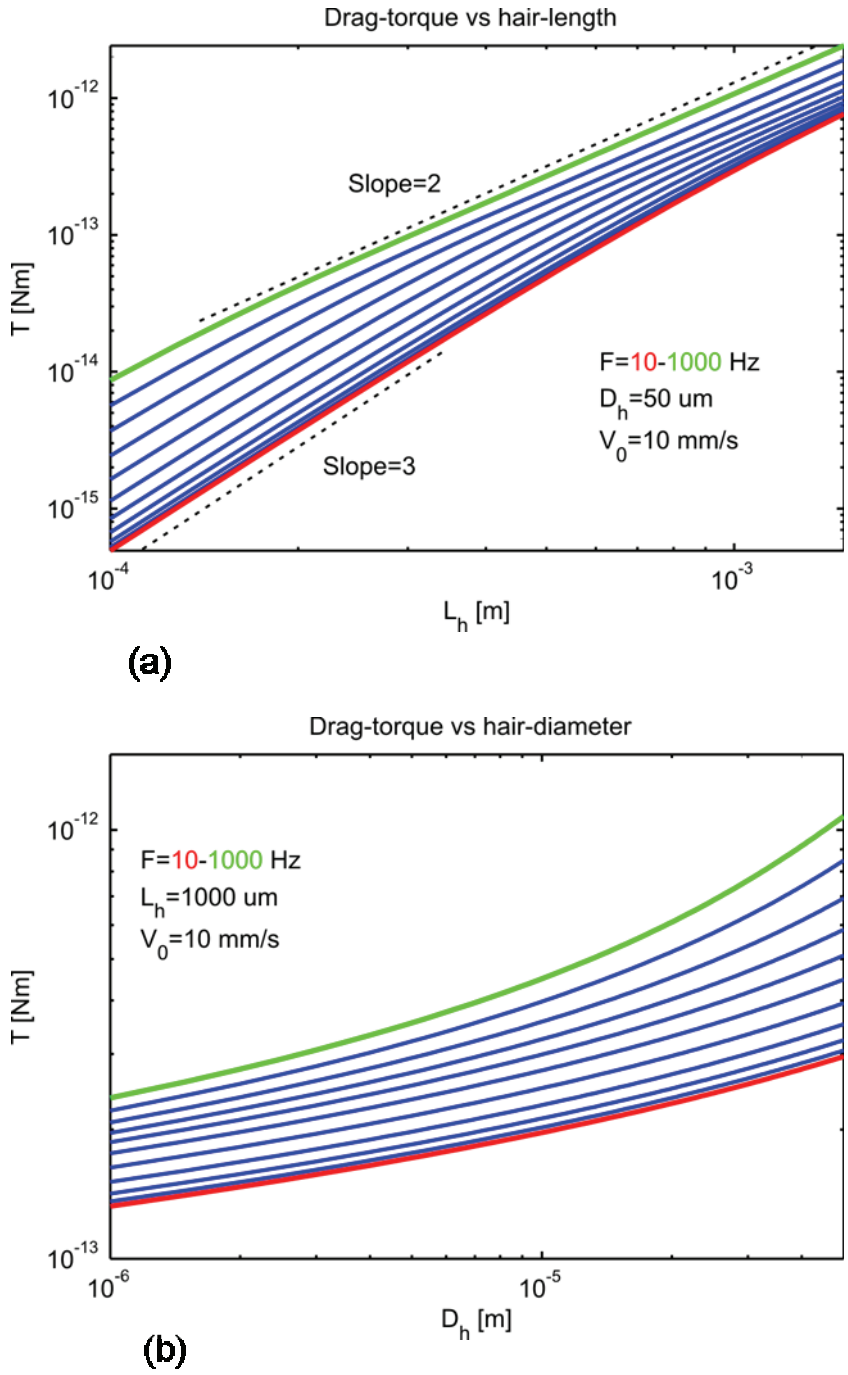

Figure 2.5 *Drag-torque generated on hairs fixed on a substrate and subjected to a harmonic flow of which the oscillation frequencies ranges from 10 -1000 Hz: (a) for different hair lengths with a hair diameter of 50 μm and (b) for different hair diameters for a 1000 μm long hair*

2.2.3 Hair sensor mechanics

Having modeled the oscillatory flow physics and the interaction of it with the hairs leading to the generation of drag forces, now it is appropriate to model the response of the hairs subjected to these drag-torques. Drag-torque acting on our hair sensor results in the

periodic tilt of the sensor membrane, which will change the sensor capacitances accordingly. In this section, we will model the tilt of the sensor membrane, for the given drag-torque. As mentioned in the beginning of this chapter, bio-physicists studying the natural hair-sensors have modeled the mechanics of the filiform hairs by an oscillating, inverted pendulum, which is basically a second-order mechanical system [1-3]. Figure 2.6 shows the model of the hair as an inverted pendulum.

The second-order mechanical system is determined by the three intrinsic mechanical parameters: (i) hair moment of inertia, J, (ii) torsional stiffness at the hair base, S and (iii) torsional resistance at the hair base, R. These parameters are responsible for balancing the hair dynamics under the action of external torque acting upon the hair. The conservation of angular momentum requires that:

$$J\ddot{\alpha} + R\dot{\alpha} + S\alpha = T \tag{2.14}$$

where α represents the rotational angle of the hair, in response to the drag-torque, T, given by equation (2.13). Combining equations (2.13) and (2.14), we get [8]:

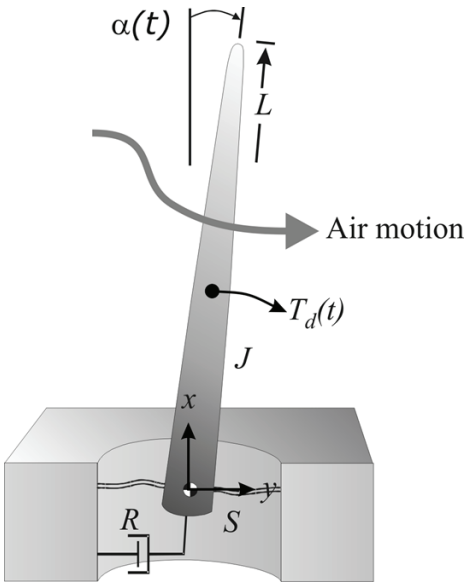

Figure 2.6 *Inverted pendulum as a model for the sensory hair*

$$\begin{aligned}\left(J + J_{\rho} + J_{\mu}\right)\ddot{\alpha} + \left(R + R_{\mu}\right)\dot{\alpha} + S\alpha &= 4\pi\mu G\int_0^L V_{\mathrm{f}}(x)\cdot x dx \\ &+ \left(\frac{\pi\rho d_{\mathrm{h}}}{4} - \frac{\pi^2\mu G}{g\omega}\right)\int_0^L \dot{V}_{\mathrm{f}}(x)\cdot x dx\end{aligned} \tag{2.15}$$

where J_ρ, J_μ and R_μ represent the contributions of the medium to the moment of inertia and damping constant of the cylinder based on the mediums density and dynamic viscosity. These additional contributions are defined as:

$$J_\rho = \frac{\pi \rho d_h^2 L^3}{12} \tag{2.16}$$

$$J_\mu = -\frac{\pi^2 \mu G L^3}{3 g \omega} \tag{2.17}$$

$$R_\mu = \frac{4}{3} \pi \mu G L^3 \tag{2.18}$$

Equation (2.16) represents the contribution to the moment of inertia due to the displacement of air along with the tilting cylinder. Equation (2.17) on the other hand represents the contribution of air viscosity to the moment of inertia. For air, the contribution of J_ρ is small compared to J and J_μ [8]. Equation (2.18) represents the additional viscous drag force, due to the interaction of air with the cylinder. For the case of our hair sensors, due to the stiff sensor springs, the hair displacement can be assumed very small. This is important since the contributions of these parameters will be different for the case of hair sensors featuring compliant springs and thin hairs (which will be quoted as the ideal requirements for the optimal performance of the sensors, as will be discussed later in this chapter.)

For a cricket (*Gryllus bimaculatus*) filiform hair of 1 mm length, Shimozawa *et al.* [1] have experimentally determined the values for the above mechanical parameters: $J \sim 5 \cdot 10^{-18}$ kg·m^2, S $\sim 2 \cdot 10^{-11}$ Nm·rad^{-1} and R $\sim 10^{-14}$ Nms·rad^{-1}. It has to be noted that these parameters are observed to scale allometrically with the hair lengths and is given as follows: (i) $S \propto L^{1.67}$, (ii) $J \propto L^{4.32}$ and (iii) $R \propto L^{2.77}$ for the filiform hairs of crickets [1]. Resonance frequencies of the filiform hairs lie in the range of 100-3000 Hz depending on the hair length and structural allometric scaling [1,3]. The best frequencies are lower since the mechanical system is moderately damped with nearly constant quality factor over the entire range of hair lengths observed. The damping is hypothesized to have evolved under the natural constraints to have the best impedance matching to the mechanical impedance of the harmonic flow [1,2]. For the optimal sensitivity of the hairs, proper mechanical impedance matching should allow for maximum energy transfer.

The equation for the angular momentum conservation given by (2.15) has been solved analytically and numerically using different methods [1,2]. For harmonic excitation torque at radial frequency ω, the steady harmonic rotational motion of the hair about its base, is given as:

$$\alpha_0(\omega) = \frac{T_0}{J_t} \cdot \frac{1}{\omega_0^2 - \omega^2 + j\omega(R_t / J_t)} \tag{2.19}$$

where T_0 is the amplitude of the drag-torque and ω_0 is the resonance frequency given by $(S/J)^{0.5}$. Here $J_t = J + J_\mu + J_\rho$ and $R_t = R + R_\mu$.

2.2.4 Transduction model

The oscillatory motion of the hair sensor, in our case, transcends as change in the capacitance between the top electrode and the bottom electrode, as discussed early in this section. The rotational angle α of the hair sensor, measured in radians, is derived from equation (2.19). It would be appropriate to recall the sensor structure before we derive the electrostatic equations concerning the eventual sensor response to the driving flows. Figure 2.7 shows the schematic of the sensor relevant to the following analysis.

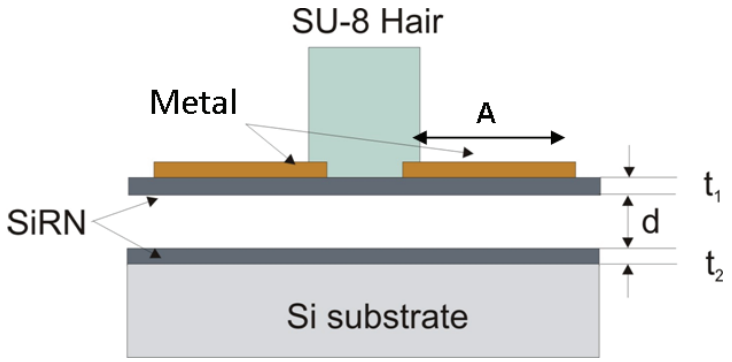

Figure 2.7 *Schematic of the sensor showing different dielectric thicknesses between the top and bottom electrodes*

The cylindrical hair is positioned centrally on a suspended rectangular shaped silicon nitride membrane (of thickness, t_1). On either side of the hair, there is a pair of independent electrodes, which form capacitors with the common bottom electrode (substrate), while being separated by a thickness of the sacrificial layer, d. There is a thin insulation and etch-stop layer of silicon nitride (of thickness, t_2) between the capacitive electrodes. In general, the capacitance of a static parallel plate capacitor of area A and separated by a dielectric layer of thickness, d is given as:

$$C = \frac{\varepsilon_0 A}{\left(d/\varepsilon_r\right)} \tag{2.20}$$

where ε_0 and ε_r are the dielectric constant of air and relative dielectric constant of dielectric material. The capacitive sensitivity is defined as the change in sensor capacitance per unit rotation of the sensor membrane α. Drag-torque induced torsional rotation of the hair sensor causes one half of its membrane to tilt upwards while the other half tilts downwards. In terms of capacitances, this transforms as decreased capacitance of one side (the side which tilts up) and increased capacitance on the other side (the side which tilts down). The capacitive sensitivity is given as:

$$\begin{aligned} \eta &= 2\cdot \left.\frac{\partial C}{\partial \alpha}\right|_{\alpha=0} = 2\cdot \lim_{\alpha\to 0}\frac{\partial}{\partial \alpha}\left(\int_A \frac{\varepsilon_0}{d_0-\alpha r}\,dA\right) \\ &= 2\cdot \int_A \lim_{\alpha\to 0}\left(\frac{\varepsilon_0 r}{\left(d_0-\alpha r\right)^2}\right)dA = 2\varepsilon_0\cdot \int_A \frac{r}{d_0^2}\,dA \end{aligned} \tag{2.21}$$

with sin (α) ≈ α, as the rotation angle in our case is usually very small. In the above equation A is the area of half the membrane (one side), r is the distance from the rotation axis and the effective dielectric thickness d_0 is given as:

$$d_0 = d + \frac{t_1 + t_2}{\varepsilon_r} \tag{2.22}$$

where d is the distance between the electrodes (sacrificial layer thickness), t_1 and t_2 are the thickness of the silicon nitride layers (thicknesses of sensor membrane and etch-stop layers respectively) and with ε_0 and ε_r the dielectric constant of air and relative dielectric constant of silicon nitride, respectively. For our hair sensors with rectangular membranes of width w and length l, the sensitivity is found to be:

$$\eta_R = 2\varepsilon_0 \int_0^w \int_0^l \frac{z}{d_0^2} dydz = \frac{\varepsilon_0 w l^2}{d_0^2} \tag{2.23}$$

2.2.5 Discussion

Previous sections have given a thorough understanding of the physics behind the fluid and hair interaction by means of theoretical models developed by bio-physicists. The mechanical response of the sensor is given in equation (2.19), which is obtained by solving equation (2.15). To obtain the electromechanical sensor response, this total mechanical response must be multiplied by the capacitive sensitivity, as expressed in equation (2.23). Figure 2.8 shows a comparison of the model and the experimentally measured response of a cricket hair of ~1 mm long, using the parameters given above.

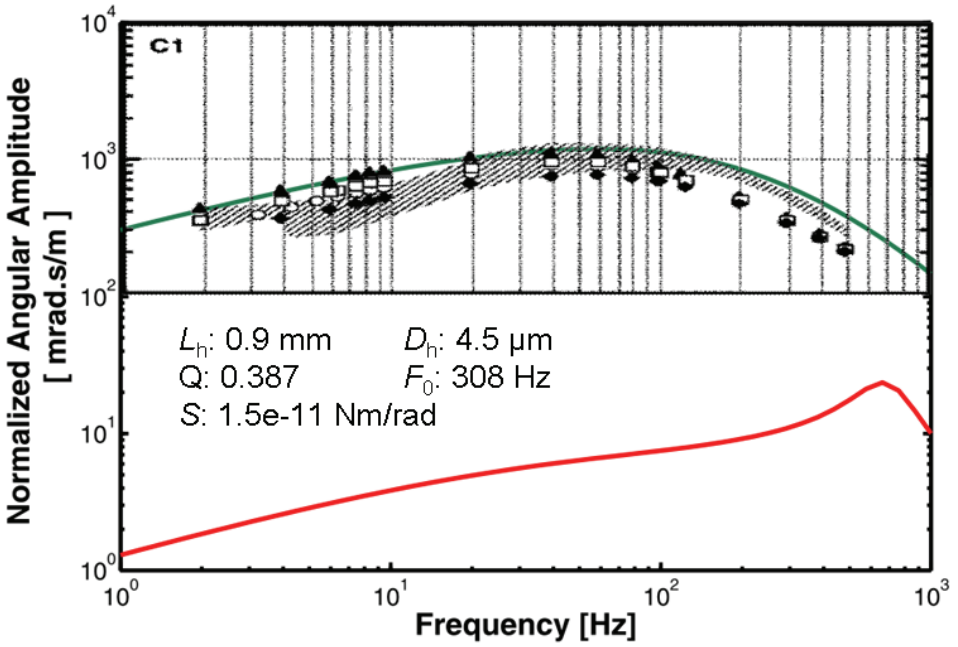

Figure 2.8 *Comparison of model (solid, green line) and measurements [3] on cricket hairs (black markers) showing excellent agreement. Parameters for the cricket hair input to the model were taken from [3]. The same models are used to predict the response of the artificial hair sensor (red, solid line).*

The same model is applied to predict the response of our artificial hair sensor, which will be very effective in order to compare it with the measurements on the hair sensors. The figure shows a model predicted response of an artificial hair sensor with a ~900 μm long and 50 μm diameter hair. One important fact that needs to be emphasized is the difference in the responses of the cricket hairs and the artificial sensor design of over two orders, especially at low frequencies. By analysis and careful design choices, this large gap can be effectively reduced. The following section is dedicated to pointing out the possibilities for design optimization.

2.3. Design optimization

While the analytical models provide a thorough understanding and a theoretical way to predict the hair sensor response under the given flow conditions, it is now important to define a certain standard in reference to optimal sensor performance. In this section, we will first define a figure of merit, in terms of sensor performance and from that we draw motivations to analyze and optimize each functional component of the hair sensor. The functional components of each hair sensor are: (i) the hair, responsible for the drag-torque reception and constituting almost exclusively the moment of inertia of the system, (ii) sensor torsional springs S of the system and (iii) sensor capacitors, which comprise the sensor membrane, electrode gaps and the electrodes itself. We will discuss in detail the possible optimizations in each of these components and draw their connections to the forthcoming chapters of this thesis.

2.3.1 Figure of merit

In order to optimize the hair-sensors and to allow a comparison between artificial and natural hair-sensors we make the following observations on the mechanics of the system [4]:

a) When the torsional spring stiffness is low, the drag-induced rotations are large providing high membrane rotation. Hence a low rotational stiffness seems desirable.

b) The resonance frequency of the hairs depends on the torsional stiffness S; the lower S is the lower the resonance frequency ω_0 at given moment of inertia J will be. It is not unreasonable to take the resonance frequency ω_0 as a measure for the bandwidth in which the sensors can be used since above this frequency the response decreases with about 12 dB/octave.

c) Longer hairs do experience larger drag-torque than smaller hairs (figure 2.5(a)) and seem to be desirable for high sensitivity.

d) At the same time hair-length L appears cubed in the inertial moment J having large impact on ω_0.

e) The diameter of the hairs has a quadratic influence on the inertial moment, but only a moderate effect on drag-torque (figure 2.5(b)). Although depending on frequency, in the frequency range of interest the relation between the drag-torque and the diameters can be approximated by $D^{1/3}$.

Sensor-optimization has (at least) two dimensions: usable bandwidth and (low-frequency) sensitivity. If one of both is (too) low the usability of the sensor is strongly hampered. We have also argued that both sensitivity and bandwidth depend strongly on S, L and D. Therefore we define a figure of merit (*FoM*) as the product of usable bandwidth (i.e. proportional to ω_0) and low frequency sensitivity (i.e. the drag-torque to which a hair is exposed divided by the rotational stiffness). Using the above simplifications we arrive at [4]:

$$FoM = \omega_0 \cdot \frac{T_d}{S} = \sqrt{\frac{S}{J}} \cdot \frac{T_d}{S} \propto \sqrt{\frac{S}{\rho L^3 D^2}} \cdot \frac{L^2 D^{1/3}}{S} = \sqrt{\frac{L}{\rho S D^{4/3}}} \qquad (2.24)$$

This *FoM* shows that sensitive sensors with a large usable bandwidth should have long, thin hairs made of low density material, and small torsional stiffness, consistent with what is seen in nature. In comparing the *FoM* of the artificial hair-sensors to the *FoM* of the crickets' hair sensors, we find that cricket hairs perform about 70 times better mechanically (for 1 mm long hairs). Crickets out-perform artificial sensors because of their low torsional stiffness ($2 \cdot 10^{-11}$ vs. $7 \cdot 10^{-9}$ Nm/rad) and small average hair-diameter (4.5 vs. 50 μm).

While the *FoM* concerns the mechanical aspects of the sensor system, and indicates the constructive ways for sensor optimization, it does not include the transduction part (sensor capacitors) where the mechanical energy is transformed into an electrical signal. To make the discussion complete, it is essential to combine the capacitive sensitivity η_R with the definition of the *FoM* and can be put them together as overall sensor Figure of Merit (*OSFoM*) given by:

$$OSFoM = FoM \cdot \eta_R \propto \sqrt{\frac{L}{\rho S D^{4/3}}} \cdot \frac{\varepsilon_0 w l^2}{d_0^2} \qquad (2.25)$$

where w and l are the electrode dimensions of a capacitor plate, ε_0 is the dielectric constant of air and d_0 is the effective gap between the electrodes, as defined in sub-section 2.2.4. Though there are not many substantial conclusions that we could arrive at concerning the design of capacitors beforehand, it comes handy at a later stage when we are met with technological problems during the fabrication of the sensors. For instance, the effective gap between the electrodes d_0 applies to perfectly flat sensor membranes and this is not always the case in practice. At many instances, the membranes are curved due to residual stress and by analysis it is feasible to incorporate the detrimental effects of this curvature and find an optimal way to reduce such an effect. Section 2.3.4 sheds more light on this.

Summing up, there are three functional components of our hair sensor system: (i) hairs, (ii) sensor springs and (iii) sensor capacitors, all of which we will focus on in the following sub-sections. These sections will address the requirements for high *OSFoM* values and at the same time, discuss the feasibility issues surrounding them. Additionally, a brief sub-section of damping coefficient, a complex parameter, of our sensor system is presented and some qualitative views with respect to sensor optimization are discussed.

2.3.2 SU-8 hairs

The hairs in our sensor arrays are made of SU-8, an epoxy-based, polymer. SU-8 is a negative-tone photoresist (UV-exposed portions of the layer remain intact upon development),

commercially available and which can be processed using standard lithography [9]. The hairs are fabricated by spinning SU-8 photoresist, soft-baking it and exposing it under a UV-light source of certain intensity for a certain specified time. It is followed with post-exposure bake and then, upon subsequent development, the hairs are finally patterned on the substrate. A detailed introduction of SU-8 technology will be presented in Chapter 3 of this thesis.

From equation (2.24) the optimization with respect to hairs comprises of three factors: (i) hair length L, (ii) hair diameter D and (iii) mass-density ρ of the hair material (which is SU-8). One favorable factor of choosing SU-8 polymer as a material for making hairs is that its mass density ($1.24 \cdot 10^3$ kg/m^3) is comparable to that of the actual cricket hairs ($1.2 \cdot 10^3$ kg/m^3). The parameters that can be chosen are the length and the diameter of the hair.

The length of the hairs is determined by the thickness of the spun SU-8 layers during fabrication. Commercially available SU-8 comes in a wide-range of varieties, depending on the thickness required when spun at a standard rate of rotation cycles per minute [9]. The achieved thickness varies from ≈ 0.2 to 450 μm per single spun layer. A very recent product claims to achieve 650 μm per single spun layer [9]. An advantage of the SU-8 technology is that it allows multi-layer processing, meaning layers can be processed one-by-one in a bottom-up approach, by repeated exposure cycles for each and then developed. The disadvantage to this approach is the difficulty in precise alignment of the layers with each other, which increases with the number of layers. In our early generations of hair sensor arrays single layers of SU-8 were spun and a hair length up to 480 μm was fabricated. In order to fabricate SU-8 hairs of ~1 mm length, we have to spin two layers of SU-8 by subsequent patterning cycles.

The diameter D of the hair is defined by the design of the photomask, which is used during the exposure, following the spinning of SU-8 layers. Before it sounds as a simple and easy step, we should mention another limitation of SU-8 technology, concerning the aspect ratio of the SU-8 structures. The aspect ratio is defined as the ratio of height of the patterned structure to the width of it. SU-8 technology allows for about a factor of 10 - 20 for its aspect ratio per single layer. It means, in relevant terms, if there is a circular opening of 20 μm in diameter on the photomask during exposure, it is possible only to make approximately 200 - 300 μm long cylinders after development and patterning

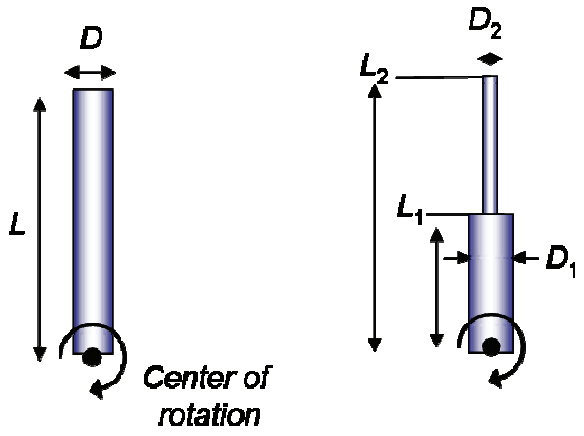

Figure 2.9 *Two-layer SU-8 hairs with a constant diameter and different diameters*

Design optimization – Two cylinder hairs

SU-8 hairs are responsible for drag-torque reception from the flows and largely constitute the moment of inertia J of the hair sensor mechanical system. The drag-torque on

the hairs is explained elaborately in the previous sections. For a cylinder of length L and diameter D (see figure 2.9 (left)), the moment of inertia for rotation around the center of the base of the hair (which sits on the rotational axis of the sensor) is given by:

$$J = \frac{\rho\pi(D/2)^4 L}{4} + \frac{\rho\pi(D/2)^2 L^3}{3} \tag{2.26}$$

and this for an SU-8 hair of ~1000 μm and a diameter of 50 μm turns out to be $7.4 \cdot 10^{-16}$ kg.m^2. Also note that the first contribution is about 500 times smaller than the second part emphasizing the importance of the hair-length for the value of J.

For the sensors with reduced torsional stiffness in their sensor springs, it is essential that the moment of inertia J of the hairs is small, in order to retain sufficient usable bandwidth. While the length of the hair is nearly fixed (by the thickness of SU-8 layers) by technology, the only way is to modify the diameter of the hairs to obtain reduction in the moment of inertia of the hair. Due to the limitation of the aspect ratio and by alignment, we are restricted with few design choices for modifying the diameter.

One way is to have hairs of two-layer SU-8 with different diameters for the top and the bottom part of the hair, as shown in the figure 2.9 (right). The moment of inertia for the modified hair geometry is given by (this will be discussed more elaborately in chapter 3):

$$\begin{aligned} J_h = {} & \frac{\rho\pi}{4}\left\{\left(\frac{D_1}{2}\right)^4 L_1 + \left(\frac{D_2}{2}\right)^4 (L_2 - L_1)\right\} \\ & + \frac{\rho\pi}{3}\left\{\left(\frac{D_1}{2}\right)^2 L_1^3 + \left(\frac{D_2}{2}\right)^2 (L_2^3 - L_1^3)\right\} \end{aligned} \tag{2.27}$$

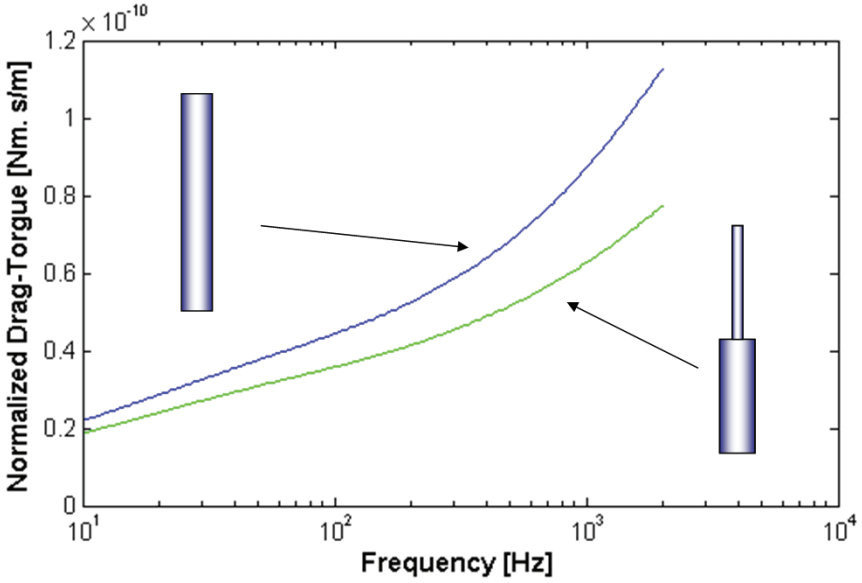

Figure 2.10 *Two-layer SU-8 hairs with constant diameter and with two diameters*

For an SU-8 hair with bottom diameter of 50 μm and a top diameter of 30 μm with a hair length of ~1000 μm, the moment of inertia as calculated using the above equation is $2.3 \cdot 10^{-16}$ kg.m^2. This translates to a reduction in the hair moment of inertia by ~65%. The comparison of drag-torque generated on both of these hairs is shown in figure 2.10. Though some noticeable amount of drag-torque is lost, it can however be compensated by the increase in overall sensitivity by means of a reduced torsional stiffness of the new spring designs.

Discussion

The hairs, comprising different top and bottom diameters, reduce the moment of inertia while sacrificing some drag-torque generated on them. However, optimal shape for the SU-8 hairs should strike a balance between drag-torque reception capability and moment of inertia. The actual filiform hairs of crickets' cerci are elongated conical-shaped [1], which serves this balance. New investigations are done to fabricate SU-8 hairs with nature-like shapes and with hollow structures, which will effectively retain the drag-torque while reducing the moment of inertia. Additionally this process will facilitate realizing hairs of varying hair lengths in a single technological process. Chapter 4 discusses this new strategy in detail.

2.3.3 Sensor springs

The sensor springs are responsible for supporting the membranes and the centrally mounted hair. In our sensors, silicon rich nitride is deposited and patterned to be used as the sensor springs. Typically two springs suspend the rectangular membrane and the torsional stiffness S (combined from both springs) plays an important role in the mechanics of the whole system. For larger FoM values, the torsional stiffness has to be small. The design values of each sensor spring (from the early generations of our sensors) are given as: spring length l_s (=75 μm), spring width w_s (=10 μm) and spring thickness t_s (=1 μm). The torsional stiffness S of (two) sensor springs is given as:

$$S = \frac{2 \cdot G_s \cdot I_p}{l_s} \tag{2.28}$$

where G_s is the shear modulus of the spring material (which is silicon rich nitride) and I_p is the polar moment of inertia of the springs. The shear modulus is related to the Youngs' modulus by the formula $G_s = E_s/(1+\upsilon)$ where υ is the Poisson's ratio of silicon rich nitride which is 0.22. This leaves us with two options, while designing for small torsional stiffness, namely: (i) longer beams and (ii) reducing the polar moment of inertia (which depends on w_s and t_s). As a quick and simple design choice for the new generation of sensors, we chose four basic spring designs from the combinations of spring length l_s of 75 and 100 μm and w_s of 10 and 5 μm, which in terms of torsional stiffness, ranges between $3.6 \cdot 10^{-9}$ - $1 \cdot 10^{-8}$ Nm/rad.

Discussion

Alternative methods are definitely required in order to realize sensor springs with smaller torsional stiffness (for instance, $S << 1 \cdot 10^{-9}$ Nm/rad). For optimal sensor performance such compliant springs, in combination with lighter hairs, are essential. However, realizing compliant springs alone is not desired, as they would result in smaller vertical stiffness of the springs resulting in an unstable system. Hence, optimal springs that are flexible in the desired

mode of operation and robust in all other modes are sought. Two new approaches are identified and investigated. The first approach is to use polymers as materials for sensor membranes and springs. Second approach is to modify the cross-section of silicon nitride springs (a T-section, instead of a rectangular one). The design and technology investigations based on these two approaches are dealt in detail in forthcoming chapter 5.

2.3.4 Sensor capacitors

Optimal capacitive sensitivity is inversely proportional to the square of the effective gap between the electrodes. The effective gap depends on the quality of the fabricated sensor membranes and it asks for perfect flatness. The early generations [10] of our hair sensors comprised of silicon rich nitride membranes on which chromium electrodes were patterned. Figure 2.11 shows an SEM image of rectangular membranes, with a large deflection at the membrane edges.

This deflection of the membranes is primarily due to the tensile stress present in the chromium thin layer (50 nm), deposited on top of the nitride membrane. The deflection results in an undesired increase in the gap between the electrodes, leading to a significant decrease in the sensitivity, as will be shown in following sub-section. In order to characterize the membrane curvature, the devices were analyzed using a White Light Interference Microscope (Polytec MSA400) and figure 2.12 shows the height profile results. An increase of approximately ~2-3 µm to the intended gap of 1 µm, at the curved edges of the membranes is clearly observed.

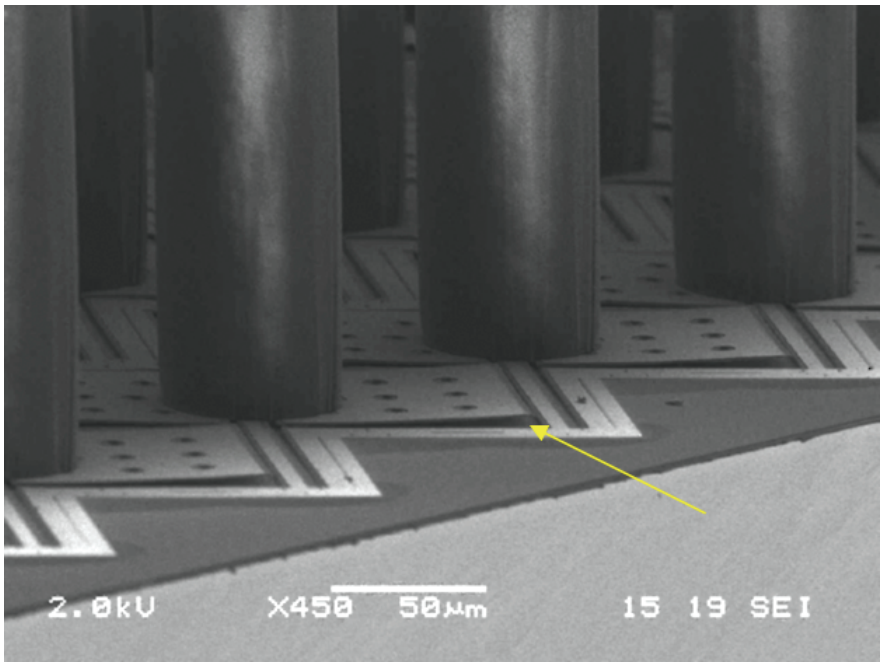

Figure 2.11 *SEM micrograph of hair sensor membrane [10] showing an undesired curvature at the edges.*

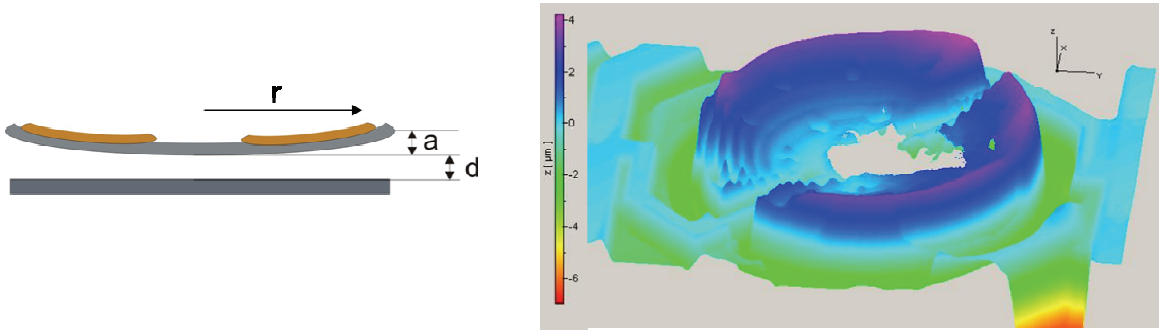

Figure 2.12 *White light interference microscopy image showing the curvature (a ~2 µm) in a circular sensor membrane.*

Deflection reduction

The deflection due to the tensile stress depends on the thickness of the chromium layer and increases along the distance from the centre (hair base) to the edges of the membrane. The curvature can be approximated by a part of a circle with a radius of curvature, R_c, which is determined from the measurements. The additional gap due to the stress is [11]:

$$a(r) = R_c\left(1-\sqrt{1-\left(\frac{r}{R_c}\right)^2}\right) \approx \frac{r^2}{2R_c} \tag{2.29}$$

where the last expression only holds for $r \ll R_c$. Such a curvature leads to an undesirable reduction in sensor capacitance and sensitivity, as shown in the modified form of equation (2.23):

$$\eta_{R,curvature} \approx \frac{\varepsilon_0 w l^2}{d_0\left(d_0+a\right)} \tag{2.30}$$

where d_o is the effective gap between the electrodes, w and l are the width and length of the membranes, respectively, and a is additional gap-distance due to the stress-induced deflection.

The silicon nitride layer is deposited by an optimized low-stress LPCVD process [10] and hence, there is a slight (engineered) tensile stress. Therefore it can be considered as a flat substrate. The bending moment due to tensile stress in the chromium layer increases with the thickness. Reducing the electrode thickness is one way to reduce curvature but this has been minimized in the current sensors to 50 nm and there are serious issues regarding its usability on further reduction (due to its conductivity). There are two possible ways to counteract the curvature effect namely: (i) alternative materials with reduced residual stress as electrode materials (e.g. Aluminum), or (ii) to reduce the curvature by adapted designs of the electrodes themselves.

Discussion

While the option of choosing a low-stress material for the electrodes is related to the technology, the other option of reducing the electrode area offers some interesting tasks from

the design point of view. Upon throwing some light on the latter case, the electrode area near the torsional beams has minor effect on the sensor's sensitivity since there will be little change in the height of this area on membrane tilt. Whereas this area plays a proportional role in the total capacitance, it hardly contributes to the change of capacitance on tilt. By reducing the electrode area near the rotational axis, as shown in figure 2.13, the maximum upward deflection at the edge of the membrane decreases thereby increasing the sensitivity. Hence it is logical to remove a portion of the electrode close to the torsional beams. If the maximum additional gap (measured at the membrane edges) is denoted by a_0, the effect of increasing length of electrodeless area (i.e. removing the electrode area close to the torsional axis, while keeping its width, w unchanged) on the additional gap is given as:

$$a_r = \frac{a_0 (l - l_0)^2}{l^2} \tag{2.31}$$

where l is the actual length of the membrane and l_0 is the length of electrodeless area (see figure 2.13).

The effect of length of the electrodeless area on the sensitivity can be calculated as:

$$\eta_{\text{R,electrodeless}} = -2\varepsilon_0 w \int_{r=l_0}^{l} \frac{r dr}{\left(d_0 + a_0 \frac{(r - l_0)^2}{l^2} \right)^2} \tag{2.32}$$

where r is the direction along the length of the membrane, perpendicular to the torsional axis and the factor 2 in the equation stands for the two plates of the sensor membrane (at either side of the axis of rotation).

Figure 2.13 shows the trend of sensitivity by reducing the portion of electrode area close to the rotational axis. For a length of electrodeless area about 40 μm, the best sensitivity can be achieved, while the additional gap due to the membrane curvature is about 0.5 μm, down from ~2.5 μm.

2.3.5 Damping coefficient

Of all the parameters, the damping coefficient of the sensor system is bit complex to investigate and maneuver precisely by design. The damping of the sensor system provides resistance to the torsional movement of the hair sensor. The damping coefficient of our sensor system comprises of two terms as shown in equation (2.15), namely, (i) torsional resistance R at the base of the hair sensor and (ii) viscous damping R_μ of the hair due to the interaction of air medium and the hair. The former term, corresponds to the damping coefficient that opposes the movement of the sensor membrane. The latter can be calculated using the equation (2.18) and is proportional to the cube of the hair length. Since it is also dependent on the frequency, the numerical estimate from 100 to 1000 Hz is in the order of 2.4 – 3.4 x 10^{-14} Nm.s.rad^{-1} (for a hair length of ~900 μm).

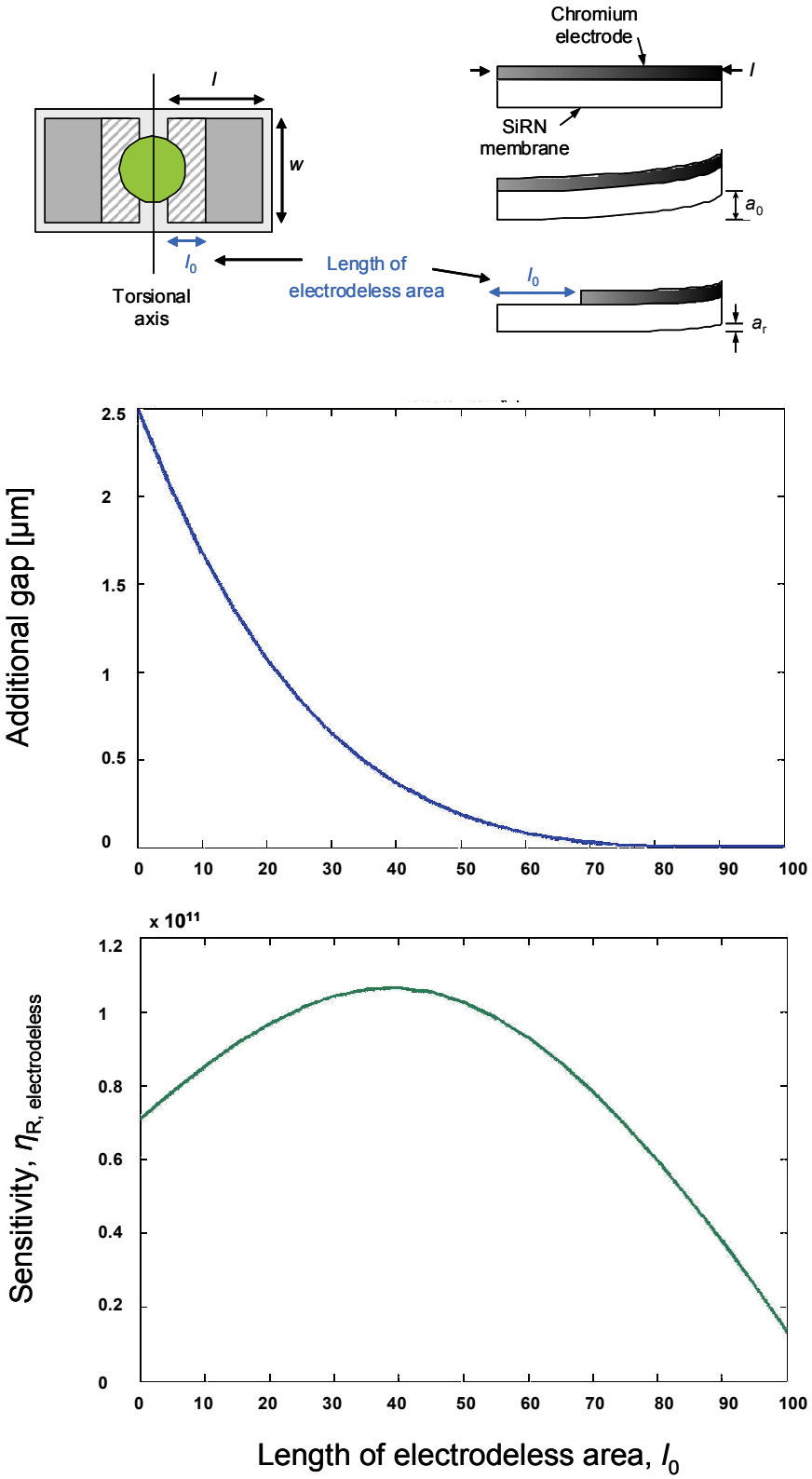

Figure 2.13 *Results showing the effect of removing electrode area near the rotational axes on the stress induced (additional) gap and on the sensitivity of the hair sensors[11]*

Squeeze-film damping

The torsion resistance *R* at the base of the sensor is actually the predominant one of both contributions. For the case of our sensors, this can be investigated by analyzing the squeeze-film damping present between the sensor membrane and the substrate. As the hairs deflect due to the drag force induced by the air flows, the sensor membrane responds by a tilt. There exists a thin film of air beneath the membrane and the substrate, which opposes this tilting movement and such resistive action is called the squeeze-film damping. The squeeze-film damping effect is commonly observed in the field of MEMS [12], since most micro parts are subjected to movements, surrounded by a medium in low-Reynold's number regime. Squeeze-film damping coefficients are difficult to calculate and are usually estimated by solving the linearized isothermal Reynold's equation [12]. Squeeze-film damping estimation for a torsional movement of sensor membrane is even more complex. Further, presence of etch holes (holes are patterned on the sensor membrane to provide access to the etch gases on the sacrificial layer), which has a significant effect on the damping, complicates the precise estimation of squeeze film damping coefficient of our sensors. However, as a work-around solution, based on the sensor response and by fitting appropriate quality factor, the approximate value of the damping coefficient can be estimated.

Discussion

It is interesting to derive insights on the effects of damping coefficient on the optimal performance of the sensors. Looking at the actual filiform hairs, it is known that the sensors correspond to moderately damped mechanical systems, with their damping coefficient scaling allometrically with the hair length [1]. Long hairs have a quality factor of 1.5-2.5 and short hairs have quality factor of 1 [6]. For systems with such moderate damping, this translates into shorter response times [6]. It seems that filiform hairs are evolved to take advantage of this aspect, as the response to the stimuli is key to their survival.

Henceforth, for optimal performance of our sensors, it is desired that damping effect is also in a similar range. The gap between the membrane and the substrate (primarily defined by the thickness of the sacrificial layer) is the only design option for modifying the damping coefficient of the system. Reducing the gap, thus favors in two aspects: (i) increase in the sensor capacitance (as discussed in previous section) and (ii) adjusted damping, implying a faster sensor response.

2.4. Conclusions

In this chapter, borrowing from the existing, well-known aerodynamic models of cricket hairs, the theoretical groundwork is laid for understanding the similar physics behind the operation of our hair sensors. A model is developed and a handle for design optimization is defined. This optimization handle will be referred to, throughout this thesis' chapters. In the previous sections, we have discussed the possible optimization in all of the functional components of the hair sensor system. Derived from the sensor model, by incorporating the suggested modifications to the existing sensor design, a new generation of improved hair sensor arrays is designed as the first step in this project. This generation of hair sensors will feature optimized hair geometry, slightly more flexible springs and quality-wise much-improved sensor membranes, which in turn improves the sensitivity.

2.5. References

[1] T. Shimozawa, T. Kumagai, Y. Baba, *"Structural and functional scaling of the cercal wind-receptor hairs in cricket"*, J. Comp. Physiol. A (1998) 183, pp. 171-186

[2] J.A.C. Humphrey, R. Devarakonda, I. Iglesias, F.G. Barth, *"Dynamics of arthropod filiform hairs. I. Mathematical modeling of the hair and air motions"*, Philosophical Transactions: Biological Science (1993) 340, pp. 423-444

[3] T. Shimozawa, M. Kanou, *"The aerodynamics and sensory physiology of range fractionation in the cercal filiform sensilla of the cricket Gryllus bimaculatus"*, J. Comp. Physiol. A (1984) 155, pp. 495-505

[4] G. J. M. Krijnen, J. Floris, M.A. Dijkstra, T.S.J. Lammerink, and R.J. Wiegerink, "*Bio-mimetic micromechanical adaptive flow-sensor arrays*", Proc. of SPIE Europe Micro-technologies for the New Millennium 2007, 2-4 May 2007

[5] G.G. Stokes, "*On the effect of the internal friction of fluids on the motion of pendulums*", Transactions of the Cambridge Philosophical Society (1850) 9:8-106

[6] L.C. Osborne, *"Signal processing in a mechanosensory array: Dynamics of cricket cercal hairs"*, PhD thesis, University of California, Berkeley (1996)

[7] T. Steinmann, J. Casas, G. Krijnen and O. Dangles, "*Air-flow sensitive hairs: boundary layers in oscillatory flows around arthropod appendages*", J. of Exp. Biol. (2006) 209, pp. 4398-4408

[8] J.A.C. Humphrey and F.G. Barth, *"Medium flow-sensing hairs: Biomechanics and models"*, Chapter 1, Advances in Insect Physiology, ed: Vol. 34, (2007) pp. 1-80

[9] SU-8 datasheets from: http://www.microchem.com/products/su_eight.htm

[10] M. Dijkstra, J.J. van Baar, R J Wiegerink, T S J Lammerink, J H de Boer and G J M Krijnen, "*Artificial sensory hairs based on the flow sensitive receptor hairs of crickets*", J. Micromech. and Microeng. (2005) 15, pp. 132-138.

[11] N. Izadi, R.K. Jaganatharaja, J. Floris and G.J.M. Krijnen, "*Optimization of cricket-inspired, biomimetic, artificial hair sensors for flow sensing*", Proc. of 9th Int. symp. on Design, Test, Integration and Packaging of MEMS/MOEMS (DTIP) (2007), Stresa, Italy, pp. 112-115

[12] M. Bao and H. Yang, *"Squeeze film air damping in MEMS"*, Sensors and Actuators A (2007), Vol. 136, pp. 3-27

3

Hair sensor arrays – Fabrication & Characterization

In a nutshell...

The third generation of hair sensors featuring the preliminary design optimization and technological improvements form the crux of this chapter. Design optimization was aimed at the reduction of torsional stiffness of the sensor springs by means of simple geometrical modifications. The hairs of reduced moment of inertia were fabricated using multi-layer spinning of SU-8 photoresist. Successfully fabricated sensor arrays were characterized extensively by both capacitive and optical techniques, to shed light on different aspects of the sensor performance. The sensor arrays, in combination with an improved measurement setup, showed an excellent directional sensitivity and a flow sensing threshold of <1 mm/s of harmonic air flows. The sensor arrays, thus served as a basis for further optimization- both in terms of design and technology, while remaining as functional starting point of our research on biomimetic hair sensors.

3.1. Introduction

The handles for design optimization, as introduced in Chapter 2, clearly set the fundamental design rules for the sensor design as: (i) reduced torsional stiffness S, (ii) reduced hair moment of inertia J, to retain the usable bandwidth and (iii) improved sensor capacitors.

The choice of materials for the sensors did not change much from our previous generations of hair sensors (Chapter 1). Silicon-rich nitride is rather stiff and strong material, renowned for its structural and mechanical properties in the field of MEMS[1] and it is used as sensor membranes and springs of the hair sensors. SU-8, which is an epoxy-based polymer, is used to fabricate the flow-receptive hairs. The only change in the choice of materials made in this new generation of sensors is with the metal for the top electrodes of the sensor capacitors (Aluminum, replaces the chromium layer, for electrodes). Poly-silicon is retained as the material for the sacrificial layer.

In this chapter, the design analysis of the sensors is further discussed in detail, in continuation to the related discussions on design optimization (chapter 2). The fabrication results of the sensors are presented and critical observations on these results and their implications on the sensor performance are discussed. However, the core of the chapter deals with the multi-faceted characterization of the sensor array performances. The sensor arrays have performed successfully and proved their functionality in a very appreciable manner and thus, marked a significant contribution to our understanding of them. This is the first time, ever since the start of the related projects – CICADA and CILIA, thoroughly characterized results were obtained from our artificial hair sensor arrays.

3.2. Design overview

The design of the sensor arrays concerns chiefly the following: (i) torsional springs, (ii) SU-8 hairs, (iii) sensor capacitors and (iv) array pattern. The geometry of the torsional springs determines the torsional stiffness of the mechanical system while the hair geometry determines the mass moment of inertia. Four different springs geometries were designed with variations in length and width, lying safe within the limits permitted by the fabrication technology. In order to reduce the membrane deflection (hence, improve sensitivity), both design-wise and technology-wise modifications were considered. For the design-wise modification, the areas of the capacitor electrodes were selectively reduced.

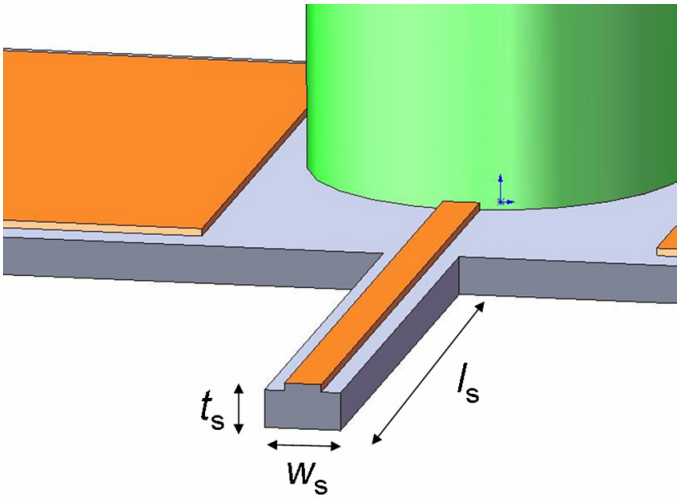

Figure 3.1 *Rectangular spring section of the hair sensor*

Those electrode areas that are in proximity to the torsional axes of the springs, contribute little to the sensitivity (since the electrode gap corresponding to these electrode areas undergo minimal change on membrane rotation and hence, contribute less to the

sensitivity). The deflection at the edges of the membrane induced by the residual stress in the electrode layer is proportional to the length of the electrode. Thus, by eliminating the electrode area that contributes less to overall sensitivity, we can effectively reduce the deflection of the membranes. Four designs of electrode areas were designed. Combinations of beam and electrode variations were created and all of the sensor designs comprised of SU-8 hairs with two-cylinder shape with dissimilar diameters.

3.2.1 Torsional springs

The torsional spring stiffness S of the sensor is given (earlier as equation 2.28):

$$S = \frac{2 \cdot G_s \cdot I_p}{l_s} \tag{3.1}$$

where G_s is the shear modulus of the spring material, i.e. silicon-rich nitride, which is related to the Young's modulus E_s and Poisson's ratio υ as $G_s = E_s/(1+\upsilon)$ and l_s is the length of the spring. The polar moment of inertia of the rectangular-section springs depends only on the width w_s and thickness t_s of the springs (see figure 3.1) as given by Roark's formula [2] as:

$$I_p = \frac{w_s t_s^3}{3} - 3.36 \frac{t_s^4}{16}\left(1 - \frac{1}{12}\frac{t_s^4}{w_s^4}\right) \qquad (w_s \geq t_s) \tag{3.2}$$

Thus, the geometry and material of the springs solely determines the torsional spring stiffness of the mechanical system. As briefly discussed in section 2.3.3, in order to achieve smaller torsional stiffness, equations (3.1) and (3.2) clearly indicate that the spring length should be large whereas the spring width and thickness should be small. The thickness of the springs t_s is actually determined by the deposited layer thickness of the silicon (rich) nitride (by LPCVD) and for this reason, throughout the design analysis, it is taken fixed as 1 μm.

Four different spring designs are chosen by varying the length and width of the springs are shown in Table 3.1. The width of the springs cannot be taken smaller than the critical width of 5 μm, since the metal layer connecting the electrodes to the actuating bond pads runs along it and such a metal layer should have 3 μm width (see figure 3.1), while allowing 1 μm on either side of it, for tolerable lithographic errors. The four designs of springs result in a torsional spring stiffness S ranging from $3.6 \cdot 10^{-9}$ - $1 \cdot 10^{-8}$ Nm/rad. However, the designed spring stiffness of our sensors are higher than those typical for 1 mm long filiform hair-sensors, which are observed to be ~ $2 \cdot 10^{-11}$.

Table 3.1 Four different designs by varying the length and width of sensor springs

Design	Spring length (l_s) (μm)	Spring width (w_s) (μm)
A	75	10
B	75	5
C	100	10
D	100	5

3.2.2 Mass moment of inertia

Optimized design of the SU-8 hair is discussed previously in section 2.3.2. The hair is designed as a two-stage hair, with two cylinders of dissimilar diameters, to be fabricated as one on top of the other. Such a design actually reduces the moment of inertia by about ~65% thus allowing for softer sensor springs (as indicated by the design optimization handle discussed in the previous chapter) The bottom cylindrical diameter is chosen as 50 μm and the top cylindrical diameter is chosen as 30 μm, In this sub-section, the calculation of the mass moment of inertia is briefly explained.

The total mass moment of inertia J_t of the sensor systems is the sum of hair moment of inertia J_h added to the moment of inertia of the sensor membrane J_m. The hair moment of inertia J_h depends on the geometry of the hair and for a straight cylindrical hair, the moment of inertia is already given by equation (2.20). Since the new generation of hair sensors will feature hairs made of two different cylindrical parts, the mass moment of inertia can be calculated (in a cylindrical coordinate system) as the volume integral of a product of small mass element "ρdV" and square of the distance "r" between the mass element and the torsional axis.

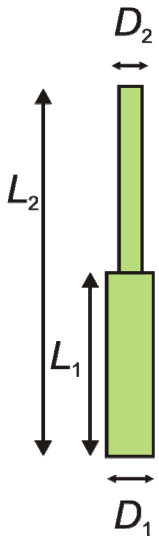

Figure 3.2 *Two-layer SU-8 hair with dissimilar diameters*

The geometrical dimensions of the hair are shown in figure 3.2. The moment of inertia J_h of the two-layer SU-8 hair about the torsional axis of the sensor is given as:

$$J_h = \iiint_V r^2 \cdot \rho dV = \rho \int_0^{L_1} \int_0^{2\pi} \int_0^{D_1/2} r^2 \cdot r dr d\phi dz + \rho \int_{L_1}^{L_2} \int_0^{2\pi} \int_0^{D_2/2} r^2 \cdot r dr d\phi dz \quad (3.3)$$

where ρ is the mass density of the SU-8. Equation (3.3) upon further simplification becomes:

$$J_h = \frac{\rho\pi}{4}\left\{\left(\frac{D_1}{2}\right)^4 L_1 + \left(\frac{D_2}{2}\right)^4 (L_2 - L_1)\right\} + \frac{\rho\pi}{3}\left\{\left(\frac{D_1}{2}\right)^2 L_1^3 + \left(\frac{D_2}{2}\right)^2 (L_2^3 - L_1^3)\right\} \quad (3.4)$$

The mass moment of inertia of the membrane J_m is calculated and given as:

$$J_m = \frac{1}{12} M_m \left(w_m^2 + t_m^2\right) \quad (3.5)$$

In the above equation, M_m is the mass of the membrane, which is given as:

$$M_m = l_m w_m t_m \rho_m \quad (3.6)$$

where l_m, w_m and t_m represent the dimensions of the rectangular membrane and ρ_m is the mass density of the silicon-rich nitride, of which the sensor membrane is made. From equations (3.4) and (3.6), the total moment of inertia of the sensor system is given as:

$$J_t = J_h + J_m \quad (3.7)$$

In practical terms, the total mass moment of inertia is approximately equal to that of the SU-8 hair, since the contribution from the nitride membranes is small. For the chosen geometrical values of the SU-8 hair, the total moment of the inertia is given as $2.3 \cdot 10^{-16}$ kg.m^2. In comparison, the moment of inertia of the actual filiform hairs (of ~1 mm long) is only ~$5 \cdot 10^{-18}$ kg·m^2.

3.2.3 Capacitor designs

The design of the capacitor electrodes is aimed at balancing the sensitivity and the reduction of the membrane deflection. The detailed discussion on the effects of electrode area reduction on the membrane deflection and the resulting sensitivity is given in section 2.3.4. From the graphs shown in figure 2.18, four different capacitor electrode areas were designed. The sensor membrane without any reduction in the electrode area consisted of a pair of electrodes designed as 90 x 64 μm^2. (w_m x l_m) The other three electrode designs consisted of reduced electrode areas of 75, 50 and 25 % of this area, respectively (see figure 3.3).

The other important parameter that is equally significant in terms of sensitivity is the gap between the electrodes of the sensor capacitors. Such a gap is defined by the thickness of the sacrificial poly-silicon layer. The sensitivity increases with the smaller inter-electrode gaps but there exists a critical limit below which the sensor membranes are prone to failure by pull-in of the membranes during electrostatic actuation (capacitive interrogation in our case). From a different perspective, through its influence of damping, this gap also determines the quality factor of the second-order mechanical system of the sensors. At smaller gaps between the electrodes the squeezed-film damping becomes prominent in determining the damping factor and hence, the dynamics of the system. Since the practical effects were unknown (at the time of design process), the design value of the sacrificial poly-silicon (and hence, the inter-

electrode gap) was chosen as 0.6 μm for a certain batch of wafers and 1 μm for another batch. This was necessary as small gap between the membrane and substrate could lead to two possible consequences: (i) membrane stiction due to pull-in and (ii) increased squeeze-film damping.

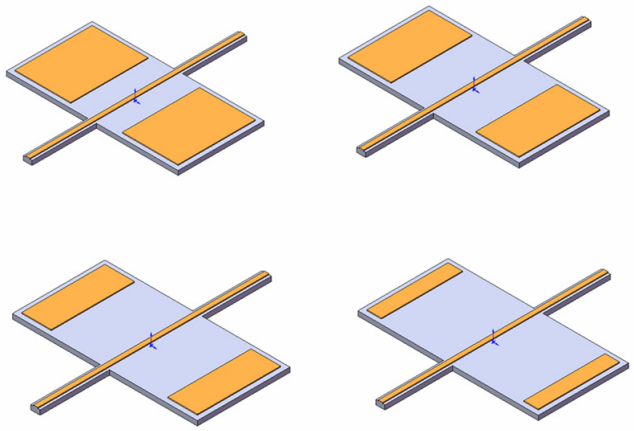

Figure 3.3 *Artistic impression of the four different sensor membranes designed with reduced electrode areas (near the torsional axis of the sensor)*

3.2.4 Array design

Different sensor designs are created based on the discussions in the previous sub-sections. Arrays consisting of 124 hair sensors arranged in 4 rows, connected in parallel arrangements were designed. Each hair sensor is placed with a 45º degrees rotation to the longitudinal axis of the sensor array chip, to allow for a compact and high-density arrangement. The sensors in the array are also electrically connected with each other in parallel fashion and together with the common bottom electrode, they act like a single large capacitor. While having hair sensors packed in a highly-dense array increases the sensor capacitance, not much is known about the viscous coupling between the hairs. Detailed investigation on viscous coupling between the artificial hair sensors was performed later in the project and is discussed in chapter 6.

3.3. Microfabrication of sensor

The fabrication of the third generation of hair sensors is discussed in detail in [6] and a short overview of it is presented here. Figure 3.4 shows the flow diagram of the sensor and the process details are given in Appendix A. The process starts with a highly conductive silicon substrate (Si P-type <100>), which serves as the common bottom electrode of the hair sensors. A 200 nm thin silicon-rich nitride (SiRN) layer is deposited on top of the substrate by low-pressure chemical vapor deposition (LPCVD) which provides insulation between the sensor electrodes and mainly serves as an etch-stop layer. Following it, a 600-1000 nm thick (depending on the batch; the sensors were fabricated in batches of 3-5 wafers each) poly-silicon layer is deposited on top of the silicon-rich nitride. The poly-silicon layer is patterned and serves as the sacrificial layer which is later etched to release the sensor membranes during the final step of this process flow. Subsequently a 1 μm-thick SiRN layer is deposited by

LPCVD which upon further patterning by reactive-ion etching forms the actual sensor membranes and torsion beams.

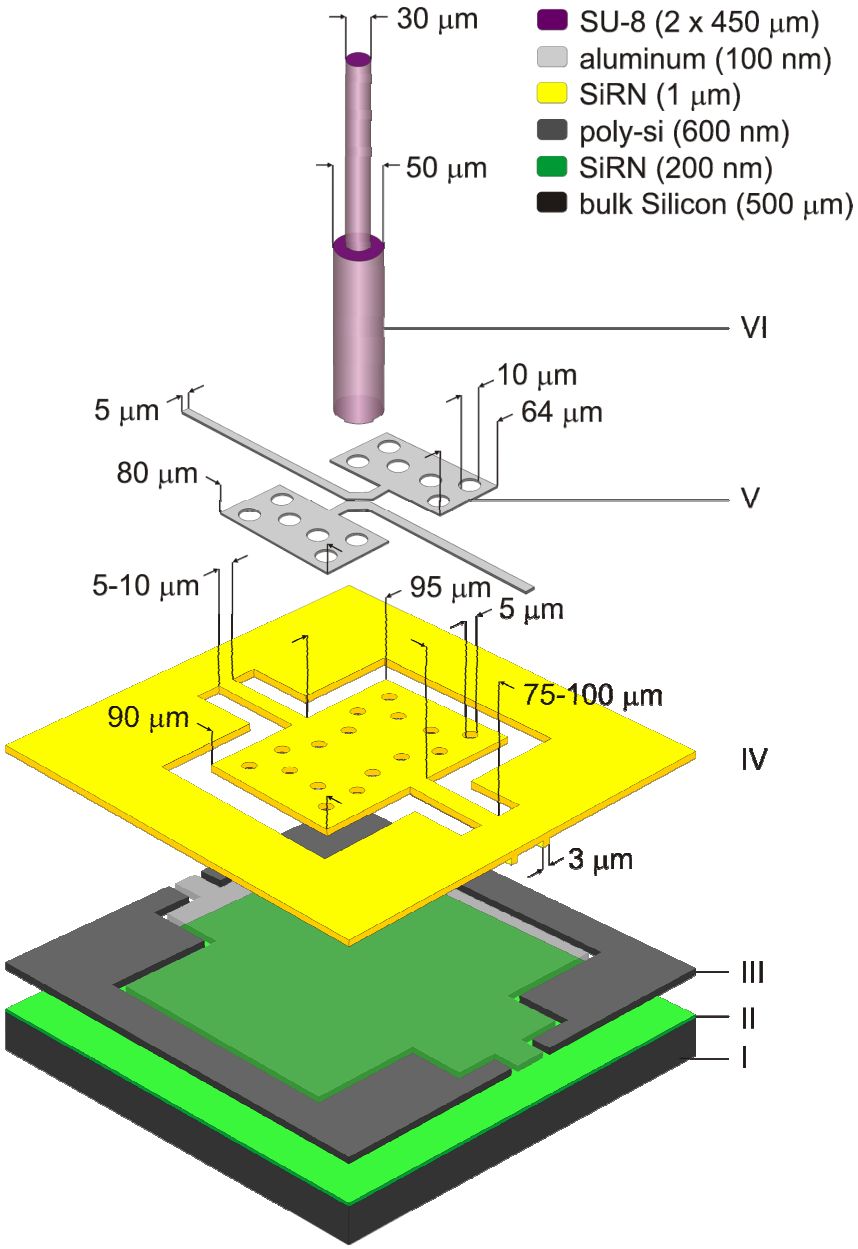

Figure 3.4 *Exploded design view of a single hair sensor showing: (I) highly conductive Silicon bulk (bottom electrode, shown in black), (II) 200-nm-thick SiRN layer for insulation and etch-stop, (III) Poly-silicon layer after the final local sacrificial layer removal, (IV) 1-µm thick SiRN layer patterned into membranes, (V) 100-nm thick aluminum for the top electrodes and (VI) two ~ 450-µm thick SU 8 layers patterned into a long hair*

A ~ 100 nm thick layer of low-stress aluminum is sputtered at room temperature and patterned by wet-etching using a standard photoresist developer (OPD 4262). The devices are now ready for the fabrication of long SU-8 hairs on top of the sensor membranes. The fabrication of ~900-µm long SU-8 hairs, is done by two consecutive photolithographic patterning steps of ~ 450 µm thick layers (SU-8 100) [4]. SU-8 polymer is a negative-tone

UV-patternable photoresist, i.e. the portion of SU-8 which is illuminated will remain after exposure and development. Due to the technological limit in the achieved aspect ratio (typically, 10-20) of SU-8 structures, the hairs are fabricated in two steps. The first layer (bottom part of the hairs) is exposed prior to deposition of the second layer (top part of hairs). This favors our design requirement to have the top and bottom diameters of the hairs to be dissimilar. Each SU-8 layer is spin-coated and then soft-baked, to remove the majority of the solvent in it. Then they are exposed to UV-light (365 nm wavelength) for certain time, depending on the thickness, and post baked. After the development step of the SU-8 hairs, the sacrificial poly-silicon was etched to release the sensor membranes. During this reactive etching step, a gas permeable glass wafer was used on top of the wafers in order to protect the device layer from ion bombardment and hence to promote selectivity by limiting the etching process as much as possible to the chemical (SF_6) component [3].

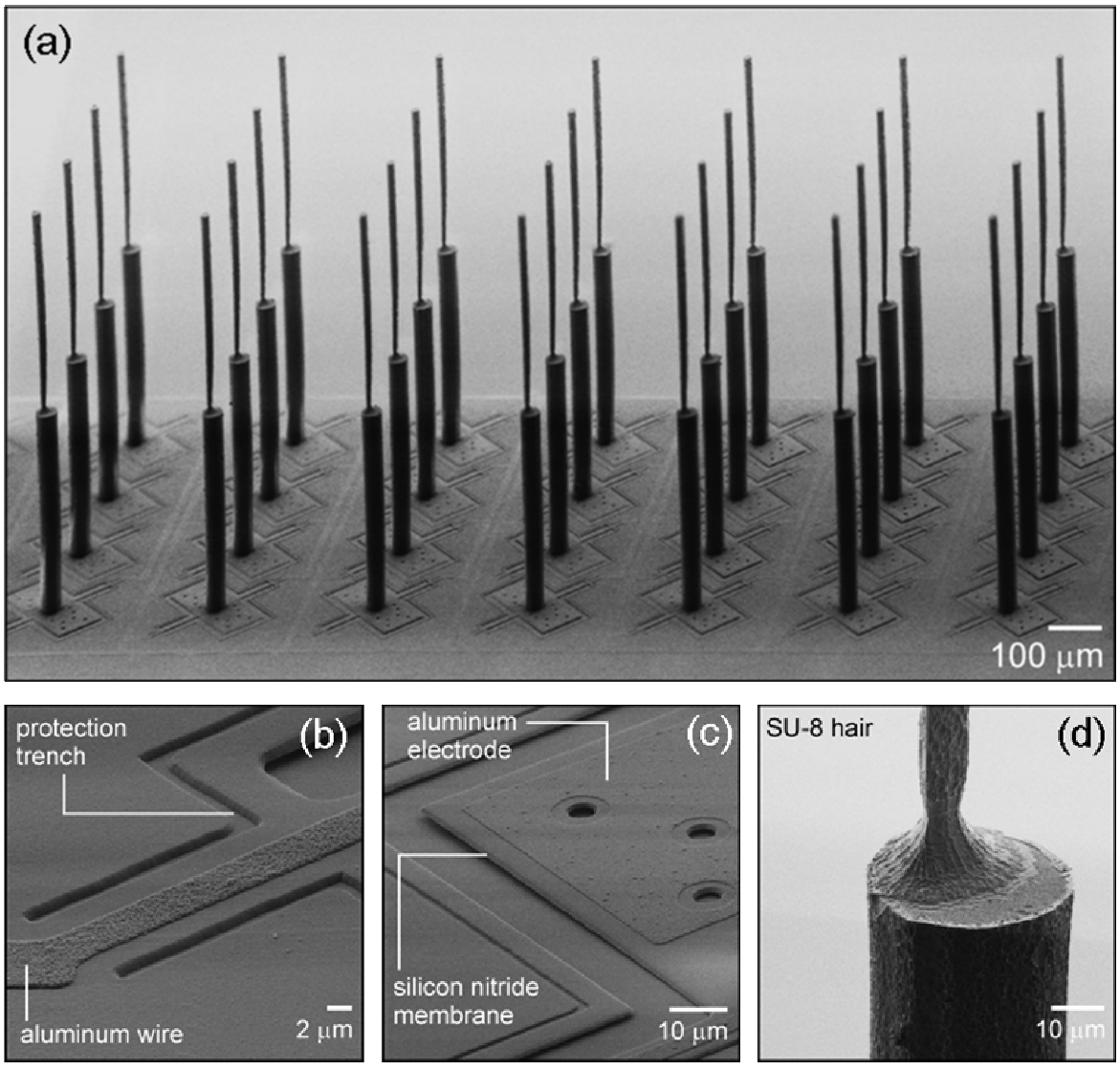

Figure 3.5 *SEM images illustrating in detail the flow-sensor array: (a) part of the array with ~ 900 μm-long hairs, (b) part of the aluminum wiring, (c) sensor membrane with aluminum electrode, and (d) connection between two segments of the SU-8 hair. Note: charging during SEM imaging is causing parts of the membrane to stick to the substrate (image c)*

3.3.1 Observations and discussion

Figure 5 shows a series of SEM images of the successfully fabricated new generation of our artificial hair sensor arrays [3]. The critical steps of the fabrication are related to the steps that will later define the mechanical characteristics of the sensors like torsional stiffness *S* and moment of inertia *J*. Using optical microscopes and scanning-electron microscopes to observe the results of the successful fabrication, the possible impact of them on the sensor performance is analyzed in this sub-section.

For the springs, the steps defining the thickness of the springs like LPCVD of silicon-rich nitride and the patterning of the springs are critical in determining the torsional stiffness *S* of the sensors. While the uniformity of LPCVD is high (hence, uniform spring thickness), the patterning of membranes and springs (which define the width and length of springs) and alignment of aluminum electrodes on the silicon-rich nitride membranes was observed to be nearly flawless. During the sacrificial layer etching, a special glass-mask is used to protect the device layers from ion-bombardment. Irrespective of this, during the final sacrificial layer etching of the polysilicon, a portion of the spring thickness is also etched unavoidably, due to the moderate selectivity of the process. This results in slight deviations of the torsional stiffness from the designed values, depending on the reduced spring thickness and width.

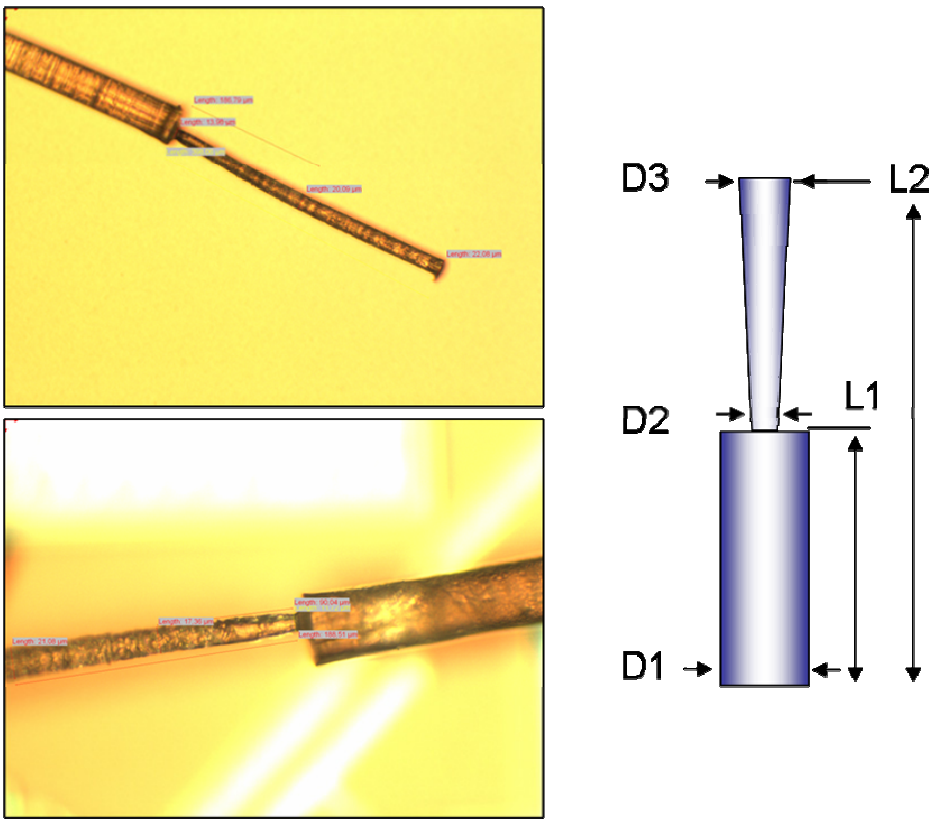

Figure 3.6 *Optical microscope observations of the hair geometry: the hair can be approximated to consist of a bottom cylindrical part and a top, inverted-conical part.*

In order to characterize the fabricated hairs, some of the hairs were broken off from different arrays, diced from different parts of the wafer. Using an optical microscope, the hair geometry was measured. As can be seen from figure 3.6, the top part of the hair is not of a pure cylindrical shape but of an inverted tapered-cone shape. The observed geometrical

dimensions of four sample hairs, which were randomly picked from different chips, showed different values for the lengths, L1 and L2 and diameters of the top and bottom parts of the hairs (D1, D2 and D3), as depicted in figure 3.6. It was observed that while the total hair length of all the samples was ~800 μm, the length of bottom (L1) and top parts (L2-L1) does vary, from chip to chip. These wide deviations are attributed to the (notorious) non-uniformity of the spun SU-8 layer thicknesses on the wafer [5].

It is also inferred that actual diameters of top and bottom parts of the hairs are found to deviate from the designed values. While the design value of D1 was 50 μm and (D3) was 30 μm, the actual values observed on the hair samples were found to be ~46 μm and ~25 μm, respectively. One possible reason for this deviation could be insufficient exposure dose due to too short exposure time. The striking observation on the hair is about their overall shape profile, which is different for the top and bottom part of the hair. The bottom part of the hair has a nearly-straight wall profile while the top part of the hair has a negatively-tapering profile. The negative-taper profile is a characteristic of negative-tone photoresists. One reason for such a profile is due to the air gap between the photomask and the photoresist, which contributes to errors in the intensity distribution [6]. Due to the non-uniformity of the SU-8 layer thickness, the coated wafers were prone to stiction to the photomask during exposure. To prevent this, a single layer of cellophane tape (~50 μm thick) was selectively (outside the essential mask area) placed on the photomask, to give a spacer, which effectively prevented stiction of the device wafers to the photomask. On the downside, this additional air gap has resulted in a deviation of the hair-geometry from the design values. This will, thus, result in a noticeable deviation in the hair moment of inertia *J*, and in turn, the mechanical resonance of the sensor itself.

Alignment of SU-8 hairs on to the sensor membrane is crucial, as any misalignment could lead to undesired sensor membrane dynamics. For the presented batch of sensor arrays, the SU-8 hairs were exposed by using a top (front-side) alignment method. Few device wafers suffered from misalignment of the hairs from the center of the membranes due to the limitations of this top alignment for thick layers of SU-8 resist. Due to the coating of thick SU-8 layers on the device wafers, a visible wafer deformation is observed, which makes it even difficult during the alignment before exposure. One of the other reasons for this misalignment could be pointed at the unevenness of the hot plate stage (used during the post-exposure baking step). Because of the uneven surface, the SU-8 reflowing could result in a slight shift from the center. Due to the above said technical limitations in alignment (because of the large thickness of the SU-8 layers) as well as curing induced deformations, the second part of the hair is also somewhat eccentric over the first part (see figure 3.5d). However this problem with alignment was solved by using backside-alignment in the subsequent generations of the hair sensor arrays. Nevertheless, this issue of hair misalignment is taken as motivation driving to look for alternate fabrication methods for the SU-8 hairs, which will be discussed in Chapter 5.

3.4. Sensor Characterization

Hair sensor arrays were subjected to extensive and multi-faceted characterization measurements, by which the actual performance of the sensors came to light. The characterization is broadly classified as (i) optical characterization and (ii) capacitive characterization. Optical characterization of the sensor arrays is aimed mainly at determination of the quality of the fabricated membranes and to get a clear idea of the dynamics of the sensor membranes. On the other hand, the capacitive characterization

focuses on the functional aspects of the sensor arrays. In both methods, commercial loudspeakers were used as the source for generation of harmonic flows. The characterization of the membrane curvature did not require any flow source. This section is further divided into sub-sections that deal with: (1) characterization of membrane curvature using a white light interference microscope (WLIM), (2) harmonic flow characterization by optical measurements (using a laser vibrometer) and (3) sensitivity to harmonic flows by means of capacitive measurements.

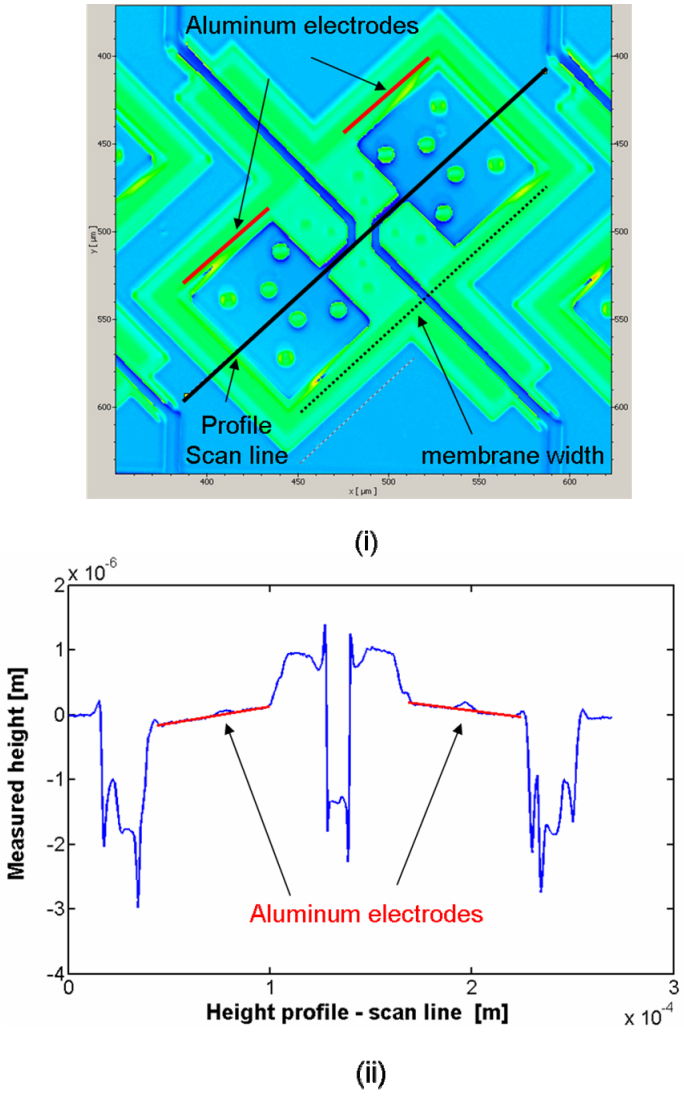

Figure 3.7 *White light interference microscopy: (i) 2D height profile image of the sensor by a white light interference microscope (WLIM); (ii) the height profile along the scan line (the red-line indicates the aluminum electrodes), shows that the membrane is slightly curved downwards at the edges.*

3.4.1 Membrane curvature

The quality of the fabricated membranes is crucial since the sensor capacitance and sensitivity strongly depend on it (see equation (2.26)). For measuring the curvature sensor

membranes (without hairs) were characterized using white light interference microscopy (Polytec, MSA 400) [7]. Figure 3.7 - (i) shows the topography of the sensor membrane (without hair) and a scan line is placed along the entire sensor (as shown in the figure). Figure 3.7 - (ii) shows the height profile along the scan line. Since the principle of white light interferometry [8] is based on the reflection of light, the accuracy of the height profile depends highly on the optical reflective properties of the layers being measured; reflecting surfaces give accurate results while transparent surfaces are likely to give ambiguous results.

In our case the measurements provide accurate information on the Aluminum layer profile present on most of the membrane area (as electrodes) but not from the transparent silicon rich nitride layers (i.e. parts not covered by Aluminum). Hence, from the profile of the Aluminum layer, it is possible to observe the membrane curvature. It was found that the membranes are slightly curved upwards or downwards at their edges (~ 200 nm). Such edge-curvature variations (upwards or downwards) correspond to the variations in processing steps of silicon-rich nitride and aluminum layers. Nevertheless, compared to a deteriorating ~2 μm curvature observed in the previous generation of sensors, the presented sensors show a significant improvement in the membrane quality with near-flat membranes. This was feasible particularly due to the replacement of chromium with low-stress aluminum as electrode material.

The various electrode designs, as discussed in section 3.2.3, aimed also at the reduction of the membrane curvature, did not provide a significant change in the quality of the membrane, which should be attributed also to the low-stress in the Aluminum layer. Since the membranes were observed to be nearly-flat, the implications of reduced electrode areas on the sensitivity are considerably changed. The discussions presented in section 2.3.4 on the effect of reduced electrode area, will only partly hold for the current scenario of sensors having near-flat membranes. In this case the optimum will be found at larger electrode area. Hence, in our present case, the sensitivity of the sensors is only(slightly) dropped by the reduction of the electrode area (e.g. for an electrode covering half of the membrane a sensitivity-reduction of 25% may be expected relative to a fully covered membrane, in case of ideal flatness).

3.4.2 Harmonic flows – Optical measurements

The membrane rotation of the hair sensor, in response to driving harmonic flows defines the operational quality and usability of the sensor arrays. Characterization of the sensor membrane dynamics provides vital information as these dynamics can reflect possible imperfections in the fabrication process itself. For instance, the desired membrane movement (due to drag-force receptive SU-8 hairs) is a torsional motion along the springs of the sensor. But if the SU-8 hair is slightly misaligned from its central position (due to technological errors), it will introduce a complex modal behavior in the membrane deflection. In order to characterize the membrane deflection, optical measurements on the sensor arrays were carried out with a laser vibrometer (Polytec, MSA 400) [7] while using a loudspeaker as the harmonic flow source.

Measurement setup

Figure 3.8 shows the schematic of the setup, where the flow-induced membrane deflections of the sensors are accurately measured by a laser vibrometer. The Laser vibrometer is placed on a vibration-reduction table and consists of an optical head, through which the laser-beam is directed and focused on the samples. Hair sensor arrays are placed on a stable platform, right under the optical head and fixed to the surface by scorch tape. Using the integral microscope on the optical head and via accompanying software, the samples can

be adjusted for a proper placement and for optimal light intensity. Using the software, laser scan points are defined on the sensor membranes and the deflections at those points are acquired and exported. The harmonic flows are generated by a small loudspeaker that is carefully placed, as close as possible, to the hair sensors. In order to avoid substrate-coupled vibrations (upon actuation), the loudspeaker is always mounted on a stable metal arm held by a tripod physically isolated from the measurement table.

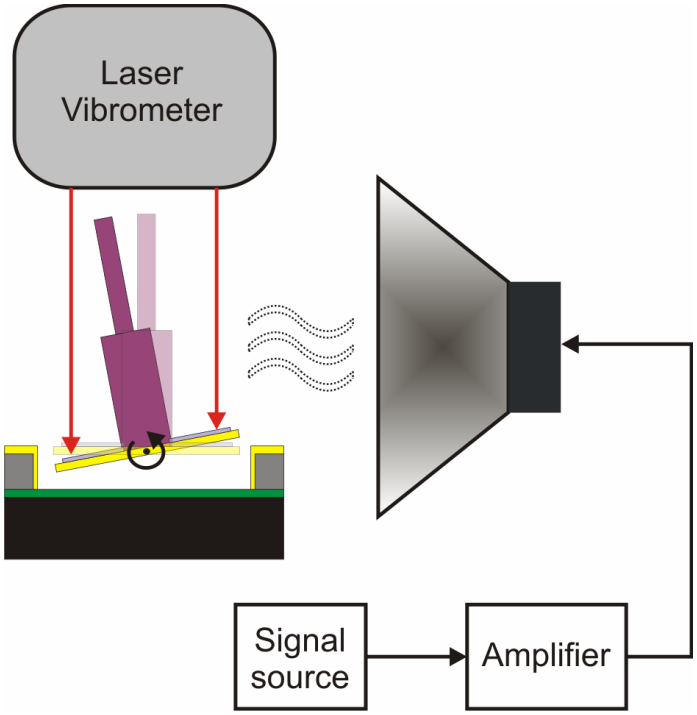

Figure 3.8 *Schematic of optical measurement setup using a laser vibrometer and a loudspeaker.*

The first task is to characterize the flow source i.e. loud speaker (Visaton, 5 cm dia.) to determine the generated flow velocities. The loudspeaker is placed under the optical head and a tiny bit of aluminum foil is glued on to the speaker membrane for better reflectivity of laser light. The loudspeaker is actuated by a sinusoidal electrical signal from the vibrometer itself and the corresponding membrane vibrations are measured simultaneously. The loudspeaker is characterized for a number of actuation voltages and corresponding frequency responses of the output flow velocities are obtained. Figure 3.9 shows the magnitude and phase of the output harmonic flow velocities for different actuation voltages. The results show a resonance frequency of the loudspeaker between 350 - 400 Hz and a respective 180º phase-shift, corresponding to the (equivalent) second-order mechanical system of the loud speaker.

Acoustic regimes: Very-near-, near- and far-fields

The results shown in figure 3.9 actually represent the vibrational velocity of the loudspeaker membrane upon electrical actuation. Such vibrations generate acoustic flows and cause both pressure variations and particle velocities in the surrounding medium. It is important to clearly state the nature of the acoustic flows to which the sensor arrays are subjected during the characterization (both optical and capacitive characterization). The acoustic regimes are classified based on the characteristics of the sound pressure (scalar

quantity) and particle velocity (vector quantity) as very-near, near and far field. The concept of the very-near field is presented in [9,10].

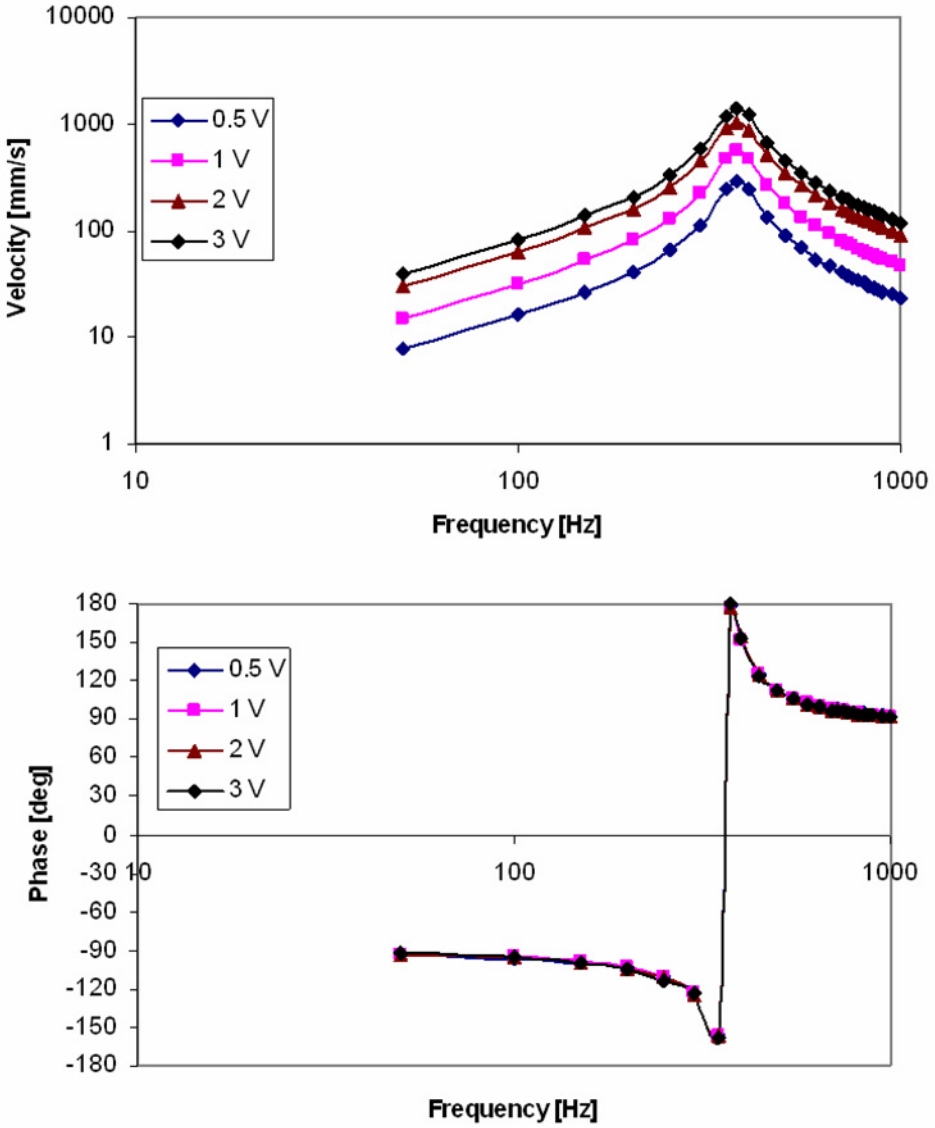

Figure 3.9 *Harmonic flow source characterization: Flow velocity output as a function of actuation voltage and frequency.*

The classification of these three acoustic regimes depends on the normal distance r, (from the acoustic source), wavelength of the acoustic flow, λ, and size of the acoustic source, L_a [10]. The very-near field exists at a distance r such that $r << L_a/2\pi << \lambda/2\pi$. In this regime, particle velocity and pressure remain constant, while particle velocity significantly dominates over the pressure level [9,10]. However, there is a significant phase delay of 80-90° between the pressure and particle velocity. The near-field exists for the distance range of r such that $L_a/2\pi << r << \lambda/2\pi$. In this range, the dominant particle velocity value drops proportional to $1/r^2$ while the pressure drops proportional to $1/r$. Near-field regime transitions to far-field

regime, as the normal distance r is such that $r >> \lambda/2\pi$. The pressure values start dominating the particle velocity, as both of them drop proportional to $1/r$ while achieving the same phase.

Clearly, for our sensor array characterization, we are interested only in the near- and very-near-fields, where the particle velocity of the acoustic flow dominates. All the measurements are performed within either of these two regimes. Optical measurements, as explained, are performed using a laser vibrometer. Due to restrictions imposed by the optical set-up (presence of optical parts of the vibrometer), only a small loud speaker (5 cm dia.) could be used which allows the sensors to be placed under the near-field of the loudspeaker. On the other hand, for the capacitive characterization, a large loudspeaker (~10 cm dia.) is used (which has a silicon wafer fixed to its vibrating membrane, to ensure uniform flow). Since there are no restrictions during capacitive measurements (discussed in the sub-section 3.4.3), the sensors are placed very close to the vibrating surface (<1 cm), thus in the very-near-field regime.

For all optical measurements (presented in this sub-section and also in chapter 4), the sensor arrays are placed at about ~2.5 cm from the small loudspeaker. Due to the size of the loudspeaker, such a distance puts the sensors in the near-field regime of the acoustic flows. As explained before, the particle velocity of the flow drops proportional to $1/r^2$. For this distance, the particle velocity should drop about 8-9 times from the loudspeaker vibrating surface. This was confirmed by measuring the flow velocities, using a commercially available particle-velocity sensor called "microflown" [11].

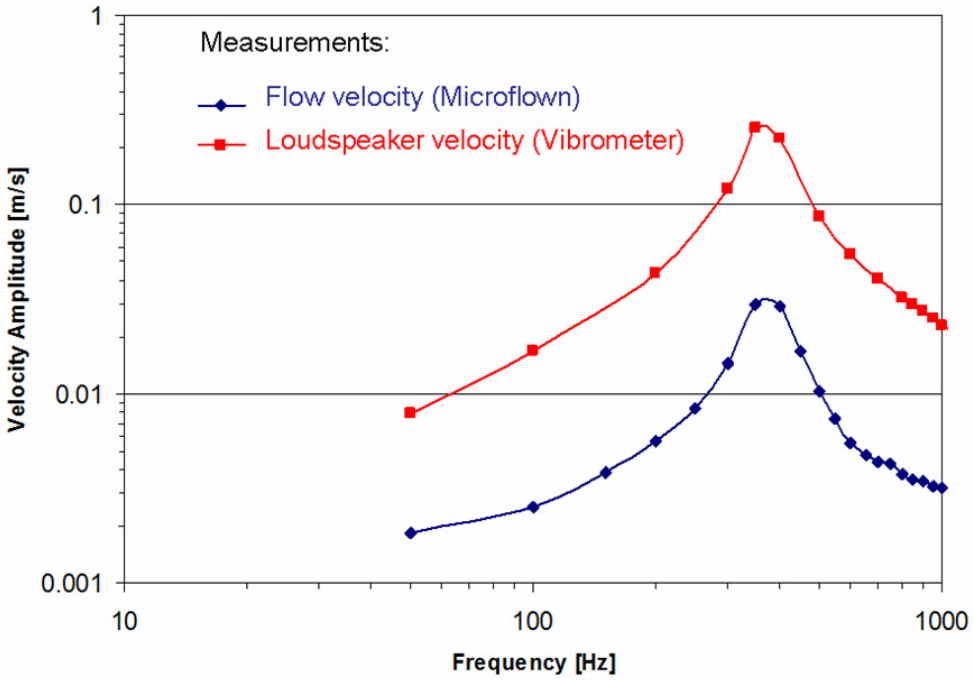

Figure 3.10 *Flow velocities measured at the surface of the loudspeaker membrane (laser vibrometer) and at 2-3 cm away from the loudspeaker membrane (using a calibrated microflown [11])*

Figure 3.10 shows the flow velocities measured at a distance ~2.5 cm away from the speaker, which is compared with corresponding laser vibrometer measurements, while the loudspeaker was actuated by applying 0.5 V amplitude. From the measurement results, it was found that over the frequencies, the velocities drop by approximately 7-10 times depending on

the flow frequency. Hence, for the analysis, the velocity drop effect was certainly taken into account and the results were corrected accordingly.

Substrate vibrations

Before performing the actual measurements, the scan-points on the sensor-membranes were measured, without the loudspeaker being actuated to get an idea of the substrate vibrations. Figure 3.11 shows the substrate vibrations measured by the laser-vibrometer, primarily due to the vibrations of the optical parts (for instance, mirrors) and of the measuring surface, indicating sub-nm noise over the desired range of frequencies. However, it was always made sure that the measurement results were substantially higher than these noise levels.

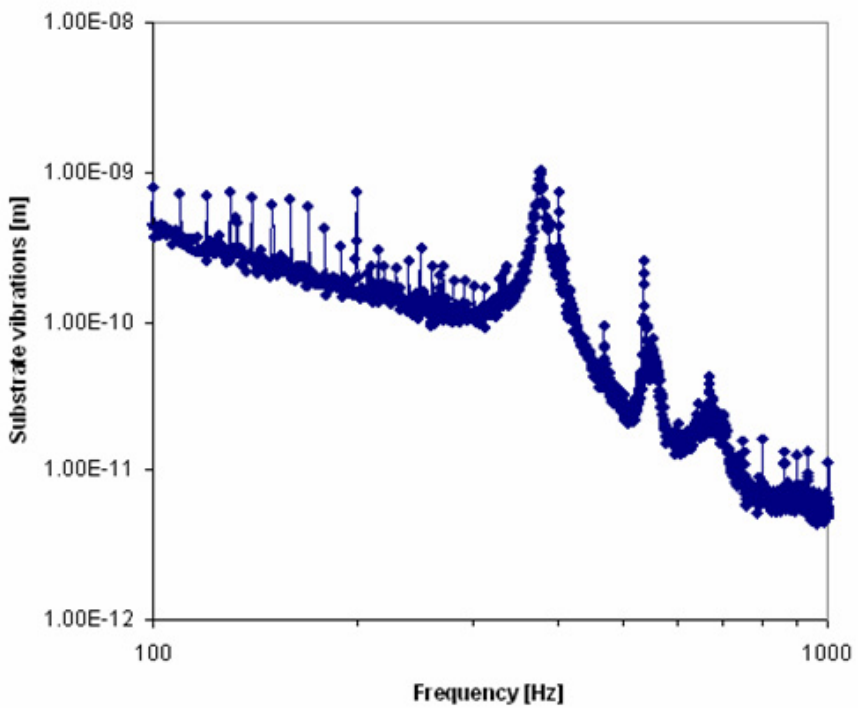

Figure 3.11 *Self-noise of the laser vibrometer, measured from the scan points, when the loudspeaker was not actuated*

Modal decomposition

For the characterization of the membrane vibrations, scan points were placed on the sensor membrane. Ideally, it would be sufficient to measure the displacements on one side of the sensor membrane in order to characterize the membrane dynamics in response to the harmonic flows. But, from a practical point of view, this is not always the case. The sensor chip placed in the acoustic field of the loudspeaker is always prone to surface-vibrations, along with the torsional motion of the sensor. Also, if the SU-8 hair is slightly misaligned, the displacements of the membranes on either side are not exactly opposite to each other. To eliminate such stray effects and obtain the desired information, we used a modal decomposition method.

From the data acquired from all scan points and by simple mathematical calculations it is possible to decompose the membrane movement into four prominent modes: (i) torsional, (ii) vertical, (iii) transversal and (iv) diagonal (see figure 3.12). Such a scheme of

decomposition effectively helps to eliminate the unnecessary modes (due to misalignment or substrate vibrations) and obtain only the desired mode of deflection (i.e. torsional mode). For the measurements, an array of sensors was placed under the laser vibrometer.

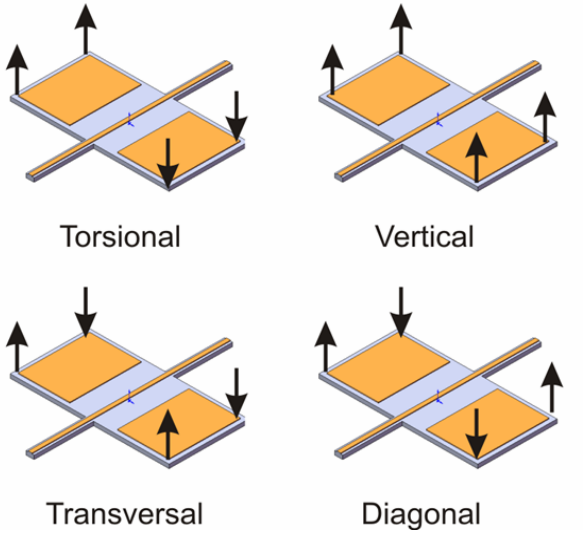

Figure 3.12 *Four prominent modal components of sensor membrane vibrations, which can be derived from the data acquired from the optical measurements.*

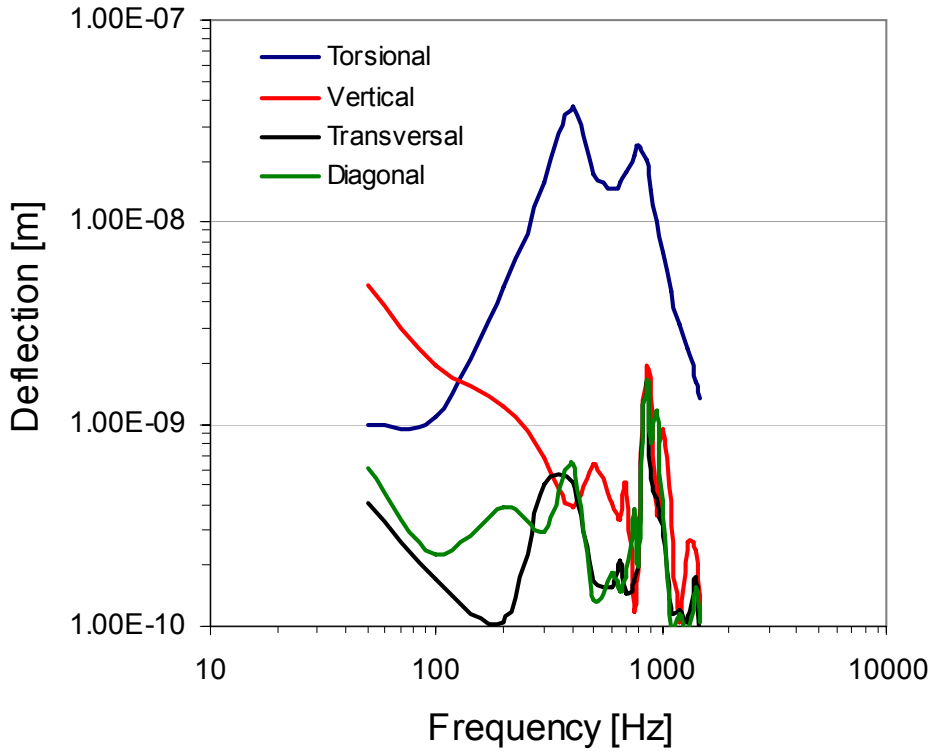

Figure 3.13 *Four prominent modal components of sensor membrane vibrations, calculated from the membrane deflection data acquired from the optical measurements. This clearly shows that the torsional mode is the predominant mode over the desired frequency*

The results from the modal decomposition of the measurements (as shown in figure 3.13) clearly indicate that the torsional mode is predominant (as expected) over the desired range of frequencies. It is to be noted that the shown results are not normalized with respect to the driving harmonic flows and they are purely represented by simple averaging and arithmetic calculations, to decompose the modes. In order to have a basic overview, only the deflections corresponding to these dynamic modes are compared. There is a significant noise observed at low frequencies (below 100 Hz) which seems to be unavoidable during such measurements. For the undesired modes, the measured values were mostly well under the self-noise of the vibrometer (Figure 3.11).

In order to normalize a mode of deflection, first the desired mode is extracted. By dividing out the driving harmonic velocity and length of the sensor membrane, we will get the normalized angular motion along the torsional springs. The result of such normalization scheme is shown in figure 3.14 for two different sensors. Sensors designed with different spring lengths (75 and 100 µm) with a spring width of 10 µm show different resonance peaks at ~800 and ~600 Hz, respectively. The error margins in the plot represent the possible driving flow variations during the measurements.

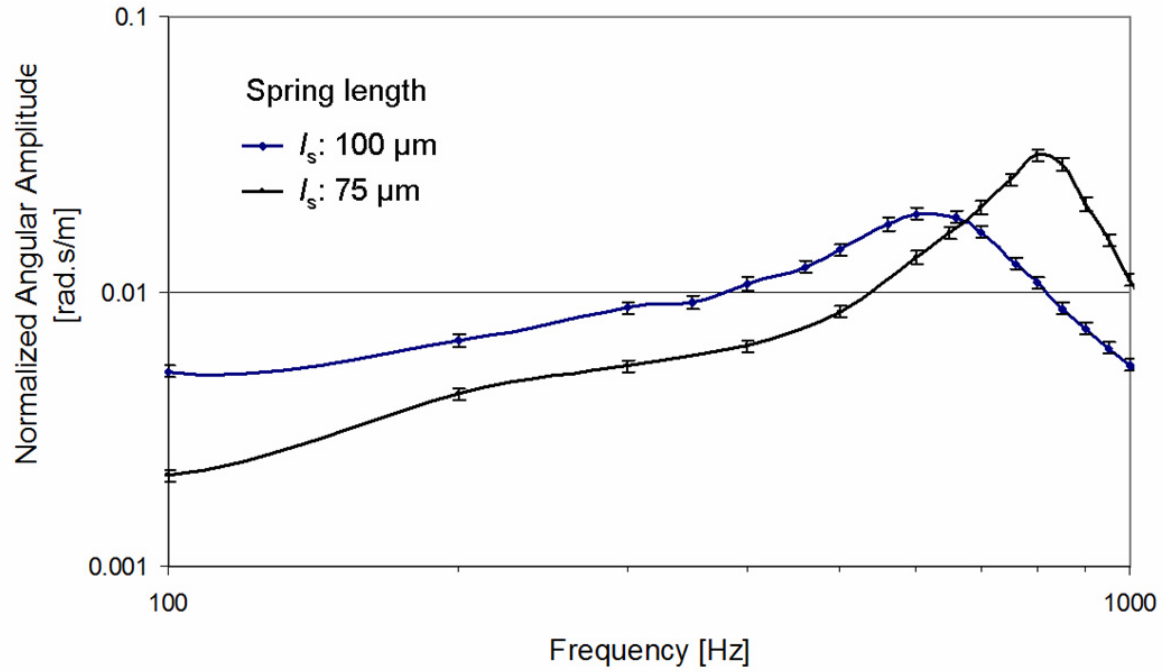

Figure 3.14 *Frequency response of sensors with different torsional spring designs. Results were calculated from decomposition of the (preferred) torsional mode and normalized by the driving harmonic flow velocities.*

3.4.3 Harmonic flows – Capacitive measurements

Capacitive measurements of the hair sensor arrays will ultimately determine the operational success and the usability of the sensors. The sensor arrays are investigated upon subjection to harmonic flows by placing the sensors in the very near-field of a loudspeaker and different aspects of the sensors - flow sensitivity and directional sensitivity, were

characterized by using a specific measurement setup [12]. The nature of the very-near-field acoustic flows was discussed in the previous sub-section..

Measurement setup

Figure 3.15 shows a schematic of the measurement setup where two 1 MHz electrical signals, 180º out of phase with each other (for acquiring differential-mode rotational signals), are fed to the top electrodes. A loudspeaker generates flows, to which the sensors react by hair rotation, inducing antisymmetric modulation of the capacitors and, hence, charge injection in the common bottom electrode. This modulated signal is amplified (by a charge amplifier) and demodulated before being fed to a lock-in amplifier to finally obtain the LF signal. This setup can be used to measure two significant properties of the sensors i.e. sensitivity and directionality of the sensors.

For characterizing the flow source, the loudspeaker is characterized to produce a wide range of flow velocities in the very-near-field ranging from 0.5 – 300 mm/s at different frequency settings (10, 100 and 400 Hz). The loudspeaker used in these measurements is different from the one used for the laser vibrometer measurements. This loudspeaker is large relative to the previous one and a silicon wafer is placed on the membrane. Placing a polished silicon wafer (of 10 cm diameter) on the vibrating loud speaker membrane provides two advantages: (i) such a planar surface is aimed at generating uniform harmonic flows and (ii) due to the large diameter of the silicon wafer, the sensor arrays can be placed relative close to it (in terms of the source diameter, i.e. in the very-near-field).

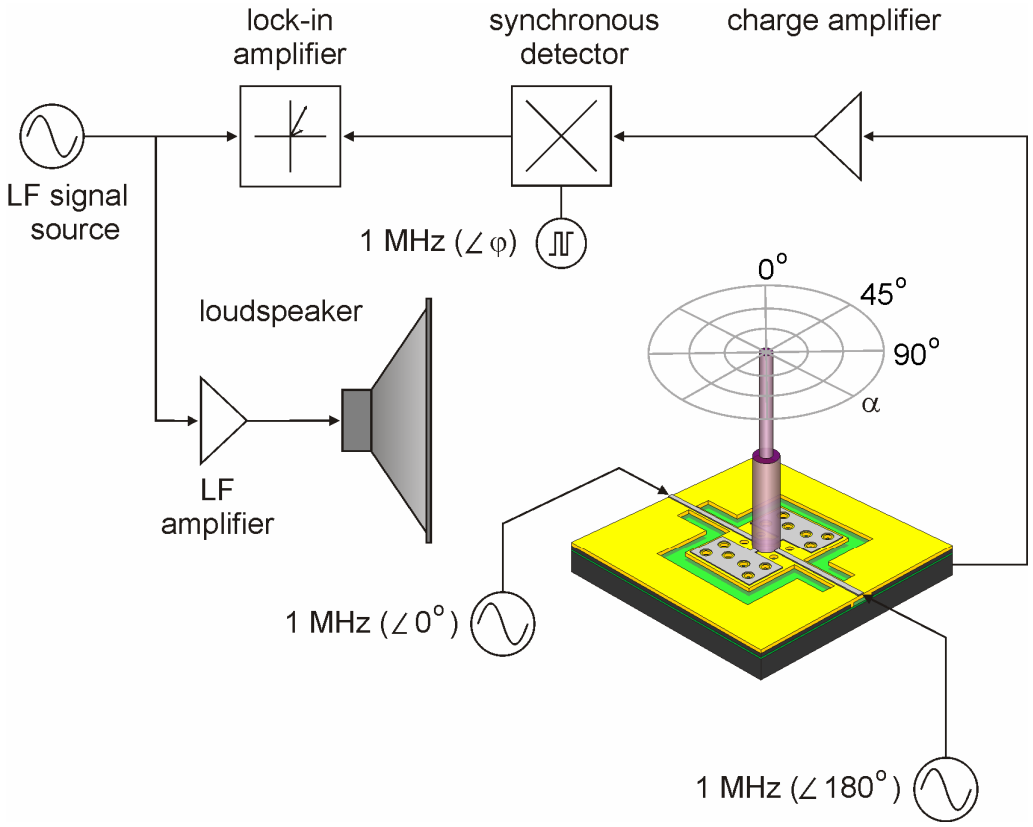

Figure 3.15 *Measurement setup for the acoustic flow driven capacitive characterization of the sensors.*

Flow sensitivity

The velocity of the loudspeaker membrane was measured for different frequencies using the laser vibrometer. The sensor arrays were placed at a distance less than 1 cm from the membrane and for such very near-field cases, the flow velocity generated by the loudspeaker is equal to the measured vibrational velocity of the loud speaker. Using the setup, the sensor response is measured and plotted against the applied flow amplitude. In addition, RMS noise measurements were also performed at different bandwidths, without the sensors being actuated by the loudspeaker.

The response threshold of the sensors can be determined by the intersection of the signals measured in a small bandwidth (1 Hz in this case) and the noise present in a certain bandwidth (0.01, 0.1 and 1 kHz). For the sensor response at 400 Hz, the lowest response limit was observed to be 0.85 mm/s (figure 3.16). It is noteworthy that actual hair sensors of crickets with a length of about 1 mm have a response threshold at ~0.03 mm/s at lower (~ 10 Hz) excitation frequencies [13].

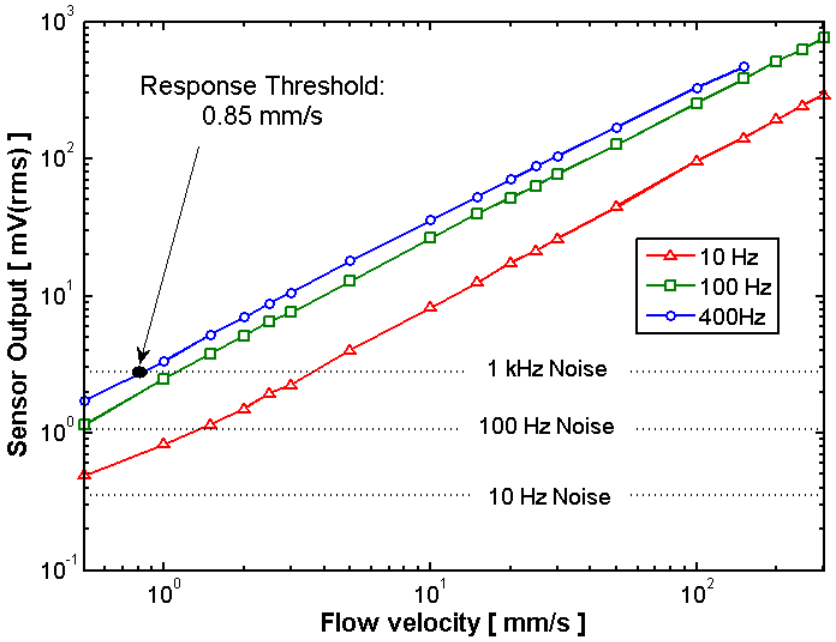

Figure 3.16 *Sensitivity measurements at three different frequencies, with the horizontal lines indicating the RMS noise levels present at various bandwidths [12].*

Directional sensitivity

For determining the directional sensitivity of the sensor arrays (which is an essential property of flow-sensors/particle velocity sensors), a different setup is used. The sensors are placed on a rotary stage, close to a loudspeaker. The loudspeaker is actuated at a fixed frequency and the signal response from the sensor arrays is recorded (from the lock-in amplifier) for every 10º rotation angle with respect to the flow source. Figure 3.17 shows a clear figure-of-eight response from the sensor arrays at different frequencies confirming a preferred directional sensitivity of the sensors [12].

The ideal figure of eight is indicated by the red-dotted line in figure 3.17. There is a ~45º rotation shift in the figure-of-eight response which is due to the fact that all the hair sensors in the chip are rotated 45º in order to allow for high density arrays. Also the response

is slightly asymmetrical (compared to an ideal response) which could be explained by the disturbances caused by the mounting electronics and the wires that come in between the source and sensors during part of the stage rotation.

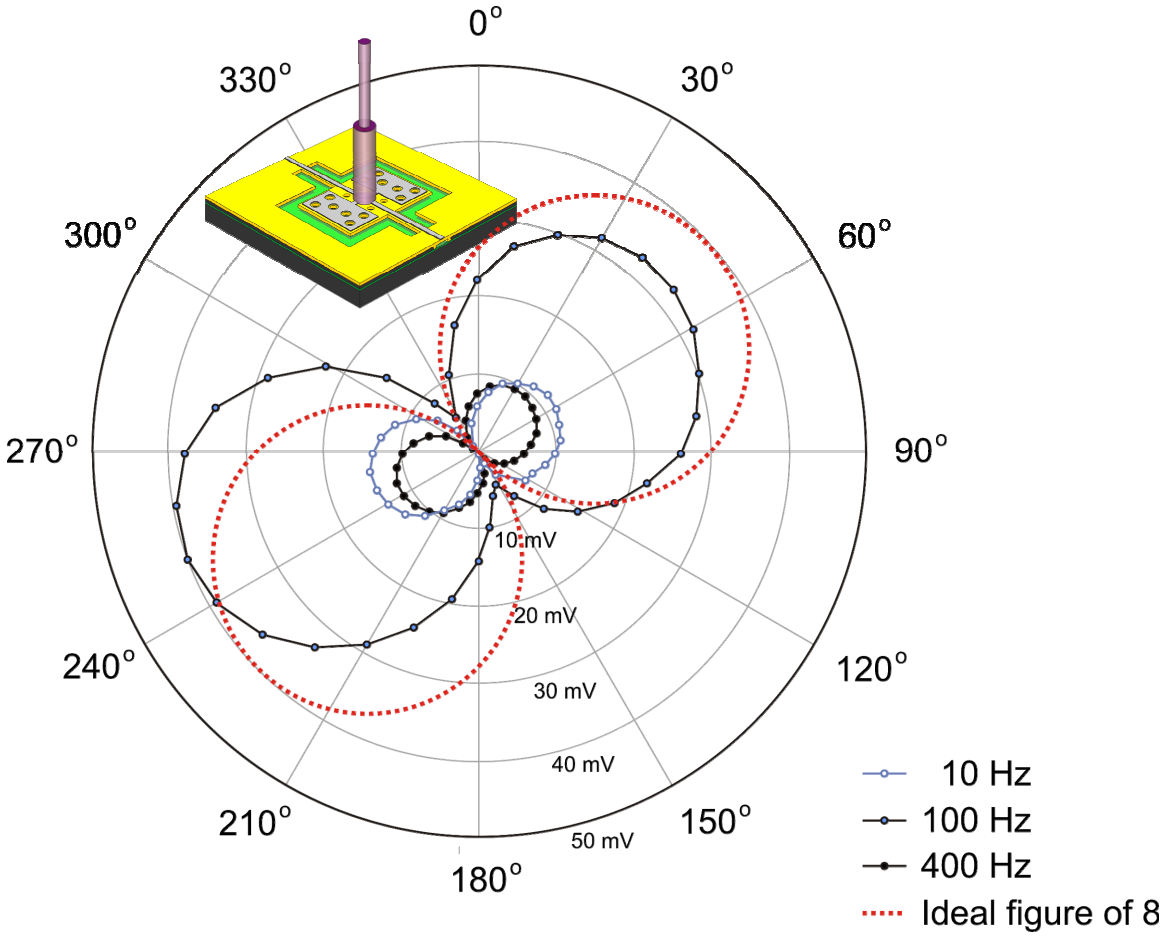

Figure 3.17 *Directionality measurements on the hair sensor arrays at three different frequencies showing a clear figure-of-eight response.*

Frequency response

Using a similar measurement setup, sensors with different torsional spring dimensions were tested and the frequency response of three such sensor arrays are shown in figure 3.18. The measurement plots show the sensor responses with different resonance frequencies in good agreement with the model. Using the sensor model, we calculated the drag-torque acting on the hair under the assumed air flow. Using this and the mechanical transfer characteristics of the sensor, the normalized angular amplitude of the rotating hair is calculated and hence, the relative change in the sensor capacitances is calculated. While the model was fed with the actual sensor dimensions, it is fitted only for the quality factors and proportionality factors.

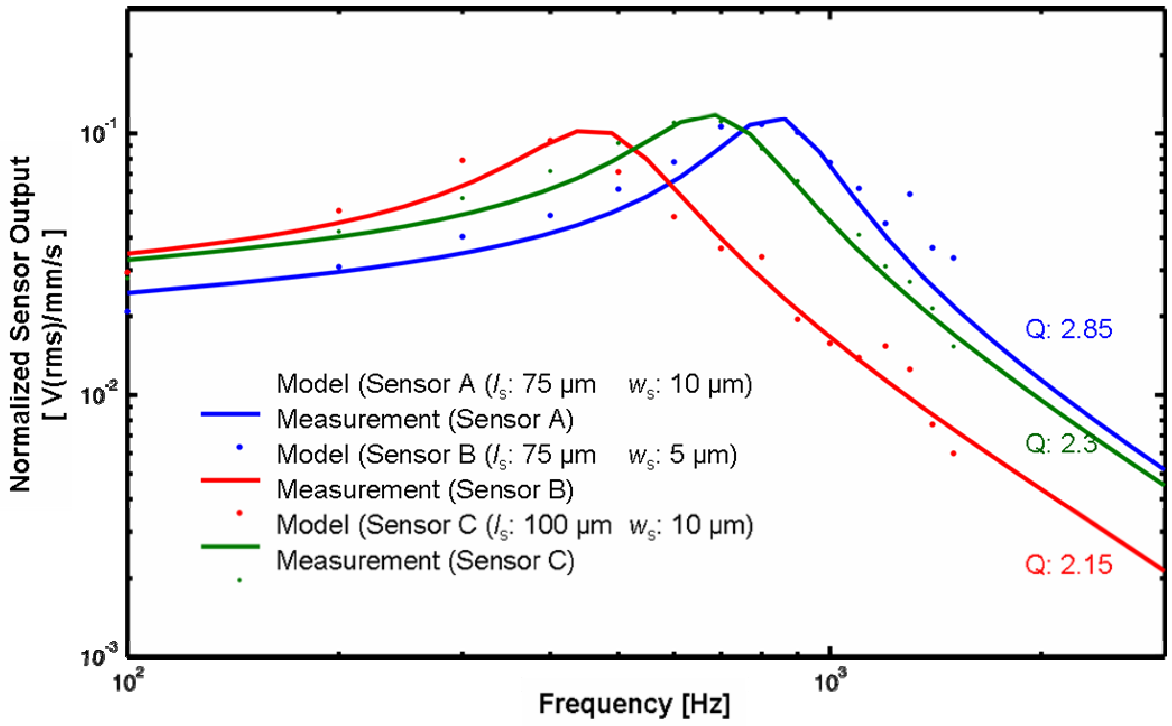

Figure 3.18 *Frequency responses showing normalized angular amplitudes from the sensors with different torsional spring designs*

3.5. Discussion

The performance of a mechano-sensory filiform hair is dependent on its efficiency in coupling energies from the source (flow) to the sensing neuron. There exists a certain mechanical transfer between the flow and the force it induces on the filiform hair structure. For an efficient coupling, the mechanical impedance of the hair-sensor should be matched [14] to the mechanical impedance of the flow and the cricket achieves such matching by proper tuning of its intrinsic mechanical parameters – hair moment of inertia J, torsional stiffness S and the torsional resistance R.

For the artificial hair sensors, only the moment of inertia J of the SU-8 hair and the torsional stiffness S of the sensor can be determined. The precise value of the damping coefficient R of the sensor has not yet been investigated. While there exists complexity to experimentally determine the damping coefficient, it should be noted that the sensors do exhibit a second-order mechanical system behavior, in combination with a boundary layer dependent driving torque, in good agreement with the models (figure 3.18). For the model calculations, while most parameters are based on the actual geometry and materials properties of the sensors, only the quality factor Q and overall proportionality factor were fitted. The quality factor represents the estimation of torsional resistance R of the hair. Numerical estimates of the torsional resistance R for the hair sensors by using the assumed quality factor Q lead to a value of about $4.8 \cdot 10^{-13}$ Nm.s.rad^{-1}. For a filiform hair of ~1mm long, the torsional resistance is given as $3 \cdot 10^{-14}$ Nm.s.rad^{-1}.

The torsional resistance R represents predominantly the combined effects of two damping mechanisms: (i) viscous damping due to the interaction between the hair and air flow [14,15] and (ii) squeeze-film damping of the air film between the sensor membrane and

the substrate. The damping coefficient due to viscous damping for the hair sensors is calculated [14,15]. Since it is dependent on the frequency, the numerical estimate from 100 to 1000 Hz is in the order of 2.4 – 3.4 x 10^{-14} Nm.s.rad^{-1}. This clearly shows that the coefficient due to the viscous damping is negligible and implies that the major part of the torsional resistance is constituted by the squeezed-film damping of the thin air film between the suspended membrane and the substrate.

It is tempting to compare the artificial hair-sensor with those of crickets. Such a comparison should include at least operational bandwidth, mechanical sensitivity and response threshold. Operational bandwidth is important since it implies the amount of (thermal-mechanical) noise to which the sensory systems are exposed. Evidently, the smaller the operational bandwidth, the lower the total noise power and, hence, the lower the response threshold. To the best of the authors knowledge there is no data on the maximum frequency that is encoded in the neuronal part of the flow-sensitive system of crickets. But given the mechanical response of the hairs with best frequencies mostly below 200 Hz [16] and given the relatively large low-frequency content of behaviorally relevant transient flows, e.g. as generated by attacking spiders [17], lying well below 200 Hz [18] one could speculate that the cricket flow-sensing system needs not be working in a bandwidth larger than 200 Hz. For this bandwidth and assuming white noise our sensors would have a threshold response of about 0.7 mm/s at 100 Hz. It may be expected that signal as well as noise power are proportional to the number of hair-sensors in the array (124) which translates into a response threshold for a single hair-sensor of about 8 mm/s. This is roughly ~2.5 orders higher than their natural counterparts

However, this is not the case. Calculation of the thermal mechanical noise [19] of our sensors indicates that this is currently not a limiting factor, i.e. electronics are still the limiting factor. One of the reasons is that for an array, owing to irregularities and parasitic capacitances, it is not possible for all hair-sensors to have the signal on both capacitors exactly in anti-phase. This implies that there will be charge injection in the common counter electrode, even in the absence of flow thereby increasing the response threshold. Another reason is that in a dense array of hairs, like in the hair-sensor arrays described here with inter hair-distance on the order of ~5 times the hair-diameter, there can exist a considerable amount of viscosity mediated hydrodynamic interaction between the hairs [20,21]. Chapter 6 of this thesis deals extensively with characterization of such effects on the hair sensor responses. For the situation of hairs aligned up along the direction of the flow this will lead to reduced exposure of the hairs to the flow resulting in reduced angular displacements. The effect becomes progressively worse as distance and/or frequency decrease and is estimated to reduce our sensor response with 25 - 50% at lower frequencies. As it turns out, single hair-sensors do not suffer from the two effects described above. Recent investigations have confirmed that single hairs can perform at response thresholds lower than reported here for entire arrays. This is possible with more advanced electronic interfacing and adaptations of the fabrication process which will be reported on in a future publication [22].

3.6. Conclusions

The hair sensor arrays featuring slightly modified spring and hair geometry were designed and successfully fabricated. The hair sensor arrays were extensively characterized for their quality and functionality. By replacing the chromium with aluminum for sensor electrodes, the sensitivity-deteriorating effect due to the membrane curvature is eliminated. This is obviously observed by means of a series of successful and well-characterized results

obtained from the sensor arrays. The sensor arrays show a flow amplitude threshold of 0.85 mm/s at 400 Hz at 1 kHz bandwidth and show a clear figure-of-eight directional sensitivity. When compared to the performance of the actual cricket hairs, the performance of the hair sensors is roughly ~2.5 orders worse, however, still marking a significant milestone: it can be argued that these sensors are about ~3.5 orders of magnitude more sensitive than the first generation [23] of hair-sensors (although these were never characterized equally well). It proofs that the model-based optimization, as introduced in chapter 2 has been very successful.

3.7. References

[1] K.E. Petersen, *"Silicon as a mechanical material"*, Proceedings of the IEEE (1982) Vol. 70, No. (5), pp. 420-457

[2] W.C. Young and R.G. Budynas, *"Roark's formulas for stress and strain"*, 7th edition, McGraw-Hill, (2002)

[3] C.M. Bruinink, R.K. Jaganatharaja, M.J. de Boer, E. Berenschot, M.L. Kolster, T.S.J. Lam-merink, R.J. Wiegerink and G.J.M. Krijnen, *"Advancements in technology and design of biomimetic flow-sensor arrays"*, Proc. IEEE Int. Conf. MEMS, 2008, pp. 152-155

[4] http://www.microchem.com/products/su_eight.htm

[5] A. Mata, A.J. Fleischman and S. Roy, *"Fabrication of multi-layer SU-8 microstructures"*, J. Micromech. and Microeng.(2006)16, pp.276-284

[6] Y.-J. Chuang, F.-G. Tseng and W.-K. Lin, *"Reduction of diffraction effect of UV exposure on SU-8 negative thick photoresist by air gap elimination"*, Microsystem Technologies.(2002) Vol. 8, pp.308-313

[7] http://www.polytec.com/eu/

[8] http://www.polytec.com/int/solutions/3-d-surface-profiling/basics-of-white-light-interferometry/

[9] R. Raangs, *"Exploring the use of the microflown"*, Chapter 5, PhD thesis, University of Twente, Enschede, the Netherlands (2005)

[10] H-E. de Bree, V.B. Svetovoy, R. Raangs, R. Visser, *"The very near field, theory, simulations and measurements"*, Proc. of 11th International Congress on Sound and Vibration, St. Petersburg,(2004).

[11] H-E. de Bree, *"The microflown"*, PhD thesis, University of Twente, Enschede, the Netherlands (1997)

[12] R.K. Jaganatharaja, C.M. Bruinink, B.M. Hagedoorn, M.L. Kolster, T.S.J. Lam-merink, R.J. Wiegerink and G.J.M. Krijnen, *"Highly-sensitive, biomimetic hair sensor arrays for*

sensing low-frequency air flows", Proc. of 15th Int. conf. on solid-state sensors, actuators and Microsystems (Transducers 09), Denver, (2009), pp. 1541-1544

[13] M. Kanou and T. Shimozawa "*A threshold analysis of cricket cercal interneurons by an alternating air-current stimulus*", J. Comp. Physiol. A (1984) Vol. 154, pp 357-365.

[14] T. Shimozawa, T. Kumagai and Y. Baba, "*Structural scaling and functional design of the cercal wind-receptor hair of cricket*", J. Comp. Physiol. A (1998)Vol. 183, pp. 171–186

[15] J.A.C. Humphrey, R. Devarakonda, I. Iglesias, F.G. Barth,*"Dynamics of arthropod filiform hairs. I. Mathematical modeling of the hair and air motions"*, Philosophical Transactions: Biological Science (1993) 340,pp.423-444

[16] T. Shimozawa, J. Murakami, T. Kumagai,*"Cricket wind receptors: thermal noise for the highest sensitivity known"*, Chapter 10, Sensors and Sensing in Biology and Engineering, ed. F.G. Barth, J.A.C. Humphrey and T.W. Secomb, Springer, Vienna, 2003.

[17] J. Casas,T. Steinmann andO. Dangles,*"The aerodynamic signature of running spiders"*, PLoS ONE (2008) 3(5): e2116.

[18] R. Kant and J.A.C. Humphrey, *"Response of cricket and spider motion-sensing hairs to airflow pulsations"*, J. R. Soc. Interface (2009) Vol. 6, pp. 1047

[19] L.C. Osborne,*"Signal processing in a mechanosensory array: Dynamics of cricket cercal hairs"*, PhD thesis, University of California, Berkeley (1996)

[20] B. Bathellier, F.G. Barth, J.T. Albert and J.A.C. Humphrey, *"Viscosity-mediated motion coupling between pairs of trichobothria on the leg of the spider Cupiennius salei"*, J. Comp. Physiol. A (2005)Vol. 191, pp. 733-746. Erratum: J. Comp. Physiol. A (2010) Vol. 196, p. 89

[21] J. Casas, T. Steinmann andG. Krijnen,*"Why do insects have such a high density of flowsensinghairs?Insights from the hydromechanics of biomimetic MEMS sensors"*, J. R. Soc. Interface (2010) Vol. 7(51), pp. 1487-1495.

[22] A.M.K. Dagamseh, C.M. Bruinink, H. Droogendijk, R.J. Wiegerink, T.S.J. Lammerink amd G.J.M. Krijnen, *"Engineering of biomimetic hair-flow sensor arrays dedicated to high-resolution flow field measurements"*, IEEE Sensors conference, Hawaii, USA, 1-4 Nov, 2010, pp. 2251-2254.

[23] M. Dijkstra, J.J. van Baar, R J Wiegerink, T S J Lammerink, J H de Boer and G J M Krijnen, "*Artificial sensory hairs based on the flow sensitive receptor hairs of crickets*", J. Micromech. and Microeng. (2005) 15, pp. 132-138.

4

Nature-like hairs

In a nutshell...

The shape of the filiform hairs on the cerci of crickets has a pivotal role in sensing. It becomes almost inevitable while engineering a bio-inspired system, to admire and learn from the course of nature's evolutionary design and trying to re-create it with man-made technologies. The artificial hairs we have made have already evolved over several design optimization phases. In this chapter the design and fabrication of artificial SU-8 hairs, of which the shape resembles that of their natural counter-part, is described. Optimizing the shape of the artificial hair is necessary for improving the sensitivity while retaining usable bandwidth of the sensors. A new technological approach involving a back-side exposure to fabricate SU-8 hairs is tested and characterized in the presented work. Such a technique opens up the possibilities to fabricate sensors with hairs of different geometry in one simplified process.

4.1. Introduction

Artificial hairs on top of the sensor membranes are the mechanical interfaces that cause the flow information to result in membrane rotations inducing capacitance changes which are eventually transformed into equivalent electrical signals. For the effective operation of our artificial hair sensors, the shape of the SU-8 hair plays a central role. The hair geometry serves two basic purposes: (i) it determines the amount of flow-induced, drag-torque acting

upon the hair and (ii) it contributes to the mass moment of inertia, which determines the mechanics of the sensory system. While the figure of merit for the sensors suggests optimal design values for our artificial hairs, there exist challenges in realizing such design goals due to the technological limitations. Nevertheless, through model-based optimization, the artificial hairs have undergone several changes over the years, either in terms of design or fabrication technology. Finding the optimum balance between the drag-torque reception and the hair moment of inertia has been the primary motivation for such optimization.

4.2. Filiform hairs on the cerci of crickets

The structural aspects of the filiform hairs (Figure 4.1) on the cerci of crickets have been extensively studied by biologists and bio-physicists [1-3]. The hairs on the cerci are found to appear in a wide range of lengths from 30 to 1500 μm with diameters occurring from 1 to 9 μm and generally being tapered towards the hair-tip. These hairs are sitting in a socket which has some degree of mechanical anisotropy that causes the direction of best sensitivity to vary over the cercus [3]. A wide range with respect to hair geometry also suggests diversity in mechanical properties and hence, sensing capabilities.

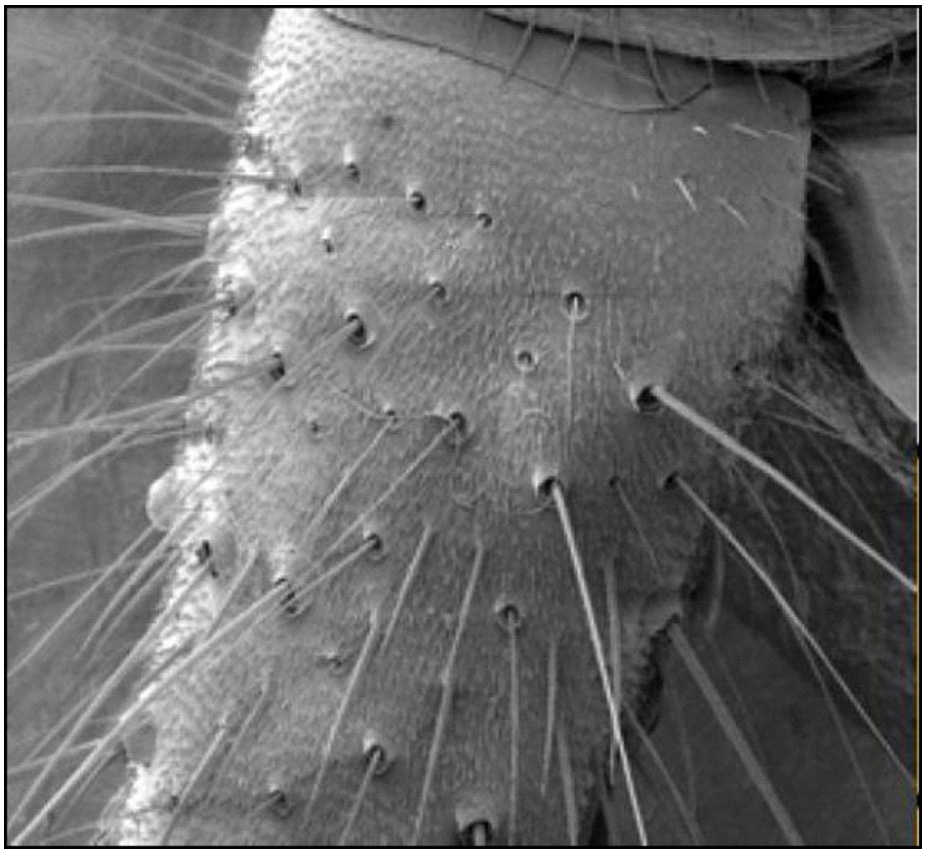

Figure 4.1 *Filiform hairs on the cerci of crickets*
[SEM image courtesy: G. Jeronimides, University of Reading, UK]

Initially, the structural effects of the cercal hairs were analyzed by assuming a cylindrical [2] or linearly tapered conical shape [3] for them. But upon more accurate measurements, the hair shape was found to follow extremely elongated paraboloids, i.e. square-root cone, whose diameter increased with the square-root of the distance from their tip

[4]. Earlier electron microscope studies showed the hairs to be hollow tubes, with the diameter of the inner hollow cavity being approximately one-third of the outer diameter [5]. The hollowness of the hair reduces the moment of inertia further. The shape of the hairs play an important role, in terms of (i) determining the moment of inertia that contributes in defining the best frequency of its mechanical system and (ii) determining the drag-torque receptive capability (which depends on the length of the hair and the effective surface area that faces the flow).

Natural hairs have shown to inspire bio-inspired engineers posing challenges in: (i) implementation of arrays of hair sensors with a wide range of hair geometry; (ii) realizing hairs with high aspect ratios (> 1:100); (iii) square-root conical shape of the hairs and (iv) sturdy and robust hairs made of compliant biological material.

4.3. Our artificial hairs – an overview

Prior to the fabrication of our first generation of hair sensors, investigations were made on realizing high-aspect ratio hair-like structures using silicon nitride (Figure 4.2). By etching trenches of different shapes on the silicon substrate, and later filling these up by silicon nitride in a low-pressure chemical vapor deposition process, it was shown possible to realize hairs of varying geometry. However, integrating such silicon-nitride hairs with a sensor element posed difficulties.

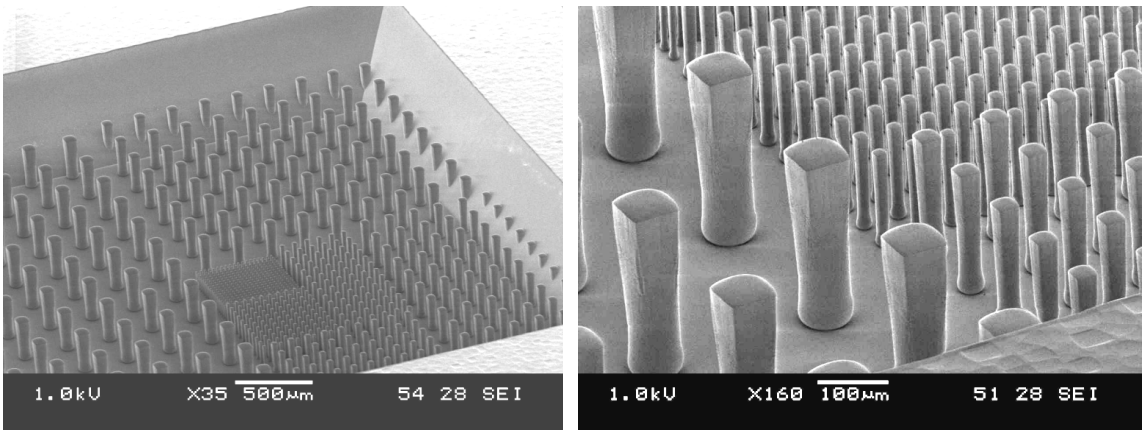

Figure 4.2 *Arrays of silicon nitride hairs [6]*

In the following generations [7,8] SU-8 hairs were introduced, SU-8 is an epoxy-based polymer with a relative (compared to silicon-nitride) low Young's modulus. The SU-8 hairs were fabricated using a standard photolithographic technique of spinning the negative-tone photoresist, exposing and then developing into a hair-like structure. First, a single layer of SU-8 photoresist was used resulting in hairs of ~450 µm length [7]. In later generations of our hair sensors, two subsequent layers of SU-8 were spun and hairs of length of up to ~900 µm were fabricated by top-side exposure [8]. The result was that hairs were long and had a cylindrical shape with a uniform diameter of ~50 µm (Figure 4.3). It is to be noted that the hair length variations depend on the number of layers spun and complexities increase with the number of layers. So far, hairs have only been realized with up to two different lengths, throughout the array.

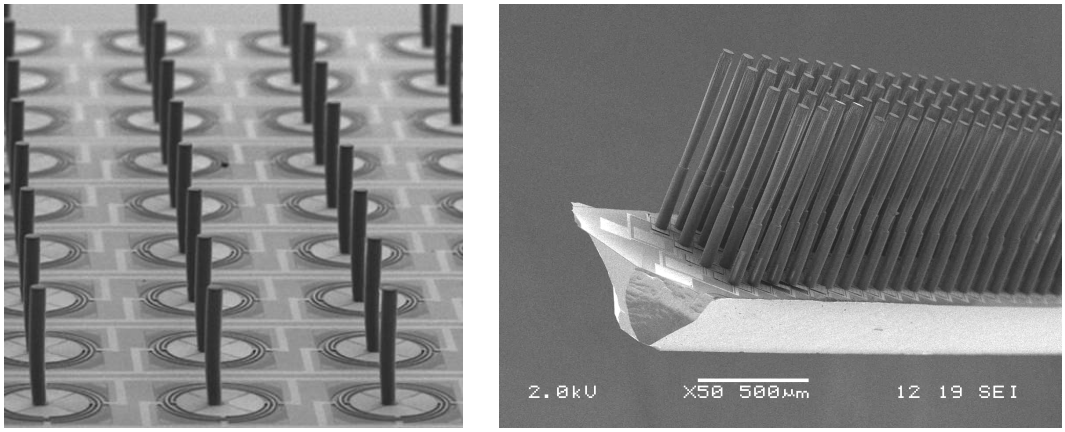

Figure 4.3 *Generations of SU-8 hairs with a cylindrical shape of ~450 µm (left) and of ~900 µm (right)*

In the current generation of sensors [9], the focus of the sensor optimization was laid on realizing springs with small torsional stiffness, which is crucial for obtaining higher mechanical sensitivity. For such sensor designs, the hairs with cylindrical shape with a large moment of inertia hamper the usability by restricting the bandwidth as a consequence of a decreasing resonance frequency for decreasing rotational stiffness at fixed moment of inertia. Within the limitations of technology, other ways to reduce the hair moment of inertia were sought. One solution is a reduction of the diameter of the upper hair part to half of that of the diameter of the lower part of the hair (i.e. $D_1 = 2D_2$, see Figure 4.4). This results in a reduction of the moment of inertia by 65 % at the cost of a slightly (15-20%) reduced drag-torque.

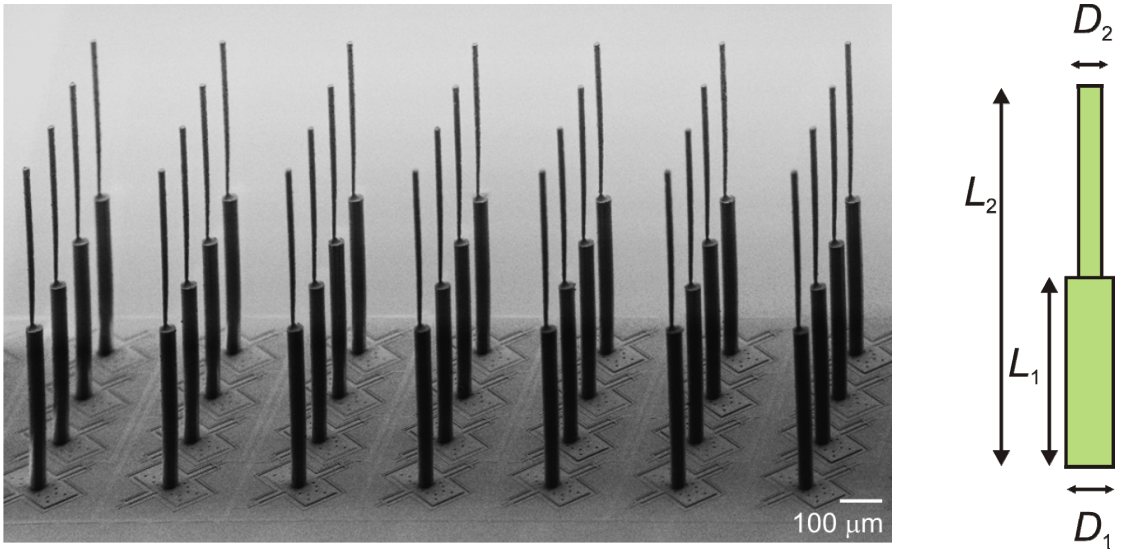

Figure 4.4 *Present generation of SU-8 hairs with two parts: top diameter is half the size of the bottom, in order to reduce the moment of inertia down to ~35% [10]*

The complexity in using multiple-spun SU-8 layers is that the alignment of the structures on subsequent layers becomes very critical. As shown in figure 4.5, aligning the top part of the hair on to the center of the bottom hair becomes difficult and it is critical to the

functionality of the hair itself. Further, due to the nature of how the light penetrates into the SU-8 layer during exposure, the developed hair has a top part which appears more like an inverted-cone. Accurate alignment of the top part to the bottom part is challenging and analyzing the effects of it on the hair-sensor performance is complex.

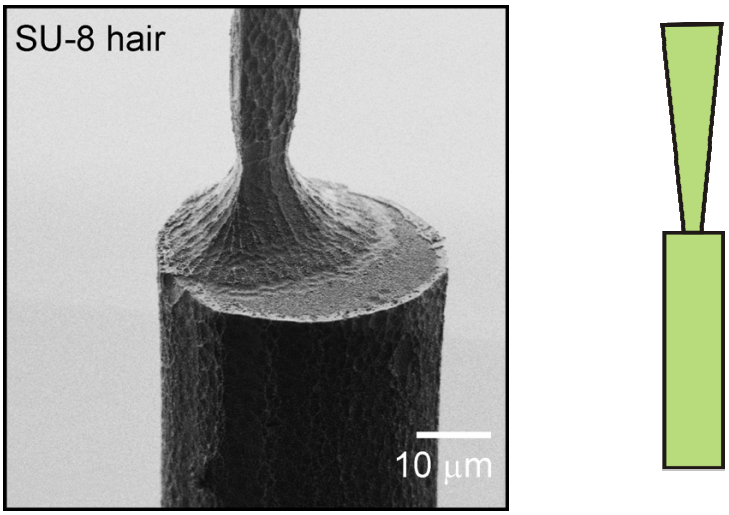

Figure 4.5 *Actual hair shape: inverted cone-shaped top part of the SU-8 hair [10]*

4.3.1 Motivation for nature-like hairs

Motivation for the nature-like hairs is driven by the necessity of realizing optimal sensor performance, as discussed in Chapter 2. Optimal performance of the sensor is defined by means of a figure of merit, which requires that (i) hairs be long (drag-torque reception) and thin (for small moment of inertia) and (ii) sensor springs be compliant (desired mode of operation) and robust (in all other modes). In the upcoming generation of hair sensors, the springs will be designed to reduce the torsional stiffness by at least one-order over the previous generations. For such compliant sensors, SU-8 hairs should have small moment of inertia for retaining the usable sensor bandwidth. However, both moment of inertia and drag-torque receptive capability are dependent on the shape of the hair. Thus, to realize an optimal hair shape, the ratio of drag-torque (T_d) generated on the hair to the moment of inertia (J) should be large. A figure of merit for the optimal hair shape can thus be defined as:

$$FoM_{(\text{hair})} = \frac{T_d(\omega, L)}{J} \tag{4.1}$$

However, this *FoM* for the optimal hair shape is dependent on the flow frequency (ω) and hair length, L. For a filiform hair of ~800 μm long, the *FoM* at 250 Hz is given as $5.9 \cdot 10^6$ [units] while for the present generation of SU-8 hair (with two different hair diameters at top and bottom) of similar length, the *FoM* at the same frequency is given as $1.17 \cdot 10^5$ [units]. This means that the shape of the filiform hair is optimal than the artificial hair by ~50 times.

Furthermore, the hair lengths of the present generation of hairs are fixed (by means of spun SU-8 layers). Since the present array of sensors act in parallel as one single capacitive sensor, this doesn't bother too much. However, the next generation of sensor arrays will

feature hairs that can be individually addressed in an array. For such designs, it is highly desired to have hairs of different lengths which facilitates in realizing arrays sensitive to a wide range of operating frequencies. It is therefore required to develop a simple fabrication scheme to fabricate hairs of different lengths.

Our new approach to fabricate SU-8 hairs is aimed at addressing the above requirements. Bottom-side exposure of SU-8 hairs will enable us to realize hairs with reduced moment of inertia and with a shape, which resembles those of filiform hairs. At the same time, such a technique is expected to provide us the facility to control the hair lengths in an array, even at the design phase.

4.4. SU-8 processing

SU-8 is a renowned material commonly used in soft lithography techniques for lab-on-a-chip applications [11]. SU-8 is a low-Young's modulus material (~4GPa) with attractive mechanical and chemical properties. The fact that it is compatible with most standard microfabrication techniques offers a great advantage and, moreover, it can also used as structural material in MEMS applications [12]. Since our artificial hairs are made of SU-8, a brief introduction of SU-8 processing and bottom-side exposure technique is presented in this section. The actual process flow of the SU-8 hairs is presented here in detail.

4.4.1 Standard processing steps

SU-8 is an epoxy-based, negative-tone near-UV photoresist polymer developed for high-aspect ratio structures and for ultra-thick layers [13]. High-aspect ratio structures are realized by means of a photo-assisted cross-linking process of the polymer. SU-8 is sensitive to conventional near-UV (350-400 nm) radiation, while UV I-line (365 nm) is mostly recommended [14]. Standard photolithography of SU-8 consists of the following steps:

(i) Resist spinning
(ii) Soft bake or pre-exposure baking
(iii) Exposure
(iv) Post-exposure baking
(v) development

An optional hard baking step might follow, depending on the requirements [14]. SU-8 photoresist comprises of epoxy resin, solvent and a photo-acid generating agent. SU-8 is available in different viscosities targeting at the layer thicknesses achieved at standard resist spinning settings [14]. During the soft-baking, most of the solvent is evaporated. The cross-linking of the epoxy happens in two-steps: (i) generation of photo-acids during the exposure and (ii) photo-acid catalyzed cross-linking of epoxy polymer under thermal conditions during the post-exposure baking step. Development of the SU-8 leaves the cross-linked polymer intact while removing the unexposed portions of the SU-8 layer. The process parameters in the above steps will vary for different desired SU-8 layer thicknesses. Also, each of the steps has a profound impact in defining characteristics of the realized SU-8 structures in terms of intrinsic stress, adhesion and profile.

4.4.2 Tapered side-wall profile

Micro structures realized using thin layers of photoresist with standard top-side exposure, result in vertical sidewalls. Vertical sidewalls are often an important requirement in microfabrication, as any tapering profile (positive or negative) will also affect the patterned profile of the underlying layers. Tapered side-wall profiles in SU-8 layers have been studied

in [15]. Some important factors that influence the quality of the side-wall profiles are suggested as [15, 16]: (a) optical wavelength, (b) intensity-profile due to the Fresnel's diffraction of the UV light through the mask opening, (c) attenuation at different depths of the thick SU-8 layer (and hence the resulting optical transmission rate at different depths) and (d) the gap between the photomask and photoresist layer.

Thicker resists result in more non-uniformity in resist-thickness across the wafer, which does not favor contact printing. For the processing the SU-8 (~900 μm thick) hairs of our sensor arrays, we used soft contact exposure with a gap ~80-100 μm between the resist and the mask. Exposure under such conditions will result in tapered side walls. This has been prominently observed in the present generation of SU-8 hairs, with negative-tapering profiles of the top parts (figure 4.5). Using a special I-line filter during exposure is recommended for improved side-wall quality [14].

4.4.3 Bottom-side exposure

The characteristic negative-tapering profile of patterned thick SU-8 layers can be made useful for fabricating hairs by bottom-side exposure. The negative-tapering profile then works in a much-favorable way in reducing the moment of inertia and such hairs could resemble the filiform hairs of crickets. Bottom-side exposure of SU-8 layers is a well-known technique, commonly used as molds in the fabrication of micro-needle arrays for drug-delivery applications [16-18]. Arrays of SU-8 hollow micro pillars are fabricated by bottom-side exposure of SU-8 layers, and electroplated, followed by mechanical polish to open the holes at the tip. Unexposed SU-8 is then removed using a developer. Bottom-side exposure gives an advantage of realizing tapered micro-needles, favored for the ease of piercing the skin for drug delivery.

4.5. Design and fabrication

For our requirements, we use bottom-side exposure for fabricating hairs with gradually tapering tips aimed to resemble the filiform hairs. The aim is to first develop a proof-of-concept process flow to fabricate SU-8 hairs by the bottom-side exposure method. Figure 4.6 shows the condensed process flow involved and the details are presented in the Appendix. The process starts with a standard glass wafer (step 1) on which ~100 nm of Aluminum is sputtered. An aluminum layer is patterned using standard photolithography using positive photoresist and by wet-etching using OPD 4262 solution (step 2). The patterned Aluminum layer serves as the mask during the bottom-side exposure of the SU-8 layer.

The first layer of SU-8 is spin-coated on the wafer under the standard settings [14] in order to achieve a layer thickness of ~400 μm. The wafer is put on the hot plate set at 95 °C for 6 hours and then left to cool down. Subsequently the second layer of SU-8 is coated and soft-baked. Next the wafers are flipped over and exposed under UV light using flood exposure settings. The exposure time is calculated based on the recommended exposure energy [14] and the intensity output of the UV source (for our case the mask aligner EVG 620 provides 12 mW/cm^2). Based on this and combined with the interest of our investigation, four different exposure times (160, 190, 220 and 250 s) were chosen for testing (step 4).

The wafers are placed on the hot plate for the post-exposure baking step for epoxy cross-linking. The hot plate is set at 75 °C for 50 min and slowly cooled down with time steps of 5 min at every 5 °C reduction. This step is important in the SU-8 processing to reduce the internal stress developed in the layer. The wafers are then developed in standard RER 600

solution (step 5) under a spray-gun. The wafers were developed for 25 cycles of each 1 min. The finished wafers are dried and put under the optical microscope for observation.

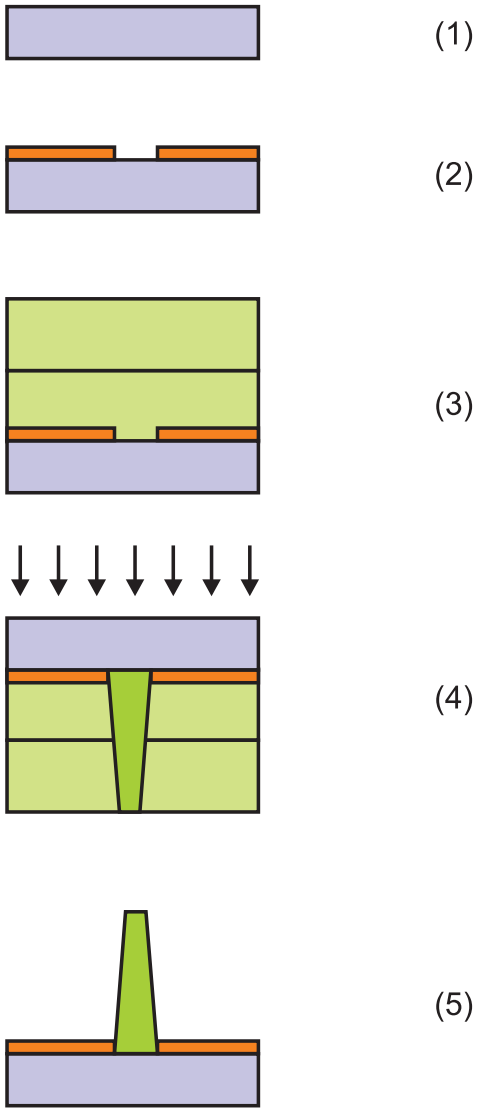

Figure 4.6 *Fabrication flow for nature-like SU-8 hairs by back-side exposure: (1) glass wafer; (2) Aluminum sputtering and patterning; (3) Spinning of two SU-8 layers of ~400 μm thickness each; (4) Bottom-side exposure and (5) SU-8 development.*

4.6. Observations

Nature-like SU-8 hairs were successfully fabricated using the bottom-side exposure method with their shapes resembling their natural counter-parts closer compared to previous versions of our artificial hairs. Figure 4.7 shows hairs with gradually-reducing diameter from the base towards the apex. These hairs were fabricated after 250 s exposure from the bottom-side of the substrate and through a circular opening of ~30 μm diameter in the Aluminum mask layer. These hairs were of ~750 μm length and the respective base and top diameters were ~43 μm and ~15 μm respectively. Using the bottom-side exposure method, hollow hairs were also fabricated. In this section the results from nature-like and hollow SU-8 hairs, as inspected optically, are discussed.

4.6.1 Nature-like hairs

Nature-like hairs were fabricated (i) using different circular patterns in the aluminum of which the opening diameters varied from 2.5 μm to 60 μm and (ii) at different exposure times – 160, 190, 220 and 250 s to analyze the importance of exposure time for the eventual hair shape. Characterization was mainly by optical microscopy, with which the hairs were measured for their lengths and diameters at different distances from the hair base. From the measurements, it was observed that the length of the nature-like hairs fabricated from a specific opening diameter, were almost uniform with a little variation of ±2%. In all the sample wafers, irrespective of exposure times, the hairs fabricated from an opening diameter of 2.5 μm were mostly missing or scarcely found after the development.

Figure 4.8 shows a high-resolution SEM image of a line-up of SU-8 hairs varying in length depending on the diameter. Figure 4.9 shows the measured hair lengths plotted against the circular opening diameters of the aluminum pattern and for different exposure times. It was clearly observed that hair length gradually increased with increasing opening diameter of the mask pattern.

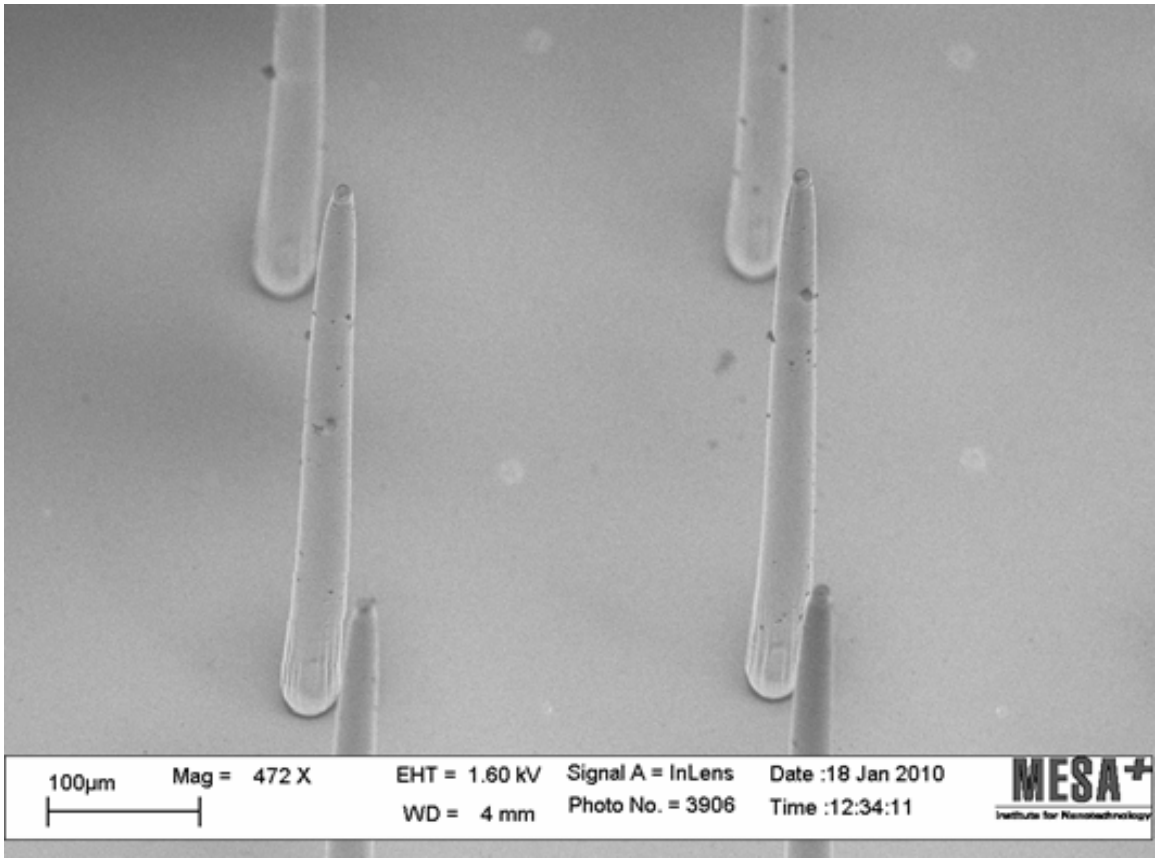

Figure 4.7 *Nature-like SU-8 hairs from an opening diameter of ~30 μm*

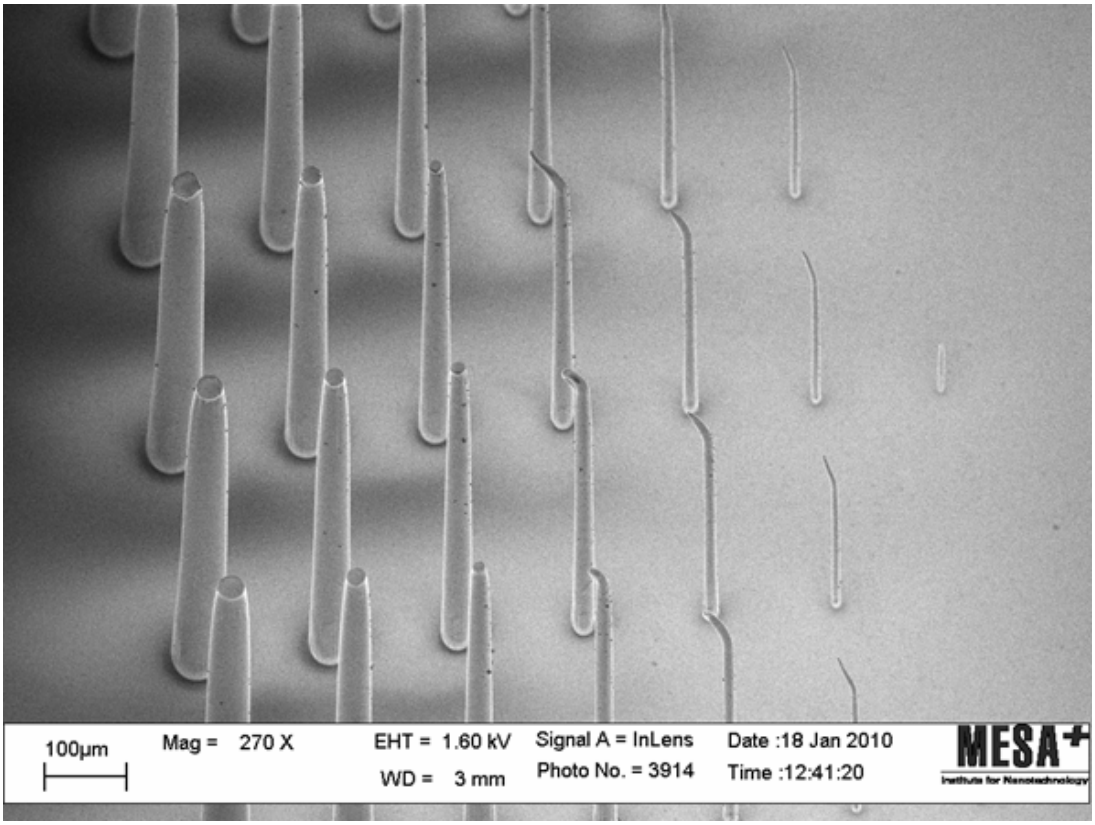

Figure 4.8 *SEM image of nature-like SU-8 hairs of different lengths fabricated from the opening diameters of 50 µm (left) to 2.5 µm (right)*

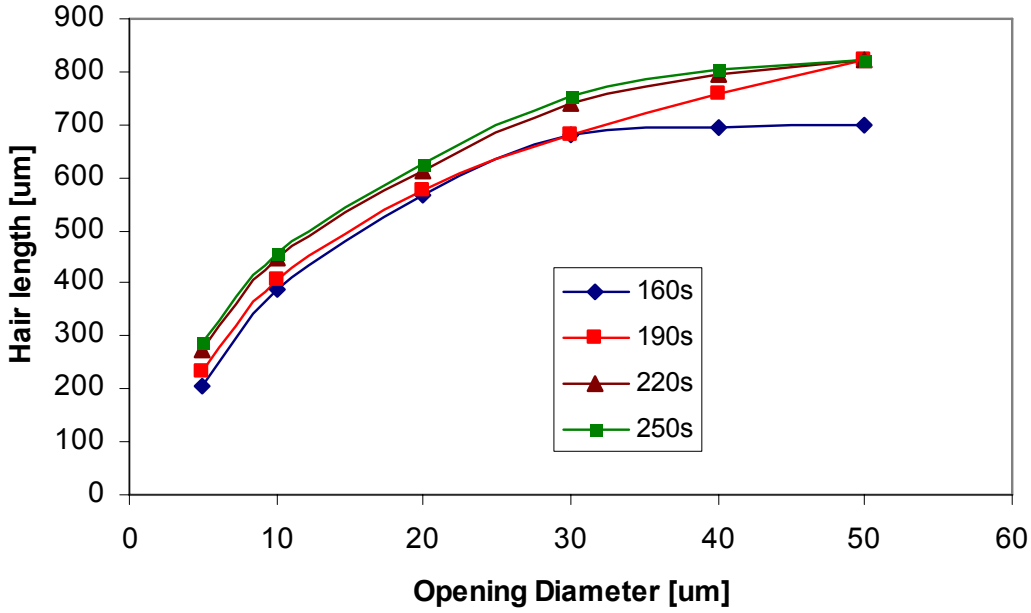

Figure 4.9 *Nature-like SU-8 hairs of different lengths based on the opening diameters(mask pattern) and for various exposure times.*

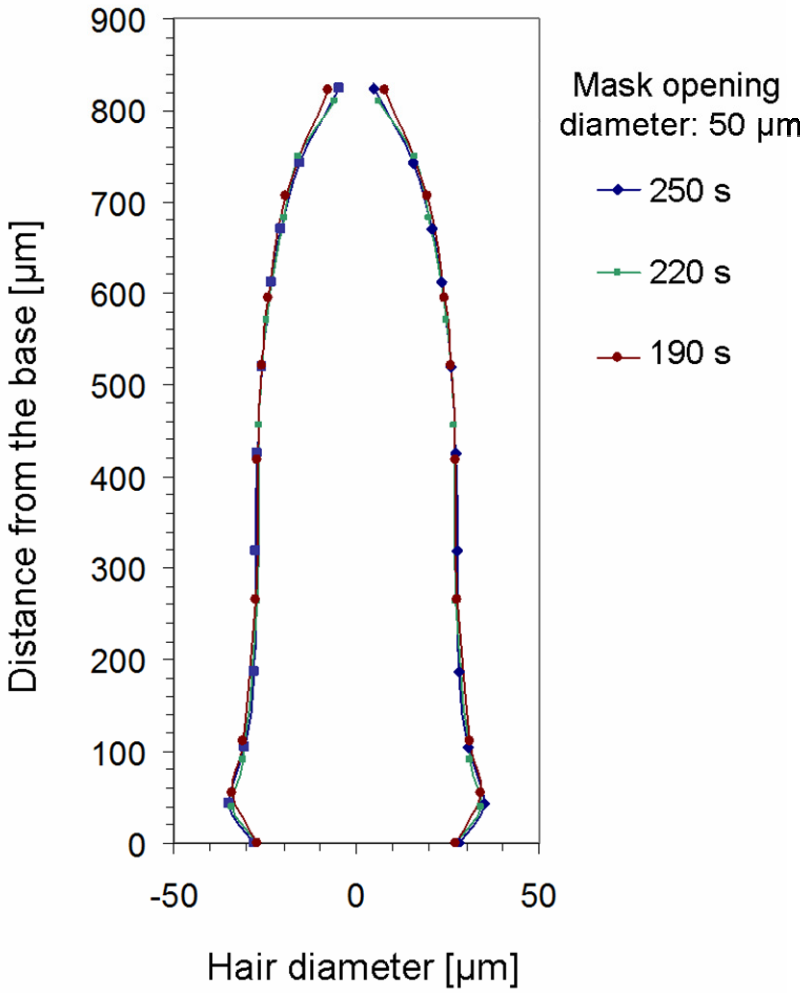

Figure 4.10 *Variation of the hair diameter with increasing distance from the base (for the hairs made from an opening diameter of 50 µm)*

Figures 4.10 and 4.11 show an interesting observation of the change in hair diameters as the distance from the base increases. The hairs were individually measured for their diameters, from which an approximately symmetrical representation of the hair shape is presented for the sake of qualitative comparison. In figure 4.10, the measurements are of hairs from an opening diameter of 50 µm at different exposure times. The overall shape of the hair seems not to be influenced substantially by the exposure time. Interestingly, all the hairs show a bulge in their diameters, which peaks around a distance of ~40-50 µm above the base. Similar characteristic profiles are observed in figure 4.11 which shows similar measurements but observed on those hairs realized from different opening diameters of mask patterns. The hairs from the opening diameters of 50, 40 and 30 µm were measured at different distances from their base until their tips. All the hairs, while showing distinct overall hair shape commonly show a bulge in their diameter, at distances close to the base. It is unclear the exact reason for such a bulge on the diameter.

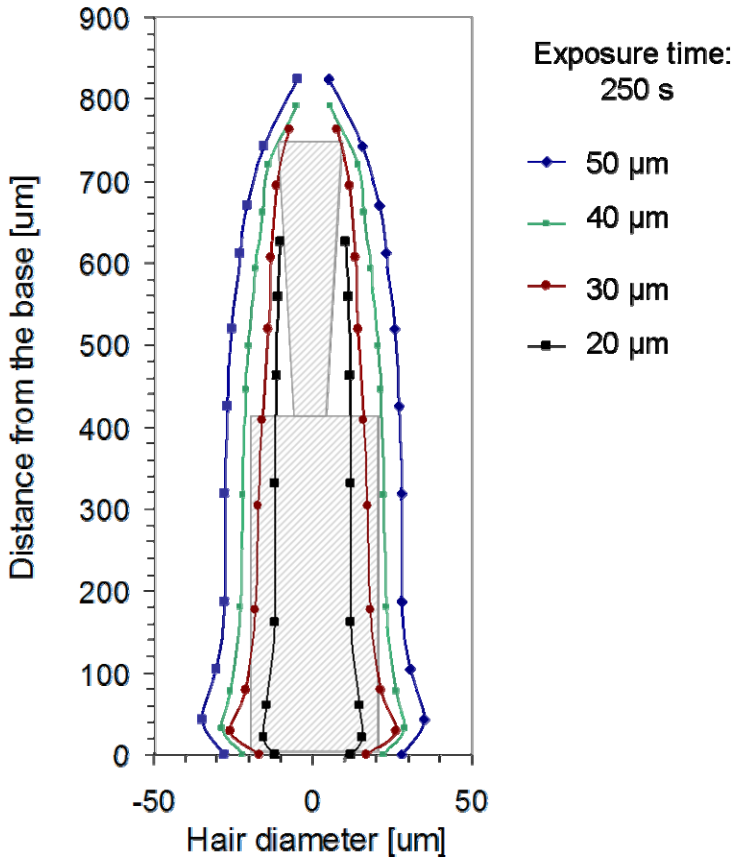

Figure 4.11 *Variations of the hair diameter with increasing distance from the base (For the hairs from different opening diameters). Shaded image represents the shape of the present SU-8 hair used on the sensor arrays.*

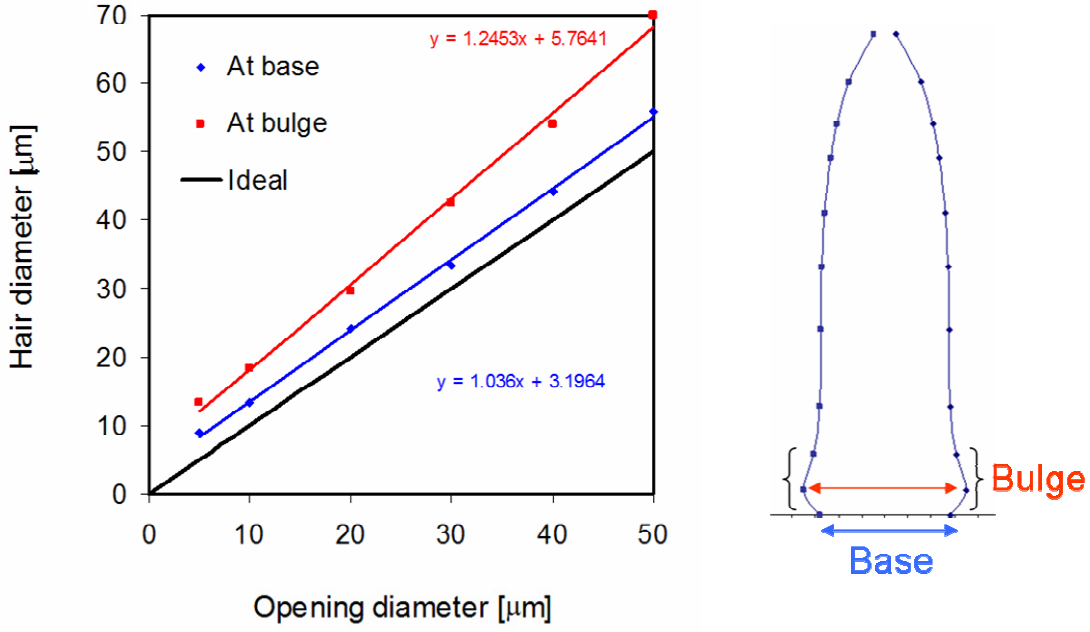

Figure 4.12 *Comparison of hair diameters measured at the base and at the bulge, with the designed values for the mask openings. The measurements are from the hairs fabricated at an exposure time of 250 s.*

Figure 4.12 shows the trend of the hair diameter measured at the base and at the bulge, with respect to the opening diameters. The measurements are from those hairs fabricated with 250 s exposure time. It is evident that the hair diameters at the hair base are slightly larger than the opening diameters, while the measured hair diameters at the bulge are fairly larger than the designed values. On the other hand, the variation of the hair diameters at the tip could not be measured precisely for all opening diameters, as some of the hairs showed curling of the tips (especially for those hairs fabricated from smaller opening diameters).

Figure 4.13 shows some intriguing effects observed at the tips of the nature-like hairs. Tip linking of the hairs (Figure 4.13 - i and ii) is observed to occur between hairs that are placed at close distance to each other. Based on the measurements on hairs of ~850 μm length and ~50 μm diameter, this effect is prevalent among hairs placed at a spacing less than or equal to 110 μm (center-to-center) between each other. Hairs of equal length placed at larger inter-hair distances do not have such linking effect; however they still may have slightly tilted tips, as shown in figure 4.13.

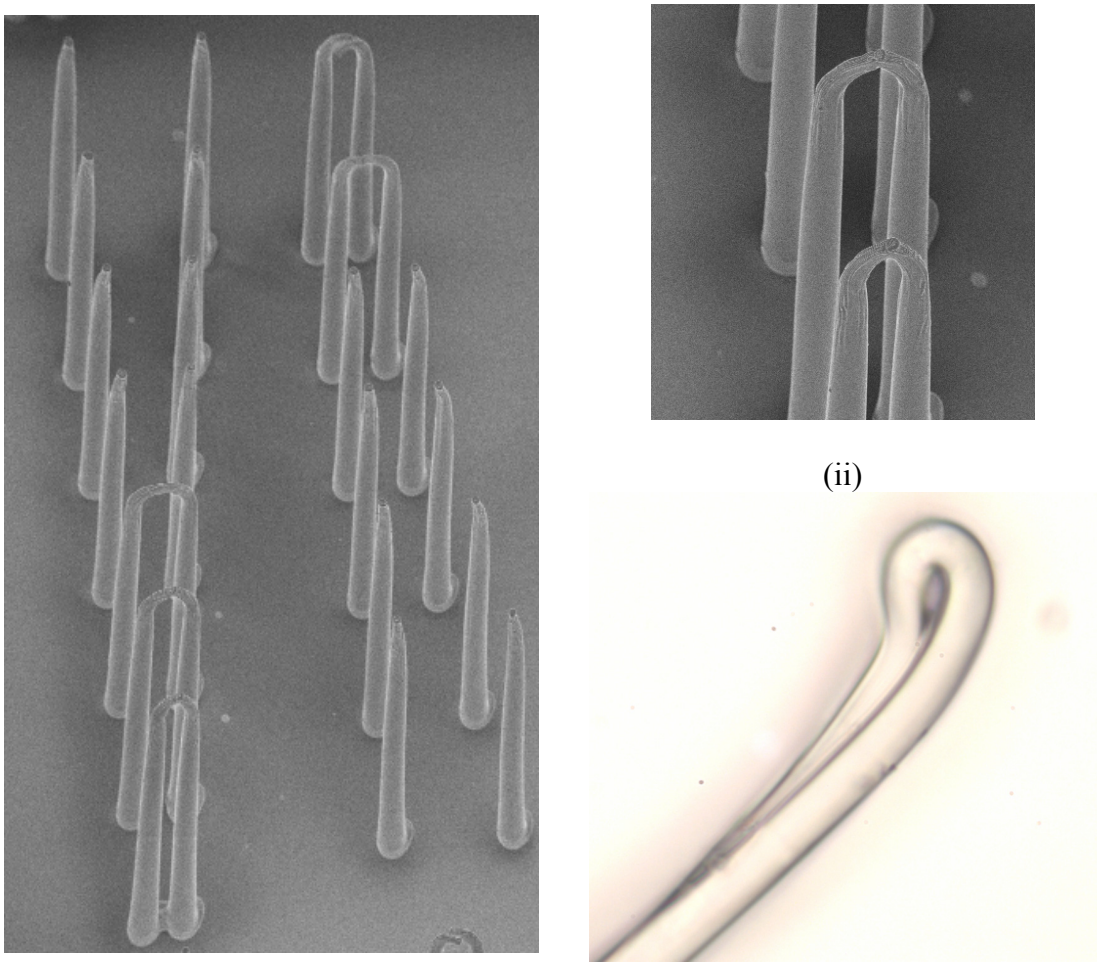

(i) (ii) (iii)

Figure 4.13 *Hairs showing tip-linking and curling effects at their tips.*

Furthermore, when the tip diameters of the hairs become smaller (usually < 10 μm), the tips tend to curl on to themselves. Such curling effect was observed in almost all hair samples fabricated from the smaller opening diameters (≤ 20 μm) of the Aluminum pattern. This was the main reason why the tip diameters could not be accurately measured. However, those hairs with a length almost equal to the thickness of the SU-8 layer (realized with larger opening diameters of the mask pattern), do not have such curled tips.

4.7. Discussion

Hairs that resemble filiform hairs are fabricated by bottom-side exposure of SU-8. Also, hairs of different length, defined by the opening diameters on the mask pattern, are successfully fabricated in one process-flow. The length and diameter of a hair fabricated from a given opening diameter of the mask pattern appear not to be influenced by the exposure times. This suggests above a certain threshold, the dose (calculated for a given intensity) seems not to impact much on the hair geometry.

4.7.1 Hair length and diameter

As seen from figure 4.9, the hair length tends to increase with the opening diameter (approximately as a function of 3rd order polynomial). Different exposure times of SU-8 were also tested and it is observed that variations in exposure time can cause up to 20% variations in hair length. On the other hand, this effect seems to occur merely at the larger diameters where it seems that the shorter exposure times are insufficient to saturate SU-8 cross-linking. This is further illustrated by the results for 220 s and 250 s: despite the 13% variation in exposure time, hair-lengths seem to hardly increase. Hence, for sufficient long exposure times the process is rather robust.

For the opening diameters up to 30 μm, the major difference in the measured hair lengths due to the exposure times is observed between those exposed at 190 s and 220 s and for those exposed longer (i.e. 250 s); no significant differences was observed. On the other hand, for those diameters above 30 μm, the major difference in the hair lengths is observed between the exposure times of 160 s and 190 s and for the hairs exposed longer than 190 s, no significant differences were observed.

Figures 4.10 and 4.11 show the hair shape profile for different exposure times and different opening diameters. Figure 4.12 shows the deviation of the measured hair diameters (at base and bulge) from the designed values. The deviation for the case of base diameters is thought to be due to process-related issues (*i.e.* due to the over-etching of the aluminum pattern). The reason for the bulged diameter observed at lengths (<100 μm) close to the base is unclear. However, the effect of such a bulge on the moment of inertia is small and its contribution to the drag-torque reception can be considered insignificant.

Figure 4.14 shows how much the hair diameter at the bulge increases for a given opening diameter, irrespective of exposure times. The measured values represent the average ratio (averaged over exposure times) of hair base diameter to their corresponding opening diameters. This ratio is observed to be decreasing with opening diameter.

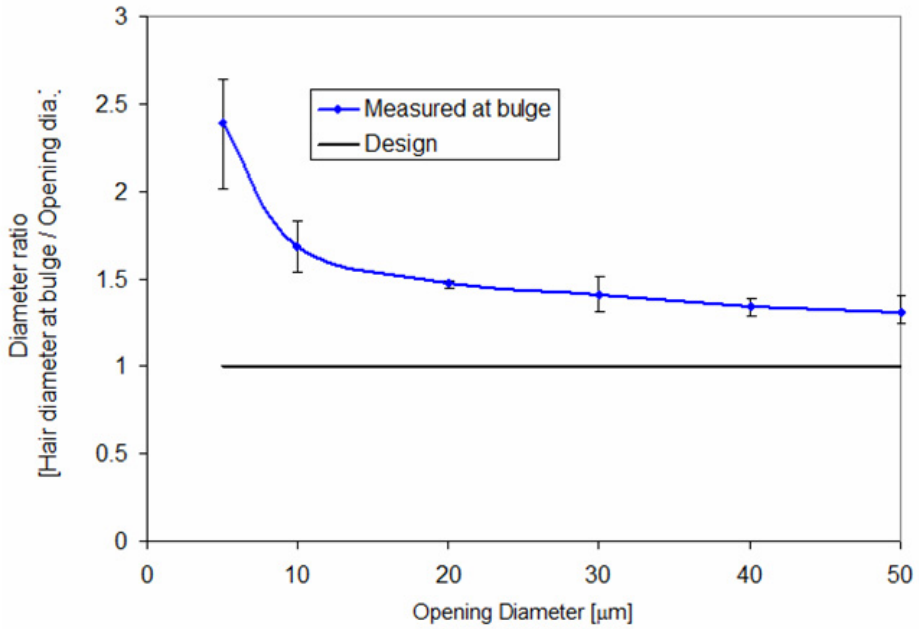

Figure 4.14 *Trend of the diameter ratio (i.e. the ratio of the hair base diameter to the given opening diameter and averaged over different exposure times).*

The decrease in the diameter is not linear but rather as a 3rd order polynomial function with the distance from the base. Figure 4.15 shows the spread of normalized diameter against the normalized length fabricated from an opening diameter of 50 μm and compared with that of a 20 μm, both exposed at 250s. For fitting, the measurement at the bulge were not considered in order to observe the behavior qualitatively. The hairs from smaller opening diameters than 20 μm, did not show any significant differences between the base and top diameters and remained, more or less, in a cylindrical shape. Such cylindrical shape however is not helpful in reducing the moment of inertia and therefore, not favored.

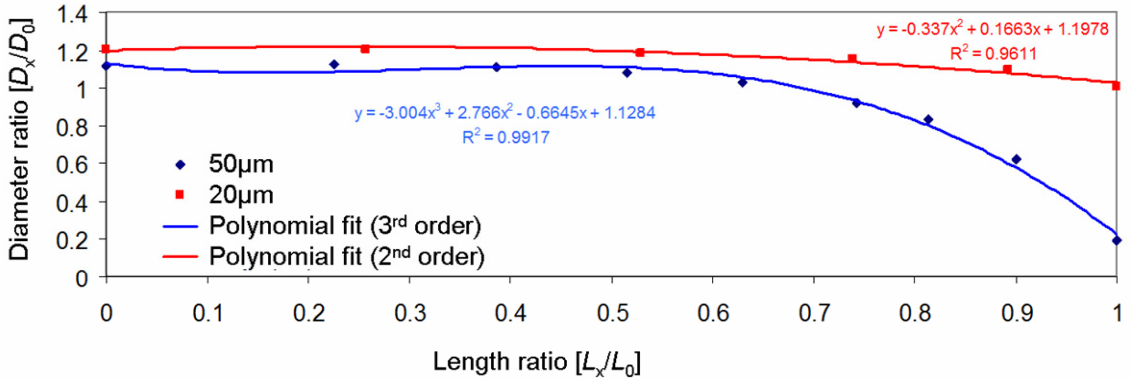

Figure 4.15 *Plot showing the fitted hair shape profile (excluding the shape at the bulge) for the hairs fabricated from 50 and 20 μm opening diameter of mask pattern. Here, L_0 and D_0 represent the total hair length and the hair diameter at the base respectively.*

Figure 4.13 shows the curling and tip-linking effects observed on the nature-like hairs. Capillary effects during spray-development could possibly be the source of the curling observed at the tips of shorter hairs and on closely-placed longer hairs. Such curled tips could

actually arrest the air flow and receive more drag-force. However, curled tips lead to substantially increased moment of inertia, which is not favored in our case. Not surprisingly, hairs serving for similar flow-sensing purpose are found in certain species of spiders (*Cupiennius salei*) and observed to have feathery or tilted tips, respectively [19].

4.7.2 Moment of inertia and drag-torque

The moment of inertia of the nature-like hairs can be calculated by assuming a simple shape consisting of two different conical frustums (figure 4.16) with one placed on top of the other. However, only for the hairs that were fabricated from a large mask openings (>= 20µm) this shape was used for calculation, while the rest assumed a single conical frustum shape. The parameters for calculating the moment of inertia were measured by optical microscope for each hair. Figure 4.16 shows the calculated moment of inertia of nature-like hairs of different lengths. The moment of inertia increases with the hair length and a fit shows that it is proportional to $L^{6.43}$. This is an exciting result as it is now possible to fabricate hairs of different lengths which are controlled at the design level (i.e. hair lengths are determined by means of the designed mask openings). This implies that future arrays of hair sensors could feature sensors sensitive to a wide range of flow frequencies (which will be feasible by means of featuring different hair lengths). Figure 4.16 also compares the nature-like hairs with the actual filiform hairs (fit from the data in [1]). Comparatively the nature-like a) hairs obey about the same trend, b) have two order of magnitude larger moment of inertia for given length and c) are fabricated from relative larger length on.

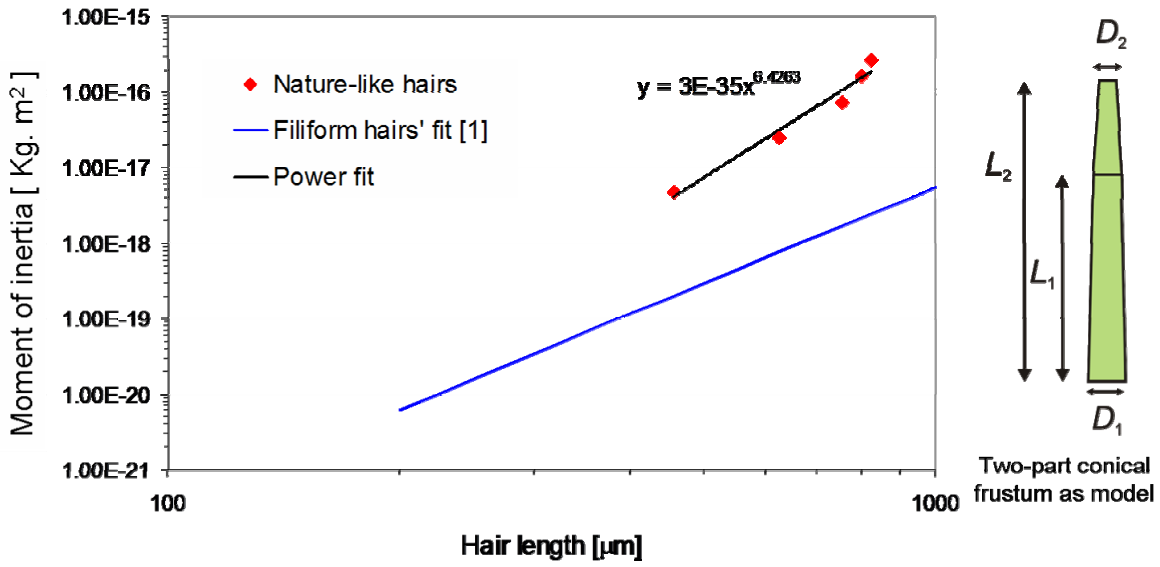

Figure 4.16 *Calculated moment of inertia of nature-like hairs for different lengths*

Calculation of drag-torque for the exact shape of the nature-like hairs is complex. Using the sensor model described in chapter 2, the drag-torque acting on the nature-like hairs can be approximately calculated and figure 4.17 shows the calculated normalized drag-torques at different frequencies for nature-like hairs depending on their length. As we know, the drag-torque depends strongly on hair length. It roughly increases with the cube of the hair length, if it is in the boundary layer and with the square of the hair length, when it sticks out

of the boundary layer. The drag-torque also depends on the hair diameter, but this dependence is weaker.

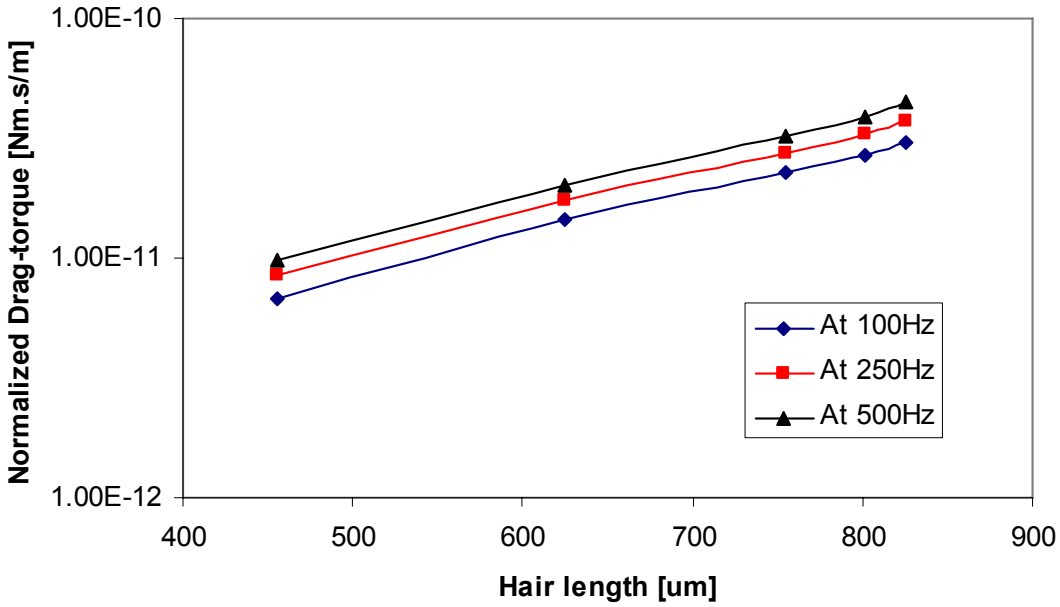

Figure 4.17 *Calculated drag-torque of nature-like hairs for different lengths and at different flow frequencies*

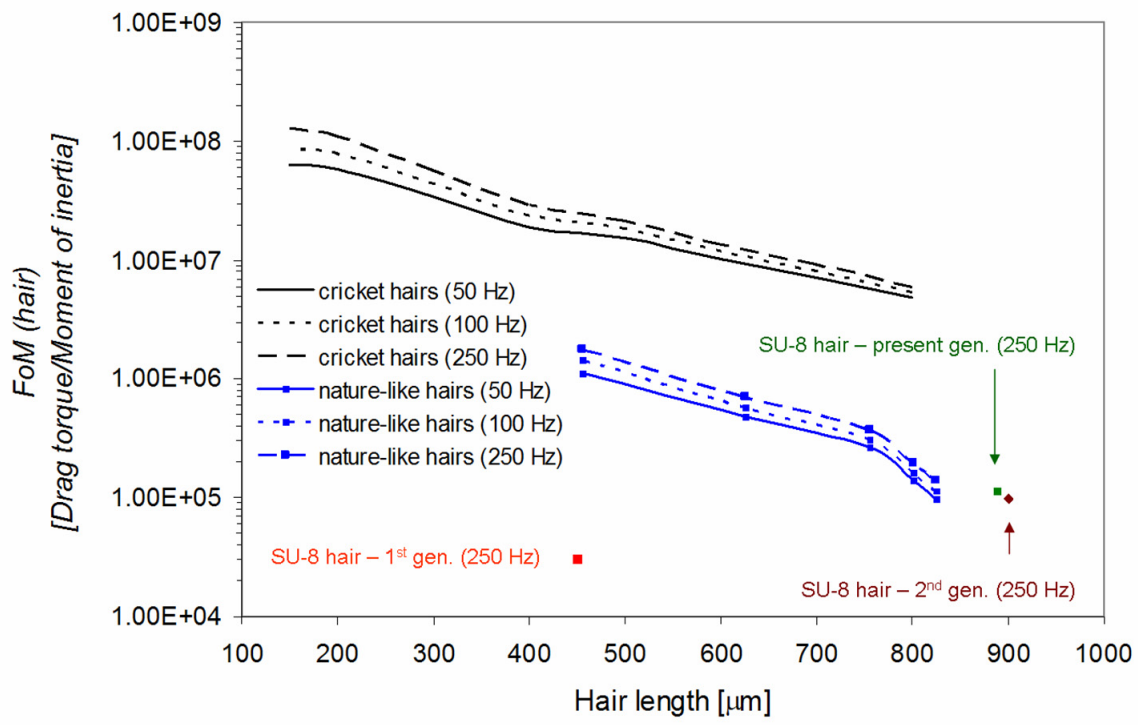

Figure 4.18 *Comparison of FoM of all artificial hair shapes and the actual filiform hairs of different lengths and at different flow frequencies.*

Figure 4.18 shows the comparison of $FoM_{(hair)}$ (defined in equation (4.1)) for all the artificial hair shapes with that of filiform hairs of crickets, for different flow frequencies. Filiform hairs show a better $FoM_{(hair)}$ compared to all of the artificial hairs so far. SU-8 hairs from the first generation [7] (length: ~450 μm and diameter: ~50 μm), second generation [9] (length: ~900 μm and diameter: 50 μm) and present generation hairs (with actual dimensions) [10] are compared with the nature-like SU-8 hairs. It is interesting to see that the nature-like hairs show a better *FoM* than the previous generation of artificial hairs.

When observing the trend of the $FoM_{(hair)}$ it is noted that it increases on decreasing hair-length. So one may wonder why not all hairs of e.g. crickets are rather short. Obviously one important aspect that has been held out of the equation is the threshold angular rotation, e.g. needed to trigger the neurons in cricket hair-sensors or to surpass the noise-floor in our artificial hair-sensors. For smaller hairs the ratio of T_d to J becomes larger but T_d still decreases increasingly requiring a softer suspension to accommodate the required rotation angles. Put in other words: as the hairs become smaller and smaller the amount of energy that can be extracted from the flow decreases, especially when the hairs are shorter than the boundary layer thickness, eventually leading to higher flow-velocity threshold values. This has e.g. been observed in crickets by Shimozawa and co-workers [20].

4.8. Conclusions and outlook

Nature-like SU-8 hairs are fabricated successfully using a bottom-side exposure method. By this technique it is possible to fabricate sensors featuring hairs of varying length, fabricated with a much simplified and single process flow. The shape of the hair resembles the actual filiform hairs of the crickets, when compared to the shape of the present SU-8 hair used on the sensor arrays.

The fabricated samples were analyzed to find the optimal exposure time and the effect of different design parameters of the aluminum pattern on the hair geometry. The exposure times chosen for the presented investigation seem to be rather insignificant in determining the hair length and the hair diameter. As intended, it is now possible to fabricate hairs of different lengths, which are determined at the design phase, by defining the opening diameter of the mask pattern.

The next challenge is to develop a new process scheme to integrate the nature-like SU-8 hairs into the existing sensor fabrication. The process flow for wafer-through etch-holes on the Silicon wafers for back-side exposure and the applicability of Aluminum as both capacitor electrode and hair mask should be tested and optimized.

4.9. References

[1] T. Shimozawa, T. Kumagai, Y. Baba, *"Structural and functional scaling of the cercal wind-receptor hairs in cricket"*, J. Comp. Physiol. A (1998) 183, pp. 171-186**.**

[2] J.A.C. Humphrey, R. Devarakonda, I. Iglesias, F.G. Barth, *"Dynamics of arthropod filiform hairs. I. Mathematical modeling of the hair and air motions"*, Philosophical Transactions: Biological Science (1993) 340, pp. 423-444.

[3] T. Shimozawa, M. Kanou, *"The aerodynamics and sensory physiology of range fractionation in the cercal filiform sensilla of the cricket Gryllus bimaculatus"*, J. Comp. Physiol. A (1984) 155, pp. 495-505.

[4] T. Shimozawa, T. Kumagai, Y. Baba, *"The shape of wind-receptor hairs of cricket and cockroach"*, J. Comp. Physiol. A (1998) 183, pp. 171-186.

[5] W. Gnatzy, *"Development of the Filiform hairs on the Cerci of Gryllus bimaculatus Deg. (Saltatoria, Gryllidae)"*, Cell Tiss. Res. (1978) 187, pp. 1-24.

[6] J.J. van Baar, M. Dijkstra, R.J. Wiegerink, T.S.J. Lammerink and G.J.M. Krijnen, "*Fabrication of arrays of artificial hairs for complex flow pattern recognition*", Proceedings of IEEE Sensors conference, Toronto, Canada, October 22-24, 2003.

[7] M. Dijkstra, J.J. van Baar, R J Wiegerink, T S J Lammerink, J H de Boer and G J M Krijnen, "*Artificial sensory hairs based on the flow sensitive receptor hairs of crickets*", J. Micromech. and Microeng. (2005) 15, pp. 132-138.

[8] S.S. Siripurapu, "*Cricket-inspired sensory hairs with capacitive motion detection*", Master thesis, University of Twente (2005).

[9] G. J. M. Krijnen, J. Floris, M.A. Dijkstra, T.S.J. Lammerink, and R.J. Wiegerink, "*Bio-mimetic micromechanical adaptive flow-sensor arrays*", Proc. of SPIE Europe Microtechnologies for the New Millennium 2007, 2-4 May 2007.

[10] C.M. Bruinink, R.K. Jaganatharaja, M.J. de Boer, E. Berenschot, M.L. Kolster, T.S.J. Lam-merink, R.J. Wiegerink and G.J.M. Krijnen, *"Advancements in technology and design of biomimetic flow-sensor arrays"*, Proc. IEEE Int. Conf. MEMS, 2008, pp. 152-155.

[11] P. Abgrall, V. Conedera, H. Camon, A-M. Gue and N-T. Nguyen, *"SU-8 as a structural material for labs-on-chips and microelectromechanical systems"*, Electrophoresis (2007) Vol. 28, pp. 4539-4551.

[12] E.H. Conradie and D.F. Moore, *"SU-8 thick photoresist processing as a functional material for MEMS applications"*, J. Micromech. Microeng. (2002) Vol. 12, pp. 368-374.

[13] M. Despont, H. Lorenz, N. Fahrni, J. Brugger, P. Renaud and P. Vettiger, *"High-aspect-ratio, ultrathick, negative-tone near-UV photoresist for MEMS applications"*, Proc. IEEE Int. Conf. MEMS, 1997, pp. 518-522.

[14] http://www.microchem.com/products/su_eight.htm

[15] Y.-J. Chuang, F.-G. Tseng and W.-K. Lin,*"Reduction of diffraction effect of UV exposure on SU-8 negative thick photoresist by air gap elimination"*, Microsystem Technologies.(2002) Vol. 8, pp.308-313

[16] H-C. Huang and C-C. Fu, *"Out-of-plane polymer hollow micro needle array integrated on a microfluidic chip"*, Proc. of IEEE Sensors, Irvine, USA, 2005, pp. 484-487.

[17] K. Kim, D.S. park, H.M. Lu,W. Che, K. Kim, J-B. Lee and C.H. Ahn, *"A tapered hollow metallic microneedle array using backside exposure of SU-8"*, J. Micromech. Microeng, (2004) Vol.14, pp. 597-603.

[18] H. Yu, K. Shibata, B. Li and X. Zhang, *"Fabrication of a hollow metallic microneedle array using scanning laser direct writing"*, Proc. of 9th Int. Conf. on Miniaturized systems for chemistry and life sciences, Boston, USA, Oct 9-13, 2005, pp. 187-189.

[19] F.G. Barth, U. Wastl, J.A.C. Humphrey, R. Devarakonda, *"Dynamics of arthropod filiform hairs. II. Mechanical properties of spider trichobothria (Cupiennius salei Keys.)"*, Philosophical Transactions: Biological Science (1993) 340, pp. 445-446.

[20] Shimozawa, T. et. al., "*Cricket wind receptors: thermal noise for the highest sensitivity known*", Ch. 10, Sensors and Sensing in Biology and Engineering, ed. Barth, Humphry and Secomb, Springer, Vienna, 2003, ISBN 3-211-83771-X.

5

Towards optimal springs

In a nutshell...

This chapter focuses on alternative ways to improve the mechanical sensitivity of the sensors, which is chiefly dependent on the torsional springs of the sensor. Realization of sensor springs of small torsional stiffness is intended. Small torsional stiffness for springs can be realized by (i) choosing an alternate structural material and (ii) modifying the cross-section of the spring appropriately. We present the results and the challenges faced while attempting both options. Our first investigation was to incorporate a well-known polymer, SU-8 as a potential option for replacing the silicon-rich nitride for the sensor membrane and torsional springs. On the other hand, a T-shaped cross-section for a spring, instead of a rectangular one, results in smaller torsional stiffnesses for the existing silicon-rich nitride springs. As a first step to achieve T-section springs, a novel process flow is developed using edge-lithography techniques to fabricate trenches with controllable widths.

5.1. Introduction

A figure of merit (*FoM*) defined for an optimal sensor performance (as introduced in chapter 2) indicate that our hair sensors need springs of small torsional stiffness to support their sensor membranes. Comparison of torsional stiffness values with the actual filiform hairs is inevitable and looking at the numbers, as discussed in previous chapters, it clearly

explains why this parameter needs special attention. Nature uses a range of tissues, with varying properties optimized for their specific functions, which are difficult to be matched by artificial counterparts. However, merely reducing the torsional stiffness is not the motivation, for doing it could seriously impede the robustness of the sensor itself and thus, its usability. Tuning the torsional stiffness, while putting emphasis on the overall stability of the sensor, is the core motivation to search for new approaches in making the sensor arrays. New design rules are set for realizing optimal springs for the sensors, which point out at two possible options: (i) an alternate structural material and (ii) modified cross-section for the springs. This chapter presents the results from our attempts on both options and, hence, is presented in two separate sections.

For the first option of choosing an alternate structural material, a negative-tone photoresist [1], SU-8, was chosen for fabricating the sensor membranes and springs. SU-8 is compatible with most MEMS technologies [2-5] and our experience [6,7] in working with it (for making sensory hairs) offered a good starting point. This apparently promising choice of a new sensor material asks for a complete rebuild of the fabrication flow. To avoid major risks it was decided to first perform a test run of the fabrication of passive sensor structures (without functional electrodes). The presented results highlight numerous technological challenges, related to the material properties of SU-8. The technological challenges faced, eventually outweighed the promised advantages of the softer springs for the artificial hair sensors.

The other intended design option was to modify the cross-section of the existing silicon-rich nitride (Si(R)N) springs. Retaining silicon-rich nitride as a sensor material assures the standardized low-stress process and hence, the quality of the sensor parts. Considering several possible cross-sections, which are quite compatible to our sensor fabrication, a T-shaped section for the spring offers the favorable design improvements. A simple analysis is made to identify the critical design parameter in a T-section spring and its impact is studied. A T-section spring is feasible by first fabricating a deep trench and subsequently filling it up with thin film layers with subsequent patterning of those layers. Hence, fabrication of simple and controllable-width trenches is the first step in realizing sensors with T-section springs. The results from a novel process flow are presented and some of the challenges faced are discussed in detail.

5.2. Optimal sensor springs

For the present generation of sensors, silicon-rich nitride is the basic structural material that is patterned as the sensor membrane and springs. Deposition of low-stress nitride results in appreciably near-flat membranes while its material properties, such as its shear modulus, cause the torsional springs to be rigid. The torsional stiffness of silicon-rich nitride springs (see chapter 3) were 2-orders of magnitude higher than that of a cricket hair sensor with comparable hair-length (~1 mm long) [8]. While it is possible to fabricate more compliant springs using nitride, as a consequence of it, the robustness of the sensors will be negatively affected and the sensor stability will become problematic. These unwanted side effects of torsional springs have to be kept in mind, while looking for alternative technologies or materials. A design approach is required for optimal spring design that balances flexibility and overall stability of the sensors.

5.2.1 Design rules

Although the hair sensors are primarily designed to operate in the torsional mode (i.e. the sensor membrane rotational axis is along the springs themselves), the membranes have several other undesired modes of deflection as well. As the figure of merit *(FoM)* (chapter 2) points towards the direction of reducing the torsional stiffness S of the system, doing so will also implicitly affect the sensor movements in the undesired modes (for instance, vertical movement of the sensor membrane). Henceforth, in the design analysis of the springs, it is essential that the springs be designed to deal safely with the undesired effects.

The torsional stiffness of the sensor springs is given as:

$$S = \frac{2 \cdot G_s \cdot I_p}{L_s} \tag{5.1}$$

whereas the vertical stiffness of the sensor springs is:

$$K = \frac{2 \cdot E_s \cdot I_s}{L_s^3} \tag{5.2}$$

where E_s is the Youngs' modulus of silicon rich nitride (=310 GPa) and I_s the area moment of inertia for bending in the vertical direction.

For the better sensor performance, we need small torsional stiffness S. In order to achieve this it is possible to design sensors with large spring length L_s. On the other hand, longer springs will weaken the vertical stiffness. As a consequence (1) the weaker vertical springs can pose serious problems with membrane stiction and pull-in (due to the voltages used for the capacitive read-out of the sensor arrays) and (2) the resonance of the vertical mode can interfere with the torsional mode causing undesired mode-coupling effects. Thus, for optimal performance, designs should provide (i) small torsional stiffness S and (ii) high stiffness K (and thus high (K/S) ratio).

Optimal spring design

Let us assume a desired (small) torsional stiffness, S_0. To achieve this, the required length of the spring is given by:

$$L_0 = \frac{I_p}{S_0} \cdot \frac{E_s}{2(1+\upsilon)} \tag{5.3}$$

Substituting equation (5.3) for the spring length L_s in the equation of vertical stiffness, i.e. equation (5.2), we get the actual stiffness ratio:

$$\frac{K}{S_0} = 8 \cdot \frac{S_0^2}{E_s^2} \cdot \frac{I_s}{I_p^3} \cdot (1+\upsilon)^3 \tag{5.4}$$

Equation (5.4) shows that in order to obtain reduced torsional stiffness and at the same time, a high ratio of vertical-to-torsional stiffness, compared to the existing silicon-rich nitride springs, there are two consistent choices:

(i) by materials:
Choosing low-Youngs' modulus E_s materials for springs allows for shorter spring lengths (hence, increasing the vertical stiffness at given S_0), or

(ii) by design:
Modifying the spring cross-sections, leading to a smaller polar moment of inertia I_p. while retaining a as large as possible areal moment I_s.

5.3. Optimal springs I: Soft springs

The ideal candidate to replace silicon-rich nitride as spring material is SU-8. A detailed section on SU-8 and its processing is presented in chapter 4. The Youngs' modulus of SU-8 is ~4 GPa [1] which is approximately 80 times smaller than that of silicon rich nitride implying that the possible gain in S_0/K ratio good be as high as 6400. Additionally, using SU-8 as springs and membranes provides good adhesion with the SU-8 hair due to the homogeneity in their material properties. As said before, SU-8 is a negative-tone photoresist compatible with microfabrication technologies, which is an added advantage. However, the residual stress of SU-8 layers [1,9] is also seen as a possible downside of this approach. Hence, the effect of residual stress on the quality of potential SU-8 sensor membranes is an interesting subject of investigation.

5.3.1 Design

In order to model the effect of replacing the silicon rich nitride with SU-8, a beam of rectangular section with width and thickness as 10 μm and 1 μm, respectively, is considered. The torsional stiffness S and the vertical stiffness K for a wide range of beam length L are calculated (see figure 5.1). To appreciate the advantage of this approach, let us assume a target value for the torsional stiffness as $1 \bullet 10^{-9}$ N.m/rad. (dashed line). To obtain this torsional stiffness with SU8, beams should have a length of 10 μm. For this beam length, the corresponding vertical stiffness is given as 20 N/m (from the figure). Compared to silicon-rich nitride beams of similar cross-section this ratio would be approximately $\sim(80)^2$ times better (i.e. improvement is proportional to square of the ratio of Young's modulus of silicon-rich nitride and SU-8, as shown in equation (5.4)).

Discussion

The first approach in terms of achieving optimal springs is to use the low-Youngs' modulus materials like SU-8 (80 times smaller). This approach intends, while resuming a rectangular cross-section, to shorten the spring length and take advantage of realizing relatively robust and compliant springs, compared to the basic approach. As a practical example illustrating the significance of this new approach, it was shown that for a target value of the torsional stiffness of $1 \cdot 10^{-9}$ [Nm/rad] the SU-8 springs vertical stiffness are expected to be 20 N/m, approximately 80 times higher compared to the existing silicon-rich nitride springs. However, these very welcome improvements come at the cost of changes in the fabrication process and new challenges with respect to SU-8 processing; SU-8 has been associated with stress and stress-gradients in various publications [10,11] and the prospect to

have this in the most critical parts of the sensors is somewhat worrying. Nevertheless, given the prospective improvement it was decided to further investigate SU-8 as spring and membrane material.

5.3.2 Fabrication and results

A simple fabrication scheme is devised to verify the credibility of SU-8, as a potential structural material for the sensors. The motivation is to fabricate proof-of-concept SU-8 membranes and springs with a long SU-8 hair at the center. For this initial step the integration of electrode layers on the membranes is omitted from the process flow and shifted to possible later test runs.

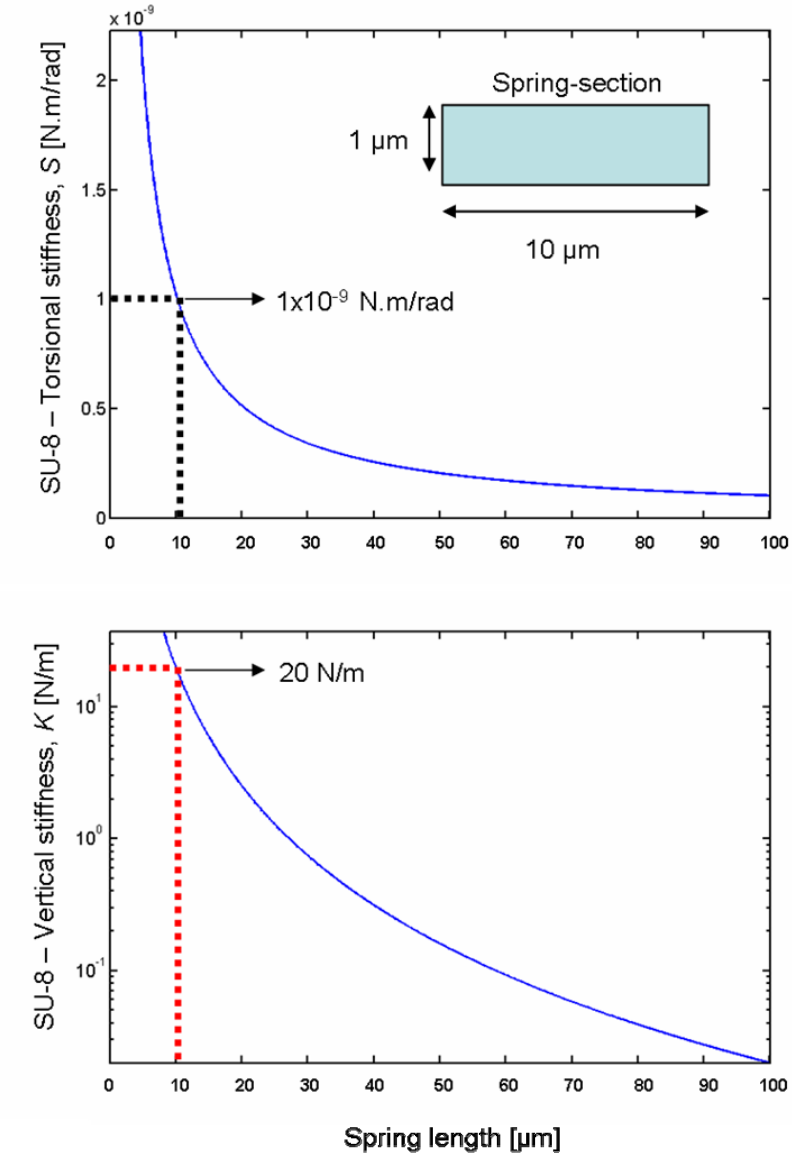

Figure 5.1 *SU-8 beams of rectangular cross-section: Torsional and vertical stiffnesses corresponding to different beam lengths. The beam width and thickness are 10 µm and 1µm respectively. For a torsional stiffness of $1 \cdot 10^{-9}$ N.m/rad, the corresponding vertical stiffness is 20 N/m (which is about 80 times higher, when compared to beams made of silicon rich nitride).*

The focus was laid on: (i) the quality of the SU-8 membranes (i.e. SU-8 process and its effect on intrinsic residual stress), (ii) compatibility issues between the layers (i.e. adhesion) and (iii) the process compatibility (i.e. effects of introducing SU-8 as structural material, while retaining several other process steps.)

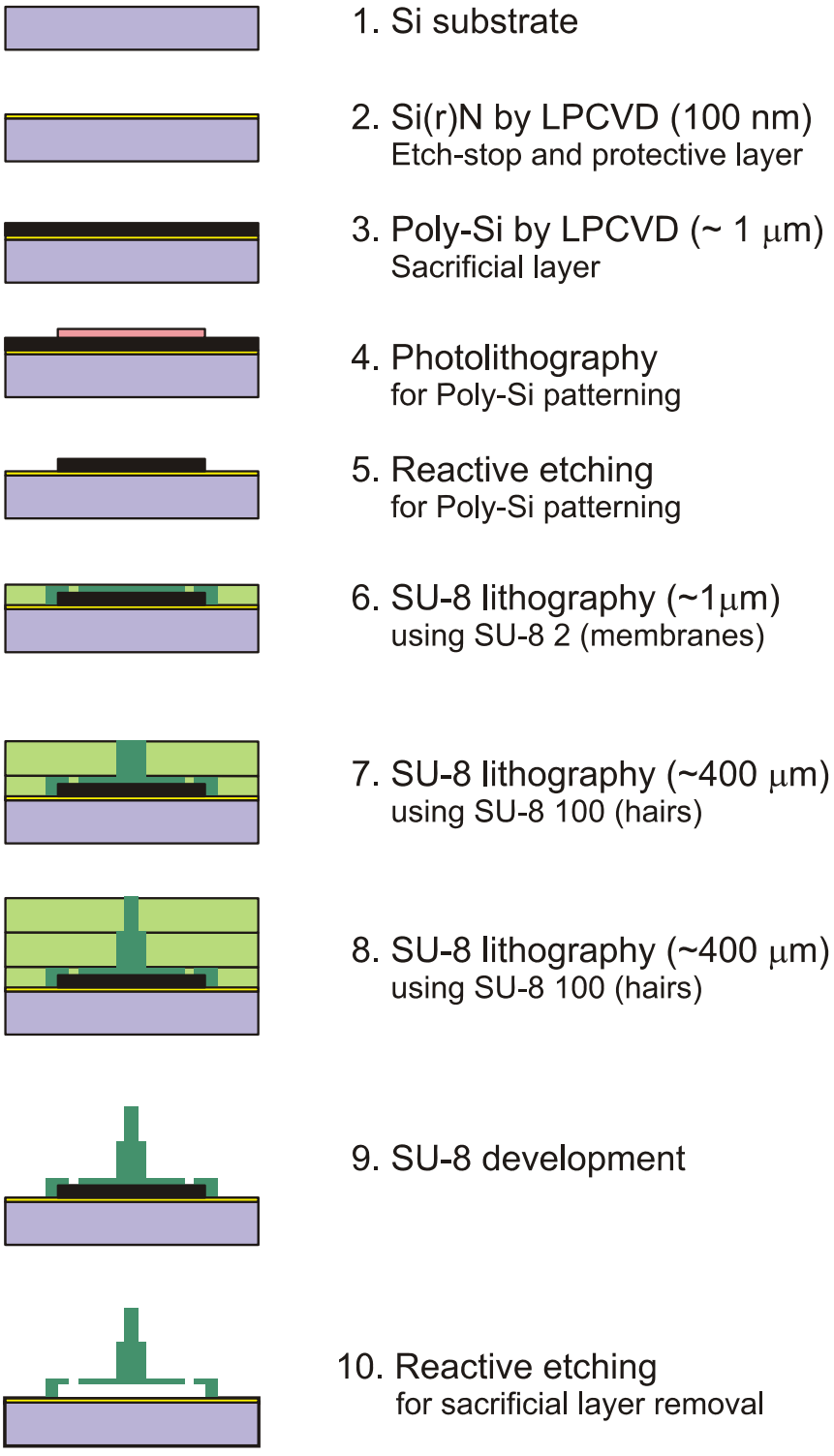

Figure 5.2 *Fabrication flow for proof-of-concept SU-8 test structures*

Fabrication process

The proof-of-concept process flow for fabrication of SU-8 membranes is shown in figure 5.2. A 100 nm thick layer of Silicon-rich nitride is deposited using a low-stress LPCVD process. This layer will act as the etch-stop layer during the final sacrificial etching step. Several options exist for the materials that can be used as sacrificial layer in combination with SU-8 [12], however, poly-silicon is retained for this process. Following it, a ~1 µm thick layer of poly-silicon is deposited, which will serve as the sacrificial layer. The poly-silicon layer is then patterned by a standard photolithography step followed by a reactive ion etching process. A different type of commercially available SU-8 type (SU-8 2), specially made for thin layers, is used for the sensor membranes. This new SU-8 is characterized with respect to the layer thickness dependence on the spin speed (see figure 5.3).

A ~1.5 µm layer of SU-8 (type: SU-8 2, Microchem [1]) is spun (at 3000 rpm) and exposed to form sensor membranes and springs using the standard photolithography steps. Following it, two subsequent layers of ~400 µm thick SU-8 (type: SU-8 100, Microchem [1]) are spun and exposed to pattern the long hair structures. The wafers are then developed in RER 600 solution and the three previously exposed layers of SU-8 are developed simultaneously. The wafers are finally subjected to reactive-ion etching to remove the poly-silicon sacrificial layer, leaving the sensor membranes suspended. A more detailed description of the process flow steps is given in Appendix C. Figure 5.4 shows SEM images of the realized SU-8 test structures.

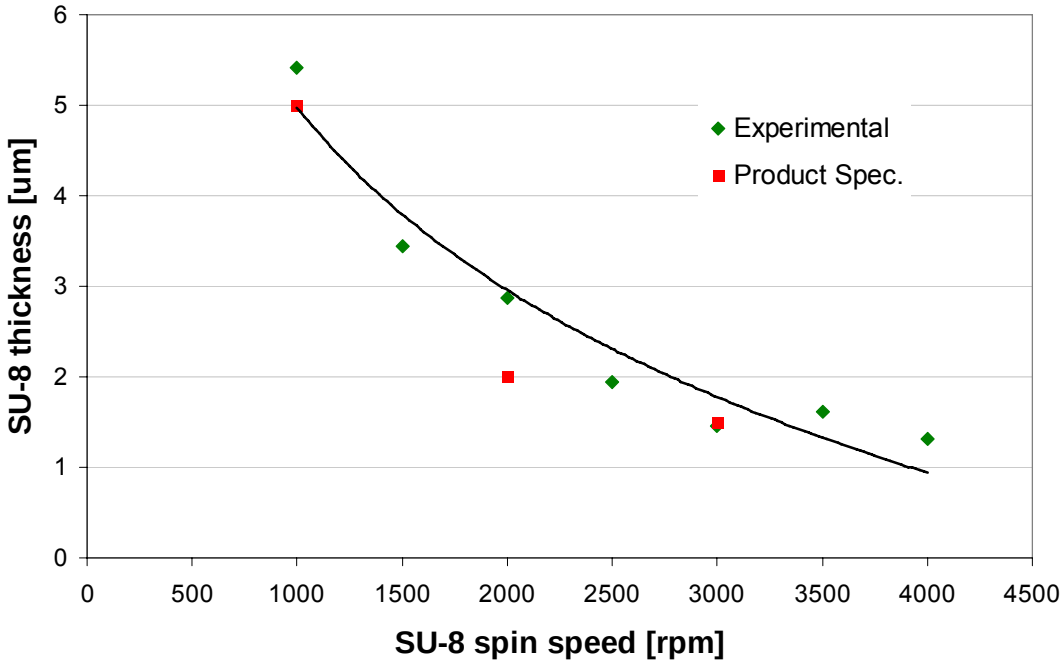

Figure 5.3 *Characterization of SU-8 2 layer thickness as a function of spin speed. A spin speed of 3000 rpm is chosen for the test structures, which approximately results in a layer thickness of 1.5 µm.*

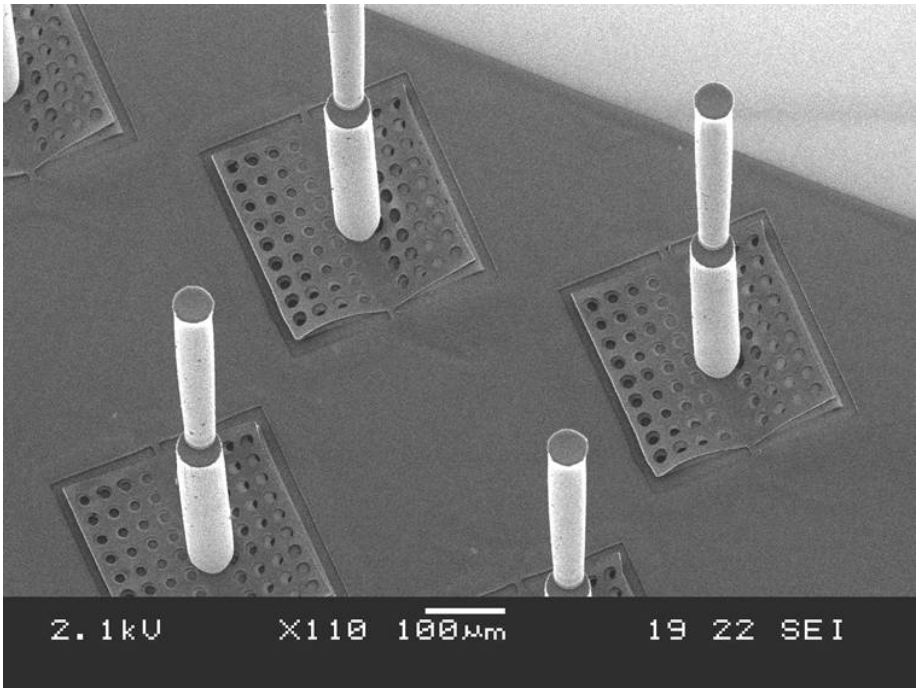

Figure 5.4 *SEM image of fabricated SU-8 test structures*

Results and discussion

The realized SU-8 test membranes were inspected using an optical microscope. Since the SU-8 layer is transparent, it turned out not to be possible to study the membranes under a white light interference microscope (Polytec [13]). Additional coating by a reflective material (metal), for the purpose of subjecting them to white light interference microscopy, was deemed unsuitable because of the added risk of modification of the actual quality of the membranes. Hence, a standard optical microscope fitted with a rough height measurement unit (based on focusing) was used for obtaining some idea about the quality of the membranes. The resolution, however, was limited to ±1 µm. Selected membranes (first observed via optical microscope) were also inspected by SEM imaging in order to get more accurate information on the membrane quality. From several repeated fabrication runs, the following challenges were found:

a. ***Intrinsic residual stress and membrane curvature***

All the optically inspected SU-8 membranes suffered from undesirable large membrane curvature (several µm). Most membranes showed ~11µm upward curvature, at the corners. Such a curvature was also observed when inspected by SEM (see figure 5.5). As discussed in chapter 2, the flatness of the membranes is very crucial for the sensitivity of the sensors. This undesirable curvature of the SU-8 membranes is the first and foremost challenge to be faced and it is primarily due to intrinsic residual stress gradients present in the SU-8 layer. There are several factors that influence it. One important contribution happens during the soft (pre-exposure) and post-exposure baking steps [1]. Slow ramping, in terms of small temperature steps, up to the recommended baking temperatures was suggested [14]. Several repeat experiments were performed trying out these different settings of baking parameters but this yielded no notable improvements in the quality.

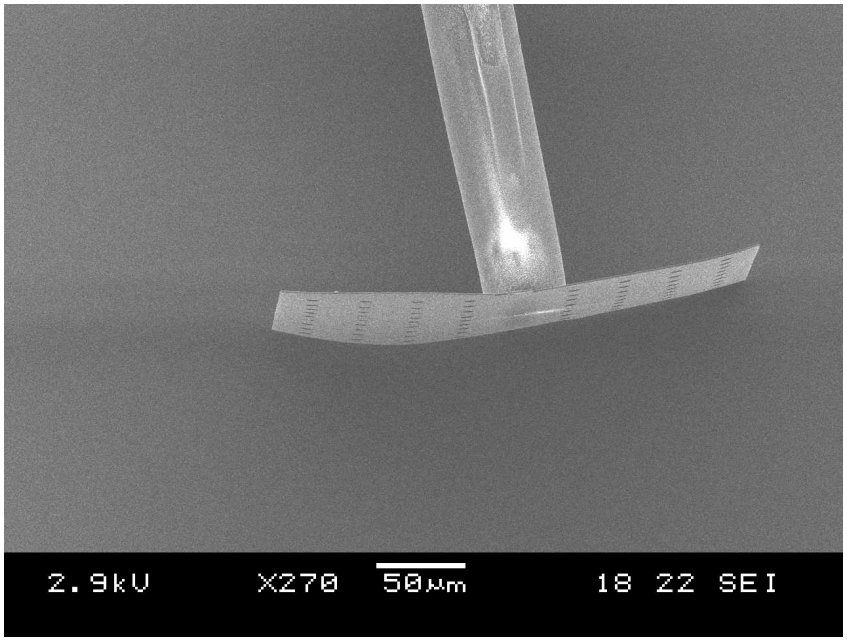

Figure 5.5 *Torn out SU-8 membrane and hair structure as imaged by SEM.*

b. *Under-exposure effects*

Figure 5.6 shows commonly observed results of an under-exposed SU-8 layer. Cracking of the SU-8 layer is seen at samples that have been exposed for (too) short times resulting in poor adhesion with the substrate. The recommended exposure times depend on the type of substrate [1]. Longer exposure times improve adhesion but with a loss of resolution. It is suggested that the right exposure time for the desired structure is derived by processing test wafers. For the presented thin layers, the exposure time was set at 12 s.

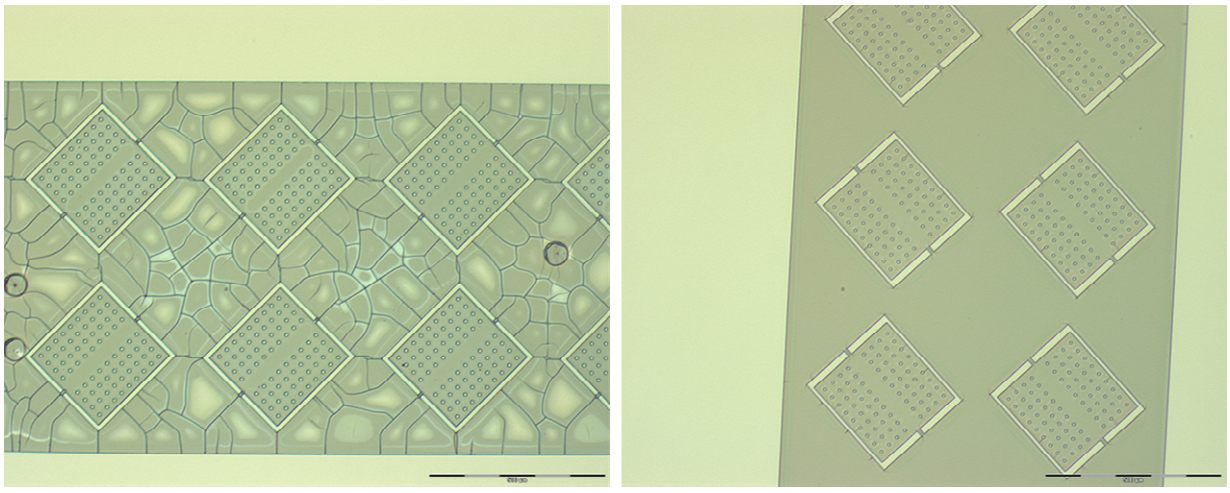

Figure 5.6 *Cracking of SU-8 layers when under-exposed. Test experiments done at different exposure times clearly show the impact and improvements in the quality of the membranes.*

c. *Adhesion to substrate*

Figure 5.7 shows the peeling-off of SU-8 layers after the development step. Such an effect was observed on more than 40% of the wafer surface. This peel-off effect could be associated with poor adhesion to the substrate (which in this case, is the silicon-rich nitride layer on top of the silicon substrate), possibly in combination with the stress in the SU-layers. After a technical discussion [13], a special adhesion promoter (Omnicoat, Microchem) was recommended and processing was done using the adhesion promoter. Alas, the test results did not show any improvement with the application of adhesion promoter. Upon further technical discussions [14,15] repeated experiments revealed that the age of the underlying silicon-rich nitride layer influences the adhesion of SU-8 layer: SU-8 processing done within 1 or 2 days after nitride processing showed good adhesion, even without an additional adhesion promoter.

d. *Contamination issues*

During initial processing experiments, strange bubbles were observed all-over the wafers (see figure 5.8), which were found to occur after the development step of SU-8. This effect was also observed in a repeat experiment. Contamination was suspected (as several particle-like substances were observed on the substrate) as a possible cause for this problem and another repeat of the process, now with a fresh sample of SU-8 solution, was performed. The test results did not show any improvement with the bubbles. This led to the questioning of the shelf-life of the current stock of SU-8 [15]. The problem was completely solved when the experiments were yet again repeated with a newly-ordered fresh solution of SU-8 (type: SU-8 2).

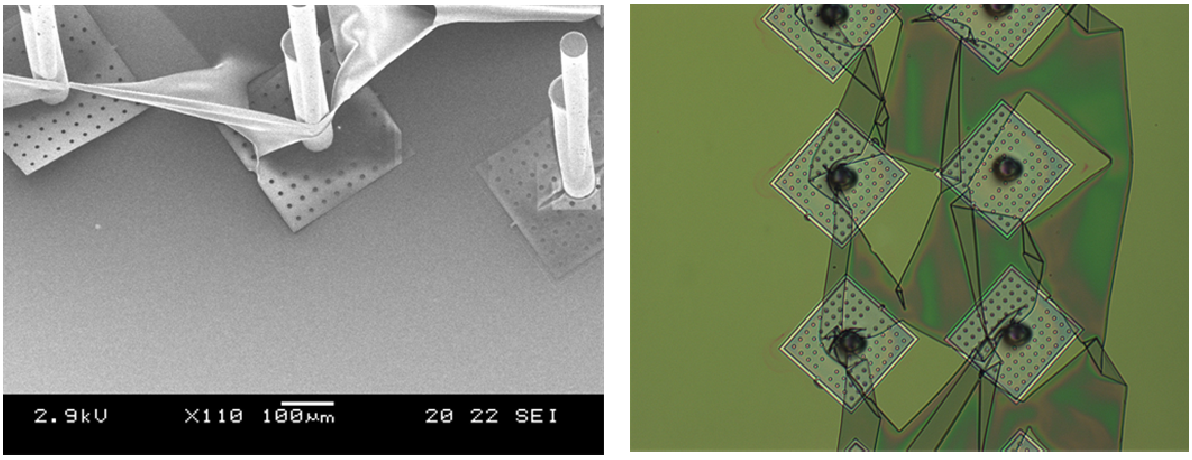

Figure 5.7 *Peeling-off of SU-8 layers due to poor adhesion to the underlying silicon-rich nitride layer.*

e. Minor issues

Other than the above said challenges, there were minor cases of membrane folding (possibly due to capillary effects during/after development) and alignment issues of SU-8 layers. Alignment issues could be solved by using back-side alignment marks, instead of top side marks, as used in the present work.

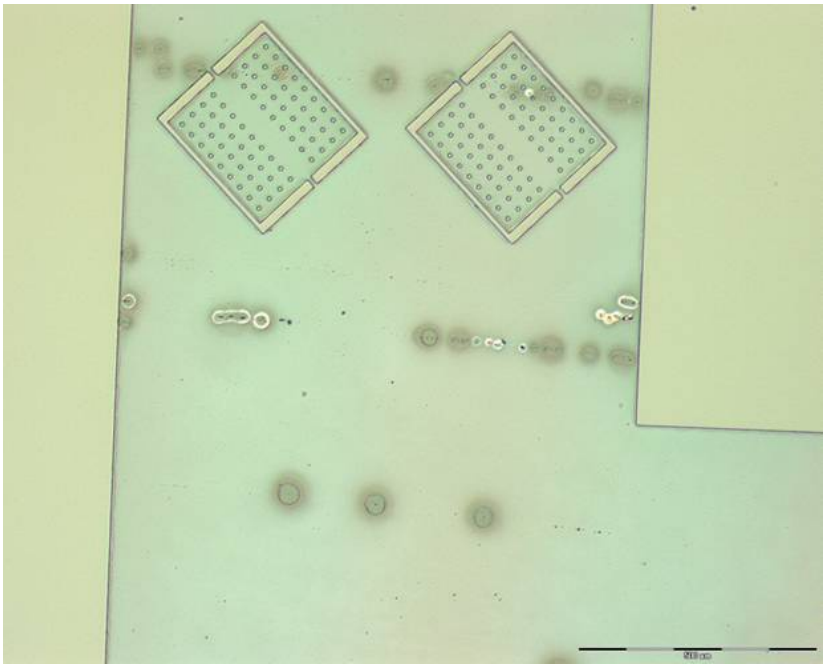

Figure 6.8 *Presence of undesired bubbles all over the SU-8 surface which was later found to be contamination due to long storage time of SU-8 stocks. A new and fresh sample of SU-8 did not have any problems related to such contaminations.*

5.3.3 Conclusions

Obviously, the chosen approach of using SU-8 as an alternative material for sensor membrane consumed a lot of processing time, while yielding less than expected quality of fabrication results. Repeatedly observed inconsistency in processing of thin layers of SU-8 is seen as a major drawback to this design approach for realizing optimal springs for the hair sensors. However, the idea of using soft polymers as a structural material for the sensor membranes is still seen as a potential option. A range of alternate polymers compatible with standard microfabrication techniques exist, for instance, PMMA [16], PDMS [17] or Parylene [18]. Nevertheless, each of these options pose large investments in fabrication process development and were deemed outside the scope of this work.

5.4. Optimal springs II: T-section springs

This section is dedicated to the design and novel fabrication of trenches for the T-section springs. Conventional lithography techniques, (available at the cleanroom), have a lowest feature size limit of 2 μm while the intended trench widths range substantially below that limit. On the other hand, there exists a renowned technique called edge-lithography [19-23], which can be extended to make the desired trenches. A novel process flow is devised using this edge-lithography. Use of repeated wet chemical etching steps in this process flow, ideally assures the uniformity of trench widths across the wafer (as compared to dry, physical etching). The results from the process flow are presented and some of the challenges faced are discussed in detail.

5.4.1 Design of T-section springs

Optimal springs are intended to have smaller torsional stiffness *S* and higher vertical to torsional stiffness ratio (*K/S*). In section 5.2, the expressions for vertical stiffness *K* and torsional stiffness *S* for the sensor springs were given. The motivation is that the stiffness ratio of any new design should be higher than the stiffness ratio corresponding to the current spring design (i.e. rectangular-section springs made of silicon-rich nitride). For simplicity, we will assume the springs are made of the same material and comparing the ratios of any new spring design with the present one is given as:

$$\left(\frac{K}{S}\right)_{\text{new}} = \frac{\left(\frac{I_s}{I_p}\cdot\frac{1}{L_s^2}\right)_{\text{new}}}{\left(\frac{I_s}{I_p}\cdot\frac{1}{L_s^2}\right)_{\text{rect}}}\cdot\left(\frac{K}{S}\right)_{\text{rect}} \tag{5.5}$$

To appreciate the improvements, let us assume for the current spring design, the spring section has dimensions *w* and *t* (where $w=n\cdot t$). The ratio of moment of inertia for a rectangular section is then given as:

$$\left(\frac{I_s}{I_p}\right)_{\text{rect}} \approx \frac{I_{xx}}{I_{xx}+I_{yy}} \approx \frac{\frac{1}{12}nt^4}{\frac{1}{12}t^4\left(n^3+n\right)} \approx \frac{1}{n^2+1} \tag{5.6}$$

For the new design, we again assume a rectangular section but with smaller width, *w* and larger thickness, *t*, where $t=n\cdot w$. For the new design, the ratio becomes:

$$\left(\frac{I_s}{I_p}\right)_{\text{new}} \approx \frac{I_{xx}}{I_{xx}+I_{yy}} \approx \frac{\frac{1}{12}n^3w^4}{\frac{1}{12}w^4\left(n^3+n\right)} \approx \frac{n^2}{n^2+1} \tag{5.7}$$

For our case, the value for *n* is ~8 and substituting it, equation (5.5) becomes:

$$\left(\frac{K}{S}\right)_{\text{new}} \approx n^2\cdot\frac{L_{rect}^2}{L_{new}^2}\cdot\left(\frac{K}{S}\right)_{rect} \tag{5.8}$$

This shows that by simply rotating the springs over 90 degrees we will get an improvement of a factor of n^2. However, for any desired value of torsional stiffness, the new design will show an additional improvement, if the spring lengths are such that $L_{\text{new}} < L_{\text{rect}}$. Choosing a modified spring-section, it is possible to realize springs that are more compliant in the torsional mode while being stiffer in the vertical mode. Care should be taken that the springs also serve as pathways on which the electrodes pass on to the sensor membranes and

there exists a certain width limitation (minimum about ~2 µm) by fabrication technology for the electrode layers to guarantee functionality. A T-shaped cross-section for the springs of the sensor is a favorable design for this case. Figure 5.9 shows an artistic impression of the T-section springs.

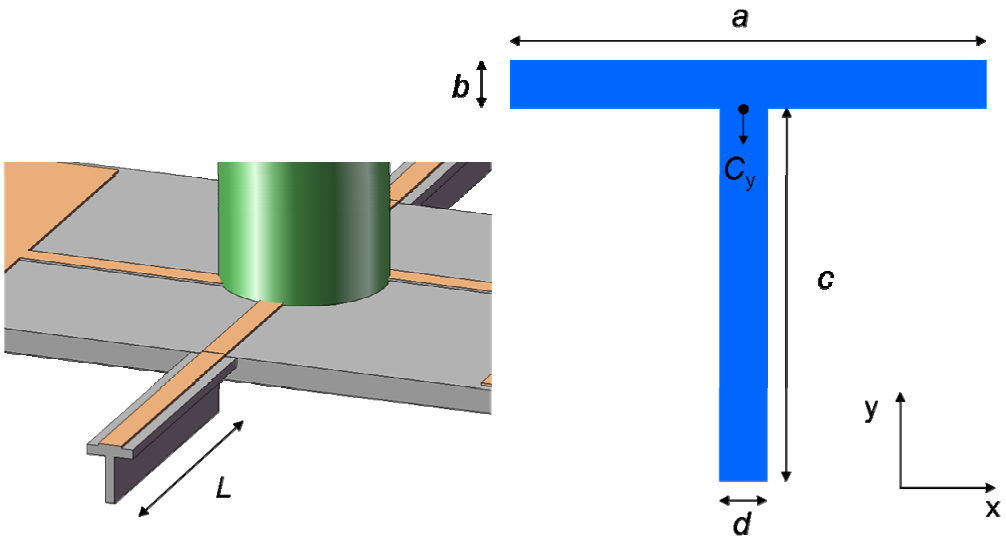

Figure 5.9 *Artistic impression of a sensor membrane supported by T-section springs.*

Design Parameter	Value (for analysis)
Flange width, *a*	10 µm
Flange thickness, *b*	250 nm
Web depth, *c*	5 µm
Web width, *d*	400 nm
Spring length, *L*	30 µm

Table 5.1 *List of standard values for design analysis*

The design parameters that determine the mechanics of such a section are flange width *a*, flange thickness *b*, web depth *c* and web width *d*. The length of a T-section spring is denoted *L*. It is necessary to understand the effect of each of these parameters, on the required design conditions. For our case, the primary design goals are: (i) reduced torsional stiffness and (ii) higher ratio of vertical-to-torsional stiffness compared to the existing designs. As a preliminary design analysis, we chose a set of standard design values (respecting technological feasibilities) to each of the five parameters. Table 5.1 shows those standard values. To analyze the importance of each of these parameters, we varied them one by one within a relevant range, while keeping the others (as listed in the table) constant.

The torsional stiffness of the spring (the combination of one T-beam on either side of the membranes) is given as:

$$S = \frac{2 \cdot G_{\mathrm{s}} \cdot I_{\mathrm{p}}}{L} \tag{5.9}$$

where G_{s} is the shear modulus of Si(R)N and I_{p} is the polar moment of inertia of the spring. The polar moment of inertia for a T-section is dependent on the geometrical parameters of the T-section. To calculate the polar moment of inertia I_{p}, we first need to calculate the y-coordinate of the centroid of such a section. The y-coordinate of the centroid is given as [24]:

$$C_{\mathrm{y}} = \frac{a \cdot b \cdot \left(\frac{b}{2}\right) + c \cdot d \cdot \left(\frac{-c}{2}\right)}{a \cdot b + c \cdot d} \tag{5.10}$$

The polar moment of inertia of the T-section is given as [6]:

$$I_{\mathrm{p}} = I_{\mathrm{xx}} + I_{\mathrm{yy}} \tag{5.11}$$

where:

$$I_{\mathrm{xx}} = \frac{1}{12}\left(a \cdot b^3 + d \cdot c^3\right) + a \cdot b \cdot \left(\frac{b}{2} + \left|C_{\mathrm{y}}\right|\right)^2 + c \cdot d \cdot \left(\frac{c}{2} - \left|C_{\mathrm{y}}\right|\right)^2 \tag{5.12}$$

and

$$I_{\mathrm{yy}} = \frac{1}{12}\left(b \cdot a^3 + c \cdot d^3\right) \tag{5.13}$$

The above method is only an estimation of the torsional stiffness. The accurate estimation of the polar moment of inertia for a T-section can be found in Roark's formula [25], which is quite complex and given as:

$$I_{\mathrm{p,\,Roark}} = \kappa_1 + \kappa_2 + \alpha \cdot D^4 \tag{5.14}$$

where:

$$\kappa_1 = a \cdot b^3 \cdot \left[\frac{1}{3} - 0.21 \cdot \frac{b}{a} \cdot \left(1 - \frac{b^4}{12 \cdot a^4}\right)\right] \tag{5.15}$$

$$\kappa_2 = c \cdot d^3 \cdot \left[\frac{1}{3} - 0.105 \cdot \frac{d}{c} \cdot \left(1 - \frac{d^4}{192 \cdot c^4} \right) \right] \tag{5.16}$$

$$\alpha = \frac{t}{t_1} \cdot \left(0.15 + 0.10 \cdot \frac{r}{b} \right) \tag{5.17}$$

$$D = \frac{(b+r)^2 + r \cdot d + \frac{d^2}{4}}{2 \cdot r + b} \tag{5.18}$$

Here, the variables are given as t=min(b,d), t_1=max(b,d) and r=0.1b. We used the Roark's expression for the rest of the analysis. The vertical stiffness of the T-section spring is given as [24]:

$$K = \frac{24 \cdot E_s \cdot I_{xx}}{L^3} \tag{5.19}$$

where E_s is the Youngs' modulus of Si(r)N and I_{xx} is given by eq. (5.12). Using all the above listed formulae, the impact of each geometrical parameter in the T-section is individually analyzed. The ratio of vertical stiffness to the torsional stiffness (K/S) should be higher to prevent any undesired mode coupling during the dynamic response of the sensors. Fitting in the right values, it can be proved theoretically that a T-section could be 1000 times stiffer in the vertical direction than a rectangular section, for a specific value of the torsional stiffness. Note that this is possible due to the fact that the vertical stiffness scales inversely proportional to the spring length cubed.

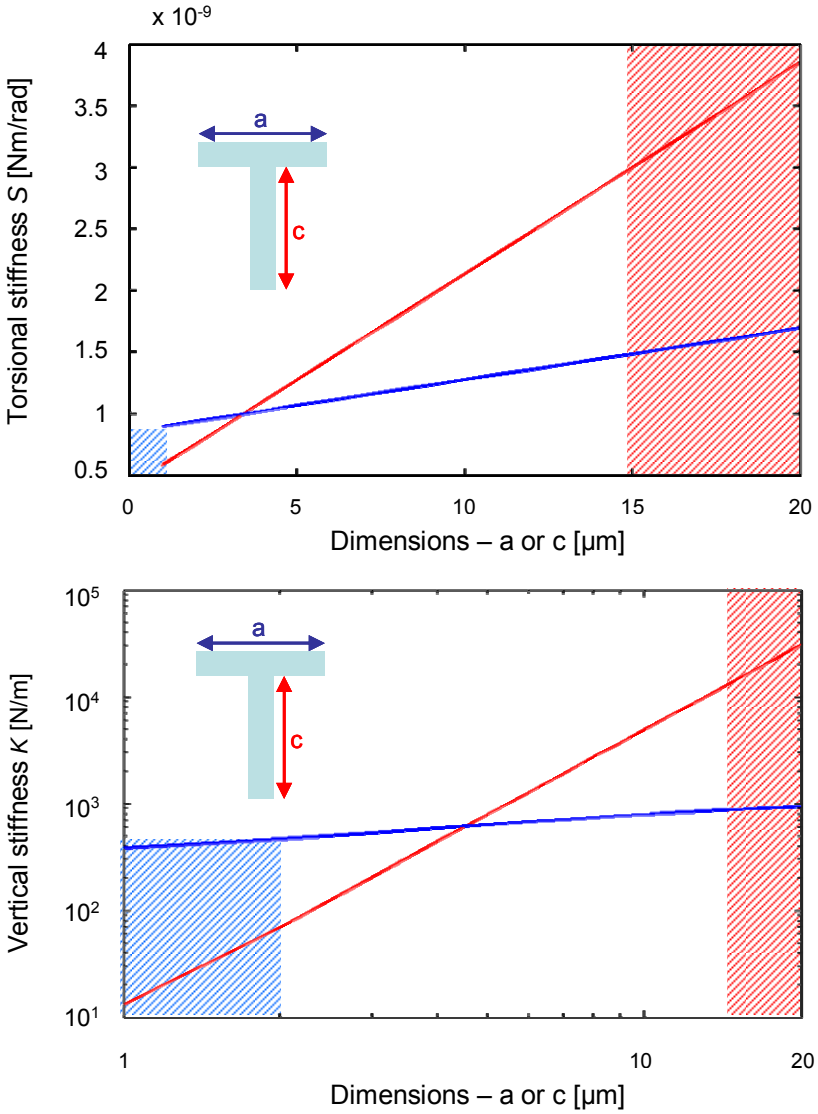

Figure 5.10 *Parameter analysis of T-beam section: Impact of parameters- a or c on torsional and vertical stiffnesses.(Shaded regions indicate either limit of technological feasibility (blue) or region of practical difficulty(red) for the corresponding parameters)*

Figure 5.10 shows the effect of parameters - *a* and *c* on torsional stiffness *S* and the vertical stiffness *K*, varied over appropriate ranges. The other parameters were chosen as per the values of table 5.1. From the torsional stiffness analysis, it is observed that for both parameters – *a* and *c*, the corresponding torsional stiffness increases linearly. On the other hand, the parameter *c* shows a strong impact on the vertical stiffness of the T-beam suspension, compared to parameter *a*. One can expect that any arm of the sensor spring which is perpendicular to the substrate (like the one defined by parameter *c* of the T-section), will be a key factor in determining the vertical stiffness, while the other parameter *a*, can be considered insignificant.

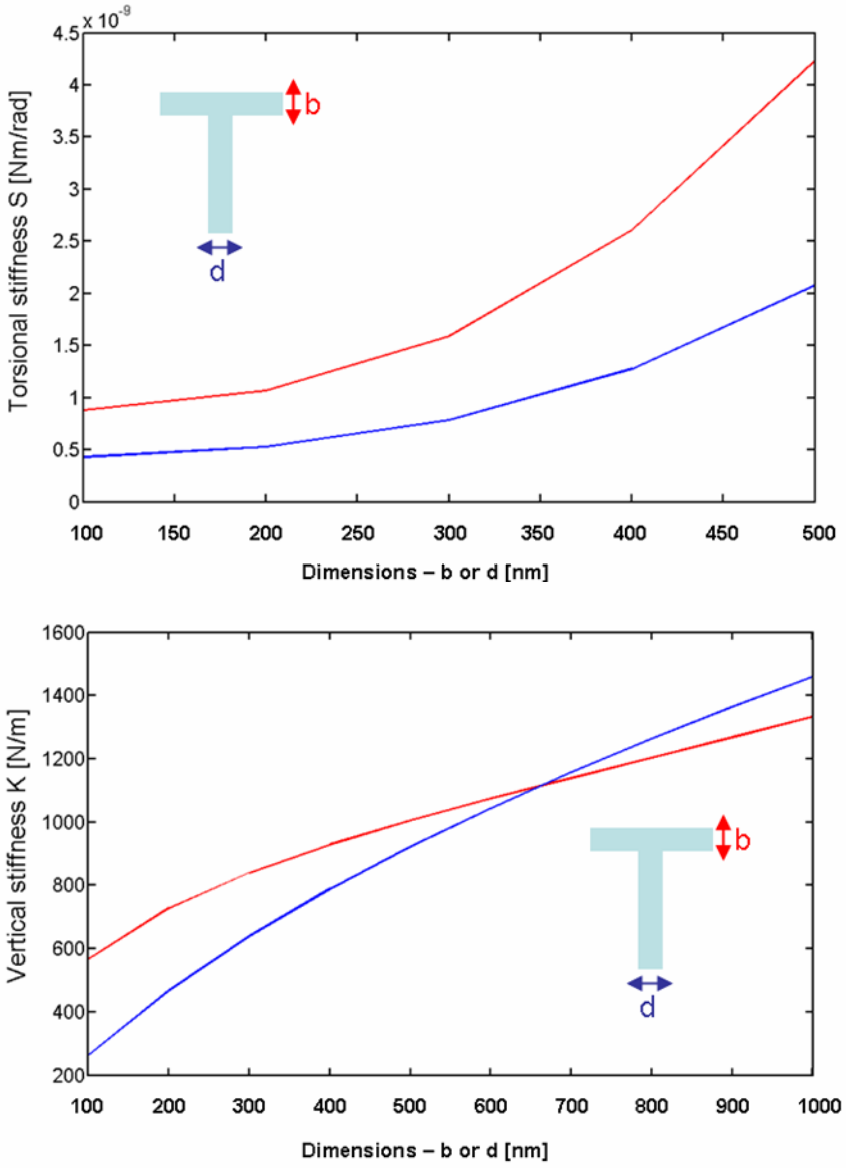

Figure 5.11 *Parameter analysis of T-beam section: Impact of parameters - b or d on torsional and vertical stiffnesses.*

Figure 5.11 shows the effect of parameters *b* and *d* on both torsional and vertical stiffness of the sensor springs. From the trends of torsional stiffness obtained by varying these two parameters, it is observed that they have a prominent role in determining the optimal design of the T-section springs. It is evident that these two parameters are very sensitive to minor technological variations and any inhomogeneity in the device layers will result in significant deviations from the design values. They also contribute significantly to the vertical stiffness of the springs. In order to ensure the precision, care should be taken to keep the technological variations far-below the 100 nm range.

From these two figures, it is clear that the parameter *c* plays a vital role in determining the vertical stiffness and the parameters- *b* and *d* dominate in determining the torsional stiffness. In order to realize T-section springs with small torsional stiffness and large vertical stiffness, we need *c* to be long and *d* to be thin. However, one left out parameter in the analysis so far is the length of the springs *L*. For the analysis of the influence of *L*, we chose selected values of two parameters- *c* and *d*, while varying the length *L* over a wide range of possible dimensions. For *c*, the chosen values were 5 and 10 μm and for *d*, the chosen values were 200, 400 and 600 nm.

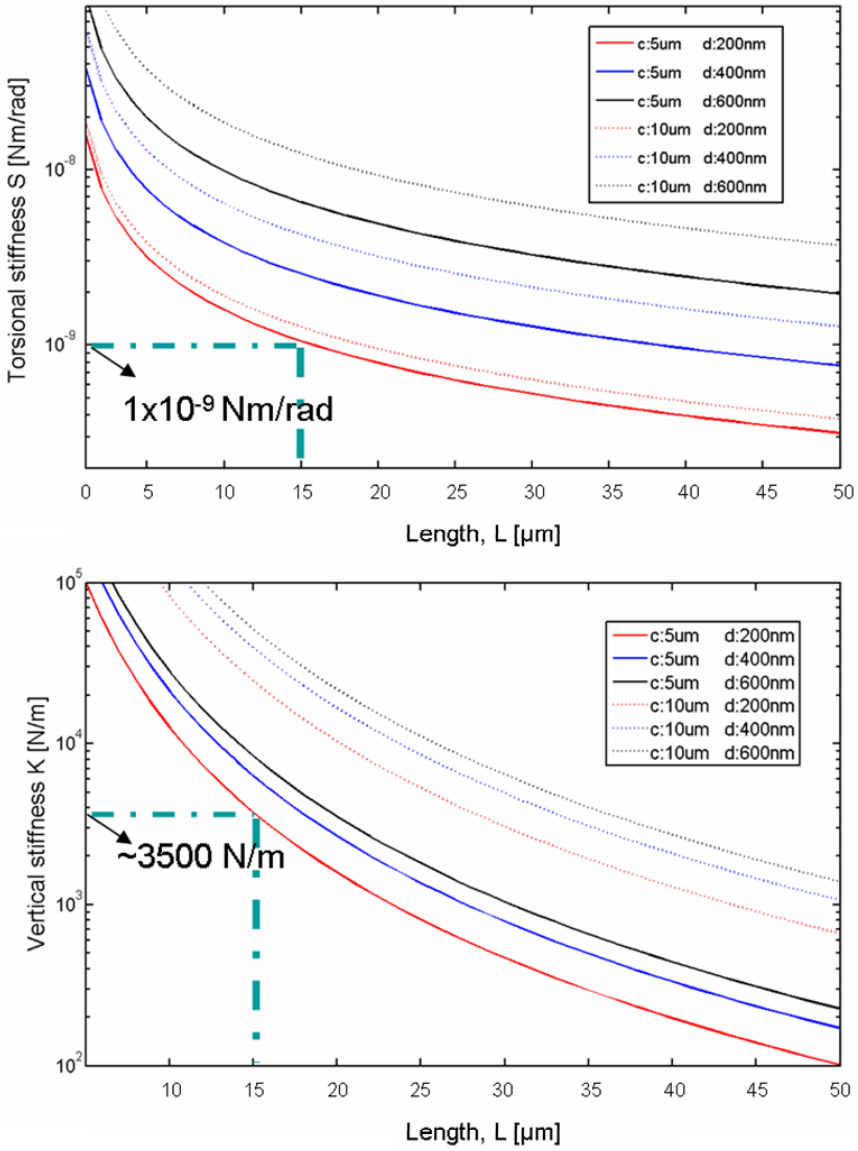

Figure 5.12 *Parameter analysis of T-beam section: Impact of beam length L, on torsional and vertical stiffnesses. For a target value of torsional stiffness ($1 \cdot 10^{-9}$ N.m/rad), the corresponding vertical stiffness obtained is ~3500 N/m. Such a value corresponds to the T-section with the parameters c and d as 5 μm and 200 nm respectively.*

Figure 5.12 shows the trends of torsional and vertical stiffnesses, for all the above cases. The desired range of torsional stiffness set as a target for the next-generation of hair

sensors is below $1 \cdot 10^{-9}$ [Nm/rad]. From the graph showing the trends in torsional stiffness, we infer that these values are obtained for spring lengths above 15 μm (L>15 μm) and web width d less than 200 nm (d<200 nm). As seen before, the parameter c has little impact in torsional stiffness contribution and it varies very little for both cases (i.e. c = 5 and 10 μm).

On the other hand, the values of vertical stiffness drastically range from 15000 to 200 [N/m] for the range of spring lengths between 10 and 40 μm, respectively. The roles of the parameters d and c are reversed for the case of vertical stiffness, as we have observed earlier. Parameter c has a substantial effect on the vertical stiffness, while varying slightly for the torsional stiffness. This clearly shows that best design choice for parameter c would be between 5 and 10 μm.

Discussion

A T-shaped cross-section for the sensor spring is analyzed for realizing springs with small torsional stiffness and a higher ratio of vertical-to-torsional stiffness. From the analysis based on the parameters of the T-section, the optimal design choices include: 10 μm <L< 40 μm; 5 μm <c< 10 μm and d< 200 nm. For this range of design values, the torsional stiffness of the T-section springs would be well below the desired target value of $1 \cdot 10^{-9}$ [Nm/rad] while the corresponding vertical stiffness ranges from 200 to ~15000 N/m. As discussed before, by incorporating T-section springs, the torsional stiffness can be reduced by more than one order of magnitude compared to the basic spring designs, while realizing 2 or 3 orders increased stiffness in vertical direction. Such attractive numbers motivate us to investigate new technological approaches to realize such springs designs. Given the fabrication quality and low-stress structural profile, silicon-rich nitride is preferred over other materials for the present approach. However, the primary step in this technology is to achieve narrow and uniform-width trenches, less than the technological limit of 2 μm.

5.4.2 Trenches for T-section springs

The integration of T-section springs to the existing fabrication process for artificial hair sensors requires a special process for the deep and narrow trenches to start with. The process flow after the trench etching is exactly the same as the one discussed in chapter 3, with the exception of modified photomasks (since the spring lengths are much smaller than the present generation of sensors). An overview of this adapted process flow, starting with a trench is shown in figure 5.13. This clearly suggests that our main focus has to be laid on the realization of critical-width trenches. The challenge is to fabricate trenches with controllable widths of <2 μm, using conventional lithography techniques. Edge lithography techniques [19-23] provide interesting alternatives for using high-end, expensive lithography systems.

Edge lithography for etch-masking layers

Trenches on a silicon substrate can be realized either by wet or dry directional (or anisotropic) etching [26,27]. In either case an etch-masking layer is necessary. The quality of the trenches also depends on the quality of the etch-mask layer. The profile and performance of the etch-mask layer should be considered with respect to the selectivity of the chosen etch process and total etch time for the trenches. Typical directional etch processes on bulk silicon use silicon dioxide or silicon nitride layers as etch-mask.

In order to realize trenches using directional etching, it is necessary to pattern the etch-mask layer of desired width. Etch-mask layers (silicon nitride or silicon dioxide) are patterned with conventional lithography techniques. However, the resolution limit of conventional

lithography, as available for this research, is 2 μm. Clearly this is not the desired option for our intended designs.

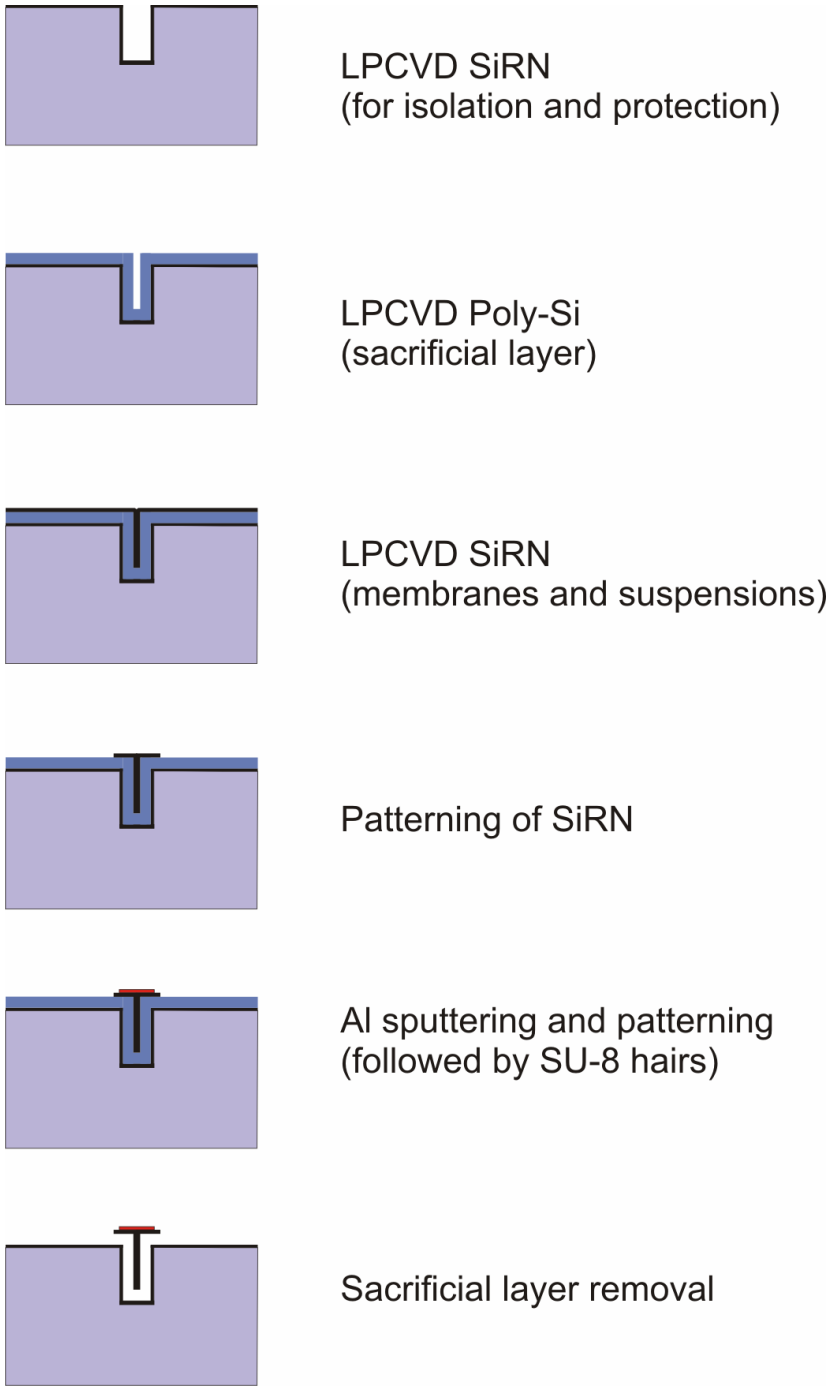

Figure 5.13 *Overview of process flow of sensors featuring T-section springs*

On the other hand, edge lithography is a novel lithography where the edge of the original pattern becomes a feature in the final pattern. This is possible by means of selectively depositing and etching materials on the edges of a pattern previously defined by standard photolithography [23]. Edge lithography has been used to pattern layers for feature sizes lower than the resolution limit of the conventional techniques. Hence, for our process of realizing trenches of <2 μm widths, we intend to use edge-lithography to pattern the etch-mask layer.

Fabrication of etch-mask layers

A novel fabrication process is developed for the etch-mask pattern prior to trench etching. Figure 5.14 and 5.15 show the complete step-by-step description of this novel process. The detailed process parameters and settings are presented in Appendix D. The process starts with a conductive silicon substrate. Subsequently a thin layer (20 nm) of silicon-rich nitride is deposited by a standard LPCVD process. This layer will be the actual etch-mask layer for the trench etch step, after several process steps. An 80 nm thick TEOS layer is deposited on top of the silicon-rich nitride layer, followed by a 100 nm thick poly-silicon layer by means of standard LPCVD steps. Next, yet another layer of silicon-rich nitride of 200 nm thickness is deposited by LPCVD.

A standard photolithography step is done and using a photoresist pattern, the top silicon-rich nitride layer is patterned by RIE. After removal of the photoresist, the edge of the resulting nitride pattern determines the width of the trenches. In this RIE step, a portion of the underlying poly-silicon layer is exposed and using the nitride-pattern as a mask, local oxidation (LOCOS) [21] is done at 950 °C by a thermal oxidation process. Only the exposed poly-silicon layer is oxidized and a thin layer (~30-40 nm) of silicon oxide is formed. The wafers are then etched in hot phosphoric acid at 180 °C. Hot phosphoric acid has a high selectivity against silicon oxide, while etching nitride at a controlled etch rate of 4 nm/min. This etching process is called ‘retractive etching’ since the nitride layer on the wafer is etched from all sides at a uniform rate resulting in a shrinkage. The nitride layer retracts about 100 nm from the edge of the LOCOS oxide during this step. Such a retraction actually exposes the underlying poly-silicon (~100 nm) while being masked by nitride and LOCOS oxide on either edges.

The wafers are subsequently etched (without delay, to prevent native oxide formation) in 5% solution of Tetra methyl ammonium hydroxide (TMAH), which has high selectivity for poly-silicon against nitride and oxide. This is the most critical step as the poly-silicon is isotropically etched on both sides, thus determining the width of the trenches. This step also exposes the underlying TEOS layer. Following it, the remaining of the silicon rich nitride layer (~100 nm) is completely etched in hot phosphoric acid at 180 °C. (Figure 5.14)

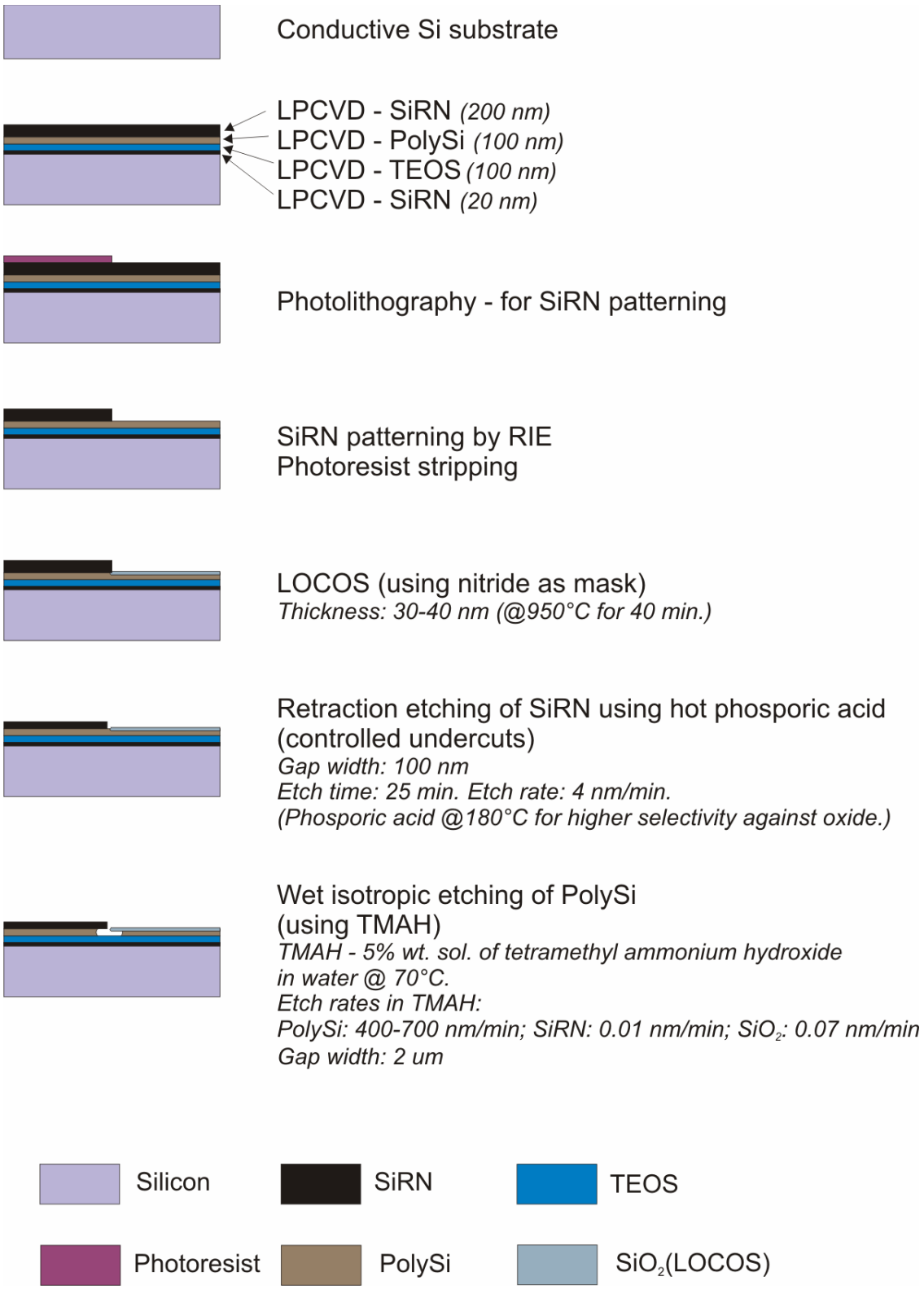

Figure 5.14 *Process flow for the fabrication of etch-mask layer for trenches using edge lithography*

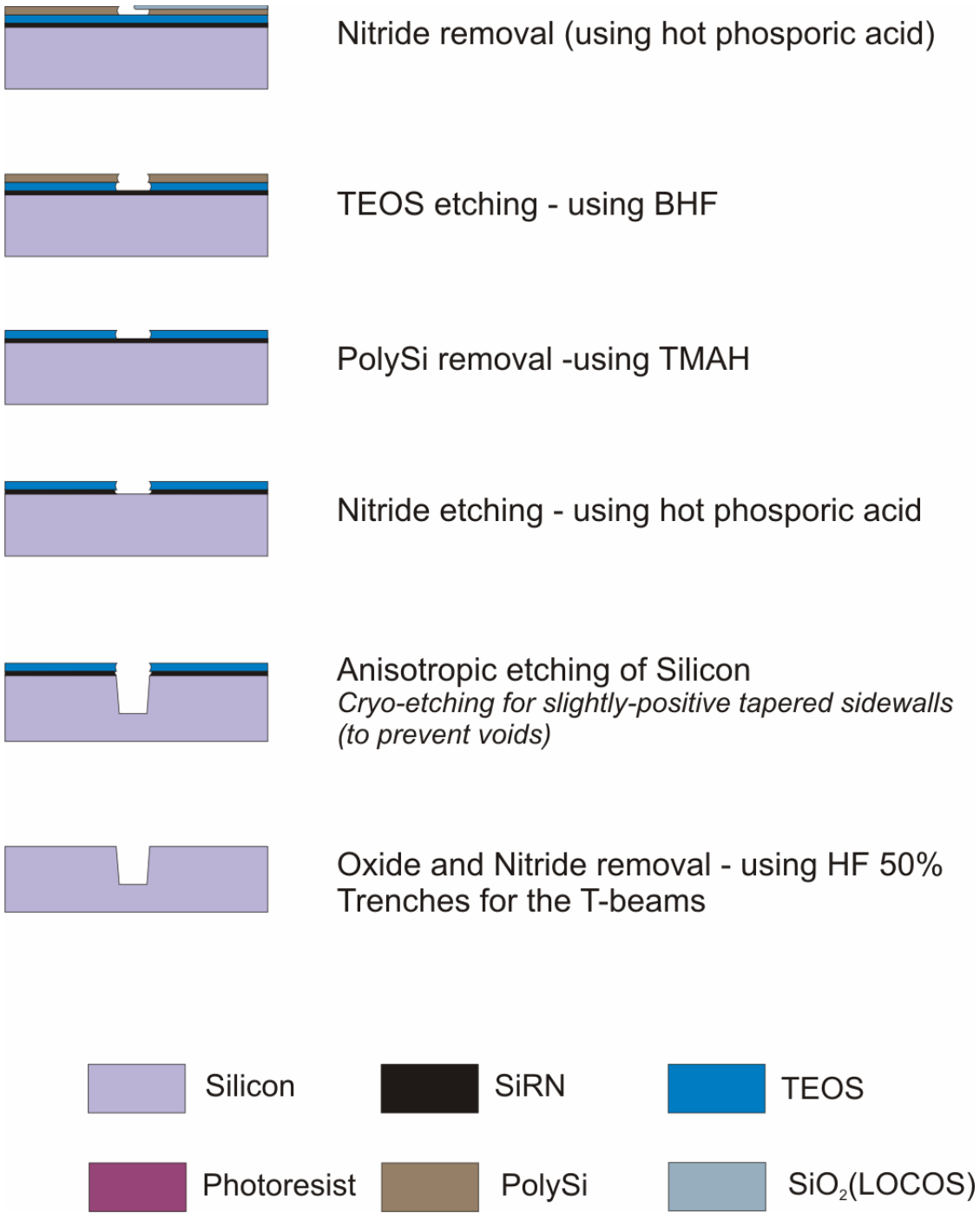

Figure 5.15 *Process flow for the fabrication of etch-mask layer for trenches using edge lithography*

The wafers are then put in buffered hydrofluoric acid (BHF), which etches the remaining of the LOCOS oxide, while simultaneously etching the partially exposed TEOS oxide layer. This, on the other hand, exposes the silicon rich nitride layer beneath the TEOS

layer. The remaining of the poly-silicon layer is then etched away in 5% of TMAH solution. Subsequently the wafer is etched again in hot phosphoric acid at 180 °C, which etches the thin silicon rich nitride (20 nm). The bi-layer of thin silicon rich nitride and TEOS oxide (~100 nm) forms the etch-mask layer for the trenches.

As it is obvious, the process consists of several stacked layers which act as mutual etching and etch-resisting layers for each other, during subsequent process steps. During the isotropic etch steps of TEOS and silicon rich nitride, it is to be noted that the actual width of the trench is increased relative to what the width determined by the poly-silicon etch step. Hence, it is very important to note that the desired width for the trenches depends on the width of the poly-silicon etch pattern and twice the thicknesses of the TEOS and SiRN layers beneath it.

Using the etch-mask layer, the wafers are then etched using the standard RIE (Adixen) at cryogenic temperatures [27]. The etch profile is desired to have a slight positive-taper which will ensure that no voids form during the trench filling of the device layers (Figure 5.13). RIE etching of the silicon substrate is done using SF_6 and oxygen as reactive gases and at cryogenic temperatures of -100 °C for about 5 minutes. The intended depth of the trenches is 10 μm.

5.4.3 Results & Discussion

During the fabrication process of the trenches for the T-section springs some challenges were encountered. Figure 5.16 shows an SEM image of an RIE patterned Silicon rich nitride feature, which forms the edge for the subsequent patterning steps. The tapered profile of the nitride does not affect the process as the edge is the only crucial part of it.

SiRN patterning by RIE
Photoresist stripping

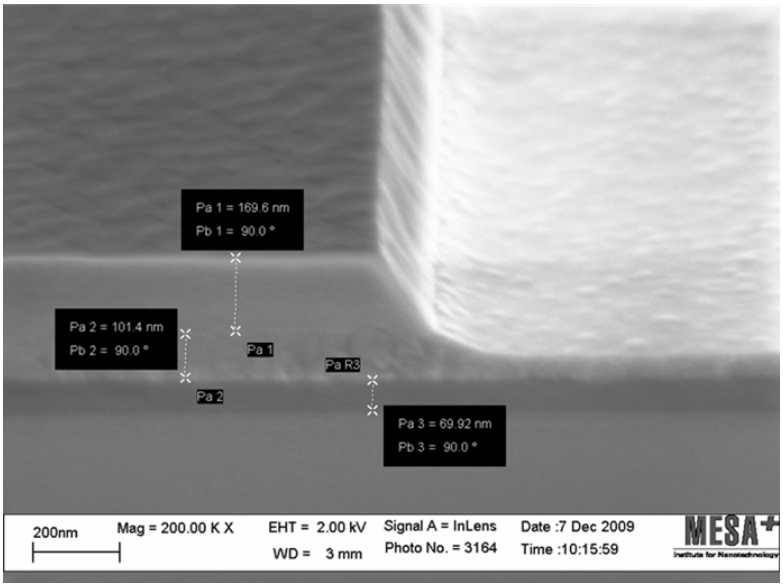

Figure 5.16 *SEM image showing silicon rich nitride etch after RIE patterning*

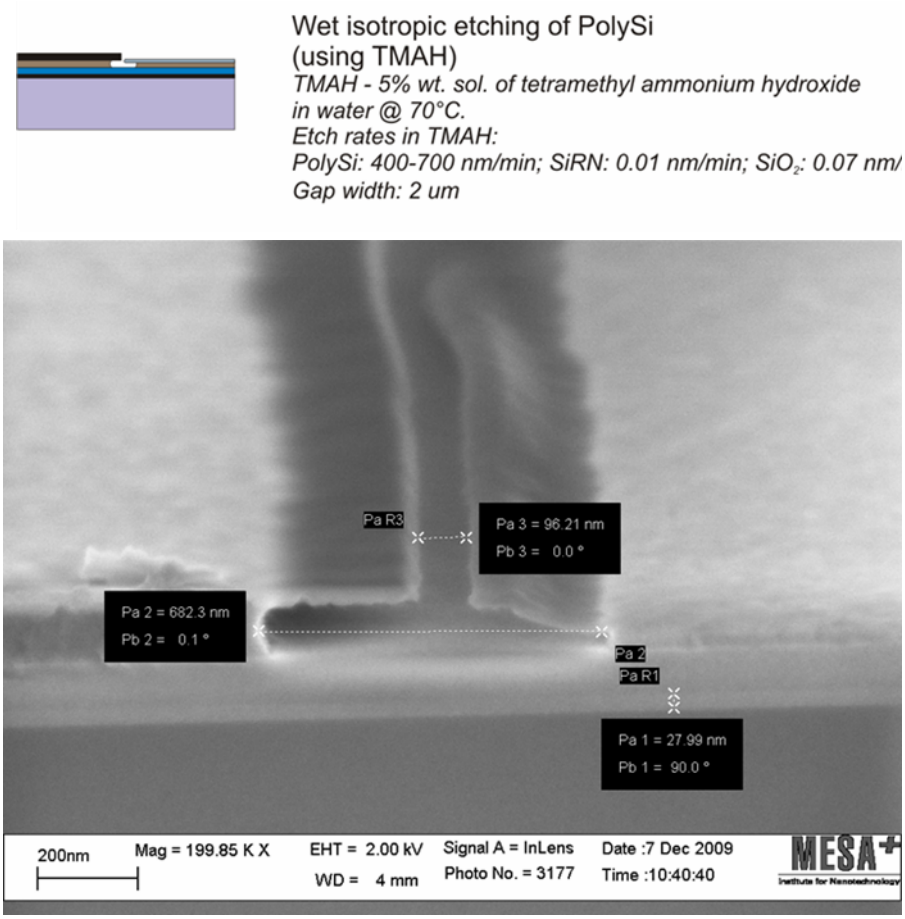

Figure 5.17 *SEM image showing the poly-silicon isotropic etch after the retraction etch of silicon rich nitride layer.*

Figure 5.17 shows an SEM image of the crucial poly-silicon etching after the retraction etching of the silicon rich nitride layer. The image shows the isotropically etched profile of the poly-silicon layer which sits beneath the nitride layer (left) and the LOCOS oxide (right). This isotropic etch width chiefly determines the width of the trenches. The image also shows the retracted nitride width, which is now seen as the central opening width (~100 nm). Such a retraction follows the pattern of the silicon rich nitride edge (as seen from a slight bending in the top of the image).

Figure 5.18 shows an SEM image after the TEOS isotropic BHF etching step, showing the resulting under-etch. Thus for a desired trench width, the extent of this under-etch should be considered. Since this is an isotropic etching, the under-etch width chiefly depends on the thickness of the TEOS layer itself, apart from the etch time. The next step which involves the etching of nitride will also result in an under-etch depending on the nitride layer thickness.

Figure 5.19 shows the optical microscope image of the final trench after the final directional RIE process. The trench widths are varied for different wafers depending on the poly-silicon etching profile. The picture shows one of these trenches with a slight positive-taper and a width of ~800 nm (sub-micron values were re-calculated based on the standard scale of the microscope image). Fabrication of such small width trenches would not have been possible with the standard lithography technique as available in this research. This is a good

proof-of-concept for the edge lithography based trench fabrication technique. By critical manipulation of the etch times, the desired width of the trench can be realized.

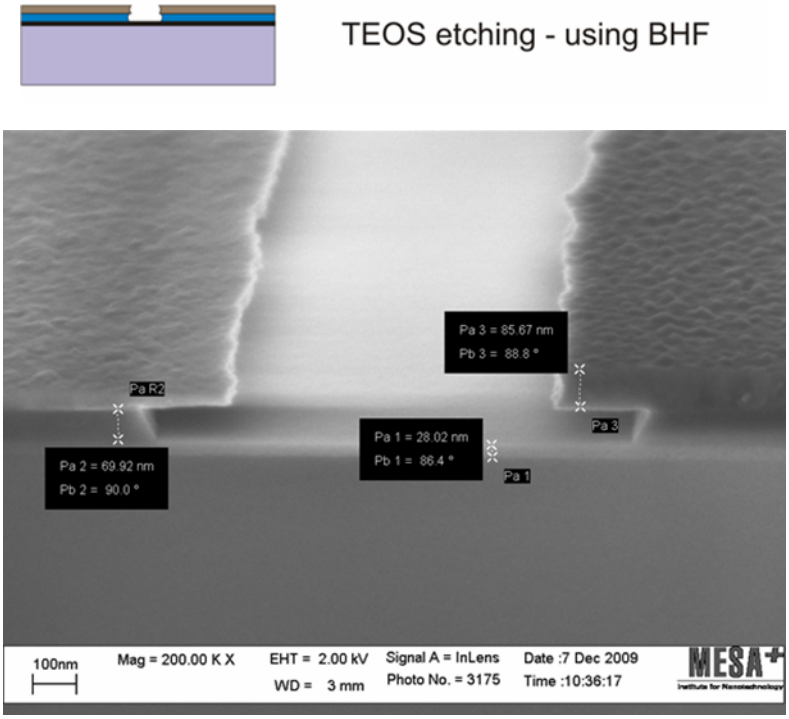

Figure 5.18 *SEM image after TEOS etching with thin nitride as etch-stop layer*

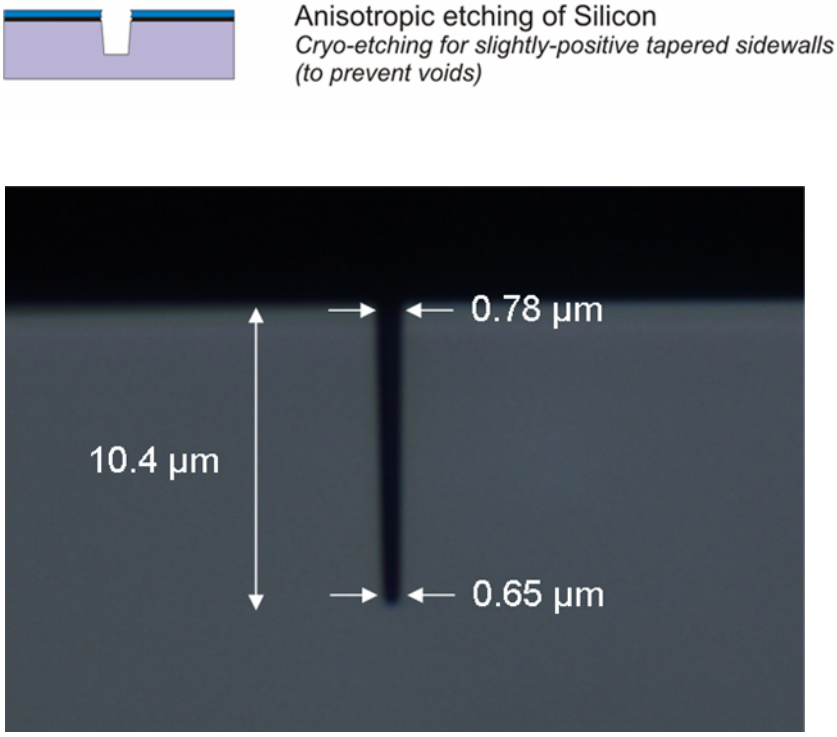

Figure 5.19 *Image of the final trench with width <0.8 µm using edge lithography*

Figure 5.20 shows some of the serious challenges faced during the process. The first challenge was with the numerous pin-holes present on the surface of the wafer (only on the parts that were exposed to plasma – during the nitride patterning step.) These pin-holes were subsequently transferred to the underlying layers during further processing. One possible solution could be to pattern the nitride using wet-etching (i.e. hot phosphoric acid at 180 °C). But such a step will require an additional TEOS layer to be deposited and patterned later. Nevertheless, this change was incorporated in the subsequent processing batches and the problem with pin-holes was completely eliminated.

The other challenge was faced during the poly-silicon removal step in TMAH solution (right after the TEOS patterning step). At some portions of the wafer, poly-silicon etching was not successful. This is due to the formation of a thin native oxide layer. This was solved in later trials by etching the native oxide by putting wafers in HF 1% solution for 1 minute prior to poly-silicon etching.

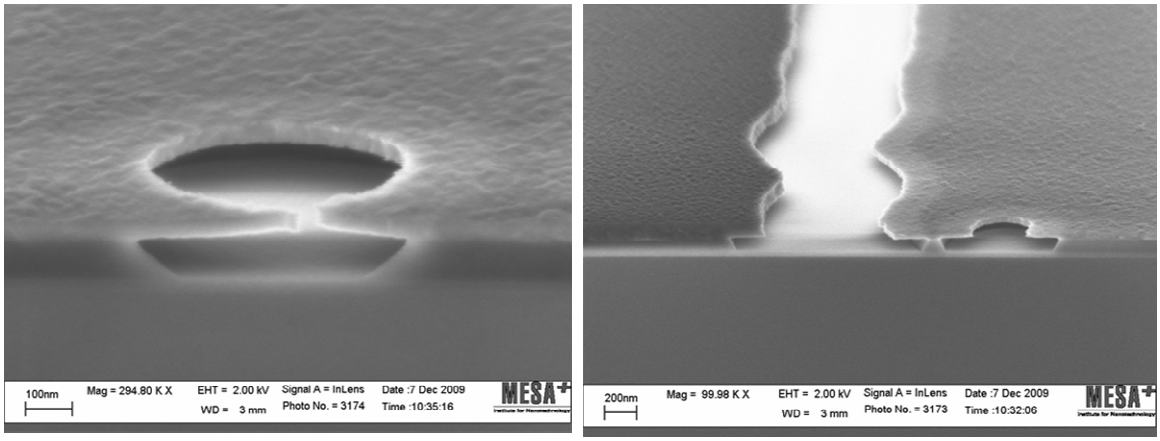

Figure 5.20 *Undesired pin-holes were observed on the wafer surface, which was exposed to RIE.*

5.4.4 Conclusions T-beams

T-beams offer the potential of a largely improved ratio of vertical spring stiffness to torsional spring stiffness, as shown in this chapter by the respective expressions. But relative to the current technology they come at the cost of more complicated fabrication schemes, e.g. a T-section spring can be realized by fabricating trenches and subsequently filling these trenches with the device layers. However, the crucial geometric parameter of the T-section requires trenches to be of uniform and controllable widths, which fall less than the technological resolution limit. Hence, a novel process using edge lithography is devised to fabricate the trenches, which will be then integrated with the existing process flow for the hair sensors. Though it was feasible to realize trenches of sub-micron width as intended, the process was met with several challenges, some of which were remedied with a few modifications in the process flow.

5.5. Conclusions

An alternative approach is sought to obtain improved performance of the sensor, aiming at a small torsional stiffness and increased vertical stiffness of the sensor springs (to prevent any undesired mode coupling during the dynamic performance of the sensors). Design analysis suggests two possible options: (i) using an alternate structural material and (ii) using

a modified cross-section for the springs. For the first option of choosing a new structural material, SU-8 is seen as a promising option and a proof-of-concept fabrication process flow is devised to verify the feasibility of this new approach. Results from the test structures presented numerous technological challenges as expected. The test SU-8 membranes show large undesired curvature due to the intrinsic residual stress and stress-gradients. As a second option, a silicon-rich nitride spring with a T-section theoretically proves to be a very good choice and the required trenches were shown to be feasible. However, both investigated technologies were sufficiently disruptive relative to the current fabrication schemes that up to date none of both has been implemented to be a full fledged fabrication process. The obtained results indicate that the T-beam approach has more potential and is likely to yield better reproducibility (e.g. as judged from the problems with variations in the quality of SU-8 layers in dependence of shelf time) than the SU-8 approach.

Further it is remarked that the important ratio of K/S_0 strongly depends on the moments of inertia I_{xx}, I_{yy} and I_p where the latter can be approximated in simple geometries by $I_p=I_{xx}+I_{yy}$. This means that there are both opportunities and limitations to improving this ratio. For a large ratio ideally I_{yy} approaches 0. However, in this case the limited in-plane (parallel to the substrate) flexibility would become a problem. Hence, this points at more robust solutions for springs made of lower Young's' modulus materials.

Alternatively one may look at more complicated (by design, preferably not more complicated in processing) spring-structures, if needed with virtual rotational axes. In this approach one could also look at nonlinear effects (spring-stiffening) for structures that are stressed beyond their linear limits. This path has not been investigated in this work but could be interesting in possible follow-up research.

5.6. References

[1] SU-8 datasheets from: http://www.microchem.com/products/su_eight.htm

[2] E.H. Conradie and D.F. Moore, *"SU-8 thick photoresist processing as a functional material for MEMS applications"*, J. Micromech. Microeng. (2002) 12, pp. 368-374

[3] H. Lorenz, M. Despont, N. Fahrni, J. Brugger, P. Vettiger and P. Renaud, *"High-aspect-ratio, ultrathick, negative-tone near-UV photoresist and its applications for MEMS"*, Sensors and Actuators A (1998) 64, pp. 33-39

[4] P. Svasek, E. Svasek, B. Lendl and M. Vellekoop, *"Fabrication of miniaturized fluidic devices using SU-8 based lithography and low temperature wafer bonding"*, Sensors and Actuators A (2004) 115, pp. 591-599

[5] F. Ceyssens and R. Puers, *"Creating multi-layered structures with freestanding parts in SU-8"*, J. Micromech. Microeng. (2006) 16, pp. S19-S23

[6] C.M. Bruinink, R.K. Jaganatharaja, M.J. de Boer, E. Berenschot, M.L. Kolster, T.S.J. Lam-merink, R.J. Wiegerink and G.J.M. Krijnen, *"Advancements in technology and design of biomimetic flow-sensor arrays"*, Proc. IEEE Int. Conf. MEMS, 2008, pp. 152-155

[7] M. Dijkstra, J.J. van Baar, R J Wiegerink, T S J Lammerink, J H de Boer and G J M Krijnen,"*Artificial sensory hairs based on the flow sensitive receptor hairs of crickets*",J. Micromech. and Microeng.(2005) 15, pp. 132-138.

[8] J.A.C. Humphrey, R. Devarakonda, I. Iglesias, F.G. Barth,*"Dynamics of arthropod filiform hairs. I. Mathematical modeling of the hair and air motions"*, Philosophical Transactions: Biological Science (1993) 340,pp.423-444

[9] D. Haefliger and A. Boisen,*"Controlled out-of-plane positioning of microfluidic components in SU-8 driven by plastic strain"*, 9th International conference on miniaturized systems for chemistry and life sciences, 9-13 Oct, 2005, pp. 178-180.

[10] D.W. Johnson, A. Jeffries, D. Minsek and R. Hurditch,*"Improving the process capability of SU-8. part II"*, J. Photopolym Sci. Technol., (2001) Vol. 14(5), pp. 689-694.

[11] R. Feng and R.J. Farris, "*Influence of processing conditions on the thermal and mechanical properties of SU-8 negative photoresist coatings*", J. Micromech. Microengg, (2003) Vol.13, p. 80.

[12] S.D. Psoma and D.W.K. Jenkins, "*Comparative assessment of different sacrificial materials for releasing SU-8 structures*", Rev. Adv. Mater. Sci. (2005)10, pp. 149-155.

[13] http://www.polytec.com/eu/

[14] Discussions with D. Altpeters, Technician (SU-8 Lithography), MESA+Cleanroom

[15] Consultations with Microchem by D. Altpeters, Technician (SU-8 Lithography), MESA+ Cleanroom

[16] PMMA datasheets from: http://www.microchem.com/products/pdf/PMMA_Data_Sheet.pdf

[17] J. Tong, C.A. Simmons and Y. Sun,*"Precision patterning of PDMS membranes and applications"*, J. Micromech. Microeng. (2008) 18, pp. 1-5

[18] Y. Suzuki,*"Micromachined high-aspect-ratio parylene spring and its application to low-frequency accelerometers"*, J. Microelectromech. Syst. (2006) 15(5), pp. 1364-1370

[19] D.C. Flanders and A.E. White,*"Application of ~100 Å linewidth structures fabricated by shadowing techniques"*, J. of Vacuum Science and Technology (1981) 19(4), pp. 892-896

[20] N.R. Tas, J.W. Berenschot, P. Mella, H.V. Jansen, M.C. Elwenspoek and A. van den Berg,*"2D-confined nanochannels fabricated by conventional micromachining"*, Nanoletters (2002) 9(2),pp. 1031-1032

[21] J. Haneveld, E. Berenschot, P. Maury and H. Jansen,*"Nano-ridge fabrication by locl oxidation of silicon edges with silicon nitride as a mask"*, J. Micromech. Microeng. (2006) 16(6), pp. S24

[22] Y. Zhao, E. Berenschot, M. de Boer, H. Jansen, N. Tas, J. Huskens and M. Elwenspoek, "*Fabrication of a silicon oxide stamp by edge lithography reinforced with silicon nitride for nanoimprint lithography*", J. Micromech. Microeng. (2008) 18(6), 064013

[23] Y. Zhao, "*High-resolution stamp fabrication by edge lithography*", PhD thesis, University of Twente, the Netherlands (2010) ISBN 978-90-365-3036-1

[24] J.M. Gere,"*Mechanics of materials*",5th edition, Brooks/Cole Thomson Learning (2001), ISBN0-534-37133-7

[25] W.C. Young and R.G. Budynas, "*Roark's formulas for stress and strain*", 7th edition, McGraw-Hill (2002) 209, ISBN 0-07-072542-X

[26] M.C. Elwenspoek and H.V. Jansen, *"Silicon micromachining"*, Cambridge University Press (1998)

[27] H. Jansen, M. de Boer, H. Wensink, B. Kloeck and M. Elwenspoek,"*The black silicon method VIII: A study of the performance of etching silicon using SF6/O2-based chemistry with cryogenical wafer cooling and a high density icp source*",Microelectronics Journal.(2001) 32(9), pp. 769-777

6

Viscosity-mediated coupling between hair sensors

In a nutshell...

Flow-sensitive hair sensors are arranged in dense arrays, both in natural and bio-inspired cases. Do the hair sensors in such closely-packed settings, affect each other's performance? Answering the question is a key to the optimal arrangement of hair sensors for future applications. A dedicated microfabricated chip consisting of artificial hair sensors was realized and used to controllably and reliably investigate viscous coupling between hair sensors. The experimental results confirm the presence of coupling effects between hair sensors when placed at inter-hair distances of <10D from each other, where D represents the hair diameter. The results present significant insights in optimal array arrangements for high spatial resolution while preserving the hair-sensors uncoupled (individual) responses.

6.1. Introduction

Arrays of high-density artificial hair-sensors are required for high spatial resolution in flow signature detection applications. Despite successful sensor-array developments, several characteristics of cercal hairs in arrays – for instance, viscosity-mediated coupling, still remain unknown or less understood. One unexplained and interesting aspect is related to the

occurrence of sensory filiform hairs in high-densities [1-3] and the associated effects on single hair-sensor performance [1,2]. The impact of one hair sensor on its neighbors is mediated by viscous coupling [1]. This effect has been debated in literature, both from theoretical and experimental viewpoints [1,4-9], but poses many practical difficulties for experimental studies on living animals [2].

The presence of viscous coupling impacts the sensitivity of the hair sensors. Hence, investigation of viscous coupling between artificial hair-sensors can make a significant contribution to the design of optimally arranged sensor arrays. Simultaneously it helps biologists to further their understanding of the functioning and bauplan of such high density sensory arrays as found on crickets, appreciating the difficulties to investigate viscous coupling effects on the actual cerci. With the major advantage of exerting control over the operation and geometry of the artificial sensory hairs, a wide range of experimental characterizations is now possible. The aim of this work is to study the presence of viscous coupling between artificial hair sensors. Initially, the parameters which play a major role in viscous coupling are identified. Using this knowledge, an experimentation platform comprising several artificial hairs arranged in specific patterns is designed and realized. The results of experiments on these structures are presented here.

6.2. Hair sensor arrays: natural and bio-inspired cases

Flow-sensitive hairs on the cerci of crickets occur in varying length and diameters and are arranged at certain specific spatial positions on the circumferential surface of the cercus [10-12]. The length of the hairs on the cerci is observed to have a bimodal distribution, with a group of short hairs and a group of long hairs [2,3]. Moreover, short hairs are abundant (more than 75%) and long hairs are relatively scarce on a cercal surface [3]. The hair diameters, as measured near the socket, range between ~1-9 μm, depending allometrically on their length, which ranges between ~100-1500 μm [1-3]. Based on careful experimental observations of the crickets of various growth stages, hair densities of ~400 (first instar) to ~100 (adults) hairs (of different lengths) per mm^2 were found at average nearest neighbor distances between 30 and 60 μm [3]. Also, it is to be noted that the adjacent hairs are of different orientation of mechanical movements and thereby, sensitive to flows of specific directions [1-3]. It has also been studied that there exists an "identifiable" pattern with respect to a hair's preferred directionality and its occurrence on the cercal surface, observed on individuals of the same species [13].

On the other hand, our artificial hair sensor arrays feature, geometrically speaking, thicker hairs (~50-60 μm) and of uniform length (~700-800 μm). The hairs are arranged in a defined pattern of about 30 rows of 4 hairs each, with an inter-hair distance of ~300 μm. The density of the artificial hair sensor arrays is roughly <10 per mm^2. Comparing this to the actual crickets, the hair sensors are relatively denser, but upon taking into account the differences in hair geometries, the normalized spacing between the hairs are more or less in a comparable range. The normalized distances between cricket hairs range approximately between 5 ~ 100 while in our artificial case, it ranges within 4-6. Most artificial arrays feature hair sensors, as characterized in the previous chapter, all of which are designed to have one specific orientation of mechanical motion and hence, shown sensitivity to one particular direction of flow.

6.3. The viscosity-mediated coupling effect

When two hairs (of length L and diameter D) are sitting too close to each other (inter-hair distance, s) in the direction of flow, it is intuitive to consider that each hair could cast a hydrodynamical shadowing effect on the other. The coupling effect depends on several factors related to the hairs and the character of the flow. While such coupling could negatively affect the individual hair performances, the paradoxical occurrence of hairs in highly dense arrangements raises an unexplained and less understood natural phenomenon. The possible existence of viscosity-mediated coupling between the filiform hairs was first suggested by J.A.C. Humphrey *et. al.* [14] in their studies involving the mechano-sensory hairs found in crickets and arachnids. This term, viscosity-mediated coupling, suggestively denotes the dominance of viscous forces in low-Reynolds' number flow regimes.

Bathellier *et. al.* made an extensive investigation, both theoretically and experimentally, on viscous coupling between hairs found in the trichobothria of *Cupiennes Salei* spiders [5]. In this work, they defined a dimensionless coefficient to define the viscous coupling and conducted several experiments on spider hairs. For the experimental tests, pairs of hairs with varying normalized distances were chosen. The angular deflection of a reference hair was optically measured, in presence of a perturbing hair and measured again in the absence of the perturbing hair (after removal). The role of the perturbing hair was investigated in three different scenarios: (i) free moving, (ii) immobilized at its base and (iii) mechanically actuated. They measured the coupling effect for the second and third cases, and determined the effect was negligible for the first case.

Further, they also proposed a theoretical model as a framework for their experimental results. Significant insights provided by their model can be summarized as: (i) the coupling coefficient is dependent on the flow frequency, (ii) the coupling effect drops with increasing distance between the hairs, (iii) a fixed or mechanically driven hair perturbs the flow more than a free-moving hair[1], and (iv) the coupling effect depends on the length of the hairs (longer hairs have more prominent effects on the reference hair than shorter ones). This paper turned out to be a seminal study for later experimental and computational works.

Cummins *et. al.*[4] and Heys *et. al* [7] continued the investigation of the viscosity mediated coupling by applying computational approaches. Cummins *et. al.* provided results that suggested significant coupling effects to be present for a wide range of normalized inter-hair distances. They also extended their models to simulate the coupling effects between a group of hairs (of different lengths) on a small patch of cercus. Their results presented very strong coupling effects on the hairs of intermediate lengths and also large phase shifts in the hair response, between being isolated and placed in a group. P.S. Alagirisamy *et. al.* [8] presented a different experimental approach and performed investigations by building scaled-up hair models. They observed significant coupling between the hairs, when the inter-hair distance normalized with the hair diameter becomes less than 20 (s/D <20).

G. Lewin *et. al*. [9] developed a finite element model to study the viscosity-mediated coupling between filiform hairs and extended it to a pair of MEMS-based hair sensors, providing an approximate theoretical prediction for the work presented in this chapter. Their models took in the actual values of the MEMS hair sensors and suggested significant coupling between our hair sensors, when s/D <10. Their work also considered the perpendicular configuration, i.e. hairs placed next to each other, both facing the flow at the same time (contrary to the cases discussed until now). For such configuration, they observed negative

[1] With respect to a free-moving reference hair (of same length). The reason for this negligible coupling between free-moving hairs is due to the cancellation of driving and damping torques [5].

coupling coefficients, suggesting an increased sensitivity of the reference hair to the flow. It is to be noted that this study provided appreciable insights into the coupling effects existing between the artificial hair sensors and in the course of this chapter, references are made to this study for comparisons.

J. Casas *et. al*. [4]'s collaborated work, in fact, precedes the presented work of this chapter and is the fore-runner in using our MEMS hairs for studying viscous coupling effects. Their work significantly filled in a long-remained void in this research by actually measuring the flow field around the hairs, instead of focusing on the hair response itself. Flow field perturbations were measured using particle image velocimetry (PIV) between the fixed hairs, arranged in wide range of inter-hair distances ($9 < s/D < 56$). They reported significant coupling and larger phase shifts between the far-field flow and inter-hair flow, at smaller inter-hair distance and at low flow frequencies.

The motivation to use MEMS hairs for studying the viscosity-mediated coupling has its prominent advantage in providing us a far more reliable control over the hair geometry and hair arrangements. Any approach to perform similar measurements on the actual cricket hairs poses many practical difficulties starting from finding the appropriate hairs for investigation. With MEMS technologies, it is relatively simple to place hairs in specific arrangements, at different distances and also, to some extent, alter the hair lengths and hair diameter [15]. Broadly expanding from the above said work, the presented work will feature specially modified hair sensors (cylindrical hairs, shorter membranes, varying hair lengths etc.) and measure the coupling effect based on the hair response itself.

6.4. Viscosity mediated coupling model

Viscous coupling between two hairs depends on a number of quantities. A simplified aerodynamic model of the viscous coupling between the cricket filiform hairs, found in literature [1,5], is recounted here and presented for its extended applicability also to our artificial hair sensors.

6.4.1 Aerodynamic model

As seen before, viscosity-mediated coupling effects between mechano-receptive hairs in crickets have been studied and modeled in literature [5-7]. Since a comparable size-match exists between the actual cricket hairs and artificial hair sensors, these models on viscosity-mediated coupling can be applied to our sensor systems, using the actual parameters. The models aim to calculate the response of a single hair (reference), for the given oscillatory flow conditions and then re-calculate the response of the reference hair, in presence of another hair (flow perturbing). A coefficient for the coupling is defined based on these two responses of the reference hair. The following model is completely based on the models derived by Bathellier *et. al*. [5].

Figure 6.1a shows the schematic of the model consisting of two cylinders-'*Per*' and '*Ref*' (standing for '*perturbing*' and '*reference*' cylinders) of diameter d, placed along the x-direction and separated by a distance s. Oscillatory air flow is assumed only along x-direction for simplicity and hence, the cylinders move in the direction of flow. The far-field harmonic air flow velocity for the x-direction is given as:

$$V_\infty(t) = V_\infty e^{(i\omega t)}\mathbf{e_x} \tag{6.1}$$

The cylinders oscillate about their bases with a torsional deflection angle, $\theta(t)$. The velocity of the cylinder ("*ref*" or "*per*") parallel to the flow-direction depends on the z-coordinate and is given by [5]:

$$V_{\mathrm{cy}}(z,t) = V^{*}_{\mathrm{cy}}(z)e^{(i\omega t)} = \mathrm{z}\,\dot{\theta}(t) \tag{6.2}$$

where,

$$V^{*}_{\mathrm{cy}}(z) = V_{\mathrm{cy,max}}(z)e^{(i\Phi)} \tag{6.3}$$

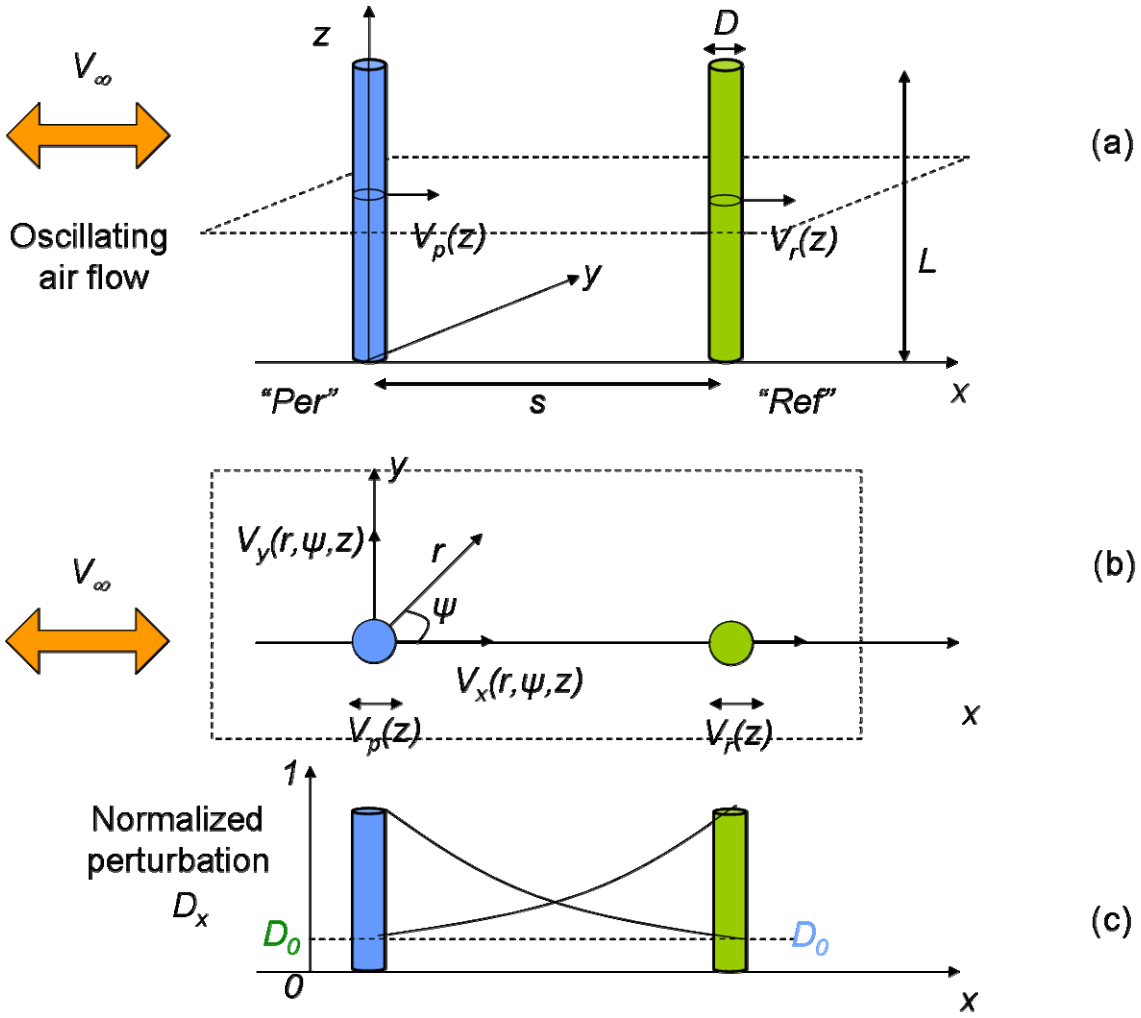

Figure 6.1 *Simple model to derive the dominant parameters of viscous coupling between a reference cylinder and a flow-perturbing one [5].*

Equation (6.3) represents the maximum amplitude and phase shift of the velocity of the oscillating cylinder ("*ref*" or "*per*"). [*Note: In the following analysis, quantities with a '*' as a superscript represent the time-independent component of its complex form.*] Such movement introduces a distortion in the air flow in the vicinity of a moving cylinder and this flow perturbation depends on the spatial position. Figure (6.1b) shows the cross-section of the flow field around the cylinders at a height z, from the base and thus presents a simplified two-

dimensional view of the conditions. It is convenient to use cylindrical coordinates with r, ψ and z for describing the near-field flow velocity distribution around the cylinders. The instantaneous x- and y- components of the air flow velocity, at a height z from the base are given as [5]:

$$V_x^*(r,\psi,z) = V_\infty - D_x(r,\psi)(V_\infty - V_{cy}^*(z)) \tag{6.4}$$

$$V_y^*(r,\psi,z) = -D_y(r,\psi)(V_\infty - V_{cy}^*(z)) \tag{6.5}$$

where D_x and D_y represent the x- and y- components of the perturbations introduced in the flow-field due to the cylinder. The no-slip conditions for this scenario is such that $V_x(d/2,\psi)=V_{cy}$ and $V_y(d/2, \psi)=0$ implying $D_x=1$ and $D_y=0$ at the cylinder surface. The near-field flow distribution around the cylinders is derived by the theory of Stokes' applied to solve the simplified Navier-Stokes' equation [5]. From equations (6.4) and (6.5), the x- and y-components of the perturbation D can be derived in terms of two dimensionless expressions- $\eta=r/D$ and $\lambda=D/2\ (i\omega\rho/\mu)^{0.5}$ and the modified Bessel functions of the second order K_0, K_1 and K_2. They are derived as:

$$\begin{aligned} D_x &= \frac{V_\infty - V_x^*(z)}{V_\infty - V_{cy}^*(z)} \\ &= -\left(\frac{K_2(\lambda)}{K_0(\lambda)}\frac{1}{4\eta^2} + \frac{2K_1'(2\lambda\eta)}{K_0(\lambda)}\right)\sin^2(\psi) \\ &\quad + \left(\frac{K_2(\lambda)}{K_0(\lambda)}\frac{1}{4\eta^2} - \frac{K_1(2\lambda\eta)}{\lambda\eta K_0(\lambda)}\right)\cos^2(\psi) \end{aligned} \tag{6.6}$$

and

$$\begin{aligned} D_y &= \frac{V_y^*(z)}{V_{cy}^*(z) - V_\infty} \\ &= -\left(\frac{K_2(\lambda)}{K_0(\lambda)}\left(\frac{1}{4\eta^2} - \frac{K_2(2\lambda\eta)}{K_2(\lambda)}\right)\right)\sin(2\psi) \end{aligned} \tag{6.7}$$

In the above expressions, D_y is not significant in determining x- or y-components of the near-field distribution as it is 0 for ψ=0 or 90°. For our case, where cylinders are in a parallel configuration along the direction of flow (hence, ψ=0 and $\eta_0=s/D$ *i.e.* the position of the cylinder '*Ref*' from '*Per*' or vice versa), the normalized perturbation (D_x) is simplified and given as [5]:

$$D_0 = \frac{1}{4\eta_0^2}\frac{K_2(\lambda)}{K_0(\lambda)} - \frac{1}{\lambda\eta_0}\frac{K_1(2\lambda\eta_0)}{K_0(\lambda)} \tag{6.8}$$

where D_0 is the actual perturbation in the flow caused by '*Per*' on the cylinder '*Ref*' (or vice versa) and the figure 6.1c shows the schematic of D_x from both of the cylinders.

The flow at any vector position r (figure 6.1) can be derived by summing up the unperturbed far-field flow velocity and velocity perturbations caused by both the cylinders. At any position r along the x-direction, the flow perturbations from the cylinders will be denoted as $D_x(r)$ *and* $D_x(r\text{-}s)$. The flow at any position r along the x-direction is given as [5]:

$$V_x^*(z) = V_\infty - A_p(V_\infty - V_p^*(z))D_x(r) - A_r(V_\infty - V_r^*(z))D_x(r-s) \tag{6.9}$$

where V_p^* and V_p^* are the velocities of the cylinders defined by equation (6.3) and A_p and A_r are two unknown complex terms. The values of these terms can be determined by applying the no-slip condition at the surface of the cylinders (i.e. $V_x^* = V_p^*$ or V_r^*), which yields two equations. The equations are solved and the values of the complex terms are given as [5]:

$$A_p(V_\infty - V_p^*(z)) = \frac{V_\infty}{1+D_0} + \frac{V_r^*(z)D_0}{1-D_0^2} - \frac{V_p^*(z)}{1-D_0^2} \tag{6.10}$$

$$A_r(V_\infty - V_r^*(z)) = \frac{V_\infty}{1+D_0} + \frac{V_p^*(z)D_0}{1-D_0^2} - \frac{V_r^*(z)}{1-D_0^2} \tag{6.11}$$

where D_0 (equation (6.8) represents the perturbation due to a cylinder at the position of another.

Viscosity-mediated coupling between a pair of hair sensors

The cylinders respond to the driving flows by angular deflection θ and the conservation of angular momentum equation is given as [1]:

$$J\frac{d^2\theta}{dt^2} + R\frac{d\theta}{dt} + S\theta = T_d \tag{6.12}$$

where J, R and S are the intrinsic mechanical parameters of the cylinder representing the moment of inertia, torsional damping constant and torsional stiffness respectively. The flow-induced drag torque T_d exerted on the cylinder can be calculated by integrating the drag-force along the length of the cylinder (as discussed in Chapter 2). In order to calculate the viscosity-mediated coupling, we need to solve equation (6.12) for two cases: (i) when the "*ref*" hair is isolated and doesn't have any contribution from a perturbing hair "*per*" and (ii) when the hair sensor has a perturbing hair sensor placed next to it, in the direction of the flow.

The drag-torque acting on an isolated cylinder ('*ref*') is given as:

$$T^*_{\mathrm{d,ref}} = \alpha \int_0^L (V_\infty - V^*_{\mathrm{r}}(z)) z dz \tag{6.13}$$

where $\alpha=4\pi\mu G\text{-}i\pi^2\mu G/g$, $G=g/(g^2+\pi^2/16)$ and $g=ln(\lambda)$ [5]. By solving equation (6.9) using equation (6.10) and filling in the contributing parameters, the complex rotational angle of the reference cylinder (isolated, without any flow perturbations) can be written as [5]:

$$\theta^*_r(\omega) = \frac{3V_\infty R_\mu}{2LJ} \frac{1}{(\omega_0^2 - \omega^2) + i\frac{\omega}{J}(R + R_\mu)} \tag{6.14}$$

where $\omega_0 = (S/J)^{0.5}$ is the resonance frequency of the hair system, ω is the driving oscillatory flow frequency and R_μ represents the damping coefficient due to the surrounding medium, which is air [5]. Now, if a perturbing hair is placed in a parallel configuration, i.e. placed along the direction of the flow ahead of the reference cylinder (figure 6.1), the drag-torque acting on the reference hair ('*ref*') in the presence of perturbing hair ('*per*') is given by [5]:

$$\begin{aligned} T^*_{\mathrm{d,per}} &= \alpha \int_0^L A_r (V_\infty - V^*_{\mathrm{r}}(z)) z dz \\ &= \alpha \int_0^L z dz \left(\frac{V_\infty}{1 + D_0} + \frac{V^*_{\mathrm{p}}(z) D_0}{1 - D_0^2} - \frac{V^*_{\mathrm{r}}(z)}{1 - D_0^2} \right) \end{aligned} \tag{6.15}$$

where $V_{\mathrm{r}}(z)$ and $V_{\mathrm{p}}(z)$ denote the velocity of the cylinders at a height z from their base. Using equation (6.12) in (6.9), the complex rotational angle of the perturbed reference hair (in response to the flow including the perturbations) is given as [5]:

$$\theta^*_p(\omega) = \frac{3V_\infty R_\mu}{2LJ} \frac{\varepsilon_1 + \varepsilon_3 \frac{2}{3} \gamma_{\mathrm{p}}}{(\omega_0^2 - \omega^2) + i\frac{\omega}{J}(R + \varepsilon_2 R_\mu)} \tag{6.16}$$

where γ_{p} is a complex quantity of which the magnitude represents the tip velocity of the perturbing cylinder, normalized by the far-field velocity V_∞. For the case where the perturbing hair is immobile or fixed, this means $\gamma_{\mathrm{p}}=0$ and equation (6.16) is simplified [5]. In equation (6.16), the term ε_1 stands for the perturbed flow[2] at the position of the reference. The term ε_2 represents the additional damping of the reference hair due to the presence of the perturbing cylinder. The term ε_3 represents the dynamic perturbation due to the movement of air medium by the movement of the perturbing cylinder. These three terms, ε_1, ε_2 and ε_3

[2] Note that when the distance between the hairs increases, D_0 becomes progressively small and ε_1 goes to 1, representing the unperturbed flow.

represent the viscous coupling between the cylinders and depend on the lengths of both cylinders [5]. For the cases of different cylinder length scenarios, the values of these constants are given as in the following table [5]:

Table 6.1 Viscous coupling terms for different lengths of the perturbing (L_p) and reference (L_r) hairs. Here D_0 is the normalized perturbation coefficient of a perturbing hair at the position of the reference hair [5].

	ε_1	ε_2	ε_3
$L_p = L_r$	$1-\frac{D_0}{1+D_0}$	$1+\frac{D_0^2}{1-D_0^2}$	$\frac{D_0}{1-D_0^2}$
$L_p > L_r$	$1-\frac{L_r^2}{L_p^2}\frac{D_0}{1+D_0}$	$1+\frac{L_r^3}{L_p^3}\frac{D_0^2}{1-D_0^2}$	$\frac{L_r^2}{L_p^2}\frac{D_0}{1-D_0^2}$
$L_p < L_r$	$1-\frac{D_0}{1+D_0}$	$1+\frac{D_0^2}{1-D_0^2}$	$\frac{L_p}{L_r}\frac{D_0}{1-D_0^2}$

By making use of the above equations, the response of the reference hair in the presence of a perturbing hair and in its absence can be derived and a coefficient for the viscosity-mediated coupling can be defined as:

$$\kappa_1 = \frac{\theta_r - \theta_p}{\theta_r} \tag{6.17}$$

By measuring the response of the reference, in presence and absence of a perturbing hair, the effect of viscosity-mediated coupling can be experimentally investigated.

Viscosity-mediated coupling between three hair sensors

As an interesting scenario, we will consider the case where three cylinders are arranged in line to the oscillating flow (see figure 6.2). The hair in the middle is treated as our reference, which is perturbed by the presence of two hairs, one on either side. From the previously discussed model (of a pair of hairs), we have seen that the flow perturbation caused by one of the hairs at the position of another, placed along the x-axis, is equal and denoted as D_0 (as in figure 6.1). This could be extended to the case of three hairs. The reference hair is subjected to the flow perturbations from the hairs ("*per1*" and "*per2*") on either side.

For the case of three hairs, the flow at the position of the reference hair, is perturbed by two perturbing hairs, one on either side. Furthermore, both perturbing hairs mutually influence each other, at a distance $2s$. Let us assume the flow perturbation of the perturbing hairs at the position of the reference hair as D_1 and flow perturbation of the perturbing hairs at the position of the other perturbing hair as D_2. The modified form of equation (6.9) (for the three hair case), is applied with the no-slip condition at the surface of reference hair and perturbing hairs as:

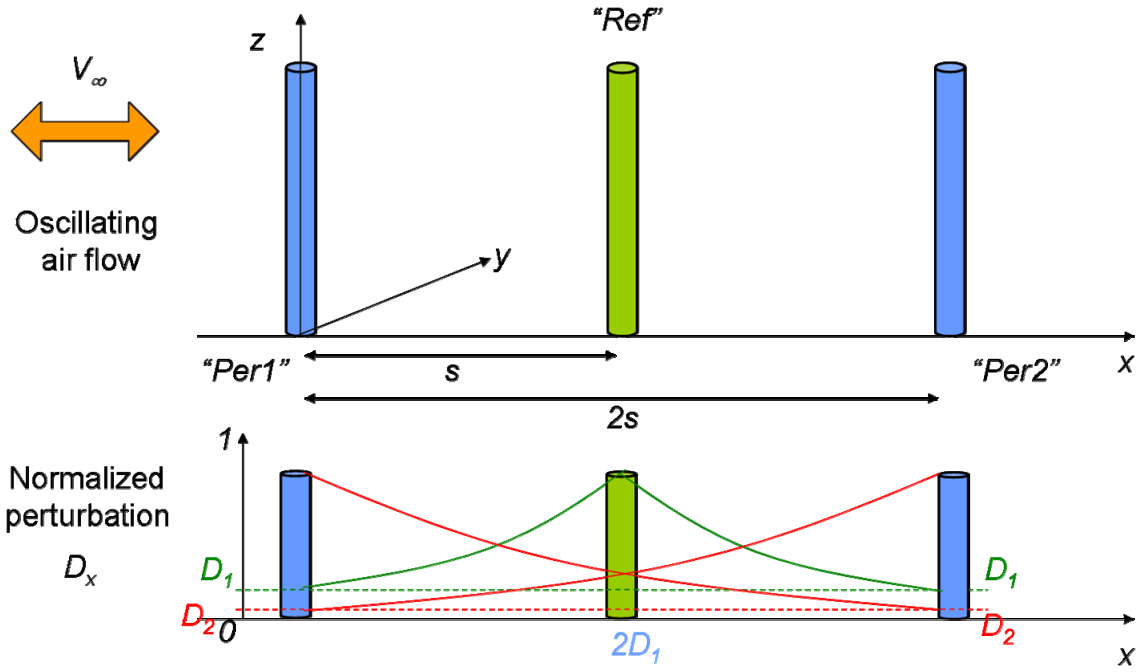

Figure 6.2 *Simple model for viscous coupling between three hairs showing: (i) D_1, between a reference hair and two flow-perturbing hairs (of same length), one on either side and (ii) D_2, between two flow-perturbing hairs*

$$V_r^*(z) = V_\infty - 2A_p(V_\infty - V_p^*(z))D_1 - A_r(V_\infty - V_r^*(z)) \tag{6.18}$$

$$\begin{aligned} V_p^*(z) = V_\infty - A_p(V_\infty - V_p^*(z)) - A_r(V_\infty - V_r^*(z))D_1 \cdots \\ - A_p(V_\infty - V_p^*(z))D_2 \end{aligned} \tag{6.19}$$

where the complex terms for perturbing hairs are assumed $A_{p1}=A_{p2}=A_p$. The value of the complex term for the case of the reference hair being perturbed by two perturbing hairs is calculated as:

$$\begin{aligned} A_r\left(V_\infty - V_r^*(z)\right) = \frac{V_\infty(1+D_2-2D_1)}{(1+D_2-2D_1^2)} + \frac{V_p^*(z)(2D_1)}{(1+D_2-2D_1^2)} \\ - \frac{V_r^*(z)(1+D_2)}{(1+D_2-2D_1^2)} \end{aligned} \tag{6.20}$$

The drag-torque acting on the "*ref*" hair in presence of two perturbing hairs can then be determined as:

$$T^*_{\mathrm{d,2per}} = \alpha \int_0^L A_{\mathrm{r}} z dz$$
$$= \alpha \int_0^L z dz \left(\frac{V_\infty (1 + D_2 - 2D_1)}{(1 + D_2 - 2D_1^2)} + \frac{V^*_{\mathrm{p}}(z)(2D_1)}{(1 + D_2 - 2D_1^2)} - \frac{V^*_{\mathrm{r}}(z)(1 + D_2)}{(1 + D_2 - 2D_1^2)} \right) \quad (6.21)$$

The complex rotational angle of the doubly-perturbed reference hair (in response to induced flow perturbations by two perturbing hairs on either side), shown in equation (4.13), is modified as:

$$\theta^*_{2p}(\omega) = \frac{3V_\infty R_\mu}{2LJ} \frac{\varepsilon_4 + \varepsilon_6 \frac{2}{3} \gamma_{\mathrm{p}}}{(\omega_0^2 - \omega^2) + i \frac{\omega}{J}(R + \varepsilon_5 R_\mu)} \quad (6.22)$$

where γ_{p} is a complex quantity of which the magnitude represents the tip velocity of the perturbing cylinder, normalized by the far-field velocity V_∞. Table 6.2 shows the values of ε_4, ε_5 and ε_6, for the case that all the cylinders (reference and perturbing) are of same length.

Table 6.2 Modified **v**iscous coupling terms equal lengths of the perturbing (L_{p}) and reference(L_{r}) cylinders for the three-cylinder model.

	ε_4	ε_5	ε_6
$L_{\mathrm{p}} = L_{\mathrm{r}}$	$\frac{(1 + D_2 - 2D_1)}{(1 + D_2 - 2D_1^2)}$	$\frac{(1 + D_2)}{(1 + D_2 - 2D_1^2)}$	$\frac{2D_1}{(1 + D_2 - 2D_1^2)}$

From equations (6.14), (6.16) and (6.21), we have rotation responses of a hair for three different cases respectively as: (i) θ_{r} corresponding to the unperturbed response, (ii) θ_{p} corresponding to the response while being perturbed by one of the hairs and (iii) $\theta_{2\mathrm{p}}$ corresponding to the response while being doubly perturbed by the hairs on either side. From these three responses, three coupling coefficients can be defined for the case of three hairs. The coefficient for the viscosity-mediated coupling of either one of the perturbing hairs on the reference hair is defined as:

$$\kappa_2 = \frac{\theta_{\mathrm{p}} - \theta_{2\mathrm{p}}}{\theta_{\mathrm{p}}} \quad (6.23)$$

This coefficient indicates the effect on the flow response of the reference hair, while one of the perturbing hairs is absent and the other one is still present. On the other hand, the coefficient for viscosity-mediated coupling of both perturbing hairs is defined as:

$$\kappa_3 = \frac{\theta_r - \theta_{2p}}{\theta_r} \tag{6.24}$$

The presented analysis comprising of two- and three-hair models provides interesting insights which can be applied to our hair sensors. The novelty in the model is the presence of the secondary coupling effects between three hairs. The effect of viscosity-mediated coupling between the hair sensors can be experimentally determined and the results can be compared with this model.

6.5. Design and fabrication

The motivation is to design a dedicated chip to characterize the impact of each parameter on the viscous coupling effects, identified in the previous section. While the basic schematic of the hair sensor is retained, slight modifications in the sensor design are made for this special chip. The fabrication of the chip is rather similar to the process flow discussed in chapter 3. However, slight modifications with respect to the hair design are made.

6.5.1 Chip design

The previous section gives a general insight into the parameters that play a role in the viscous coupling between the hairs. The three chief parameters are identified, namely:

1. normalized distance between the hairs (*s/D*)
2. hair length (*L*) and
3. driving flow frequency (ω)

Of these three, only the first two are concerned with the design itself, while the flow frequency is varied during the actual characterization experiments. For the dedicated chip, sensors are chiefly varied based on their inter-hair distance or their lengths. Other than these, there are additional design variations taken into account, namely:

(i) impact of a fixed and a free-moving perturbing hair
(ii) impact of a perturbing hair, in front and back-side of the reference hair sensor

The dedicated chip is designed in such a way as to comprise specific arrangements, to characterize all the above said parameters in a single dedicated platform. For these arrangements, it is necessary that the hair sensors are slightly modified from their original dimensions. The membrane of the sensor is modified to 100x100 μm^2 (compared to 200x100 μm^2, for the normal sensors discussed in chapter 3). Reduction in the membrane size helps in arranging the sensors very close to each other. The springs to suspend the sensor membrane are 100 μm long, 6 μm wide and ~1 μm thick (same thickness as the membrane itself).

Each arrangement is designed to vary a particular factor, either the normalized distance or the hair length. Each of these arrangements is placed in a row, on the dedicated chip and each such row is placed at ~500 μm (*i.e. s/D* ~ 10) away from the next row. The effect of viscous coupling between SU-8 hairs arranged in perpendicular configuration has been modeled by [9]. While there exist some coupling effect it was reported that at distances (*s/D* >5), the coupling is less than 0.1 at 160 Hz. Hence, this large spatial gap between the rows is expected to yield minimal mutual impact of neighboring-rows.

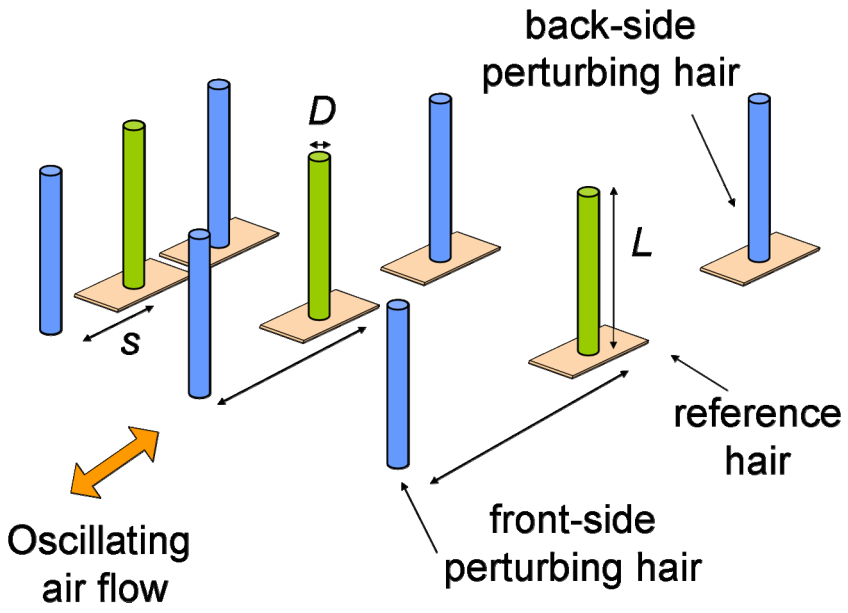

Figure 6.3 *Schematic of the hair sensors arranged on the chip at varying distances (s) between them.*

Normalized distance between the hairs

The normalized distance between the hairs plays an important role and to characterize it, three hairs are arranged next to each other, at specific distances (figure 6.3). The chosen inter-hair distances (*s,* center-to-center) are of 150, 200, 300, 400 and 600 μm, which for a hair of 50 μm diameter (*D*), transforms into normalized distances ranging from 3 - 12. The hair sensor in the middle of the three acts as the reference for the characterization, while the first and the third hairs in the arrangement are the flow-perturbing hairs from the front-side and the back-side (i.e. in the direction of driving air flows).

Also, it is to be noted that, while all the hair sensors in these arrangements are of free-moving type, the first flow-perturbing hair is either fixed to the substrate (hence, doesn't have a sensor membrane) or a free-moving one (as others in the arrangement). Based on this, two different groups are designed for the characterization of normalized distance between the hairs, one featuring all free-moving hair sensors placed at different distances and the other featuring a fixed hair to face the flow first, while others are normal free-moving sensors. This is to characterize the coupling impact of a fixed and a free-moving hair on the reference hair sensor.

Hair length variations

To characterize the impact of hair length in the viscous coupling effect, two designs are chosen: (i) longer hairs of ~800 μm and (ii) shorter hairs of ~400 μm (see figure 6.4). The longer hairs are designed to have a constant diameter of 50 μm, for both top and bottom parts (which is in contrast to the long hairs used in the normal version of the hair sensors with 50 μm for bottom and 30 μm for the top part of the hair). Since there are two types of hair involved (i.e. perturbing and reference hairs), three possible combinations are chosen as follows:

(i) Front-side perturbing hair is short and the other hairs are long

(ii) Both perturbing hairs and the reference hair are equally long

These two combinations were designed for two different inter-hair distances, 150 and 300 μm and grouped separately.

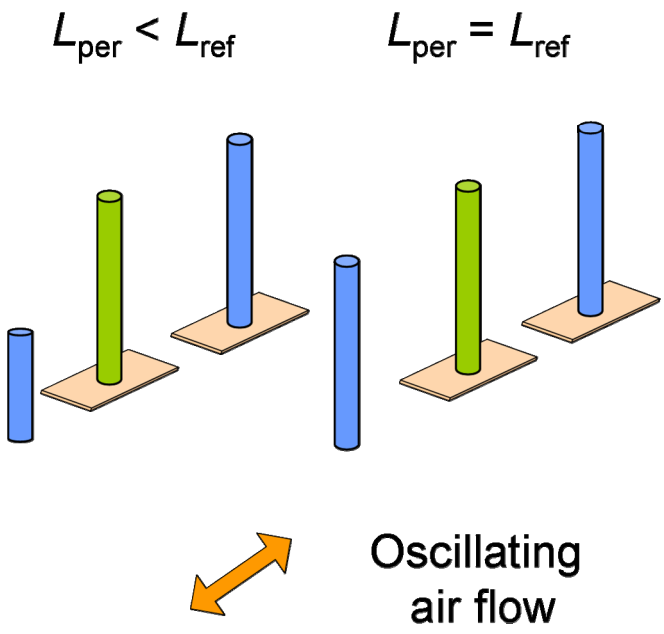

Figure 6.4 *Schematic of arrangement of hair sensors with varying hair length, placed at two different inter-hair distances (150 and 300 μm).*

All these design combinations are put together on a single platform and diced manually. The wide space between the different groups facilitates to manually remove the unwanted hairs during the measurements.

6.5.2 Microfabrication

The chip is fabricated using micromachining similar to the process flow presented in chapter 3 and details are presented in Appendix A. A schematic of the hair sensors is shown in figure 6.5. A brief overview is presented here. First, a protective layer of silicon-rich nitride is deposited using LPCVD, followed by the deposition of a ~800 nm thick poly-silicon layer. This poly-silicon layer acts as a sacrificial layer for the final release of the structures. A ~1 μm thick silicon-rich nitride layer is deposited and patterned to form the sensor membranes and springs. The membrane is covered by a thin layer of Aluminum (which functionally serves as the top electrode of the sensor capacitors, but in the current studies, only serves as a reflecting surface during optical characterization). Long hairs are made by two subsequent layers of SU-8 (of ~350 μm each) using standard lithography techniques. Finally the sensor membrane is released by selective-etching of the sacrificial poly-silicon layer (Figure 6.5) using a XeF_2 etcher. Figure 6.6 shows SEM images from different portions of a successfully realized chip.

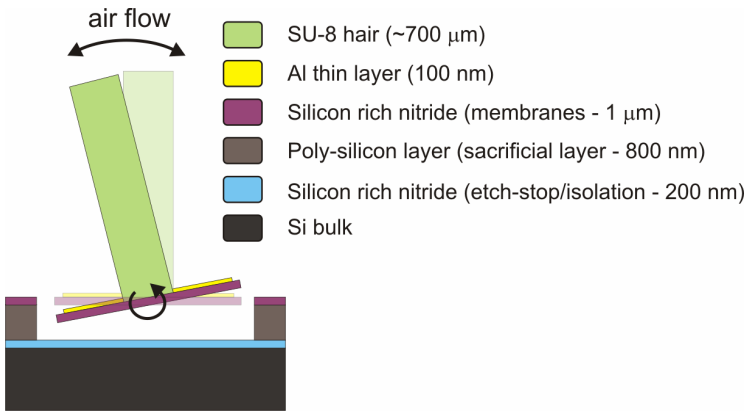

Figure 6.5 *Schematic of the artificial hair sensor: an SU-8 hair acts as a flow-receptor, mounted on the suspended silicon rich nitride membrane. An aluminum thin layer serves for optical measurement of the membrane tilt.*

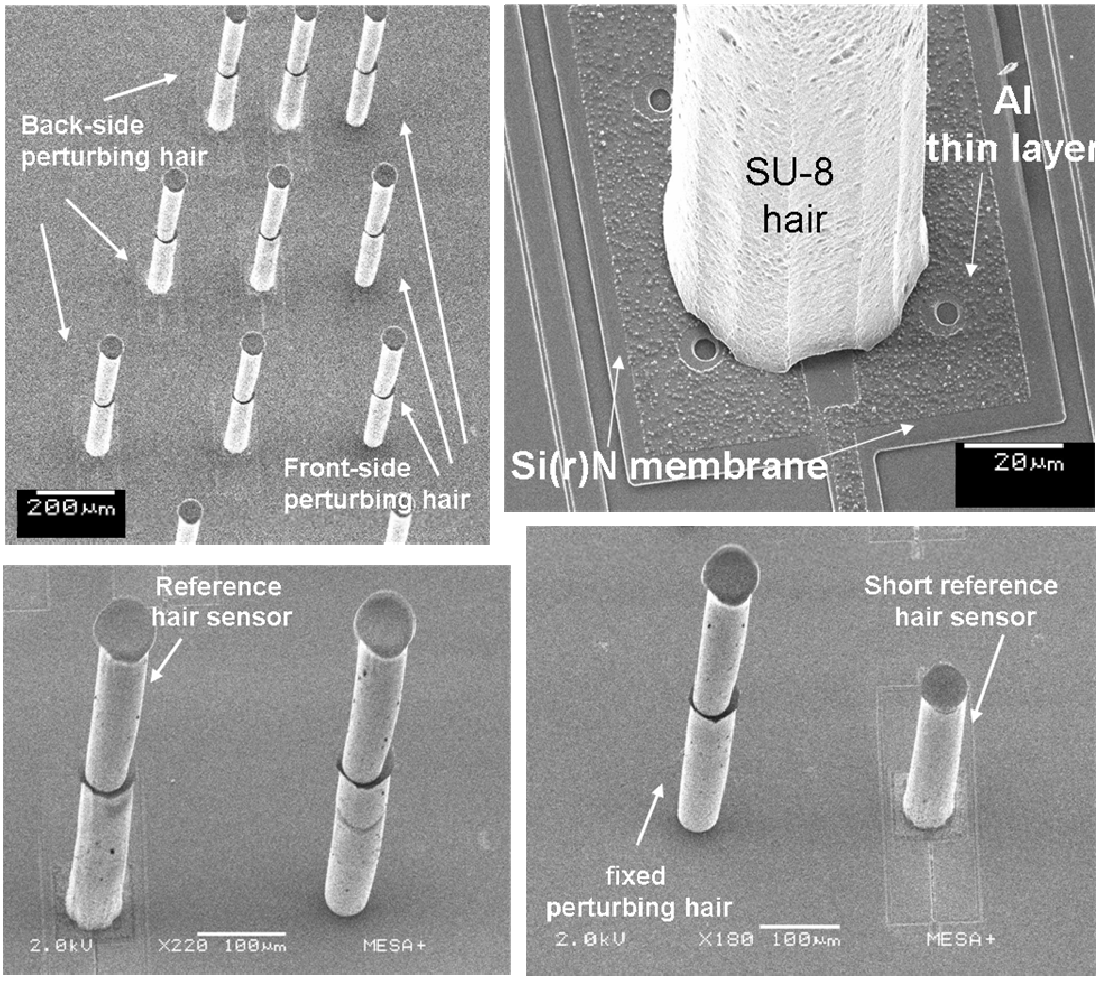

Figure 6.6 *SEM images showing different portions of the novel chip for characterization of viscosity-mediated coupling. Pictures are: (top-left) hair sensors are arranged at various inter-hair distances, (top-right) close-up of the Si(r)N membrane and hair base, (bottom-left) free-moving reference hair sensor placed near a fixed perturbing hair of same length, (bottom-right) fixed perturbing hair in front of a short hair reference sensor.*

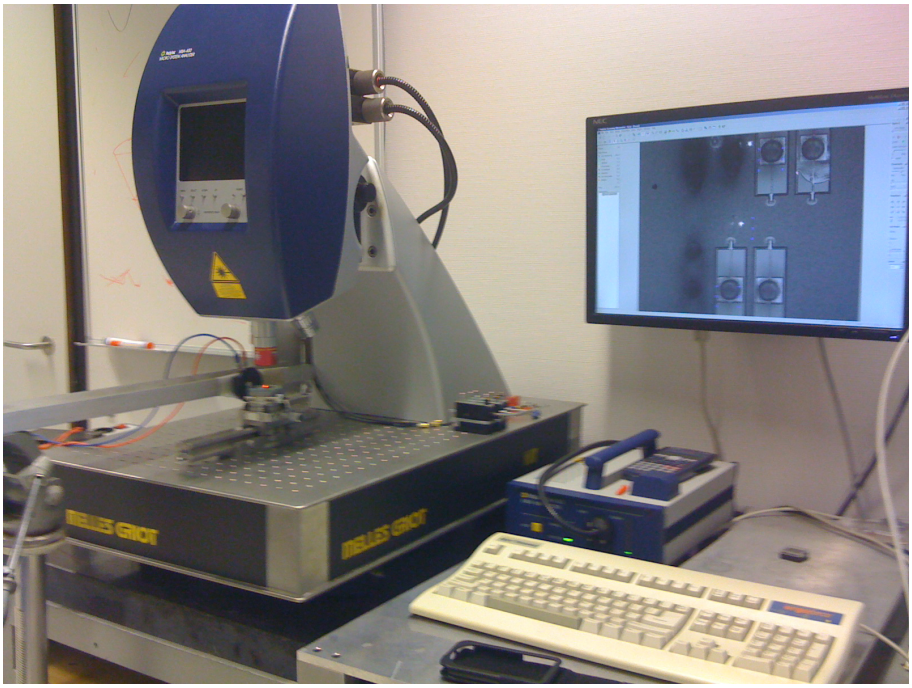

Figure 6.7 *Snapshot showing the laser vibrometer, accompanied by the integrated optical microscope. The vibrometer software, by which the laser scan points are positioned, aids in accurate placement of the sensor chip, before and after the manual removal of perturbing hairs.*

6.6. Characterization and results

6.6.1 Measurement setup

The hair-sensors are exposed to the near-field of a small loudspeaker (diameter, 4 cm) and their mechanical responses are optically characterized by a laser vibrometer (Polytec, MSA400) [10]. Figure 6.7 and 6.8 show a snapshot of the laser vibrometer and a schematic of the measurement setup, respectively. In order to calibrate the generated flow field, the loudspeaker is first placed under the laser vibrometer measuring the movement of its membrane under given actuating voltages and frequencies.

The sensor chip is then placed on a steady platform under the laser vibrometer. The loudspeaker is mounted on a separate stand to avoid any unwanted coupling of mechanical vibrations to the measurement system. The sensors were always placed in such a way that the hairs were exposed to the flow from the center of the loudspeaker membrane (where the flow is assumed to have high uniformity [10]) and at the nearest possible position from the loudspeaker to ensure all the measurements were performed in the near-field [13] of the loudspeaker.

Using the laser vibrometer the dynamics of the hair-sensor under given flow fields were accurately measured. Scan points were placed (using software) on both edges of the suspended membranes (on top of the Aluminum layers, for better reflectivity) and maximum displacements were measured. From these displacements and the distance between the scan points, the rotational angles were calculated.

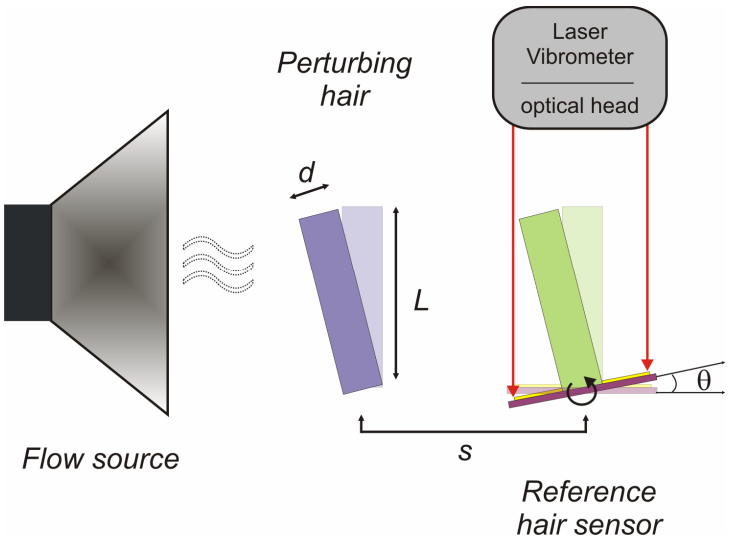

Figure 6.8 *Experimental setup comprising of a flow source (loud speaker), the chip with artificial hair sensors and the laser vibrometer. The rotational angle of the sensor membrane is measured in presence and absence of a flow perturbing hair.*

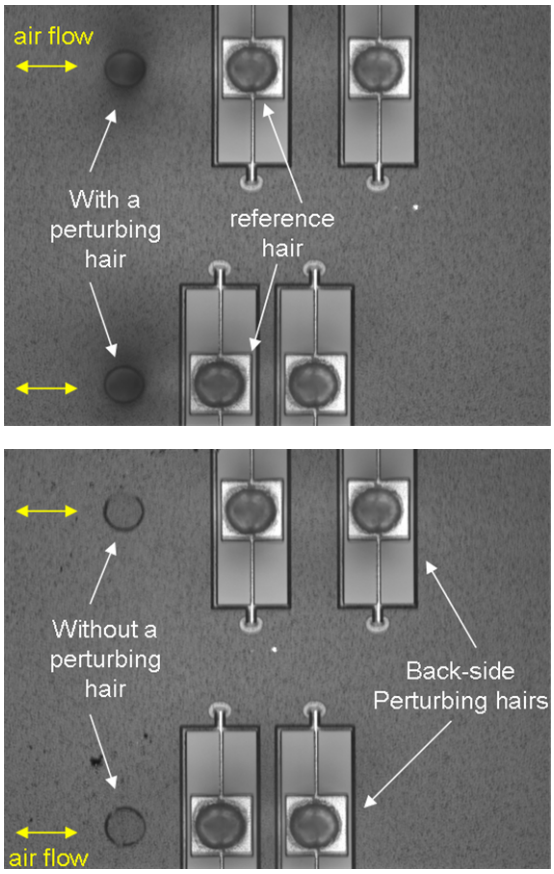

Figure 6.9 *Microscopic images of the laser vibrometer showing the near-identical situations for the optical characterization, before and after manual removal of perturbing hairs. This accurate placement of the chip was aided by the use of the laser scan points from the vibrometer.*

In order to characterize the viscosity-mediated coupling between the hair sensors measurements were performed on a reference hair sensor, with the presence of one or two hair sensors nearby and repeated in the absence of it (after manual removal of the perturbing hair(s)). For both measurements the corresponding rotational angle of the reference sensor was calculated and hence, the coupling coefficient was determined. However, the manual removal of the perturbing hair is tedious and care was taken to ensure that both measurements took place in near-identical conditions. The hair was removed using a micro-probe and the chip was placed back into the system, exactly at the same position as before (see figure 6.9). The precise placement was aided by the scan points of the laser vibrometer software.

6.6.2 Results

Measurements were done on chips containing three free-moving hair sensors in a row. The sensor in the middle is our reference sensor and optical measurements were made on it, for three different cases: (i) when two perturbing hair sensors were present, (ii) when one of the hair sensors (at the back-side) was removed and (iii) when both perturbing hairs were removed. The measurements were repeated for three normalized distances (s/D ~ 2.1, 2.9 and 8.6). Figure 6.10 shows the normalized frequency response of the reference hair sensor (θ_{2p}, θ_p and θ_r), for the three different cases of flow perturbation at three different normalized distances. The error margins in the measurement values accounts for the possible variations in the flow source and variations in positioning of the sensors (manually done with the aid of the laser vibrometer software, as described before). The responses are compared with the model, as presented in section 6.4. The response of the reference hair was observed to be distinct for each case of normalized distance and shows clear influence by the normalized distance between the hair sensors.

Figure 6.11 shows the coefficients of viscous coupling (κ_1, κ_2 and κ_3) calculated from the above measurement results, for the three normalized distances. The results are compared with model predictions as discussed in section 6.4. The measurements show reasonable agreement with the model and show significant coupling at smaller normalized distances (s/D ~ 2.1 and 2.9) but the coupling effect strongly reduces at larger distance (s/D ~ 8.6). The coupling coefficients were observed to be substantial at low frequencies and gradually decrease with frequency. Furthermore, one interesting aspect is observed at the normalized distance (s/D ~2.1), where a clear difference between the measured values show $\kappa_1 < \kappa_2$. At longer distances (s/D ~2.9 and ~8.6) this becomes $\kappa_1 \sim \kappa_2$ as the second neighbor coupling strongly reduces.

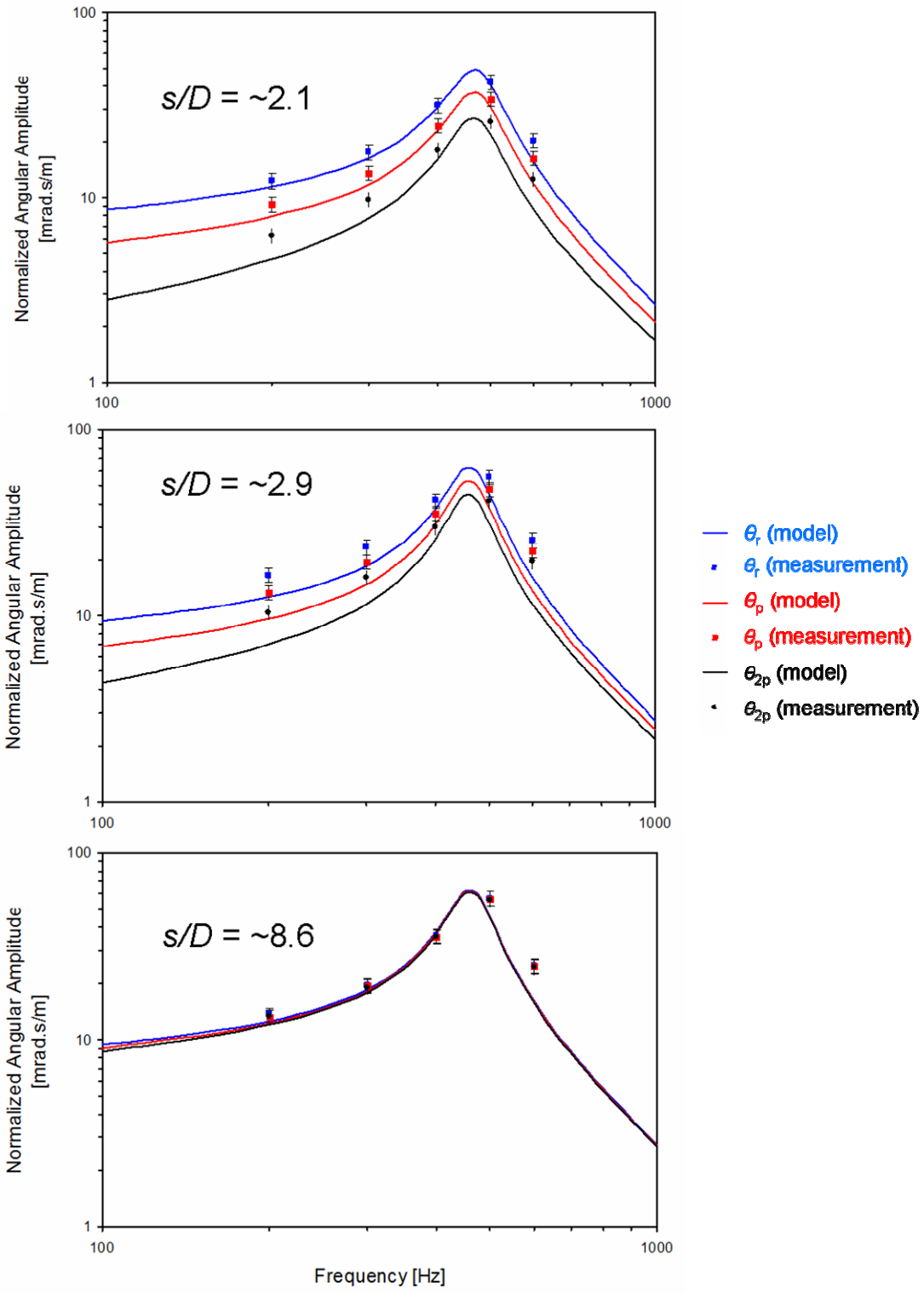

Figure 6.10 *Normalized angular responses of the reference hair sensor for three different cases: (i) when both perturbing hair sensors were present at the front and back side (θ_{2p}), (ii) when the back-side perturbing hair was removed (θ_p) and (iii) when both perturbing hair sensors were removed (θ_r). The measurements were made for three normalized distances (s/D ~ 2.1, 2.9 and 8.5) which shows clear influence of the distance on the coupling effect.*

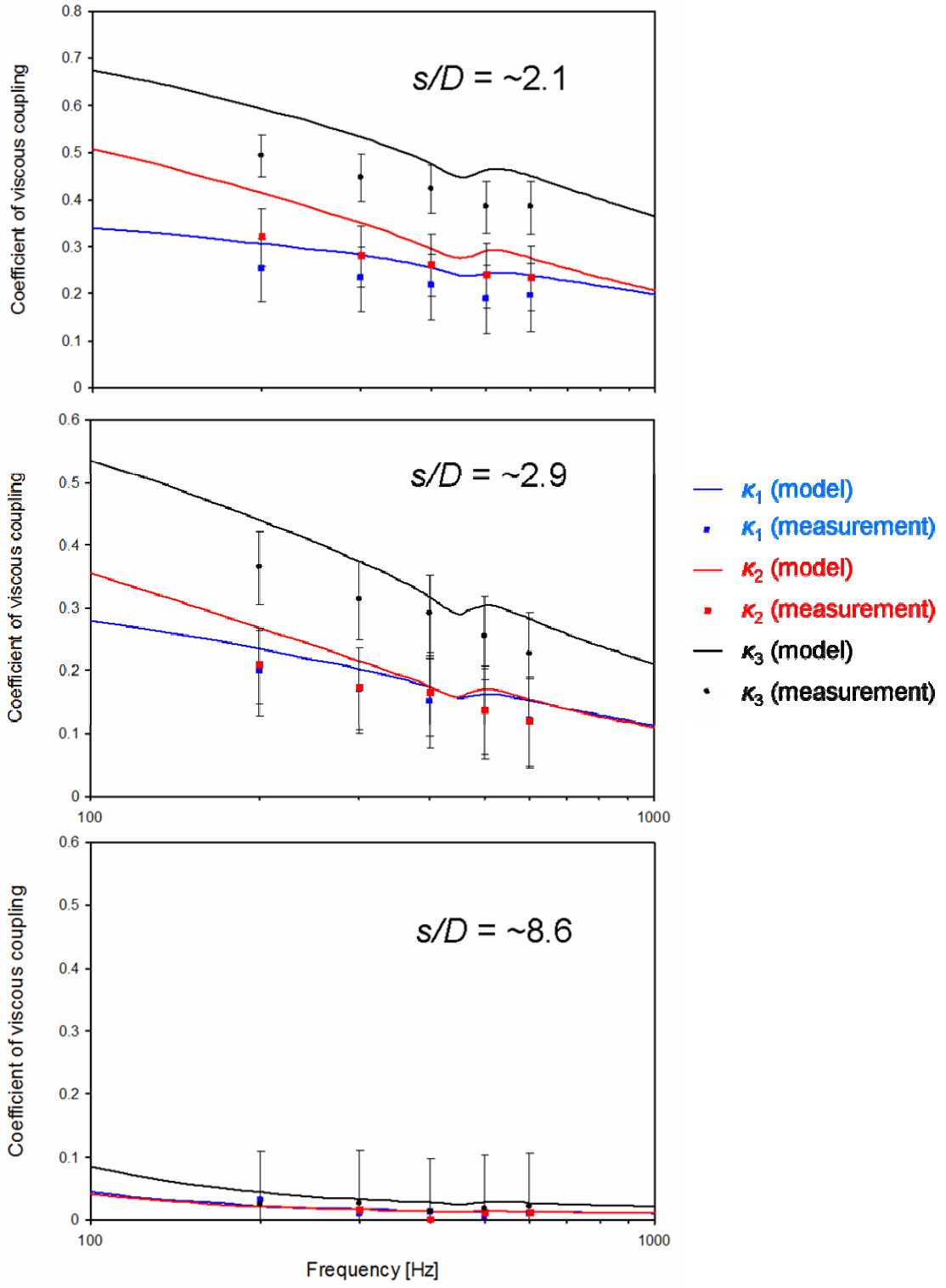

Figure 6.11 *Coefficients of viscous coupling (κ_1, κ_2 and κ_3, as defined in section 6.4) calculated from the measurements performed at three normalized distances. Significant coupling is observed at smaller distances between the hair sensors and the effect reduces greatly at higher distances. Comparisons are made with the models and show reasonable agreement.*

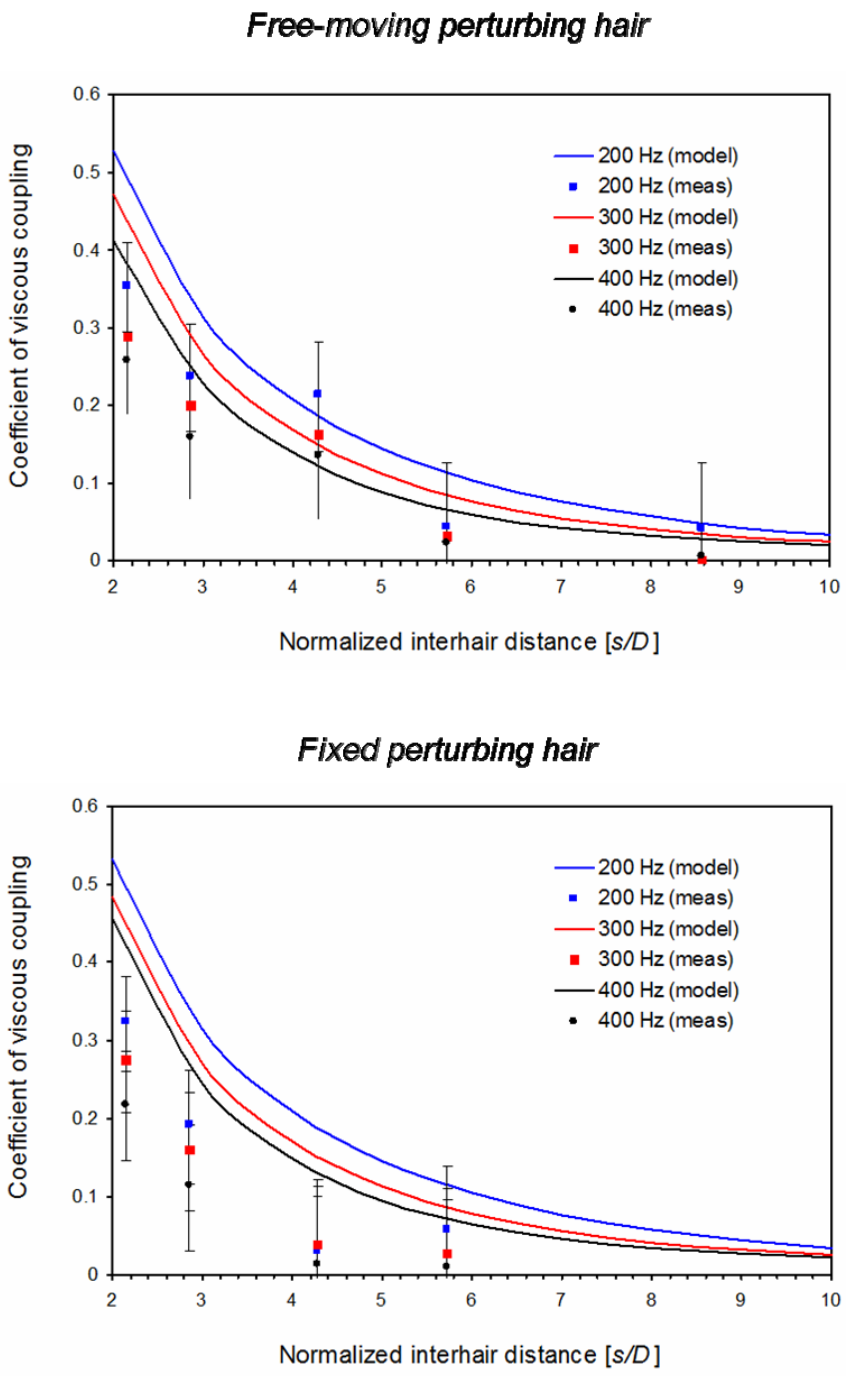

Figure 6.12 *Measurement results showing the effect of a free-moving or fixed front-side perturbing hair on the reference hair sensor (while in presence of free back-side hair, for both cases). The coefficient of coupling (κ_2) is measured at different normalized distances and for the frequencies – 200, 300 and 400 Hz.*

Figure 6.12 shows the effect of a free-moving and a fixed perturbing hair (on the front-side) on the reference hair sensor. A back-side perturbing hair sensor was present in all the measurements and only the front-side perturbing hair sensor (fixed or free) was removed.

The measured coefficient of viscous coupling (κ_2, in this case) measured at different normalized distances (s/D) are shown at frequencies – 200, 300 and 400 Hz. The results are compared with the models presented in section 6.4. For the case of determining the effect of the fixed hair sensor, equation (6.22) is modified by assuming $\gamma_p = 0$ (similar to Bathellier *et. al.* [5]). The coefficient of viscous coupling for both cases was observed to be significant at lower frequencies but seen to decrease with frequency.

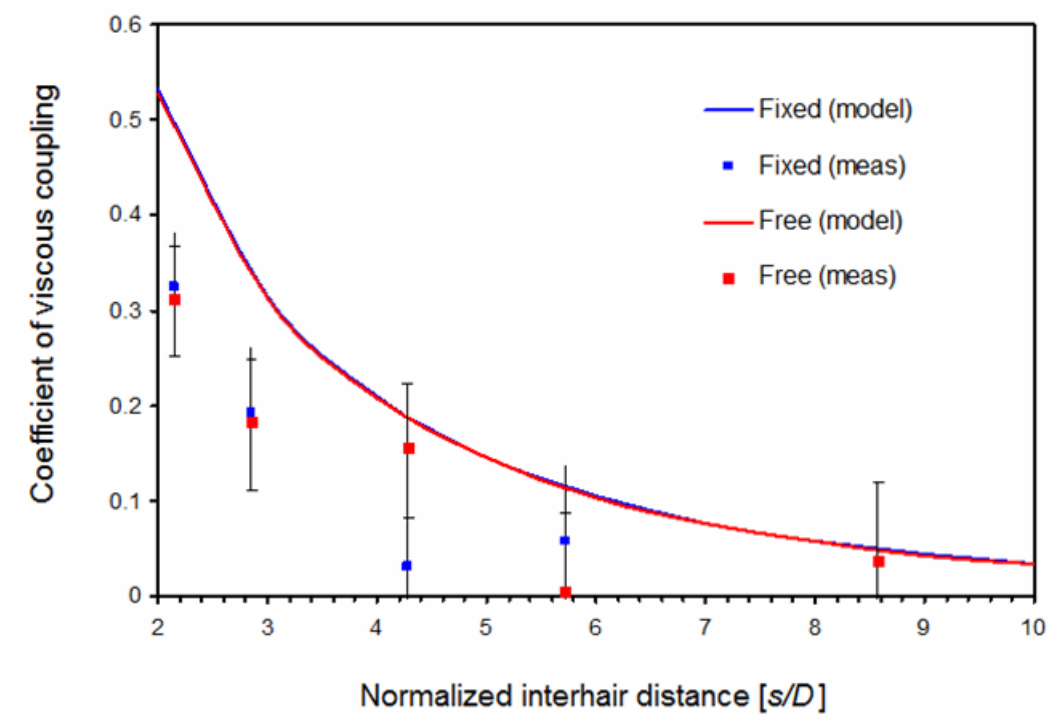

Figure 6.13 *Comparison of coefficient of viscous coupling at 200 Hz, for a free-moving or fixed front-side perturbing hair on the reference hair sensor (while in presence of free back-side hair, for both cases). The coefficient of coupling (κ_2) is observed to be almost similar for both cases.*

Figure 6.13 shows the coefficient of coupling for fixed and free-moving front-side perturbing hair measured at 200 Hz. Interestingly, the measurements reveal that both free-moving and fixed perturbing hair sensors have not much different coupling with the reference hair sensor. This is also shown in the model predictions for both cases. But this is contrary to the measurement observations on the actual filiform hairs by Bathellier *et. al.* [5], where fixed hair contributes to significant coupling and free-moving hairs contribute very little. This result is discussed more in the next section.

Figure 6.14 compares the effect of length of a fixed perturbing hair on the reference hair (while a back-side perturbing hair is present) at short normalized distance ($s/D \sim 2.14$). Two different fixed perturbing hairs are considered here: (i) both perturbing hairs and reference hair is of same length (ii) the front-side perturbing hair is shorter than the reference hair. Significant effects are observed when the hairs are of equal length. Clearly a short perturbing hair has less impact on a longer reference hair ($\kappa < 0.1$).

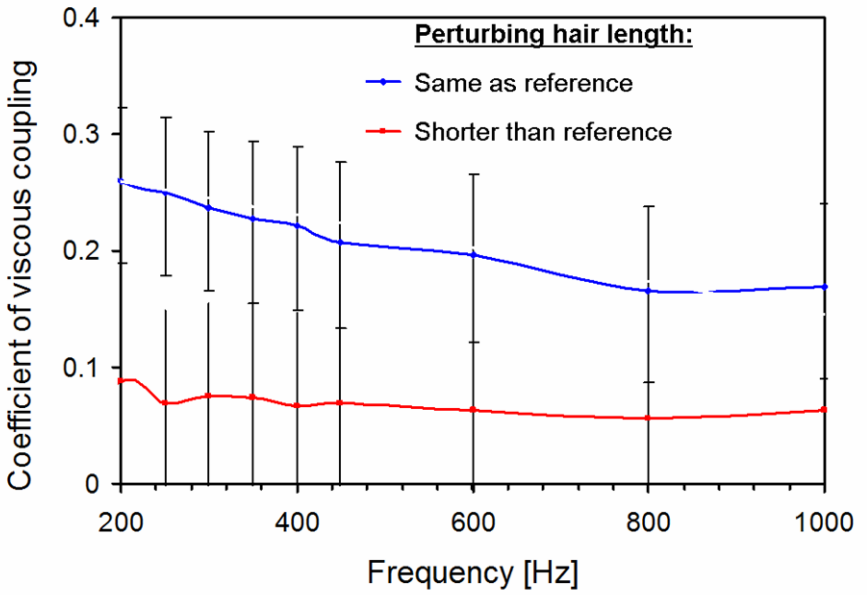

Figure 6.14 *Results indicating that the length of the perturbing hair has significant effect on viscous coupling to the reference hair (in presence of a back-side perturbing hair). Front-side fixed perturbing hair was of two different lengths: (i) same as the reference and (ii) half the length of the reference hair. The hairs were at a normalized distance, s/D ~ 2.1.*

6.7. Discussion

The quality of the fabricated chips for viscous coupling has one important critical remark. It has to do with the geometry of the hair. While the designed value for the hair diameter is 50 μm the observed diameter of the hairs were ~70 μm. Such a variation is attributed to the over-exposure setting of the two SU-8 layers. The reason for such a setting is that these chips were fabricated along with a number of normal hair sensor arrays, which feature the hairs with two dissimilar top and bottom diameters. In our previous fabrication runs, we observed the top part of those hairs being too fragile and as an interim control action, it was decided to increase the exposure time of the SU-8 layers. Since the chips for viscous coupling were present along with them, they resulted in larger hair diameters. However, such increase in the diameter substantially increases the hair moment of inertia, which will eventually reduce the best frequency of the hair sensor. This could actually help us in the case of characterization of viscous coupling effect, as the effect is prominent at low frequencies. On the other hand, such large diameters actually alter the normalized distances between the hairs from their design values (for instance, inter-hair distance, *s* of 150 μm, the normalized distance *s/D* changes from 3 to 2.14, for design and measured hair diameters of 50 and 70 μm, respectively.) Further, in reality, the shape of the actual hair is never a perfect cylinder (as assumed in the models) and usually has slight variations at both ends and at center of it (where two dissimilar layers of the hair, meet).

Figure 6.11 compares the calculated and measured coefficient of viscous coupling at three different cases of perturbations (i.e. (i) when two perturbing hairs are present, (ii) when one perturbing hair is present and (iii) when no perturbing hairs are present). The model presented in section 6.4 has been used taking the actual hair sensor dimensions into account

and shows reasonable agreement with the measurements while predicting the overall trends very well. For the case of *s/D* ~2.1, an interesting observation is made where the coefficients (κ_1 and κ_2) show significant difference in their values over the various frequencies (*i.e.* $\kappa_1 < \kappa_2$). While it is observed as $\kappa_1 = \kappa_2$ at other normalized distances (*s/D* ~2.9 and 8.6), this is a clear evidence of (as in *s/D* ~ 2.1) secondary perturbation effects of the hairs. At closer distances, the back-side perturbing hair affects the front-side perturbing hair and vice versa.

Figure 6.12 compares the coupling effect of a free-moving and a fixed perturbing hair on the reference hair (in presence of a free-moving back-side perturbing hair). It was observed that both cases showed similar coupling effect on the reference hair sensor. It is very interesting to compare the results with the similar cases discussed in literature. For the actual spider hairs, a fixed hair has a stronger coupling impact than free-moving hairs [5]. But as a stark contrast, our results show more or less similar coupling effects for both cases (see figure 6.13). Not surprisingly, we think this has to do with the large stiffness of our sensor springs, compared to those of actual trichobothria [18]. Due to the large torsional stiffness, the motion of the fixed and free-moving hairs under the flow conditions, do not make a stark difference. This is also evident from the model predictions shown for both cases, which take the actual torsional stiffness values into account.

Figure 6.14 shows the impact of hair length variations of the perturbing hair on the reference hair. As expected, the longer hair shows stronger coupling than a shorter one. Such a behavior is theoretically predicted in literature [5] and our results confirm these predictions for the artificial hair sensors as well.

In section 6.3, it was mentioned that G. Lewin *et. al.* [9] developed an FEM model for viscous coupling which was extended to our artificial hair sensors. The model was designed to incorporate the artificial sensor's geometrical parameters, i.e. hair length of 1000 μm and 50 μm diameter. Figure 6.15 shows the results of our measurements compared with both Bathellier's [5] and Lewin's [9] models. Only the coefficient of viscous coupling between two hair sensors is considered (i.e. κ_1) in the comparison, as both models were incorporated for two hairs. While the measurements show reasonable agreement with the models, it has to be noted that the difference between the model values comes from the fact that our measurements were done at 200 Hz as opposed to Lewin's published model results which were evaluated at 160 Hz. Hence, Lewin's results are expected to show a higher estimate than Bathellier's model. Nevertheless, comparing the models with the measured coupling coefficients it seems both models are over-estimating the viscous coupling effects for our artificial sensors.

The first set of results, already gives a solid critical remark to the existing design of array patterns. As per the current design, the hairs (~700 μm long) are separated by 300 μm (i.e. for a hair diameter of 70 μm, the normalized distance, s/D ~ 4.2) and the results clearly show the coupling effect is high ($\kappa > 0.1$) for such a distance. It can be assumed that the present sensor arrays do suffer from significant viscous coupling effects. Hence, the most important insight that can be derived from the presented results will be the crucial design rule for minimum distance between the hairs of our sensor arrays. Future generations of our hair sensor-arrays will feature hairs of different lengths and shapes, individually addressed for flow imaging applications. From the observations from the effect of short and long hairs on the reference hair sensor, it can be confidently assumed that for future design of arrays comprising different hair lengths, sensors with long hairs can be surrounded by shorter ones without high viscous coupling.

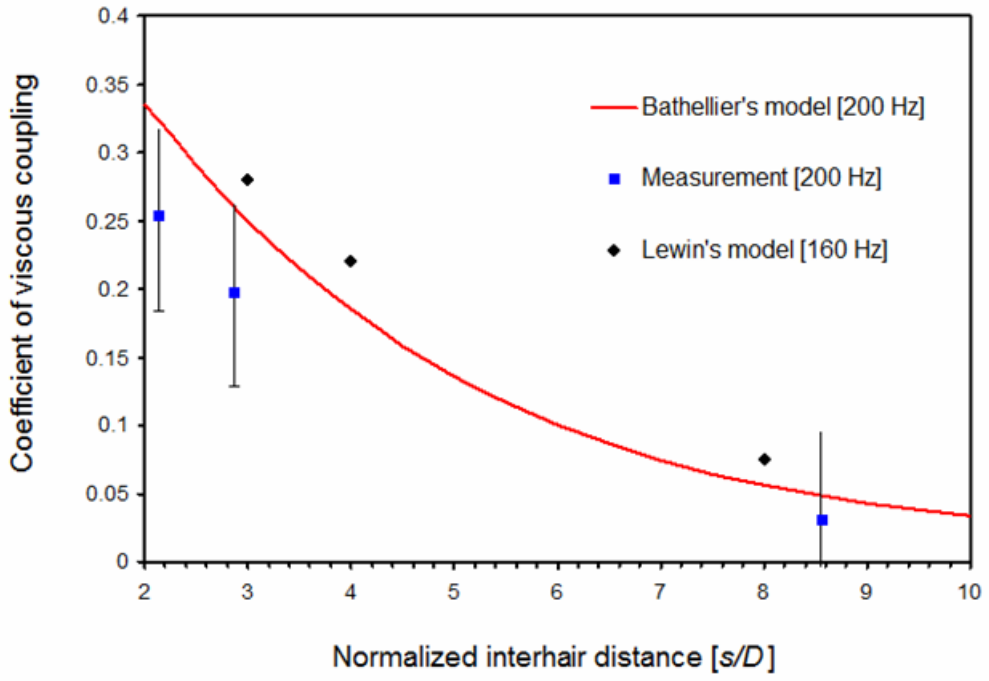

Figure 6.15 *Comparison of coefficient of viscous coupling (κ_1) at 200 Hz, between a perturbing hair sensor and a reference hair sensor with model results from B. Bathellier [5] and Lewin [9].*

6.8. Conclusions

A microfabricated chip featuring artificial hair sensors arranged in specifically designed patterns to characterize the presence of viscosity-mediated coupling is presented. The results show significant coupling effects between hairs, when placed close to each other and at lower flow frequencies. The length of the perturbing hair has a significant influence on the coupling effect on the reference hair sensor. The measurements were in good agreement with the theoretical models, which was implemented for 2 hairs and extended to include the situation of 3 hairs. The experimental and theoretical results provide important guidelines towards optimal sensor array designs while simultaneously shedding some light on biophysical effects in closely-packed hair sensor arrays.

6.9. References

[1] J.A.C. Humphrey and F.G. Barth, *"Medium flow-sensing hairs: Biomechanics and models"*, Advances in Insect physiology – Insect Mechanics and control, Ed. by J. Casas and S.J. Simpson, Elsevier (2007) Vol. 34, pp. 1-80.

[2] T. Shimozawa, T. Kumagai, Y. Baba, *"Structural and functional scaling of the cercal wind-receptor hairs in cricket"*, J. Comp. Physiol. A (1998) 183, pp. 171-186

[3] O. Dangles, D. Pierre, C. Magal, F. Vannier and J. Casas, *"Ontogeny of air-motion sensing in cricket"*, J. Exp. Biol. (2006) Vol. 209, pp. 4363-4370.

[4] J. Casas, T. Steinmann and G. Krijnen, *"Why do insects have such a high density of flowsensing hairs*? *Insights from the hydromechanics of biomimetic MEMS sensors"*, J. R. Soc. Interface (2010) Vol. 7 (51), pp. 1487-1495.

[5] (a) B. Bathellier, F.G. Barth, J.T. Albert and J.A.C. Humphrey, *"Viscosity-mediated motion coupling between pairs of trichobothria on the leg of the spider Cupiennius salei"*, J. Comp. Physiol. A (2005) Vol. 191, pp. 733-746. (b) Erratum: J. Comp. Physiol. A (2010) Vol. 196, p. 89

[6] B. Cummins, T. Gedeon, I. Klapper and R. Cortez, "*Interaction between arthropod filiform hairs in a fluid environment*", J. of Theo. Biol. (2007) Vol. 247, pp. 266-280

[7] J.J. Heys, T. Gedeon, B.C. Knott, Y.Kim, *"Modeling arthropod filiform hair motion using the penalty immersed boundary method"*, J. Biomechanics. (2008) 41, pp. 977-984.

[8] Pasupathy S. Alagirisamy, George Jeronimidis and Valerie Le Moàl, *"An investigation of viscous-mediated coupling of crickets cercal hair sensors using a scaled up model"*, Proc. SPIE, San diego, USA (2009) Vol. 7401, pp. -------

[9] G.C. Lewin and J. Hallam, "*A computational fluid dynamics model of viscous coupling of hairs*", J. Comp. Physiol. A (2010) Vol. 196, No. 6, pp. 385-395

[10] J. Palka, R.B. Levine, M. Schubiger, *"The circus-to-giant inter-neuron system of crickets. I. Some attributes of the sensory cells"*, J. Comp. Physiol. (1977), Vol. 119, pp. 267-283.

[11] M.A. Landolfa and J.P. Miller, *"Stimulus-response propertiesof cricket cercal filiform receptors"*, J. Comp. Physiol. A (1995), Vol. 177, pp. 749-757.

[12] F.E. Theunissen and J.P. Miller, *"Representation of sensory information in the cricket cercal sensory system. II. Information theoretic calculation of system accuracy and optimal tuning curve widths of four primary interneurons"*, J. Neurophysiol. (1991), Vol. 66, pp. 1690-1703.

[13] M.A. Landolfa and G.A. Jacobs, *"Direction sensitivity of the filiform hair population of the cricket cercal system"*, J. Comp. Physiol. A (1995), Vol. 177, pp. 759-766.

[14] J.A.C. Humphrey, R. Devarakonda, I. Iglesias, F.G. Barth, *"Dynamics of arthropod filiform hairs. I. Mathematical modeling of the hair and air motions"*, Philosophical Transactions: Biological Science (1993) 340, pp. 423-444.

[15] Bjorn Hagedoorn,*"Viscous coupling between bio-inspired hair sensors"*, Master thesis, University of Twente (2009).

[16] http://www.polytec.com/eu/

[17] H-E. de Bree, V.B. Svetovoy, R. Raangs, R. Visser, *"The very near field, theory, simulations and measurements"*, Proc. of 11th International Congress on Sound and Vibration, St. Petersburg, (2004).

[18] F.G. Barth, U. Wastl, J.A.C. Humphrey, R. Devarakonda, *"Dynamics of arthropod filiform hairs. II. Mechanical parameters of spider trichobothria (Cupiennes salei Keys.)"*, Philosophical Transactions: Biological Science (1993) 340, pp. 445-461.

7

Conclusions and outlook

In a nutshell...

This chapter provides the closing remarks on the presented work on the development of artificial hair sensor arrays. A brief account on the achievements and the challenges faced during this work is presented. Further, an overview of the possible future works in continuation to the presented work is discussed here.

7.1. Introduction

This work reports the successful realization of artificial hair sensor arrays capable of sensing low-frequency air flows. These hair sensors are inspired by filiform hairs on the cerci of crickets. Each hair sensor features SU-8 hair, mounted on a suspended silicon-rich nitride membrane with a pair of Aluminum electrodes. The silicon substrate acts as a bottom electrode, forming a pair of sensor capacitors. Whenever there is an air flow, the hair deflects and induces a membrane tilt causing a change in the sensor capacitors. Flow sensing is then performed by means of differential capacitive sensing technique. The choice of capacitive read-out is made over alternative techniques like (i) piezo-resistivity [1] and (ii) hot-wire or thermal anemometry [2]. In most hair-based flow sensors (see Chapter 1), piezo-resistive technique is preferred for its simple read-out circuitry. Thermal anemometry has shown

remarkable flow sensitivities, but at the expense of relatively large power consumption. Contrarily, capacitive read-out offers a read-out technique with relatively low-power consumption, insensitive to external temperature variations but all at the expense of complex read-out circuitry. However, our choice of capacitive read-out can be justified in its capability of simultaneous actuation and sensing [3] and in using smart techniques to reduce the complexity of the read-out circuits to individually address an array of sensors (see outlook section).

During the design phase, a sensor model was implemented and a figure of merit was defined to provide design guidelines for achieving optimal sensor performance (Chapter 2). The presented hair sensor arrays were extensively characterized for their quality and functionality. By replacing chromium with aluminum as electrode material, the sensitivity-deteriorating effect due to membrane curvature (observed in our previous generation of hair sensor arrays) is greatly eliminated. This is obviously observed by means of a series of successful and well-characterized results obtained from the sensor arrays (chapter 3). The sensor arrays show a flow amplitude threshold of 0.85 mm/s at 400 Hz at 1 kHz bandwidth and show a clear figure-of-eight directional sensitivity.

Comparison of our artificial hair sensor arrays to their natural counterparts becomes inevitable. When compared to the performance of the actual filiform hairs, the performance of the presented hair sensors is roughly ~2.5 orders worse, however, still marking a significant milestone: it can be argued that these sensors are about ~3.5 orders of magnitude more sensitive than the first generation of hair-sensors (although these were never characterized equally well). One interesting aspect about the filiform hairs is their exceptional performance even at the thermal-mechanical noise levels. In comparison, our sensor arrays do suffer from poor signal-to-noise ratio. Further ways of improvements are pointed out by the figure of merit, defined as the product of sensitivity and usable bandwidth. However, such a definition clearly ignores the thermal-mechanical noise effects in it. Recently, an estimation of thermal-mechanical noise level at a given bandwidth of 1 kHz for the presented sensor arrays was made and it shows a flow sensitivity limit of ~50 μm/s [4]. Inclusion of thermal-mechanical noise effect in the figure of merit, along with sensitivity and bandwidth will certainly influence the design of optimized sensors. On the other hand, significant contribution to the noise levels is made due to the presence of undesired parasitic capacitance. This is due to the fact that the presented sensors use the silicon substrate as the common electrode of the sensor capacitor. Thus, new technologies are sought to drastically improve the sensor performance (see outlook section).

The shape of the hairs is an important aspect of the sensor dynamics, which determines the drag-torque receptive capability and the moment of inertia of the hairs. Nature-like SU-8 hairs, which closely resemble the actual filiform hairs, are fabricated successfully using a bottom-side exposure method (chapter 4). Most importantly, by means of this technique it is now possible to fabricate sensors featuring hairs of varying length. Previously, SU-8 hairs were fabricated by conventional top-side exposure method, which limits the option of incorporating variations in the hair length. A proof-of-concept fabrication flow using bottom-side exposure is developed and demonstrated in this work. The fabricated samples were analyzed to find the optimal exposure time and the effect of different design parameters of the aluminum pattern on the hair geometry. The exposure times chosen in the investigations seem to indicate that the hair length and hair diameter do not critically depend on it. By this new approach, the length of the artificial hairs can be determined at the design phase, by appropriately defining the opening diameter of the mask pattern.

Small torsional stiffness for the sensor springs is pointed out by the figure of merit as an important requirement for optimal sensor performance. With compliant springs featuring small torsional stiffness, there is a possible risk of undesired mode coupling (i.e. vertical mode of movements interfering with the intended torsional rotation of the sensor membrane) during normal sensor operation. To prevent this, a high ratio between the stiffness of undesired mode to desired mode is also considered as a design rule. Design analysis presented in chapter 5 suggests two possible options: (i) using an alternate structural material and (ii) using a modified cross-section for the springs. For the first option of choosing a new structural material, SU-8 is seen as a promising option and a proof-of-concept fabrication process flow is devised to verify the feasibility of this new approach. Results from the test structures presented numerous technological challenges, as expected. The SU-8 test structures show large undesired curvature due to the intrinsic residual stress and stress-gradients. As a second option, silicon-rich nitride springs with a T-shaped cross-section are considered. For realization it is important to fabricate controllable and uniform-width trenches on the substrate. A novel technique to fabricate trenches using edge lithography is developed and shown to be feasible.

However, both investigated technologies to realize optimal springs were sufficiently disruptive relative to the current fabrication schemes that up to date none of both has been implemented to be a full fledged fabrication process. The obtained results indicate that the T-beam approach has more potential and is likely to yield better reproducibility (e.g. as judged from the problems with variations in the quality of SU-8 layers in dependence of shelf time) than the SU-8 approach. Further it is remarked that the important ratio of K/S_0 strongly depends on the moments of inertia I_{xx}, I_{yy} and I_p where the latter can be approximated in simple geometries by $I_p=I_{xx}+I_{yy}$. This means that there are both opportunities and limitations to improving this ratio. For a large ratio ideally I_{yy} approaches 0. However, in this case the limited in-plane (parallel to the substrate) flexibility would become a problem. Hence, this points at more robust solutions for springs made of lower Young's' modulus materials.

Further, interesting results have been observed with viscosity-mediated coupling between the artificial hair sensors (chapter 6). A microfabricated chip was realized featuring three artificial hair sensors arranged in a row, at different inter-hair distances from each other. Characterization results confirm the presence of viscosity-mediated coupling between the hair sensors. The results show significant coupling effects between hairs, when placed close to each other (normalized distance, $s/d < 6$) and at lower flow frequencies. The length of the perturbing hair also has a significant influence on the coupling effect on the reference hair sensor. The measurements were in good agreement with the theoretical models. Interestingly, new results show that when three hair sensors are placed close to each other, in addition to the primary coupling effect (between the perturbing hair and the reference hair), the secondary coupling effects (between the perturbing hairs on either side of the reference hair) also become prominent. The experimental and theoretical results provide important guidelines towards optimal sensor array designs while simultaneously shedding light on biophysical effects in closely-packed hair sensor arrays.

7.2. Outlook

An ideal system of artificial hair sensor arrays, inspired by the filiform hairs of crickets, preferably has the following operational characteristics: (i) 3-dimensional flow-field sensing capability (ii) high single-hair sensitivity, (iii) smart interfacing to address each of the hair

sensors in an array (in real time and with high signal-to-noise ratio) (iv) low power consumption and (v) mechanically robust system. The presented hair sensor arrays are only at the primary level on comparison to such an ideal system. This section highlights the possible future works, aimed at the realization of above said ideal sensor system.

Towards flow-field measurements

One of the important motivations for realizing flow-sensor arrays is to be able to measure the flow-field. To realize it, sensor arrays should have the facility to individually address each sensor in an array. But the presented sensor arrays are electrically inter-connected to each other and hence together they form a large sensor capacitor. Primary investigations of addressing four different sensor arrays simultaneously using frequency division multiplexing has been successfully implemented [5] and now this work is being extended for addressing individual sensors in an array. For the case of addressing each sensor, one of the critical issues is the presence of the parasitic capacitance which hinders the detection of small capacitive changes from the sensor. In the present generation of sensor arrays, parasitic capacitance originates from the conductive silicon substrate which is used as the common electrode of the sensor capacitor. Such undesired parasitic capacitance can be greatly reduced by using Silicon on insulator (SOI) wafers and patterning the bottom electrodes to be insulated from the substrate by trench insulation. In the recent generation, impressive performance from a single-hair sensor has been demonstrated [1].

Interestingly, the implemented arrays were used in the application of dipole source-localization, inspired by the lateral-line sensors found in fish [6]. The lateral-line system of fish consists of a bundle of hair-like structures, capable of sensing the flow field around it to localize their prey or predator. The presented sensor arrays are successfully proven to be able to detect and reconstruct the dipole flow field [6]. Additionally, in parallel to this work, artificial flow sensor arrays operating in water were developed [7].

Towards 3D-flow measurements

One notable difference between the actual filiform hairs and our sensors is the nature of the substrate on which the hairs are arranged. Unlike our sensors, the filiform hairs are arranged on a conical surface of the cerci, thus facilitating 3-dimensional flow sensing [8]. Prior to the presented work, early attempts were made by gluing three individual chips with artificial hair sensors in a cerci-like arrangement (see figure 7.1) [9]. However, it has to be noted that this arrangement was not functional and no real characterization were made so far.

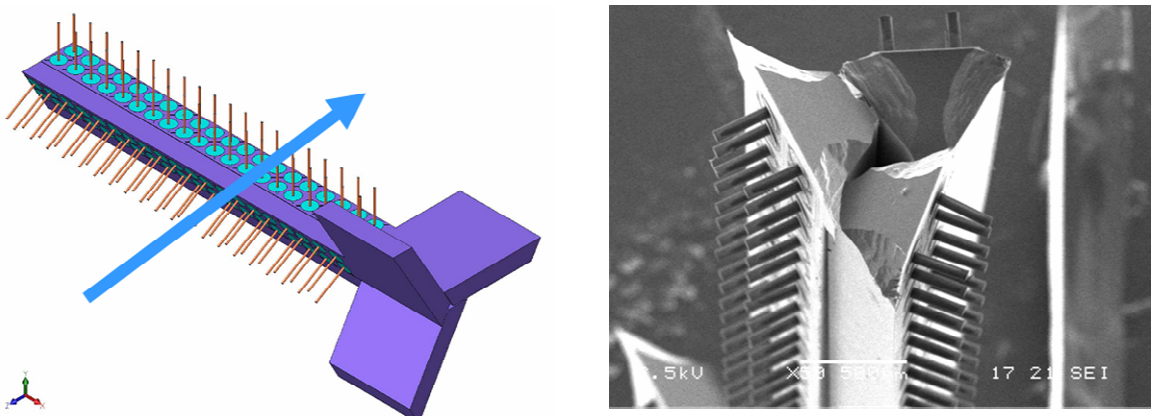

Figure 7.1 *Model schematic of the hair sensor featuring the nature-like hair [9]*

Nature-like hairs

Integrating the nature-like hairs (as presented in chapter 4) to our sensors, requires a new process flow. The key technique involved in realizing nature-like hairs is the bottom-side exposure of SU-8 layers. To facilitate this approach in the existing process flow, we need:

(i) Wafer-through holes to enable back-side UV-light exposure.
(ii) A sacrificial layer (to release the sensor membranes) which will also act as etch-stop layer for the wafer-through holes.
(iii) A transparent material for the sensor membranes.
(iv) An electrode layer that also acts as a mask for exposure of the nature-like hair.

Figure 7.2 shows a model schematic of a sensor featuring nature-like hair. The implementation of bottom-exposure on the real device layers needs a thorough process optimization, in order to replicate the results obtained in chapter 4. First steps of such a process integration was performed by realizing high aspect-ratio, wafer-through holes of ~80 µm diameter using standard DRIE process (Deep Reactive Ion Etching). A layer of SU-8 (~5 µm) was used as the etch mask and silicon-rich nitride as an etch-stop layer. The next step would be to coat a thick layer of SU-8 on top and characterize the quality of the resulting hairs as function of exposure parameters.

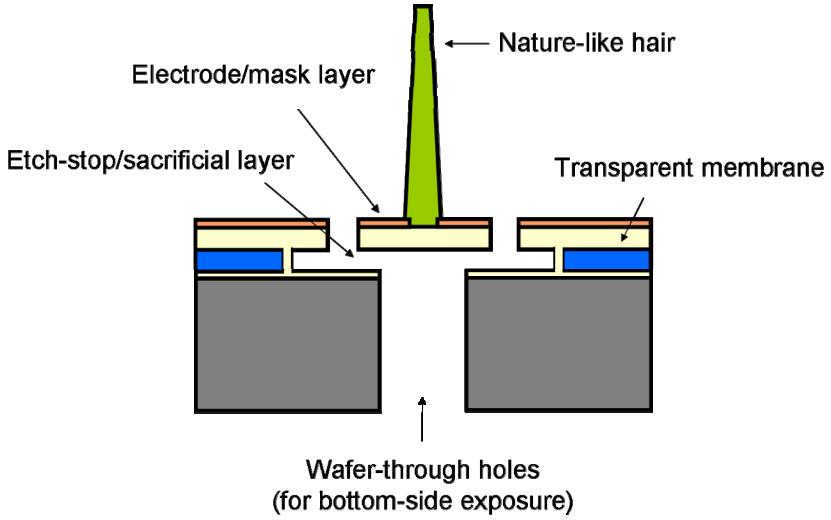

Figure 7.2 *Model schematic of the hair sensor featuring the nature-like hair*

Optimal springs

While the possibility of implementing flexible sensor springs with SU-8 was not successful due to challenges faced during the process, it is still suggested that such an investigation be performed with other potential polymer materials. For instance, Parylene-C [10,11] has specifically positive aspects (low-stress, low Young's modulus, etc) and reliable layer deposition (conformal coating by LPCVD). However, this process will require extensive characterization on compatibility of Parylene-C to the existing process. Alternatively one may also look at more complicated (by design, preferably not more complicated in processing) spring-structures, if needed with virtual rotational axes. In this approach one could also look

at nonlinear effects (spring-stiffening) for structures that are stressed beyond their linear limits.

The pre-requisite for realizing optimal springs indicated by the figure of merit is to have small torsional stiffness for the sensor springs. More emphasis is given on designing sensor springs with high vertical-to-torsional stiffness ratio, to reduce the undesired mode coupling. This will also improve stability along the vertical direction. However, small torsional stiffness for sensor springs can pose a possible risk on robustness of the sensor. With compliant springs, the sensor membranes could be easily subjected to pull-in and stiction during the desired mode of operation. In order to prevent stiction, possible solutions suggested are: (i) applying anti-stiction coating to the layers, (ii) incorporating "dimples" or "bumps" to reduce the effective contact surface area and (iii) surface roughening of the contact layers [12]. The recent generation of hair sensors is fabricated with anti-stiction bumps underneath the sensor membranes [13].

Parametric amplification

Parametric amplification is a process which can occur when two periodic signals of different frequencies are mixed non-linearly. Such non-linear mixing could result in the amplification of the output signal. Recently, parametric amplification is being investigated on the hair sensor arrays [14]. Inferences from these investigations will be greatly helpful in building up an optimal artificial flow sensory system.

In summary, optimized hair sensor arrays capable of sensing low-frequency air flows have been realized and characterized. Ways to improve the sensor design and performance have been investigated and some have been shown to lead to better sensor performance. Device physics tells us that more improvements are possible but some of the changes required are accompanied by new challenges, lying ahead of accomplishing the dream of real-time flow perception using artificial sensor arrays.

7.3. References

[1] C. Liu, "*Micromachined biomimetic artificial haircell sensors"*, Bioinspiration & Biomimetics (2007) Vol. 2, S162.

[2] H-E. de Bree, "*The microflown"*, PhD thesis, University of Twente, Enschede, the Netherlands (1997)

[3] J. Floris, N. Izadi, R.K. Jaganatharaja, R.J. Wiegerink, T.S.J. Lammerink, and G.J.M. Krijnen, "*Adaptation for frequency focusing and increased sensitivity in biomimetic flow sensors using electrostatic spring softening*", Proc. of 14th Int. conf. on solid-state sensors, actuators and microsystems (Transducers & Eurosensors '07), Lyon, France, 10-14 June 2007.

[4] A.M.K. Dagamseh and G.J.M. Krijnen, " Thermal noise estimation in bio-inspired hair flow sensor", Proc. of 1st International conference on Natural and Biomimetic Mechanosensing, Dresden, Germany, 26-28 Oct, 2009.

[5] A.M.K. Dagamseh, C.M. Bruinink, H. Droogendijk, R.J. Wiegerink, T.S.J. Lammerink and G.J.M. Krijnen, *"Engineering of biomimetic hair-flow sensor arrays dedicated to high-resolution flow field measurements"*, IEEE Sensors conference, Hawaii, USA, 1-4 Nov, 2010, pp. 2251-2254.

[6] A.M.K. Dagamseh, T.S.J. Lammerink, C.M. Bruinink, R.J. Wiegerink and G.J.M. Krijnen, "*Dipole source localization using bio-mimetic flow sensor arrays*", Procedia Chemistry (2009), Vol. 1, pp. 891-894.

[7] N. Izadi, *"Bio-inspired MEMS aquatic flow sensor arrays"*, PhD thesis, University of Twente, Enschede, the Netherlands (2011).

[8] T. Steinmann, J. Casas, G. Krijnen and O. Dangles, "*Air-flow sensitive hairs: boundary layers in oscillatory flows around arthropod appendages*", J. of Exp. Biol. (2006) 209, pp. 4398-4408

[9] G. J. M. Krijnen, J. Floris, M.A. Dijkstra, T.S.J. Lammerink, and R.J. Wiegerink, "*Bio-mimetic micromechanical adaptive flow-sensor arrays*", Proc. of SPIE Europe Micro-technologies for the New Millennium 2007, 2-4 May 2007

[10] Y. Suzuki and Y-C. Tai, *"Micromachined high-aspect-ratio Parylene spring and its application to low-frequency accelerometers"*, J. Microelectromech. Syst. (2006) 15(5), pp. 1364-1370

[11] S. Aoyagi, K. Furukawa, D. Ono, K. Ymashita, T. Tanaka, K. Inoue, M. Okuyama, *"Development of a capacitive ultrasonic sensor having parylene diaphragm and characterization of receiving performance of arrayed device"*, Sensors and Actuators A (2008) 145-146, pp. 94-102.

[12] N. Tas, T. Sonnenberg, H. Jansen, R. Legtenberg and M. Elwenspoek, *"Stiction in surface micromachining"*, J. Microelectromech. Syst. (1996) 6, pp. 385-397.

[13] H. Droogendijk, *current work*.

[14] H. Droogendijk, C.M. Bruinink, R.G.P. Sanders and G.J.M. Krijnen, "*Non-degenerate parametric amplification and filtering in biomimetic hair flow sensors*", Proc. Transducers 2011, June 5 – 9, 2011, Beijing, paper W3P.016, pp. 2034 – 2038.

8

Summary

8.1. Summary

Crickets, like many other arthropods, are evolved with an astonishing sensory system, which plays a vital role in their survival. Located at the rear-end of the crickets, are a pair of sensory appendages called cerci, carrying numerous mechano-receptive filiform hairs. These filiform hairs are capable of detecting minute air fluctuations in their environment, down to 0.03 mm/s amplitude. The filiform hairs respond by rotation to air movement, thereby initiating a neural response. The cercal filiform hair sensors have fascinated biologists and recently inspired MEMS engineers in developing a new line of bio-inspired mechanical sensors (Chapter 1).

This work reports the successful realization of artificial hair sensor arrays capable of sensing low-frequency air-flows. Each hair sensor consists of a SU-8 hair, mounted on a suspended silicon-rich nitride membrane with a pair of Aluminum electrodes. The silicon substrate acts as a bottom electrode, forming a pair of sensor capacitors. When there is an air flow, the hair deflects and induces a membrane tilt causing a change in the sensor capacitors. Flow sensing is then performed employing a differential capacitive sensing technique. By means of a sensor model, a figure of merit is defined to derive the design guidelines for optimal sensor performance (Chapter 2). For optimal performance, sensors need long and thin

hairs and small torsional stiffness for the sensor springs. The inter-spacing between the hairs placed in an array also plays a significant role in optimal performance.

A new generation of hair sensor arrays are designed and implemented by incorporating design and technological improvements (Chapter 3). The presented hair sensor arrays were extensively characterized for their quality and functionality. By replacing Chromium with Aluminum as electrode material, the sensitivity-deteriorating effect due to membrane curvature (observed in our previous generation of hair sensor arrays) is greatly eliminated. The sensor arrays show a flow amplitude threshold of 0.85 mm/s at 400 Hz at 1 kHz bandwidth and show a clear figure-of-eight directional sensitivity.

The hair geometry plays an important role in determining the drag-torque receptive capability and the moment of inertia of the hairs. Unlike artificial hairs, the actual filiform hairs on cerci are of an elongated-conical shape. In this work, new approaches to realize SU-8 hairs, which closely resemble natural hairs, are demonstrated by means of a proof-of-concept fabrication flow (Chapter 4). Nature-like SU-8 hairs are fabricated successfully using a bottom-side exposure method. Further, by means of this new technique it is now possible to fabricate sensors featuring hairs of varying lengths. The fabricated samples clearly showed appreciable variations in the hair length and shape depending on the diameter of the mask openings. Hence, by appropriately defining the opening diameter of the mask pattern, the length of the SU-8 hair can be determined at the design phase.

Small torsional stiffness for the sensor springs is sought as indicated by the figure of merit for optimal sensor performance. But with compliant springs, there is a risk of undesired mode coupling (e.g. vertical modes of movement interfering with the intended torsional rotation of the sensor membrane) during normal sensor operation. To prevent this, a high ratio between the stiffness of the undesired mode to the desired mode is also considered as a design rule. Design analysis suggests two possible options (Chapter 5): (i) using an alternate structural material and (ii) using a modified cross-section for the springs.

For the first option of using alternate structural material, SU-8 is seen as a promising choice and a proof-of-concept fabrication process flow is devised. Results from the test structures presented numerous technological challenges, as expected. The SU-8 test structures show large undesired curvature due to the intrinsic residual stress and stress-gradients. On the other hand, for the second option, silicon-rich nitride springs with a T-shaped cross-section are considered. To realize them, it is important to fabricate controllable and uniform-width trenches on the substrate. A novel technique to fabricate trenches using edge lithography is developed and shown to be feasible. However, both investigated technologies to realize optimal springs were considerably disruptive relative to the current fabrication scheme, that up to date neither of both has been implemented in a full fledged fabrication process.

Artificial hair sensors are arranged in highly dense arrays which could lead to non-negligible viscosity-mediated coupling between the hairs. A dedicated microfabricated chip was realized featuring three artificial hair sensors arranged in a row, at different inter-hair distances from each other (Chapter 6). Characterization results confirm the presence of viscosity-mediated coupling between the hair sensors. The results show significant coupling effects between hairs, when placed close to each other (normalized distance, $s/d < 6$) and at lower flow frequencies. Interestingly, our results show that when three hair sensors are placed close to each other, in addition to the primary coupling effect (between the perturbing hair and the reference hair), the secondary coupling effects (between the perturbing hairs on either side of the reference hair) also become prominent. The experimental and theoretical results provide important guidelines towards optimal sensor array designs while simultaneously shedding light on biophysical effects in closely-packed hair sensor arrays.

8.2. Samenvatting

Krekels zijn, net als vele andere geleedpotigen, geëvolueerd met een verbazingwekkend sensorisch systeem, dat een centrale rol in hun essentiële overlevingsmechanisme speelt. Aan de achterzijde van de krekel bevindt zich een paar sensorische organen (cerci), die tal van mechanisch-gevoelige haren bevatten. Onder andere zogeheten filiforme (dunnen) haren die in in staat zijn om zeer kleine lucht verplaatsingen (met ondergrens van snelheden van 0,03 mm/s) in hun omgeving te detecteren. De filiforme haren worden door deze lucht bewegingen geroteerd, hetgeen vervolgens een neurale respons initieert. Deze filiforme haren hebben biologen gefascineerd en MEMS ingenieurs onlangs geïnspireerd bij de ontwikkeling van een nieuw type bio-geïnspireerde mechanische sensoren (hoofdstuk 1).

Dit onderzoek beschrijft de succesvolle realisatie van kunstmatige haarsensoren die in staat zijn om laag-frequente luchtstromen waar te nemen. Elke haarsensor bestaat uit een SU-8 haar, die is geplaatst op een vrijhangend membraan van silicium-rijk nitride met een paar aluminium elektroden. Het silicium substraat fungeert als een onderelektrode, die tesamen met de aluminium bovenelectrodes de condensator van de sensor vormen. Bij de aanwezigheid van een luchstroom roteert de haar waardoor het membraan kantelt en dus een capaciteitsverandering in de condensator van de sensor optreedt. Het uitlezen van deze capaciteitsverandering wordt vervolgens gedaan door middel van een differentieel detectietechniek. Met behulp van een sensor model is een kwaliteits-indicator gedefinieerd om ontwerp-richtlijnen af te leiden voor een optimale prestatie van de haarsensor (hoofdstuk 2). Voor een optimale prestatie hebben sensoren lange en dunne haren nodig en een kleine torsieveerstijfheid. De tussenafstand van de haren in een reeks van sensoren speelt tevens een belangrijke rol in de optimale prestatie.

Een nieuwe generatie van haarsensoren is ontworpen door de verbeteringen in het design en de technologie te intergreren (hoofdstuk 3). De gepresenteerde haarsensor is uitvoerig gekarakteriseerd op kwaliteit en functionaliteit. Door chroom als electrode materiaal te vervangen door aluminium was het mogelijk om het negatieve effect van membraankromming (waargenomen bij onze eerste-generatie van haarsensoren) op de sensorgevoeligheid te elimineren. De haarsensoren tonen een drempelwaarde van 0,85 mm/s voor een 400 Hz signaal (gemeten bij een bandbreedte van 1 kHz) en een duidelijke directionele gevoeligheid.

De geometrie van de haar speelt een belangrijke rol in het bepalen van het receptief vermogen, middels de invloed op de stromingsweerstand, en het traagheidsmoment van de haren. De filiforme haren op cerci zijn, in tegenstelling tot kunstmatige haren, langwerpig en kegelvormig. Dit onderzoek toont nieuwe benaderingen om SU-8 haren te realiseren die sterke overeenkomsten vertonen met natuurlijke filiforme haren door middel van een concept fabricageproces (hoofdstuk 4). Natuur-gelijkende SU-8 haren zijn succesvol gemaakt met behulp van een belichtingsmethode via de onderkant van de wafer. Het is tevens met deze nieuwe techniek mogelijk om sensoren te vervaardigen met haren van verschillende lengtes. De resultaten tonen een duidelijke afhankelijkheid van haar-lengte en -vorm van de diameter van de maskeropening. Door op de juiste diameters in het maskerpatroon te definieren kan de lengte van de SU-8 haren reeds worden bepaald in de ontwerpfase.

Een kleine torsieveerstijfheid van de sensor is, zoals aangegeven door de kwaliteits-indicator, nodig voor een optimale prestatie van de sensor. Bij compliante veren bestaat een risico dat ongewenste moduskoppelingen (zoals trillingen in de verticale richtingen) tijdens de normale werking van de sensor interfereren met de beoogde rotatie van het membraan. Om dit te voorkomen is een grote verhouding van de stijfheden van ongewenste en gewenste modi

tevens een vereiste in het ontwerp. De analyse van het ontwerp suggereert twee mogelijke opties (hoofdstuk 5): (i) door een alternatief constructiemateriaal te gebruiken en (ii) door een aangepaste dwarsdoorsnede van de torsiebalken te gebruiken.

Voor de eerste optie van het gebruik van alternatief constructiemateriaal is SU-8 een veelbelovende keuze en een concept fabricageproces is bedacht. De resultaten van de teststructuren tonen, zoals verwacht, talrijke technologische uitdagingen. De SU-8 teststructuren hebben een grote ongewenste kromming als gevolg van intrinsieke stress en stress-gradiënten in het SU-8. Voor de tweede optie zijn silicium-rijke nitride veren met een t-vormige dwarsdoorsnede overwogen. Om deze te kunnen realiseren is het belangrijk om controleerbare en uniforme openingen in het substraat te vervaardigen. Een nieuwe techniek om met behulp van rand-lithografie openingen in een substraat te vervaardigen is ontwikkeld tot een haalbaar fabricageproces. Echter, beide onderzochte opties om optimale veren te realiseren zijn lastig te implementeren in het huidige fabricageproces en daarom is tot op heden hiertoe geen poging ondernomen.

Kunstmatige haarsensoren kunnen gerangschikt worden in zeer dichte matrices waarin koppeling tussen de haren kan plaats vinden t.g.v. viskeuze effecten. Een speciale chip, waarop structuren van drie kunstmatige haarsensoren op rij met verschillende tussenafstanden zijn gedefinieerd, is gerealiseerd (hoofdstuk 6). De resultaten bevestigen de aanwezigheid van viskeuze koppeling tussen de haarsensoren. De koppelingseffecten worden significant als de haren dicht bij elkaar zijn geplaatst (genormaliseerde afstand, s/d <6) en bij lagere flow frequenties. Uit onze resultaten blijkt dat wanneer drie haarsensoren dicht bij elkaar zijn geplaatst in aanvulling op het primaire koppelingseffect (tussen de storende haren en de referentie haar) tevens het secundaire koppelingseffecten (tussen de storende haren aan weerszijden van de referentie haar) prominent wordt. De experimentele en theoretische resultaten leveren belangrijke richtlijnen voor optimale sensor ontwerpen en werpen tegelijktijd licht op de biofysische effecten in dichtgepakte sensoren.

9

Appendices

A. Process flow for hair sensor arrays (Chapter 3)

Step	Process	Parameters	Remarks
01	Substrate selection - Silicon <100> DSP (low resistance)	Orientation: <100> Diameter: 100mm Thickness: 525 +/- 25 µm Polished: Double side Resistivity: 0.010-0.015 Ω·cm Type: p	To be used as common electrode Use at least 6 dummy wafers (SSP)
02	Cleaning Standard	HNO_3 (100%) Selectipur: MERCK HNO_3 (69%) VLSI: MERCK • Beaker 1: fumic HNO_3 (100 %), 5 min • Beaker 2: fumic HNO_3 (100 %), 5 min • Quick Dump Rinse <0.1 µS • Beaker 3: boiling (95 °C) HNO_3 (69 %), 10 min • Quick Dump Rinse <0.1 µS • Spin drying	
03	Etching HF (1%)	HF (1%) VLSI: MERCK • Quick Dump Rinse <0.1 µS • Spin drying	For native oxide removal

04	LPCVD Si_3N_4 stoichiometric	Tempress LPCVD F1 Tube: F1 • Program: Nitr01 • SiH_2Cl_2 flow: 22 sccm • NH_3 flow: 66 sccm • Temperature: 800 °C • Pressure: 200 mTorr • Stress: 1,09±40 MPa Deposition rate: 4-6 nm/min N_f: 2.008	Use blank dummies Thickness: 200 nm Time: ~42 min Isolation /etch-stop layer
05	Ellipsometer Measurement	Plasmos Ellipsometer	
06	Cleaning Standard	HNO_3 (100%) Selectipur: MERCK HNO_3 (69%) VLSI: MERCK • Beaker 1: fumic HNO_3 (100 %), 5 min • Beaker 2: fumic HNO_3 (100 %), 5 min • Quick Dump Rinse <0.1 µS • Beaker 3: boiling (95 °C) HNO_3 (69 %), 10 min • Quick Dump Rinse <0.1 µS • Spin drying	
07	Micro Balance Measurement	Satotius Micro Balance	Before deposition
08	LPCVD Poly Si - 590°C	Tempress LPCVD Tube: F2 Program: senspoly • SiH4 flow: 50 sccm • temperature: 590°C • pressure: 250mTorr • deposition rate: 3.3 nm/min • Stress: 30 MPa	Layer thickness: 600 nm. In some of the batches, 800 nm.
09	Micro Balance Measurement	Satotius Micro Balance	After deposition Calculate layer thickness (conversion factor: 26.5 nm/mg).
10	Annealing	Furnace B3 Standby temperature: 800 °C • Program: ANN-1100-N_2 • Temp.: 1100 °C • Gas: N_2 • Flow: 1 l/min • Ramp: 20 °C/min	To lower stress Time: 2 hrs
11	Lithography - Priming (liquid)	HexaMethylDiSilazane (HMDS) • Dehydration bake (120 °C): 5 min • Spin program: 4 (4000 rpm, 20 sec)	
12	Lithography - Coating Olin907-17	• Spinning acceleration: 4000 rpm/s • Spinning speed: 4000 rpm • Spinning time: 20 s	

		• Prebake (95 °C): 90 s	
13	Lithography - Alignment & Exposure Olin 907-17 (EVG 20)	Electronic Vision Group 20 Mask Aligner • Hg-lamp: 12 mW/cm^2 • Exposure Time: 4 s	Mask: SACRI
14	Lithography - Development Olin Resist	Developer: OPD4262 • After Exposure Bake (120 °C): 60 sec Development: • Time: 30 sec in Beaker 1 • Time: 15-30 sec in Beaker 2 • Quick Dump Rinse <0.1 □S • Spin drying	
15	Optical microscopic inspection - Lithography	Microscope	
16	Plasma etching chamber (Etske) - Cleaning	Elektrotech PF310/340 Select chamber for desired etch process Select electrode for desired etch process • Electrode temp.: 10°C or 25°C • O2 flow: 20sccm • pressure: 50mTorr • power: 150W • DC-Bias: 780V Chamber is clean when plasma color is white	
17	Plasma etching of Poly Si (Etske)	Elektrotech PF310/340 Clean chamber Styros electrode • Electrode temp.: 10 °C • SF_6 flow: 30 sccm • CHF_3 flow: 7 sccm • O_2 flow: 11 sccm • Pressure: 100 mTorr • Power: 75 W Use etch steps of maximal 5 min. Vent system and continue. Small gaps exhibit RIE-lag!	Etch rate poly-Si: 500 nm/min, End of etching is done on visual inspection by optical microscope (time = ~80 s). Note: use dummy wafers on top of quartz electrode in order to increase uniformity and decrease etch rate
18	Stripping of Olin PR	Wet-Bench 3-2 HNO3 (100%) Selectipur: MERCK 100453 • Time: 20min • Quick Dump Rinse <0.1µS • Spin drying • Visual microscopic inspection	
19	Cleaning Standard	HNO_3 (100%) Selectipur: MERCK HNO_3 (69%) VLSI: MERCK • Beaker 1: fumic HNO_3 (100 %), 5 min • Beaker 2: fumic HNO_3 (100 %), 5 min • Quick Dump Rinse <0.1 µS • Beaker 3: boiling (95 °C) HNO_3 (69 %), 10 min • Quick Dump Rinse <0.1 µS • Spin drying	

20	Etching HF (1%)	HF (1%) VLSI: MERCK • Quick Dump Rinse <0.1 µS • Spin drying	Native oxide removal Time: ~1 min
21	LPCVD SiRN - low stress	Tempress LPCVD/HC Tube: G3 • SiH_2Cl_2 flow: 150 sccm • NH_3 flow: 50 sccm • Temperature: 830 °C • Pressure: 200 mTorr • Program: SiRN02 Deposition rate: ~6.6 nm/min N_f: 2.18	NOTE: use G4 LPCVD furnace for more uniform layers. deposition time: 122 min layer thickness: 1000 nm deposition rate: 8.2 nm/min stress ~300 MPa
22	Ellipsometer Measurement	Plasmos Ellipsometer	
23	Cleaning Standard	HNO_3 (100%) Selectipur: MERCK HNO_3 (69%) VLSI: MERCK • Beaker 1: fumic HNO_3 (100 %), 5 min • Beaker 2: fumic HNO_3 (100 %), 5 min • Quick Dump Rinse <0.1 µS • Beaker 3: boiling (95 °C) HNO_3 (69 %), 10 min • Quick Dump Rinse <0.1 µS • Spin drying	
24	Lithography - Priming (liquid)	HexaMethylDiSilazane (HMDS) • Dehydration bake (120 °C): 5 min • Spin program: 4 (4000 rpm, 20 sec)	
25	Lithography - Coating Olin907-17	• Spinning acceleration: 4000 rpm/s • Spinning speed: 4000 rpm • Spinning time: 20 s • Prebake (95 °C): 90 s	
26	Lithography - Alignment & Exposure Olin 907-17 (EVG 20)	Electronic Vision Group 20 Mask Aligner • Hg-lamp: 12 mW/cm^2 • Exposure Time: 4 s	Mask: MEMBR
27	Lithography - Development Olin Resist	Developer: OPD4262 • After Exposure Bake (120 °C): 60 sec Development: • Time: 30 sec in Beaker 1 • Time: 15-30 sec in Beaker 2 • Quick Dump Rinse <0.1 □S • Spin drying	
28	Optical microscopic inspection - Lithography	Microscope	
29	Plasma etching chamber (Etske) -	Elektrotech PF310/340 Select chamber for desired etch process Select electrode for desired etch process	

	Cleaning	• Electrode temp.: 10°C or 25°C • O2 flow: 20sccm • pressure: 50mTorr • power: 150W • DC-Bias: 780V Chamber is clean when plasma color is white	
30	Plasma etching of SiRN (Etske)	Elektrotech PF310/340 Dirty chamber Styros electrode • Electrode temp.: 10°C • CHF3 flow: 25sccm • O2 flow: 5sccm • pressure: 10mTorr • power: 75W Etchrate SiN = 50nm/min (for VDC=-460V) Etchrate SiN = 75 nm/min (for VDC = -580V) Etchrate Olin resist = 95nm/min If DC-Bias < 375V apply chamber clean	Etch rate SiRN = 65 nm/min, selectivity towards OLIN907 = 0.8 and silicon = 2. End of etching is done on visual inspection (t = 18-20 min). NOTE: use 100W as RF power to maintain the SiRN etch rate.
31	Stripping of Olin PR by oxygen plasma	Tepla 300 Barrel Etcher (2.45 GHz) Ultra clean system only (no metals except Al) • See list with recipes in CR • O_2 flow: 200 sccm (50 %) • Power: up to 1000 W • Pressure: 1 mbar • Time: see recipes on the wall	Program 06 Time: 30 min
32	Cleaning Standard	HNO_3 (100%) Selectipur: MERCK HNO_3 (69%) VLSI: MERCK • Beaker 1: fumic HNO_3 (100 %), 5 min • Beaker 2: fumic HNO_3 (100 %), 5 min • Quick Dump Rinse <0.1 µS • Beaker 3: boiling (95 °C) HNO_3 (69 %), 10 min • Quick Dump Rinse <0.1 µS • Spin drying	
33	Etching HF (1%)	HF (1%) VLSI: MERCK • Quick Dump Rinse <0.1 µS • Spin drying	For native oxide removal
34	Sputtering of Al, resist compatible (Oxford)	Oxford PL 400 • Program: 100 nm Al pos 1 Change program parameters to: • Power: 700W • Pressure: 10 mTorr Deposition rate (100 mm wafer): 88 nm/min	Thickness: 100 nm
35	Lithography - Priming (liquid)	HexaMethylDiSilazane (HMDS) • Dehydration bake (120 °C): 5 min • Spin program: 4 (4000 rpm, 20 sec)	
36	Lithography - Coating	• Spinning acceleration: 4000 rpm/s • Spinning speed: 4000 rpm	

	Olin907-17	• Spinning time: 20 s • Prebake (95 °C): 90 s	
37	Lithography - Alignment & Exposure Olin 907-17 (EVG 20)	Electronic Vision Group 20 Mask Aligner • Hg-lamp: 12 mW/cm^2 • Exposure Time: 4 s	Mask: ELECT
38	Lithography - Development Olin Resist	Developer: OPD4262 • After Exposure Bake (120 °C): 60 sec Development: • Time: 30 sec in Beaker 1 • Time: 15-30 sec in Beaker 2 • Quick Dump Rinse <0.1 □S • Spin drying	
39	Optical microscopic inspection - Lithography	Microscope	
40	Wet etching of Al	Wet-Bench 2 Aluminium etch: MERCK 115435.2500 • Temp.: 55°C • Quick Dump Rinse <0.1µS • Spin drying Etch rates = 1µm/min	NEW recipe: Al etching in OPD4262 (etch rate ~ 14 nm/min, t = 6 min)
41	Stripping of polymers in HNO_3, multipurpose	Wet-Bench 2 HNO3 (100%) Selectipur: MERCK 100453 • Beaker 1: HNO3 (100%) 20min • Quick Dump Rinse <0.1µS • Spin drying	
42	Lithography - Coating SU-8 100 (Delta20)	Süss MicroTec Spinner Delta 20 • Spin program: 8 30 sec at 500 rpm, acc. 100 rpm/min 30 sec at 1000 rpm, acc. 100 rpm/min • Thickness: >380 µm • Prebake (95 °C): 10 min at 50 °C 30 min at 65 °C 210 min at 95 °C let it cool down on the hot plate	First Layer Leave the wafers on the flat surface of the hot plate for 2 hrs before soft bake Wait overnight before exposure to avoid stiction (and use tape on the mask)
43	Lithography - Alignment & Exposure SU-8 100 (EVG)	Electronic Vision Group 20 Mask Aligner • Hg-lamp: 12 mW/cm^2 • Exposure Time: 120 sec	Mask: HAIR1 Soft contact
44	Lithography - Coating SU-8 100 (Delta20)	Süss MicroTec Spinner Delta 20 • Spin program: 5 30 sec at 500 rpm, acc. 100 rpm/min 30 sec at 3000 rpm, acc. 100 rpm/min • Thickness: >380 □m • Prebake (95 °C): 10 min at 50 °C 30 min at 65 °C	Second Layer Wait overnight before exposure to avoid stiction (and use tape on the mask)

<table>
<tr><td></td><td></td><td>210 min at 95 °C
let it cool down on the hot plate</td><td></td></tr>
<tr><td>45</td><td>Lithography - Alignment & Exposure SU-8 100 (EVG)</td><td>Electronic Vision Group 20 Mask Aligner
• Hg-lamp: 12 mW/cm^2
• Exposure Time: 150-170 sec</td><td>Mask: HAIR2
Soft contact</td></tr>
<tr><td>46</td><td>Lithography - Development SU-8 100</td><td>Developer: RER600
• After Exposure Bake:
10 min at 50 °C
10 min at 65 °C
50 min at 75 °C
cool down in 5 °C steps each for 5 min
Development:
• Time: 40 min (40 cycles of 1 min)
• Method: Spray
• IPA Rinse
• Spin drying</td><td>Do not rinse with water
Do not use high speed spin drying</td></tr>
<tr><td>47</td><td>Plasma etching of poly-Silicon (Oxford Plasma Lab 100)</td><td>Oxford Plasma Lab 100
<table><tr><th>Parameters</th><th>Value</th></tr><tr><td>SF_6 (sccm)</td><td>120</td></tr><tr><td>He (sccm)</td><td>20</td></tr><tr><td>ICP (W)</td><td>600</td></tr><tr><td>CCP (W)</td><td>0</td></tr><tr><td>Pressure (mTorr)</td><td>10</td></tr><tr><td>Electrode temp. (°C)</td><td>20</td></tr></table></td><td>Note: prior to etching perform O2 plasma step (40 min, TEPLA 300) to remove residual SU8 and a 1 min pre-etch (CCP 3W, Vdc -20V) on Oxford Plasma Lab 100.
Use special gas permeable cap on top of the wafer.</td></tr>
</table>

B. Process flow for nature-like hairs (Chapter 4)

Step	Process	Parameters	Remarks
01	Substrate selection – Borofloat or Pyrex	Diameter: 100 mm Thickness: 500 µm	
02	Cleaning Standard	HNO_3 (100%) Selectipur: MERCK HNO_3 (69%) VLSI: MERCK • Beaker 1: fumic HNO_3 (100 %), 5 min • Beaker 2: fumic HNO_3 (100 %), 5 min • Quick Dump Rinse <0.1 µS • Beaker 3: boiling (95 °C) HNO_3 (69 %), 10 min • Quick Dump Rinse <0.1 µS • Spin drying	
03	Sputtering of Al, resist compatible (Oxford)	Oxford PL 400 • Program: 100 nm Al pos 1 Change program parameters to:	Thickness: 100 nm

		• Power: 700W • Pressure: 10 mTorr Deposition rate (100 mm wafer): 88 nm/min	
04	Lithography - Priming (liquid)	HexaMethylDiSilazane (HMDS) • Dehydration bake (120 °C): 5 min • Spin program: 4 (4000 rpm, 20 sec)	
05	Lithography - Coating Olin907-17	• Spinning acceleration: 4000 rpm/s • Spinning speed: 4000 rpm • Spinning time: 20 s • Prebake (95 °C): 90 s	
06	Lithography - Alignment & Exposure Olin 907-17 (EVG 20)	Electronic Vision Group 20 Mask Aligner • Hg-lamp: 12 mW/cm^2 • Exposure Time: 4 s	Mask: ELECT
07	Lithography - Development Olin Resist	Developer: OPD4262 • After Exposure Bake (120 °C): 60 sec Development: • Time: 30 sec in Beaker 1 • Time: 15-30 sec in Beaker 2 • Quick Dump Rinse <0.1 □S • Spin drying	
08	Optical microscopic inspection - Lithography	Microscope	
09	Wet etching of Al	Wet-Bench 2 Aluminium etch: MERCK 115435.2500 • Temp.: 55°C • Quick Dump Rinse <0.1µS • Spin drying Etch rates = 1µm/min	NEW recipe: Al etching in OPD4262 (etch rate ~ 14 nm/min, t = 6 min)
10	Stripping of polymers in HNO_3, multipurpose	Wet-Bench 2 HNO3 (100%) Selectipur: MERCK 100453 • Beaker 1: HNO3 (100%) 20min • Quick Dump Rinse <0.1µS • Spin drying	
11	Lithography - Coating SU-8 100 (Delta20)	Süss MicroTec Spinner Delta 20 • Spin program: 8 30 sec at 500 rpm, acc. 100 rpm/min 30 sec at 1000 rpm, acc. 100 rpm/min • Thickness: >380 µm • Prebake (95 °C): 10 min at 50 °C 30 min at 65 °C 210 min at 95 °C let it cool down on the hot plate	First Layer Leave the wafers on the flat surface of the hot plate for 2 hrs before soft bake Wait overnight before exposure to avoid stiction
12	Lithography - Coating SU-8 100 (Delta20)	Süss MicroTec Spinner Delta 20 • Spin program: 5 30 sec at 500 rpm, acc. 100 rpm/min	Second Layer Wait overnight before

		30 sec at 3000 rpm, acc. 100 rpm/min • Thickness: >380 □m • Prebake (95 °C): 10 min at 50 °C 30 min at 65 °C 210 min at 95 °C let it cool down on the hot plate	exposure to avoid stiction
13	Lithography - Alignment & Exposure SU-8 100 (EVG)	Electronic Vision Group 20 Mask Aligner • Hg-lamp: 12 mW/cm^2 • Exposure Time: 160-250 sec	Bottom-side exposure using Flood exposure recipe.
14	Lithography - Development SU-8 100	Developer: RER600 • After Exposure Bake: 10 min at 50 °C 10 min at 65 °C 50 min at 75 °C cool down in 5 °C steps each for 5 min Development: • Time: 25 min (25 cycles of 1 min) • Method: Spray • IPA Rinse • Spin drying	Do not rinse with water Do not use high speed spin drying

C. Process flow for SU-8 springs and membranes (Chapter 5)

Step	Process	Parameters	Remarks
01	Substrate selection - Silicon <100> DSP (low resistance)	Orientation: <100> Diameter: 100mm Thickness: 525 +/- 25 µm Polished: Double side Resistivity: 0.010-0.015 Ω·cm Type: p	
02	Cleaning Standard	HNO_3 (100%) Selectipur: MERCK HNO_3 (69%) VLSI: MERCK • Beaker 1: fumic HNO_3 (100 %), 5 min • Beaker 2: fumic HNO_3 (100 %), 5 min • Quick Dump Rinse <0.1 µS • Beaker 3: boiling (95 °C) HNO_3 (69 %), 10 min • Quick Dump Rinse <0.1 µS • Spin drying	
03	Etching HF (1%)	HF (1%) VLSI: MERCK • Quick Dump Rinse <0.1 µS • Spin drying	For native oxide removal
04	LPCVD Si_3N_4 stoichiometric	Tempress LPCVD F1 Tube: F1 • Program: Nitr01 • SiH_2Cl_2 flow: 22 sccm	Use blank dummies Thickness: 200 nm Time: ~42 min

		• NH_3 flow: 66 sccm • Temperature: 800 °C • Pressure: 200 mTorr • Stress: 1,09±40 MPa Deposition rate: 4-6 nm/min N_f: 2.008	Isolation /etch-stop layer
05	Ellipsometer Measurement	Plasmos Ellipsometer	
06	Cleaning Standard	HNO_3 (100%) Selectipur: MERCK HNO_3 (69%) VLSI: MERCK • Beaker 1: fumic HNO_3 (100 %), 5 min • Beaker 2: fumic HNO_3 (100 %), 5 min • Quick Dump Rinse <0.1 µS • Beaker 3: boiling (95 °C) HNO_3 (69 %), 10 min • Quick Dump Rinse <0.1 µS • Spin drying	
07	Micro Balance Measurement	Satotius Micro Balance	Before deposition
08	LPCVD Poly Si - 590°C	Tempress LPCVD Tube: F2 Program: senspoly • SiH4 flow: 50 sccm • temperature: 590°C • pressure: 250mTorr • deposition rate: 3.3 nm/min • Stress: 30 MPa	Layer thickness: 600 nm.
09	Micro Balance Measurement	Satotius Micro Balance	After deposition Calculate layer thickness (conversion factor: 26.5 nm/mg).
10	Annealing	Furnace B3 Standby temperature: 800 °C • Program: ANN-1100-N_2 • Temp.: 1100 °C • Gas: N_2 • Flow: 1 l/min • Ramp: 20 °C/min	To lower stress Time: 2 hrs
11	Lithography - Priming (liquid)	HexaMethylDiSilazane (HMDS) • Dehydration bake (120 °C): 5 min • Spin program: 4 (4000 rpm, 20 sec)	
12	Lithography - Coating Olin907-17	• Spinning acceleration: 4000 rpm/s • Spinning speed: 4000 rpm • Spinning time: 20 s • Prebake (95 °C): 90 s	
13	Lithography - Alignment & Exposure	Electronic Vision Group 20 Mask Aligner • Hg-lamp: 12 mW/cm^2	Mask: SACRI

	Olin 907-17 (EVG 20)	• Exposure Time: 4 s	
14	Lithography - Development Olin Resist	Developer: OPD4262 • After Exposure Bake (120 °C): 60 sec Development: • Time: 30 sec in Beaker 1 • Time: 15-30 sec in Beaker 2 • Quick Dump Rinse <0.1 □S • Spin drying	
15	Optical microscopic inspection - Lithography	Microscope	
16	Plasma etching chamber (Etske) - Cleaning	Elektrotech PF310/340 Select chamber for desired etch process Select electrode for desired etch process • Electrode temp.: 10°C or 25°C • O2 flow: 20sccm • pressure: 50mTorr • power: 150W • DC-Bias: 780V Chamber is clean when plasma color is white	
17	Plasma etching of Poly Si (Etske)	Elektrotech PF310/340 Clean chamber Styros electrode • Electrode temp.: 10 °C • SF_6 flow: 30 sccm • CHF_3 flow: 7 sccm • O_2 flow: 11 sccm • Pressure: 100 mTorr • Power: 75 W Use etch steps of maximal 5 min. Vent system and continue. Small gaps exhibit RIE-lag!	Etch rate poly-Si: 500 nm/min, End of etching is done on visual inspection by optical microscope (time = ~80 s). Note: use dummy wafers on top of quartz electrode in order to increase uniformity and decrease etch rate
18	Stripping of Olin PR	Wet-Bench 3-2 HNO3 (100%) Selectipur: MERCK 100453 • Time: 20min • Quick Dump Rinse <0.1µS • Spin drying • Visual microscopic inspection	
19	Cleaning Standard	HNO_3 (100%) Selectipur: MERCK HNO_3 (69%) VLSI: MERCK • Beaker 1: fumic HNO_3 (100 %), 5 min • Beaker 2: fumic HNO_3 (100 %), 5 min • Quick Dump Rinse <0.1 µS • Beaker 3: boiling (95 °C) HNO_3 (69 %), 10 min • Quick Dump Rinse <0.1 µS • Spin drying	
20	Lithography - Coating SU-8 2 (Delta20)	Süss MicroTec Spinner Delta 20 • Spin program: 5 10 sec at 500 rpm, acc. 100	Wait 1 hr before exposure to avoid stiction

		rpm/min 30 sec at 3000 rpm, acc. 100 rpm/min • Thickness: 2 μm • Prebake (95 °C): 2 min	
21	Lithography - Alignment & Exposure SU-8 2 (EVG)	Electronic Vision Group 20 Mask Aligner • Hg-lamp: 12 mW/cm^2 • Exposure Time: 12 sec	Mask: MEMBR Soft contact
22	Lithography - Coating SU-8 100 (Delta20)	Süss MicroTec Spinner Delta 20 • Spin program: 8 30 sec at 500 rpm, acc. 100 rpm/min 30 sec at 1000 rpm, acc. 100 rpm/min • Thickness: >380 μm • Prebake (95 °C): 10 min at 50 °C 30 min at 65 °C 210 min at 95 °C let it cool down on the hot plate	First Layer Leave the wafers on the flat surface of the hot plate for 2 hrs before soft bake Wait overnight before exposure to avoid stiction (and use tape on the mask)
23	Lithography - Alignment & Exposure SU-8 100 (EVG)	Electronic Vision Group 20 Mask Aligner • Hg-lamp: 12 mW/cm^2 • Exposure Time: 120 sec	Mask: HAIR1 Soft contact
24	Lithography - Coating SU-8 100 (Delta20)	Süss MicroTec Spinner Delta 20 • Spin program: 5 30 sec at 500 rpm, acc. 100 rpm/min 30 sec at 3000 rpm, acc. 100 rpm/min • Thickness: >380 □m • Prebake (95 °C): 10 min at 50 °C 30 min at 65 °C 210 min at 95 °C let it cool down on the hot plate	Second Layer Wait overnight before exposure to avoid stiction (and use tape on the mask)
25	Lithography - Alignment & Exposure SU-8 100 (EVG)	Electronic Vision Group 20 Mask Aligner • Hg-lamp: 12 mW/cm^2 • Exposure Time: 150-170 sec	Mask: HAIR2 Soft contact
26	Lithography - Development SU-8 100	Developer: RER600 • After Exposure Bake: 10 min at 50 °C 10 min at 65 °C 50 min at 75 °C cool down in 5 °C steps each for 5 min Development: • Time: 40 min (40 cycles of 1 min) • Method: Spray • IPA Rinse • Spin drying	Do not rinse with water Do not use high speed spin drying

<table>
<tr>
<td>27</td>
<td>Plasma etching of poly-Silicon (Oxford Plasma Lab 100)</td>
<td>Oxford Plasma Lab 100
<table>
<tr><th>Parameters</th><th>Value</th></tr>
<tr><td>SF_6 (sccm)</td><td>120</td></tr>
<tr><td>He (sccm)</td><td>20</td></tr>
<tr><td>ICP (W)</td><td>600</td></tr>
<tr><td>CCP (W)</td><td>0</td></tr>
<tr><td>Pressure (mTorr)</td><td>10</td></tr>
<tr><td>Electrode temp. (°C)</td><td>20</td></tr>
</table>
</td>
<td>Note: prior to etching perform O2 plasma step (40 min, TEPLA 300) to remove residual SU8 and a 1 min pre-etch (CCP 3W, Vdc -20V) on Oxford Plasma Lab 100.
Use special gas permeable cap on top of the wafer.</td>
</tr>
</table>

D. Process flow for trenches using edge lithography (Chapter 5)

Step	Process	Parameters	Remarks
01	Substrate selection - Silicon <100> DSP (low resistance)	Orientation: <100> Diameter: 100mm Thickness: 525 +/- 25 µm Polished: Double side Resistivity: 0.010-0.015 Ω·cm Type: p	
02	Cleaning Standard	HNO_3 (100%) Selectipur: MERCK HNO_3 (69%) VLSI: MERCK • Beaker 1: fumic HNO_3 (100 %), 5 min • Beaker 2: fumic HNO_3 (100 %), 5 min • Quick Dump Rinse <0.1 µS • Beaker 3: boiling (95 °C) HNO_3 (69 %), 10 min • Quick Dump Rinse <0.1 µS • Spin drying	
03	Etching HF (1%)	HF (1%) VLSI: MERCK • Quick Dump Rinse <0.1 µS • Spin drying	For native oxide removal
04	LPCVD SiRN - low stress	Tempress LPCVD/HC Tube: G3 • SiH_2Cl_2 flow: 150 sccm • NH_3 flow: 50 sccm • Temperature: 830 °C • Pressure: 200 mTorr • Program: SiRN02 Deposition rate: ~6.6 nm/min N_f: 2.18	NOTE: use G4 LPCVD furnace for more uniform layers. Deposition time: 3 min Layer thickness: 20 nm
05	Ellipsometer Measurement	Plasmos Ellipsometer	
06	LPCVD TEOS	Tempress LPCVD B4 Tube: B4 TEOS	Deposition time:

		• Bubbler: 40°C • N_2 flow: 250 sccm • Temperature: 700 °C • Pressure: 150 mTorr • Program: TEOS 05 Deposition rate: 10.7 nm/min N_f: 1.44	10 min Layer thickness: 100 nm
07	Micro Balance Measurement	Satotius Micro Balance	Before deposition
08	LPCVD Poly Si - 590°C	Tempress LPCVD Tube: F2 Program: senspoly • SiH4 flow: 50 sccm • temperature: 590°C • pressure: 250mTorr • deposition rate: 3.3 nm/min • Stress: 30 MPa	Layer thickness: 100 nm. Time: 30 min
09	Micro Balance Measurement	Satotius Micro Balance	After deposition Calculate layer thickness (conversion factor: 26.5 nm/mg).
10	Cleaning Standard	HNO_3 (100%) Selectipur: MERCK HNO_3 (69%) VLSI: MERCK • Beaker 1: fumic HNO_3 (100 %), 5 min • Beaker 2: fumic HNO_3 (100 %), 5 min • Quick Dump Rinse <0.1 µS • Beaker 3: boiling (95 °C) HNO_3 (69 %), 10 min • Quick Dump Rinse <0.1 µS • Spin drying	
11	Ellipsometer Measurement	Plasmos Ellipsometer	
12	LPCVD SiRN - low stress	Tempress LPCVD/HC Tube: G3 • SiH_2Cl_2 flow: 150 sccm • NH_3 flow: 50 sccm • Temperature: 830 °C • Pressure: 200 mTorr • Program: SiRN02 Deposition rate: ~6.6 nm/min N_f: 2.18	NOTE: use G4 LPCVD furnace for more uniform layers. deposition time: 122 min layer thickness: 200 nm deposition rate: 8.2 nm/min
13	Ellipsometer Measurement	Plasmos Ellipsometer	
14	Cleaning Standard	HNO_3 (100%) Selectipur: MERCK HNO_3 (69%) VLSI: MERCK • Beaker 1: fumic HNO_3 (100 %), 5 min • Beaker 2: fumic HNO_3 (100 %), 5 min • Quick Dump Rinse <0.1 µS	

		• Beaker 3: boiling (95 °C) HNO_3 (69 %), 10 min • Quick Dump Rinse <0.1 µS • Spin drying	
15	Lithography - Priming (liquid)	HexaMethylDiSilazane (HMDS) • Dehydration bake (120 °C): 5 min • Spin program: 4 (4000 rpm, 20 sec)	
16	Lithography - Coating Olin907-17	• Spinning acceleration: 4000 rpm/s • Spinning speed: 4000 rpm • Spinning time: 20 s • Prebake (95 °C): 90 s	
17	Lithography - Alignment & Exposure Olin 907-17 (EVG 20)	Electronic Vision Group 20 Mask Aligner • Hg-lamp: 12 mW/cm^2 • Exposure Time: 5 s	Mask: BMASK
18	Lithography - Development Olin Resist	Developer: OPD4262 • After Exposure Bake (120 °C): 60 sec Development: • Time: 30 sec in Beaker 1 • Time: 15-30 sec in Beaker 2 • Quick Dump Rinse <0.1 □S • Spin drying	
19	Optical microscopic inspection - Lithography	Microscope	
20	Plasma etching chamber (Etske) - Cleaning	Elektrotech PF310/340 Select chamber for desired etch process Select electrode for desired etch process • Electrode temp.: 10°C or 25°C • O2 flow: 20sccm • pressure: 50mTorr • power: 150W • DC-Bias: 780V Chamber is clean when plasma color is white	
21	Plasma etching of SiRN (Etske)	Elektrotech PF310/340 Dirty chamber Styros electrode • Electrode temp.: 10°C • CHF3 flow: 25sccm • O2 flow: 5sccm • pressure: 10mTorr • power: 75W Etchrate SiN = 50nm/min (for VDC=-460V) Etchrate SiN = 75 nm/min (for VDC = -580V) Etchrate Olin resist = 95nm/min If DC-Bias < 375V apply chamber clean	Etch rate SiRN = 65 nm/min, selectivity towards OLIN907 = 0.8 and silicon = 2. End of etching is done on visual inspection (t = 4.5 min). NOTE: use 100W as RF power to maintain the SiRN etch rate.
22	Stripping of Olin PR	Wet-Bench 3-2 HNO3 (100%) Selectipur: MERCK 100453 • Time: 20min	

		• Quick Dump Rinse <0.1µS • Spin drying • Visual microscopic inspection	
23	Cleaning Standard	HNO_3 (100%) Selectipur: MERCK HNO_3 (69%) VLSI: MERCK • Beaker 1: fumic HNO_3 (100 %), 5 min • Beaker 2: fumic HNO_3 (100 %), 5 min • Quick Dump Rinse <0.1 µS • Beaker 3: boiling (95 °C) HNO_3 (69 %), 10 min • Quick Dump Rinse <0.1 µS • Spin drying	Flurocarbon residues from plasma etching can be removed by oxidizing the wafers in B2 furnace for 10 min and etching in HF until the wafers turn hydrophobic.
24	Dry oxidation at 950 °C	Furnace A2 Standby temperature: 700 °C • Program: Dry950 • Temp: 700 °C • Gas: O_2	LOCOS Time: 30 min
25	Etching of SiRN using Hot H_3PO_4	Wet bench 3-1 H_3PO_4 (100%) MERCK • Temp: 180 °C • Quick Dump Rinse <0.1 µS • Spin drying	Retraction etching width: 100 nm Time: 25 min
26	Etching of PolySi using TMAH	Wet bench 2 TMAH (5%) • Temp: 70 °C	Isotropic etching width: ~2 µm (depends on the target trench width) Time: ~2 min PolySi etch rate: 400-700 nm/min SiRN etch rate: 0.01 nm/min
27	Etching of SiRN using Hot H_3PO_4	Wet bench 3-1 H_3PO_4 (100%) MERCK • Temp: 180 °C • Quick Dump Rinse <0.1 µS • Spin drying	Removal of SiRN Time: 25-35 min
28	Etching of TEOS in BHF (7:1)	Wet bench 3-3 NH_4F/HF (7:1) VLSI: BASF • Quick Dump Rinse <0.1 µS • Spin drying	TEOS etch rate: 180 nm/min Time: 90 s
29	Etching of PolySi using TMAH	Wet bench 2 TMAH (5%) • Temp: 70 °C	Poly Si removal Time: <2 min PolySi etch rate: 400-700 nm/min SiRN etch rate: 0.01

			nm/min
30	Etching of SiRN using Hot H_3PO_4	Wet bench 3-1 H_3PO_4 (100%) MERCK • Temp: 180 °C • Quick Dump Rinse <0.1 µS • Spin drying	Layer thickness: 20 nm Time: 3-4 min
31	Plasma etching of Si (Adixen)	Adixen SE Cleaning before etching • Temp: -100 °C • SF6 flow: 100 sccm • O2 flow: 10 sccm • Valve: 100% • ICP: 500 W • CCP: 20 W (20/20 ms, on/off) • SH: 200 mm	Time: 10 min
32	Etching HF (50%)	HF (50%) VLSI: MERCK • Quick Dump Rinse <0.1 µS • Spin drying	Remove TEOS Time: 1 min
33	Etching of SiRN using Hot H_3PO_4	Wet bench 3-1 H_3PO_4 (100%) MERCK • Temp: 180 °C • Quick Dump Rinse <0.1 µS • Spin drying	Removal of SiRN Time: 3-4 min

10

Acknowledgements

First and foremost, my sincere thanks to Amma-Ayya for being my big source of motivation and for the unconditional love, that you keep showering on me, which reaches me across several thousands of miles.

It is hard to believe that the last four and a half years have passed so quickly and here, as I write these lines, it feels as though it all began just yesterday. These four years or so have turned out to be the most significant part of both my career and personal life. These years have introduced many new persons into my life. Making use of this part of the thesis, I want to thank everyone, who has made a lasting impact on me.

Sifu Gijs, I truly consider myself lucky to have worked with you. You have been a wonderful person and you have been a huge inspiration to me all these years. I have always learnt something, in every meeting - be it, in the office or outside. I am greatly indebted for all your critical remarks and support especially during the writing of the thesis. I enjoyed the fatherly advice you gave me, as I was leaving to Mexico City – "Don't do anything over there, which I did not do" ☺.

Thanks to Miko, for accepting me as a part of TST group. Erwin and Meint, thanks for sharing your overwhelming knowledge during several of our discussions and helping me out with several processing in the cleanroom. Erwin, especially, for the superb fun we had in Cancun. Remco, for the nice discussions we had at many occasions and delightful times in Cancun (along with Ceska). Marcel, for helping me with the measurements and for all the nice times during our Cilia meetings. It is a great pleasure to have met and known talented scientists across Europe through bi-annual Cilia project meetings. Many thanks to Jerome,

George, Greg, Emma and many others for all the fruitful discussions during the Cilia meetings. Pasu, for your friendship and the nice times we had. Thanks to my PhD promotion committee members, for spending their time in reading my work and for their suggestions.

At any point of time, my friends have been the best part. I am greatly indebted to my friends, more than anything, for always being with me throughout this adventurous journey. Nima, very happy to have found in you, a best buddy. Ours has been a natural friendship and almost every bit of our times in TST has been very memorable. I had great times in organizing parties and travels, exploring most of Europe and US. More than anything, I owe you a lot for helping me in the most significant moments of my PhD life. Susy, for being my beloved '*schatje*' and sending me surprising early morning sms' or cute cards every once in a while. It has been pleasant memories to be in the company of you and Kees. Chris, for the charming friendship and all the insightful(?) cleanroom sessions. All the times we shared are so memorable and all our inside-jokes bring a flashing smile in me readily. It is a great pleasure to be in the company of you, Irisha and the twins.

Faizans, for the unique family-like friendship we share, right from the beginning. Your company has always been wonderful, despite the annoying language factor ☺. Faizan, especially, I am indebted to all your helps and support in the neediest times and for the nice times we spent discussing about world cinema. I will be hanging around you guys for the years to come and keep giving you some hard times ☺. Amir, for being my very special friend and a great teacher. I have learnt many things from you on music, art, literature and philosophy. It's always a sheer pleasure just to be an audience to your stand-ups. Somy, for being my loveable friend of similar wavelength and for all the funny chats we share, every now and then. Katja, for the good friend in you and for all the nice times we had during trips and parties. Hope to have great fun, for the years to come. Great to be friends with Esly, Matin, Hadi, Narges and Mahdiar and thanks for all the fun times we shared over the years.

Two persons are very special and have been a big support throughout the PhD life (and especially during the writing of my thesis): Baanu (Mubassira), for our trusted friendship and for all the pleasant times in sharing and listening to your trademark- "*mokka jokes*" ☺. Allwin, for the memorable friendship we share all these years and for all our expertly(?) discussions on the world politics, philosophy and cricket. I owe you both a lot!

Chakku baby (a.k.a. Shahina), for all the fun (esp. about "*mallu"*s) and a charming friendship we share right from the very beginning. I have always enjoyed your company. By the way, you still owe me 30 dinners! Rajagopal (mama), for the fun-filled first year. Bjorn, for being a good and tech-savvy friend throughout your study and after that. Joost, for the charming office-mate I found in you. I am indebted for all our Sunday discussions on physics and explaining me with ease.

Yiping, for your great help in cleanroom (in particular, with edge lithography) and for the fun times we had during conferences in Portugal and Athens. Ahmad, for the nice times we had in several of our project-related meetings and for all the mutual fun we constantly make at each other. Harmen, for helping me out with models and support during the needy times. Pino, for keeping the whole TST smiling with your timely jokes and for your great *promotie* movies. I am a big fan of them. Robert, for the fun in coffee corner and during TST sailing trip. Henri and Theo, for the brief nice moments we had shared. Henk, Ganesh and Satie, for your helps at different points of time. Srini, Imran and Sandeep, for the nice times and great help during the initial years. Shrey, for the nice times we had during your stay at UT and Rajeev, for the nice and scary "paranormal" times we had ☺. Leon, Johan, and Wabe for the nice moments we had during the ECS sessions and at conferences in Athens and Leon.

Marcel, Kechun, Doekle, Dennis, Marcus, Florian and many others for the nice times we had as a part of TST group.

I am also greatly indebted to Bert (GL, ASML) and Marten (PL, ASML), along with my new colleagues, for their support and providing a fun-filled work environment. Special thanks to Dorothe for spending time to shoot the cover photograph of my thesis. Thanks to Erik (Xelvin b.v.) for his constant support and Peter te Boome, for his help.

Sinie, for your love and special care. Belen, my beloved Spanish room mate, for your great company. I had great moments - watching all the horror movies (with 4D effects ☺) and our Kung-fu lessons with Frensly. Thanks to all my Mexican and German friends (from Hamburg and Freiburg), for the nice moments.

Best moments throughout my life have been the times I spent reading books. This time frame of four years, however, has introduced two important authors, who have affected me. Osho, in whose writings/discourses, I find the words of my own. Reading him, is such a delight and enlightening. Charu Nivedhita, whose writings create a constant stir inside me and open up a new horizon with every new page.

My all-time best friends from India – Gandhi, Deepz and Sri, for their charm and love, which reaches me, wherever I am. KR, my best friend since child hood, for all your support and friendship throughout the years. I can't think anyone other than you, with whom I can be myself the most and cherish the memorable portions of our childhood and schooling. Sorry and thanks ra, as always. Bala, Gayathri, Kiruthiga akka, Visu and Vijay, for their love and support. My beloved Slovakian sister, Ida, for her constant inspiration and warmth. Thanks to all my school teachers of Chinmaya Vidhyalaya, Rajapalayam for providing me a unique schooling experience.

It was great to have known and spend some memorable moments with Ami, Uncle and Api. Ami, for the charming and hilarious friend in you, hiding the generation gap between us. And Ado, Nadeembhai and Sana, for the pleasant chats. For the memorable times I had spent with the little ones - my beloved Aakif, Muhammad and Miru, my princess.

Bathu and Sivaram, my beloved sister and brother-in-law, for their endless support and love. Shashank, my four-year-old nephew (who is now the head-of-my-family), for his ever-charming weekend chats. My two-week-old, cute little niece, Sahana, whom I am dying to meet.

Sabz, this journey would not be complete without acknowledging your support and company in the past 4 years. Thanks for the greatest friendship we share and for the radiant beam of love and trust, you constantly shine upon me, which keeps me going. And for all the special moments we've had, I might need a separate book to write more.

And, as always, 1 2 3.